The Journal of Gemmology

Volume 38 / No. 4 / 2022

Demantoid from Iran

Heat-Treated Pink-to-Red Spinel

'Star of David' Pattern and Macrosteps on Corundum Crystals

Fluorcarletonite, a New Gem Material

SSEF
SCHWEIZERISCHES GEMMOLOGISCHES INSTITUT
SWISS GEMMOLOGICAL INSTITUTE
INSTITUT SUISSE DE GEMMOLOGIE

Gem-A
THE GEMMOLOGICAL ASSOCIATION OF GREAT BRITAIN

SSEF

SCHWEIZERISCHES GEMMOLOGISCHES INSTITUT
SWISS GEMMOLOGICAL INSTITUTE
INSTITUT SUISSE DE GEMMOLOGIE

ORIGIN DETERMINATION · TREATMENT DETECTION

DIAMOND GRADING · PEARL TESTING

EDUCATION · RESEARCH

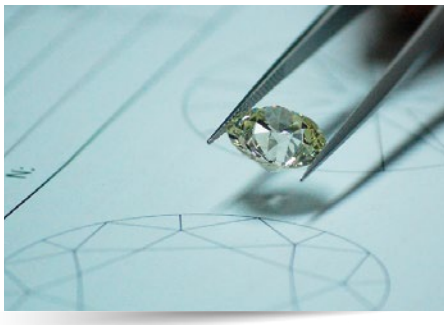

THE SCIENCE OF GEMSTONE TESTING™

Aeschengraben 26, 4051 Basel, Switzerland Tel. +41 61 262 06 40 Fax + 41 61 262 06 41 admin@ssef.ch www.ssef.ch

The Journal of Gemmology

Volume 38 / No. 4 / 2022

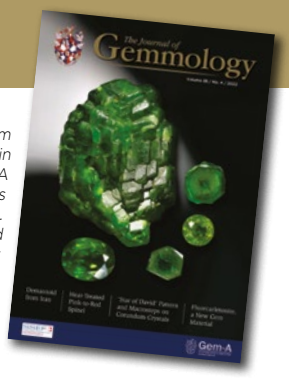

Cover photo: *Demantoid has been mined from serpentinite-hosted deposits in Kerman Province in south-east Iran for the past two decades. A mineralogical and gemmological overview of this material is provided on pp. 329-347 of this issue. The crystal specimen shown here weighs 51 g, and clockwise to the right are a 1.08 ct slice, a 0.65 ct faceted stone, a 1.28 ct slice and a 1.41 ct faceted oval. Specimens courtesy of The Gem Trader (Cave Creek, Arizona, USA); photo by Brad Payne.*

COLUMNS

Photo by B. Rahimzadeh

ARTICLES

Photo by Brad Payne

Photo by V. Pardieu

The Journal is published by Gem-A in collaboration with SSEF and with the support of AGL.

Gem-A THE GEMMOLOGICAL ASSOCIATION OF GREAT BRITAIN

SSEF SCHWEIZERISCHES GEMMOLOGISCHES INSTITUT SWISS GEMMOLOGICAL INSTITUTE INSTITUT SUISSE DE GEMMOLOGIE

AGL AMERICAN GEMOLOGICAL LABORATORIES

The Journal of Gemmology

COVERED BY THE FOLLOWING ABSTRACTING AND INDEXING SERVICES:

Clarivate Analytics' (formerly Thomson Reuters/ISI) Science Citation Index Expanded (in the Web of Science), *Journal Citation Reports (Science Edition)* and *Current Contents (Physical, Chemical and Earth Sciences)*; Elsevier's Scopus; Australian Research Council's Excellence in Research for Australia (ERA) Journal List; China National Knowledge Infrastructure (CNKI Scholar); EBSCO's Academic Search Ultimate; ProQuest (Cambridge Scientific Abstracts); GeoRef; CrossRef; Chemical Abstracts (CA Plus); Mineralogical Abstracts; Index Copernicus ICI Journals Master List; Gale Academic OneFile; British Library Document Supply Service; and Copyright Clearance Center's RightFind application.

Science Citation Index Expanded
Web of Science Clarivate Analytics

CONTENT SUBMISSION

The Editor-in-Chief is glad to consider original articles, news items, conference reports, announcements and calendar entries on subjects of gemmological interest for publication in *The Journal of Gemmology*. A guide to the various sections and the preparation of manuscripts is given at https://gem-a.com/membership/journal-of-gemmology/submissions, or contact the Editor-in-Chief.

SUBSCRIPTIONS

Gem-A members receive *The Journal* as part of their membership package, full details of which are given at https://gem-a.com/membership. Laboratories, libraries, museums and similar institutions may become direct subscribers to *The Journal*; download the form from *The Journal*'s home page.

ADVERTISING

Enquiries about advertising in *The Journal* should be directed to advertising@gem-a.com. For more information, see https://gem-a.com/news-publications/media-pack-2022.

DESIGN & PRODUCTION

Zest Design, London. www.zest-uk.com

PRINTER

Paragon Leycol, London, https://www.dg3leycol.com

Mixed Sources
Product group from well-managed forests and other controlled sources
www.fsc.org Cert no. TT-COC-002454
© 1996 Forest Stewardship Council
FSC

ISSN 1355-4565 (Print), ISSN 2632-1718 (Online)

Gem-A
THE GEMMOLOGICAL ASSOCIATION OF GREAT BRITAIN

21 Ely Place
London EC1N 6TD
UK
t: +44 (0)20 7404 3334
f: +44 (0)20 7404 8843
e: information@gem-a.com
w: https://gem-a.com

Registered Charity No. 1109555
A company limited by guarantee and registered in England No. 1945780
Registered office: Palladium House, 1–4 Argyll Street, London W1F 7LD

What's New

INSTRUMENTATION

ASDI-500 Automated Diamond Spectral Inspection System

In October 2022, the Swiss Gemmological Institute SSEF and UNIMEC SA, a robotics company also headquartered in Switzerland, announced the release of the ASDI-500, a new version of the Automated Diamond Spectral Inspection device. Officially unveiled during the November 2022 GemGenève gem and jewellery show, the updated instrument is designed to automatically screen large batches of round, colourless to near-colourless (D–J), polished melee (0.5–3.80 mm in diameter) in order to separate synthetics and simulants from natural diamonds. Visit https://www.ssef.ch/asdi-500.

NEWS AND PUBLICATIONS

De Beers *Diamond Insight Report 2022*

The Diamond Insight Report 2022: A New Diamond World was released by De Beers in early November as a 41-page PDF file. The report focuses on future trends in diamond marketing. It begins with a 'diamond value chain dashboard'—a review of diamond jewellery and polished diamond demand in 2021 as a basis for future projections, with a slowdown predicted for countries with higher inflation. The report also emphasises the importance of 'trusted brands' in future diamond marketing, as well as 'phygital' retail (a combination of physical and digital channels) and the three-dimensional immersive marketing possibilities of the new Web3 and the metaverse. A webinar covering highlights of the report is also available as a 53-minute video. Visit https://www.debeersgroup.com/reports/insights/the-diamond-insight-report-2022.

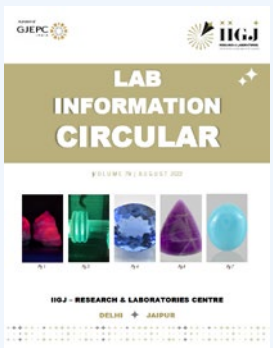

IIGJ-RLC *Lab Information Circular* Vol. 79

Released in August 2022, this latest issue of the *Lab Information Circular* features content from the Research & Laboratories Centre of the Indian Institute of Gems & Jewellery (IIGJ-RLC), a merger of the Gem Testing Laboratory (GTL Jaipur) and the Indian Gemmological Institute – Gem Testing Laboratory (IGI-GTL Delhi). This issue covers hackmanite, IIGJ-RLC's new country-of-origin determination service for emerald, aquamarine vs Maxixe-type blue beryl, dyed synthetic rock crystal, spurrite, quartz coloured by malachite and 'Zachery-treated' turquoise. Download the report at https://iigj.org/wp-content/uploads/2022/08/LIC_August_2022-1.pdf.

JNA's *Pearl Report 2022–2023*

JNA released its *Pearl Report 2022–2023* in mid-2022. The 52-page publication includes a number of articles (in both English and Chinese) that cover the state of the international pearl trade, design trends, marketing concepts, tracing using blockchain technology, pearl identification and classification, and profiles of specific regions/producers. View the report as a flip book or download the PDF file at https://news.jewellerynet.com/uploads/ebook/Supplement/Pearl-Report_2022-2023.

Rapaport Report on Blood Diamonds

In June 2022, a Rapaport Special Report was published titled 'What Should We Do About Blood Diamonds?'. It is organised into four sections. The 'Reports' section includes articles on various issues surrounding blood diamonds, which are defined as being involved in physical torture. The section on 'Industry Views' presents position statements from various major diamond organisations and companies. The 'Legal' section addresses USA laws and sanctions. The final section, 'Doing Good', describes how various groups are addressing the issues, concluding with a 'social responsibility directory' assembled by Rapaport. Download the 44-page PDF file at https://www.diamonds.net/getfile.aspx?FileID=46&Download=yes.

OTHER RESOURCES

Assure Program Developments

The Assure Program's testing of diamond verification instruments provides third-party oversight of commercially available devices for the screening or detection of natural and synthetic diamonds. In November 2022, the Natural Diamond Council launched a new online portal for the Assure 2.0 Directory, which incorporates important enhancements to the sample sets and test regime. The updated portal features an improved filtering system so users can review instruments based on specific needs such as types of diamonds, volumes processed, instrument size, etc. The original Assure 1.0 Directory also remains available. Visit https://www.naturaldiamonds.com/council/assure-testing-program.

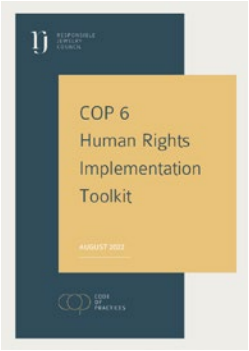

RJC Human Rights Due Diligence Toolkit

In August 2022, the Responsible Jewellery Council released *COP 6 Human Rights Implementation Toolkit*, an update of the 2013 version. It includes context on human rights and offers practical steps for carrying out due diligence in the jewellery industry depending on a company's size and role. Worksheets help the user define the objectives and scope of their human rights due diligence, create a policy checklist, identify and assess their impacts on the supply chain, establish priorities, track activities, address grievances, and more. Download the 57-page document at https://www.responsiblejewellery.com/wp-content/uploads/200622_RJC_HRDD-Toolkit_final_August-release.pdf.

Sustainable Jewellery Practices Course

In October 2022, sustainable jewellery consultant Christina T. Miller launched an introductory, four-lesson course titled *Foundations for Sustainable Jewelry Practices*. The course includes videos, graphics, activities and additional resources to help jewellers understand the social and environmental impacts of the gem and jewellery industry. Lesson 1 examines the current state of the industry and why it needs to change; Lesson 2 covers the terminology used to discuss sustainability; Lesson 3 provides a basic overview of how jewellery materials are produced; and Lesson 4 addresses how to take action. To enrol, visit https://www.christinatmiller.com/foundations-sustainable-jewelry.

Webinars and Other Online Gemmological Education

Since the start of the COVID-19 pandemic, a number of gem-industry organisations and other groups have provided webinars (and other archived video and audio content) on their websites or YouTube channels that are of interest to gemmologists. See also those listed in previous What's New sections starting with Vol. 37, No. 2, 2020.

- **6th Mediterranean Gemmological and Jewellery Conference Lectures**
  Videos of 14 lectures and workshops from the 6th Mediterranean Gemmological and Jewellery Conference, held 12–14 August 2022 in Thessaloniki, Greece, are now available online. The topics cover opal testing and value; identification of colourless and coloured diamonds; emerald, ruby and sapphire country-of-origin determination; identification of major gems and their origin; spinel history, origin, treatments, marketing and pricing; diamond morphology and origin; diamond identification using fluorescence; using portable instruments for screening and identifying lab-grown diamonds; responsible sourcing and marketing of coloured stones; antique jewellery; and more. Some of them are freely available and others must be purchased. Visit https://www.brankogems.com/shop/product-category/conference-recordings.

MEDITERRANEAN GEMMOLOGICAL AND JEWELLERY CONFERENCE

- **GemGenève Talks Online**
  Recorded talks from the November 2022 GemGenève gem and jewellery show in Geneva are now available online. As of this writing, 17 videos are available by subscription, some in English and some in French. Topics include gem mining in Sri Lanka and Zambia, Roman micromosaic jewels, collecting antique jewellery, and presentations on Fabergé and Bulgari. Educational videos from previous GemGenève shows are also available. Visit https://digital.gemgeneve.com/live-talks.

GEMGENÈVE

- **Hong Kong International Jewellery Show Seminars**
  Five videos of seminars and workshops held during the July–August 2022 Hong Kong International Jewellery Show are now available online. In addition to covering a *fei cui* jadeite standard, topics mostly focus on gem and jewellery marketing. Some of the presentations are in English, but access requires registration. Visit https://www.hktdc.com/event/hkjewellery/en/intelligence-hub.

- **Maine Tourmaline Find 50th Anniversary**
  In October 1972, a large pocket of gem tourmaline was discovered in Newry, Maine, USA. Fifty years later, the Maine Mineral & Gem Museum has organised a series of special events to celebrate this important find. Visit https://mainemineralmuseum.org/the-big-find to view a video about the landmark discovery, as well as a link to the museum's entire video archive.

- **SSEF 50th Anniversary Presentations**
  In September 2022, the Swiss Gemmological Institute SSEF held a symposium in Basel, Switzerland, to celebrate its 50th anniversary. Videos of presentations and discussions are now available online at https://www.ssef.ch/50years, and include a variety of topics such as auctioneering, Colombian emeralds, the evolution of the diamond trade, the cultured pearl industry, the Lesotho Legend (a 910 ct rough diamond), the valuation of jadeite, a review of the science of gem testing, and more.

MISCELLANEOUS

Portuguese Crown Jewels on Display

In June 2022, the Museu Tesouro Real (Royal Treasure Museum) in Lisbon, Portugal, opened its new permanent exhibit of the Portuguese crown jewels. The collection consists of more than 1,000 pieces that include not only jewels but also coins, insignia, decorations and other items associated with Portuguese royalty. The exhibit occupies the west wing of the Ajuda National Palace, Portugal's last royal palace that was begun in the eighteenth century but only completed this year. For a video and other information about the exhibit, go to https://www.tesouroreal.pt/en/pages/acf04850; visit the 'Collections' page to view photos of some individual pieces.

What's New provides announcements of new instruments/technology, publications, online resources and more. Inclusion in What's New does not imply recommendation or endorsement by Gem-A. Entries were prepared by Carol M. Stockton unless otherwise noted.

An innovator in gemstone reporting

• Identification of colored gemstones • Country of origin determination • Full quality and color grading analysis

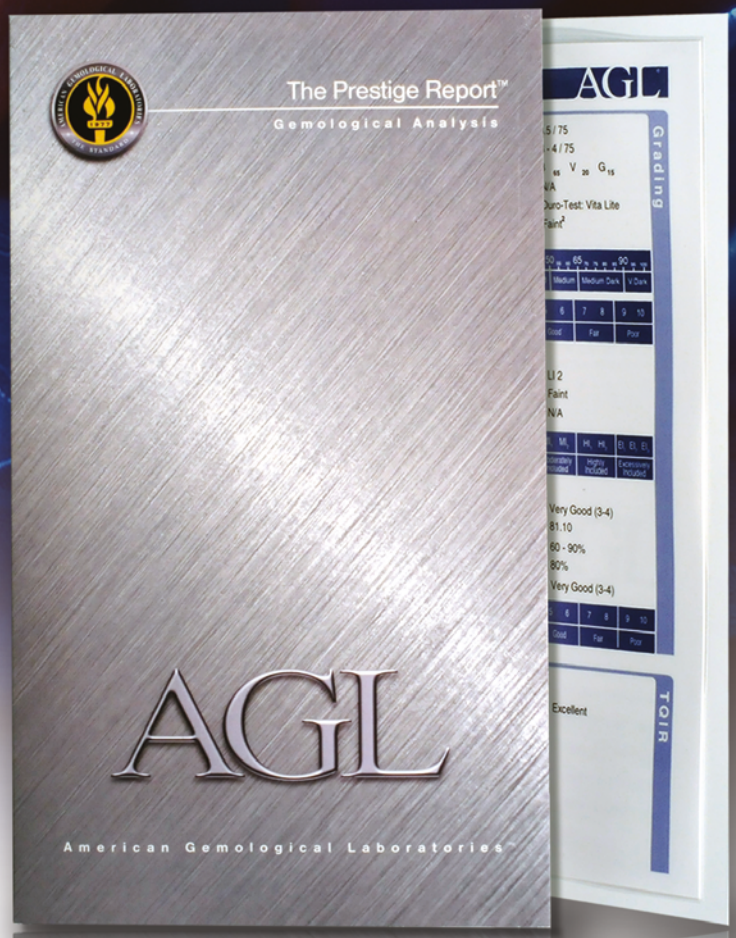

AMERICAN GEMOLOGICAL LABORATORIES AGL

580 5th Ave • Suite 706 • New York, NY 10036, USA
www.aglgemlab.com • +1 (212) 704 - 0727

Gem Notes

COLOURED STONES

Update on Emerald Mining at Campos Verdes, Goiás, Brazil

Campos Verdes, located about 20 km north of Santa Terezinha de Goiás in Goiás State, Brazil, was an important source of gem-quality emerald in the 1980s. The mineralisation is hosted by talc schists that are intersected by pegmatites, and the emeralds contain an inclusion assemblage that commonly consists of chromite, talc, calcite and pyrite (Cassedanne & Sauer 1984; Biondi 1990; Lariucci *et al*. 1990). According to the present author's observations, the mineralised talc schist is greenish grey, fine- to medium-grained and has a foliated structure with discontinuous lenses and layers of carbonates, biotite and quartzofeldspathic veins. Also present is non-mineralised talc schist with a more greyish appearance, as well as carbonate-chlorite-quartz schist, amphibole-chlorite schist, biotitites and local albitites. The protoliths of the host rocks are inferred to be intermediate volcanics with intercalations of ultramafic volcanics that were affected by regional metamorphism and metasomatism, as well as subsequent hydrothermal alteration. A granitic body is exposed at São José do Alegre (a few kilometres northwest of the emerald mining area), and it is probably the source of the pegmatites that supplied the hydrothermal fluids necessary for the formation of the emeralds.

After the easily exploited near-surface areas of the deposits were exhausted at the end of the 1980s, most of the small-scale miners (*garimpeiros*) who worked in the area were replaced by mining companies capable of exploring at deeper depths. Core drilling, geological studies and geophysical surveys were undertaken, and commercial quantities of emerald have been mined in underground workings at depths up to 620 m. The mining area can currently be divided into five parts: (1) the 'old' section that exploits the eastern part of the mineralised belt, where the two largest mines in the region are located (Itaobi and Veraobi); (2) the 'new' section, which is worked by Mineração Peneri and is adjacent to the Nego Velho mine on the east that is famous for producing large quantities of emerald; (3) the Netinho section, which includes the currently active São Geraldo mine; (4) the Délio Braz section, which parallels the other sections on their west side and has been exploited to a depth of 450 m; and (5) the Kley section, which was discovered in 2006 and hosts mineralised horizons at 48, 52 and 128 m depth. Core drilling has revealed another emerald-bearing zone at Kley at 340 m depth that has not yet been mined.

Starting in March 2022, emeralds have been produced by a new joint venture between Lúvio Verde Mining (Campos Verdes) and Fodiens in Prosterum (London), from an area located just south of the previously mined sections listed above. The deepest shaft reaches 153 m and adjoining tunnels follow the zones of mineralised schist. The mined material is brought to the surface using a winch (Figure 1) and is then transported about 7 km to the washing plant. Since Lúvio Verde first started producing emeralds in 2007, they have mined

Figure 1: At the Lúvio Verde Mining joint venture, a winch is employed to transport the emerald-bearing talc schist to the surface in a large rubber container (left), and this system is also used in conjunction with a special harness to transport personnel in and out of the mine (right); the author is shown wearing a black shirt. Photos courtesy of M. C. Zenetos.

approximately 11,000 kg of mixed-quality (both gem and non-gem) emerald consisting of crystals that mostly range from 1 to 7 g each (e.g. Figure 2), although exceptionally they have recovered large pieces weighing up to 160 g. A limited amount of the emerald has been faceted for certain customers, and recently 2,000+ carats were cut that weighed 0.25–14 ct each (mostly <5 ct; e.g. Figure 3). The author is assisting with validating the production and performing due diligence, as the joint venture is seeking additional funding in order to mine deeper levels of the deposit. In the future, if funding can be obtained, the joint venture plans to renovate and expand existing buildings, construct new buildings and make other improvements in infrastructure, including acquiring new equipment and hiring additional professionals and service providers.

The Campos Verdes area shows excellent potential for continued commercial emerald production, although further investment will be needed in order to mine deeper portions of the deposits.

Miguel Carlos Zenetos (mzenetos@hotmail.com)
GGG Laboratory
Balneário Camboriú, Santa Catarina, Brazil

Figure 2: Rough emeralds from the Lúvio Verde Mining joint venture are sorted and packaged by director Claiton Roberto (foreground) and assistant Ze Val. The crystals range up to approximately 7 g each. Photo by M. C. Zenetos.

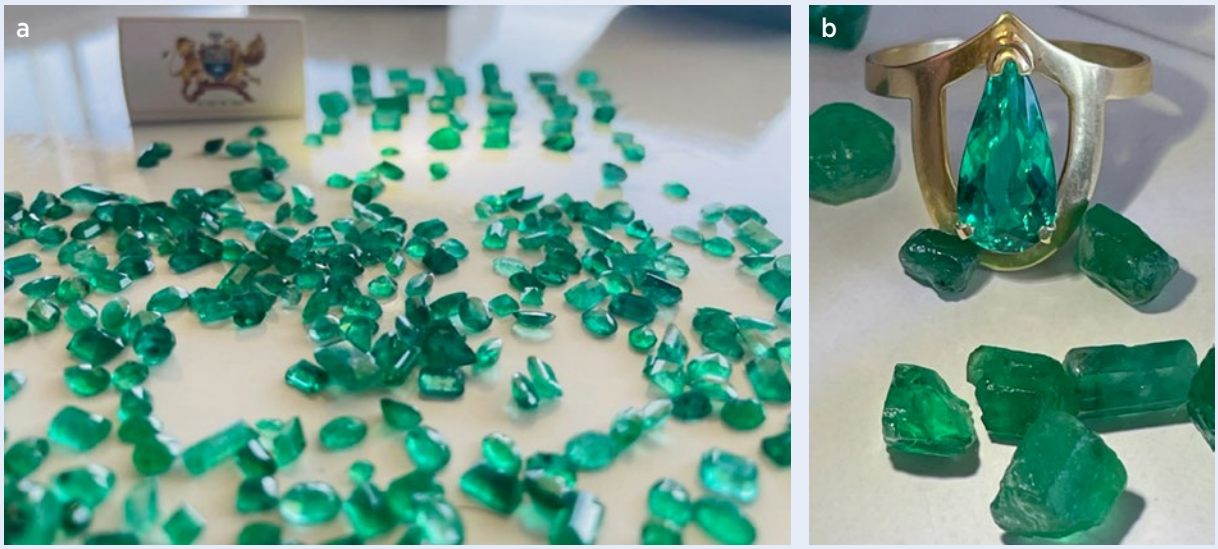

Figure 3: (**a**) These faceted emeralds from the Lúvio Verde Mining joint venture weigh <5 ct each and are from a parcel weighing 395 carats. (**b**) The Lúvio Verde emerald in this ring is 3.15 ct. Photos by M. C. Zenetos.

References

Biondi, J.C. 1990. Depósitos de esmeralda de Santa Terezinha (GO). *Revista Brasileira de Geociências*, **20**(1), 7–24, https://doi.org/10.25249/0375-7536.1990724.

Cassedanne, J.P. & Sauer, D.A. 1984. The Santa Terezinha de Goiás emerald deposit. *Gems & Gemology*, **20**(1), 4–13, https://doi.org/10.5741/gems.20.1.4.

Lariucci, C., Leite, C.R. & Santos, R.H. de A. 1990. Gênese e inclusões das esmeraldas de Santa Terezinha de Goiás - GO. *Revista Brasileira de Geociências*, **20**(1), 25–31, https://doi.org/10.25249/0375-7536.19902531.

Asteriated Quartz Sphere with Sagenitic Rutile Inclusions

An inclusion pattern consisting of planes formed by a sagenitic network of twinned and untwinned rutile crystals has been documented as producing six-rayed asterism in quartz cabochons from Myanmar (Schmetzer & Steinbach 2014). The sagenitic network was formed by elongated blades or flattened needles of rutile, which were located within one or even two planes of the host quartz.

Here the authors describe a similar pattern of rutile inclusions forming a sagenitic network within a quartz sphere measuring 12.5 mm in diameter that shows six-rayed asterism in reflected light (Figure 4). The sample was purchased in 2022 at a mineral fair in France. The vendor indicated it was from Brazil, but no further information was available. Similar spheres with six-rayed stars, up to 50 mm in diameter, were available at the vendor's booth.

Microscopic examination showed that the sphere contained an almost opaque layer (Figure 5) formed by numerous elongated reddish brown to brownish yellow needles or blades of rutile. Only a few needles were seen with an orientation oblique to this layer (again, see Figure 5). Between crossed polarisers a complex interference pattern was visible, most likely due to twinning of the quartz host. The plane formed by the non-transparent layer of inclusions was slightly inclined to the *c*-axis of the quartz host and was somewhat displaced from its centre. A few healed fractures with fluid inclusions were also present.

Figure 4: Six-rayed asterism is displayed by this 12.5-mm-diameter rutilated quartz sphere. Photo by K. Schmetzer; fibre-optic illumination.

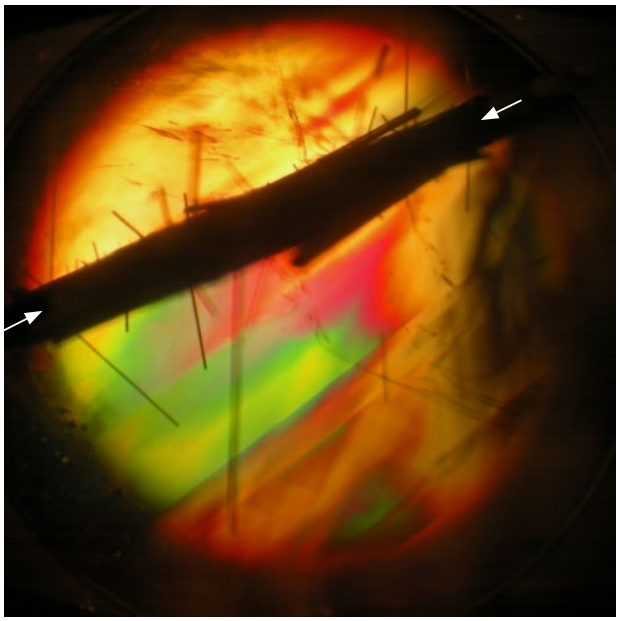

Figure 5: The 12.5-mm-diameter quartz sphere shown in Figure 4 contains a non-transparent layer (see white arrows) formed by a dense network of elongated rutile needles or blades. Some of the rutile needles are also inclined to this dominant non-transparent layer. As seen here between crossed polarisers, a complex interference pattern can be observed in a view parallel to the optic axis of the quartz. Photo by K. Schmetzer.

The rutile inclusions forming the non-transparent plane were oriented in three directions within and above the non-transparent layer (Figure 6a). Incident light reflected from the rutile needles or blades to form three intersecting light bands and, thus, six-rayed asterism. The six-rayed star was visible in orientations more-or-less perpendicular to the non-transparent layer and could be seen from both sides of the layer (Figure 6b, c).

Dr Karl Schmetzer (SchmetzerKarl@hotmail.com)
Petershausen, Germany

Martin P. Steinbach
Steinbach – Gems with a Star
Idar-Oberstein, Germany

Reference

Schmetzer, K. & Steinbach, M.P. 2014. Quartz with sagenitic rutile inclusions from Myanmar. *Australian Gemmologist*, **25**(5), 175–177.

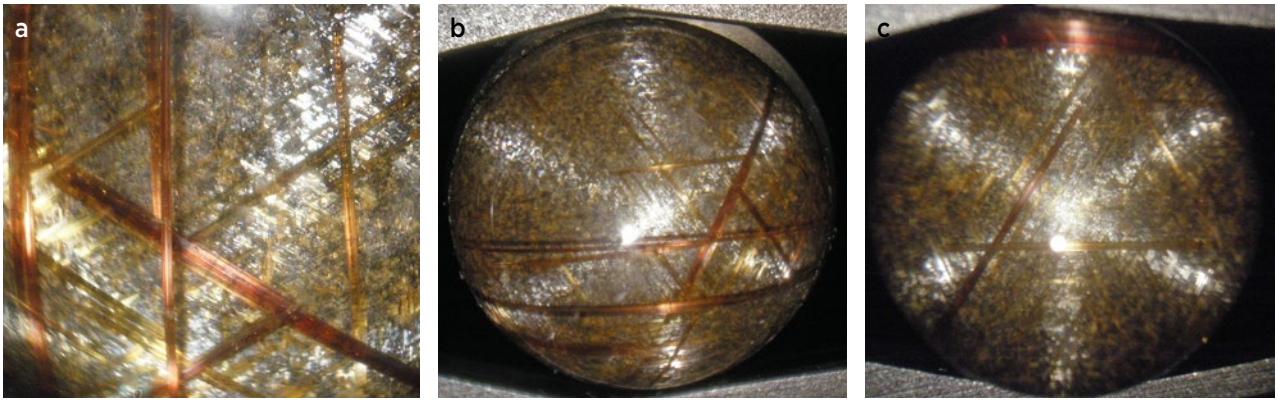

Figure 6: (**a**) A dense network is formed by rutile needles or blades oriented in three directions within the quartz host; field of view 7.6 × 5.7 mm. (**b**, **c**) A six-rayed star is seen with reflected light more-or-less perpendicular to both sides of the non-transparent plane formed by the oriented rutile needles. Photos by K. Schmetzer; fibre-optic illumination.

Interesting Inclusions in a Purple Spinel from Tanzania

In recent years, Tanzanian spinels have received more and more attention in the Chinese gem market. Recently, a 6.67 ct purple spinel reportedly from Tanzania was submitted to Guild Gem Laboratories (Shenzhen) for identification. The stone displayed attractive purple colouration and strong red fluorescence to long-wave UV radiation (Figure 7). Its RI of 1.715 and hydrostatic SG of 3.59 were consistent with those of natural spinel. The ultraviolet-visible-near infrared (UV-Vis-NIR) spectrum showed characteristic absorption maxima attributed to Fe^{2+} (373, 557 and 588 nm), Fe^{3+} (476 nm), Cr^{3+}±V^{3+} (about 540 nm) and Co^{2+} (622 nm; cf. Belley & Palke 2021). In addition, we observed a strong Cr-related signature consisting of a closely spaced group of fluorescent lines at around 700 nm (Figure 8). Chemical analysis with energy-dispersive X-ray fluorescence (EDXRF) spectroscopy showed abundant Fe (5950 ppm), appreciable Zn (920 ppm), and smaller amounts of Cr (210 ppm) and V (110 ppm); no Co was measured due to the relatively high detection limit of EDXRF. Based on the UV-Vis-NIR spectrum and chemical data, the purple colouration of this spinel was due to a combination of Fe, Cr±V, and Co.

Microscopic examination showed a distinctive array of oriented birefringent geometric lamellae (Figure 9), similar to those described in spinel from the Morogoro area of Tanzania (Schmetzer & Berger 1992). Careful observation from various angles revealed that there were four different sets of the lamellar inclusions, which appeared to be oriented parallel to octahedral {111} faces and {111} twin planes of the spinel host. An angle of about 110° was measured with a protractor between two sets of thin lamellae (Figure 9b). Schmetzer and Berger (1992) likewise documented four sets of lamellae in their samples, and they measured angles of 109.47° and 70.53° between them. Using transmission electron microscopy, they identified the lamellar inclusions as högbomite, a

Figure 7: (**a**) This 6.67 ct spinel from Tanzania displays bright purple colouration. (**b**) The stone fluoresces strong red to long-wave UV radiation. Photos by H. Zhao.

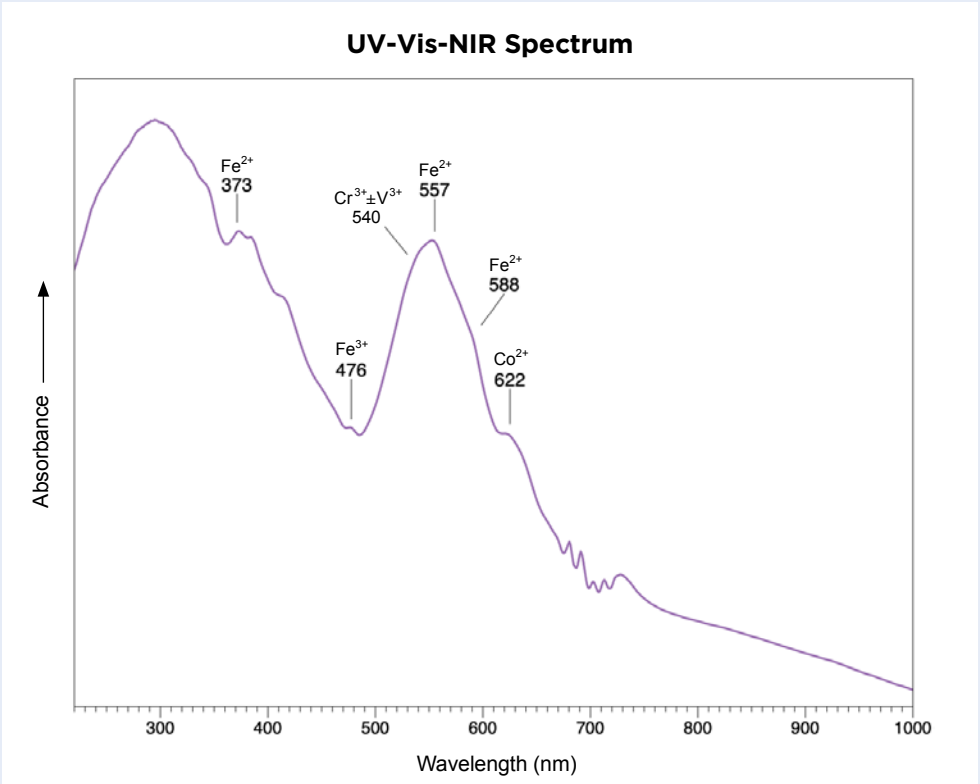

Figure 8: The UV-Vis-NIR spectrum of the purple spinel displays a broad band in the visible range with maxima at about 540 and 557 nm, and a shoulder at 588 nm, as well as small peaks at 373, 476 and 622 nm, and fluorescence lines at around 700 nm associated with Cr. The path length of the beam was approximately 12.5 mm.

hexagonal Fe-Mg-Al-Ti oxide. It has a structure similar to that of spinel with partial replacement of Mg by Ti. Subsequent work has demonstrated that the {111} twin boundary in spinel is relatively low in Mg (Daneu *et al*. 2007).

Also present throughout this spinel were strings of minute inclusions, which were oriented parallel to one of the directions of the lamellae described above (Figure 10a). Such oriented dot-like minerals are commonly seen in Tanzanian spinels. Raman analysis identified the colourless particles as diaspore and the black ones as graphite (Figure 10b). To our knowledge, this is the first time diaspore has been identified in a Tanzanian spinel.

Xueying Sun, Yujie Gao (peter.gao@guildgemlab.com) and Huixin Zhao
Guild Gem Laboratories
Shenzhen, China

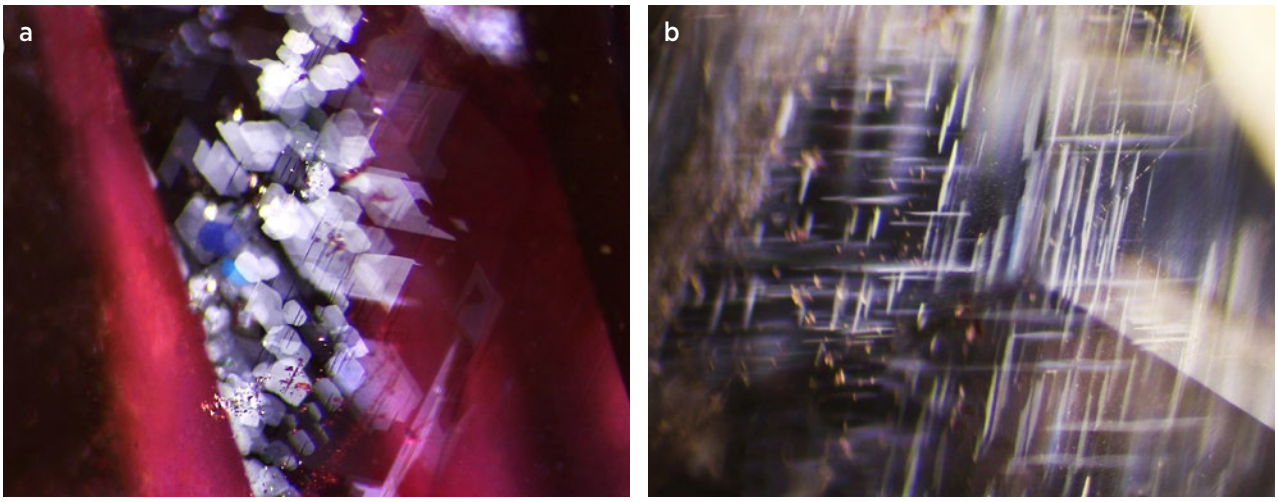

Figure 9: Oriented lamellae are seen in the spinel. (**a**) These lamellar inclusions show a hexagonal outline. (**b**) The angle between two sets of thin lamellae was measured as about 110°. Photomicrographs by H. Zhao; image width (a) 1.1 mm and (b) 2.1 mm.

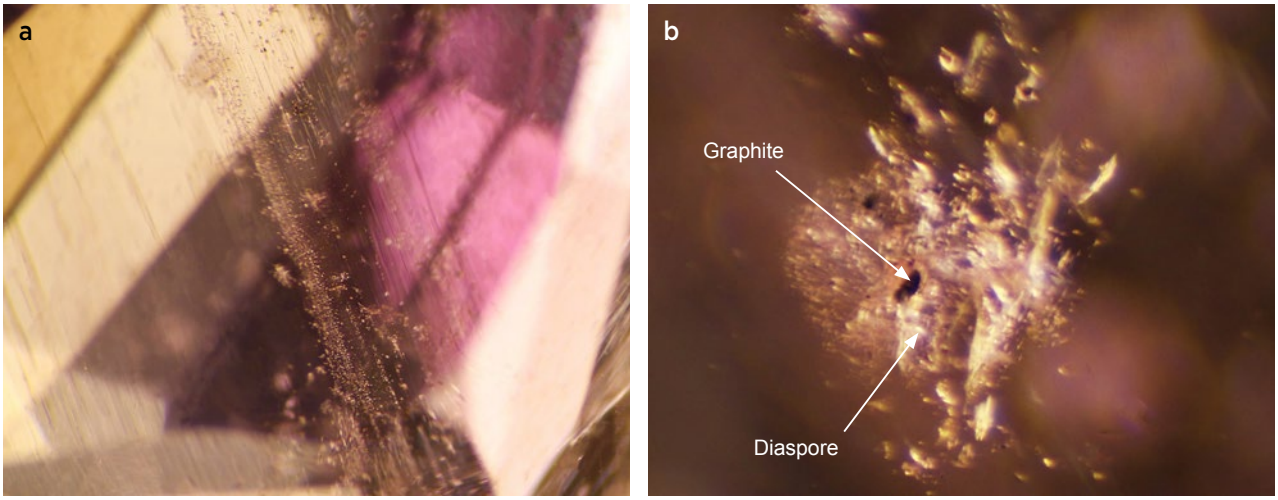

Figure 10: (**a**) The spinel contains lines of fine particles that are parallel to one of the directions of the lamellar inclusions. (**b**) These particles were found to consist of colourless diaspore and black graphite. Photomicrograph by H. Zhao; image width (a) 2.4 mm and (b) 0.1 mm.

References

Belley, P. & Palke, A. 2021. Purple gem spinel from Vietnam and Afghanistan: Comparison of trace element chemistry, cause of color, and inclusions. *Gems & Gemology*, **57**(3), 228–238, https://doi.org/10.5741/gems.57.3.228.

Daneu, N., Rečnik, A., Yamazaki, T. & Dolenec, T. 2007. Structure and chemistry of (111) twin boundaries in $MgAl_2O_4$ spinel crystals from Mogok. *Physics and Chemistry of Minerals*, **34**(4), 233–247, https://doi.org/10.1007/s00269-007-0142-1.

Schmetzer, K. & Berger, A. 1992. Lamellar inclusions in spinels from Morogoro area, Tanzania. *Journal of Gemmology*, **23**(2), 93–94, https://doi.org/10.15506/JoG.1992.23.2.93.

Separating Elbaite from Liddicoatite Paraíba-type Tourmaline

Paraíba-type (Cu-bearing) tourmaline, initially found in Brazil about three decades ago (Fritsch *et al.* 1990), is one of the most sought-after varieties, consisting of blue-to-green (or yellowish green) stones coloured mainly by Cu and Mn. Nowadays, the vast majority of this tourmaline consists of elbaite (and also fluor-elbaite) from Brazil, Nigeria and Mozambique, but it is also rarely liddicoatite (currently known as fluor-liddicoatite) from Mozambique (Karampelas & Klemm 2010; Katsurada & Sun 2017; Milisenda & Müller 2017; Katsurada *et al.* 2019).

The Laboratoire Français de Gemmologie (LFG) received three neon-blue pear-shaped stones for identification (0.48, 0.53 and 1.14 ct; Figure 11, top row). Standard gemmological methods and Raman spectroscopy identified all three samples as tourmaline, and UV-Vis-NIR spectroscopy confirmed that they were coloured by Cu and Mn (Fritsch *et al.* 1990). Microscopic examination of these Paraíba-type tourmalines showed

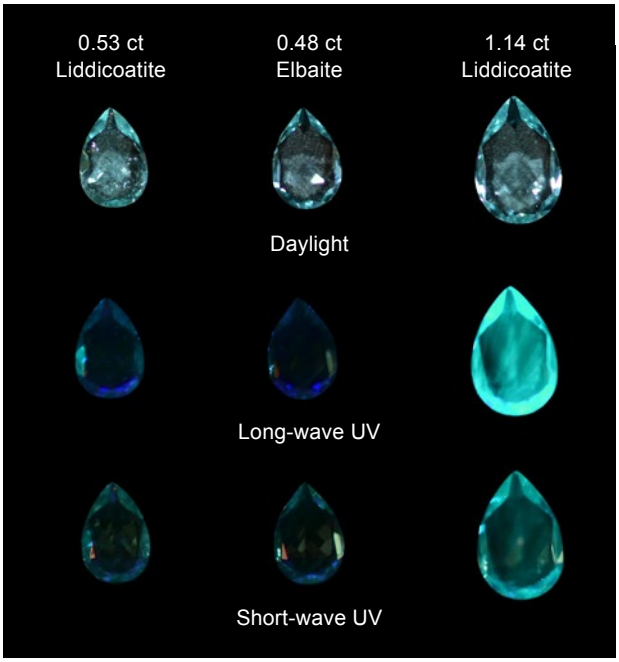

Figure 11: The three Paraíba-type tourmalines documented in this report are shown in daylight and while exposed to long- and short-wave UV radiation. Photos by U. Hennebois, LFG.

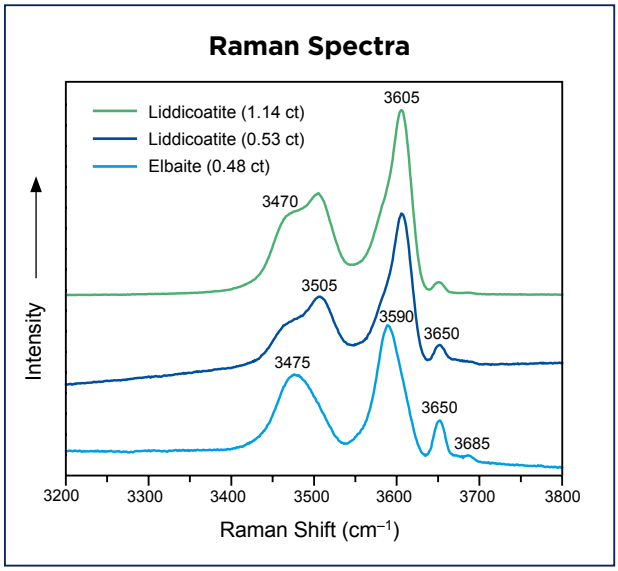

Figure 12: Raman spectra of the three Paraíba-type tourmalines show some distinct differences in the 3400–3700 cm^{-1} region, corresponding to whether they are liddicoatite or elbaite.

no clear indications of heating. However, EDXRF spectroscopy of all three samples indicated a CuO:MnO ratio below 0.5, suggesting that they had been heat treated (cf. Okrusch *et al*. 2016). Interestingly, the EDXRF results also showed that the 0.53 and 1.14 ct samples contained a higher concentration of Ca than the sum of Na-plus-other-alkalis, while the 0.48 ct stone contained less Ca than Na-plus-other-alkalis. EDXRF is not an accurate method to measure Na, but these results suggested that the first two samples were liddicoatite while the third was elbaite, although other quantitative chemical data would be needed for confirmation.

Polarised Raman spectroscopy has also been used to separate these two tourmaline species, as liddicoatite presents a vibration around 3605 cm^{-1}, and elbaite below around 3595 cm^{-1}, due to slightly different OH-stretching modes (Watenphul *et al*. 2016). The present samples showed equivalent Raman features when analysed in random spots (Figure 12)—with no polariser, using a 514 nm diode-pumped solid-state laser—thus confirming their identity as liddicoatite (0.53 and 1.14 ct) and elbaite (0.48 ct). The EDXRF results also showed relatively high contents of Ga, Bi and Pb for the two Ca-dominant samples, in accordance with Paraíba-type liddicoatite from Mozambique (Katsurada & Sun 2017; Milisenda & Müller 2017; Katsurada *et al*. 2019). The 0.48 ct elbaite contained more than 400 ppmw Ga, suggesting that it is also from Mozambique (Katsurada *et al*. 2019).

Under 3 W long-wave (365 nm) and short-wave (254 nm) UV lamps, the 1.14 ct liddicoatite luminesced a greenish colour (Figure 11), like that reported previously for Paraíba-type liddicoatite (Katsurada & Sun 2017). However, the 0.53 ct liddicoatite and 0.48 ct elbaite were inert (again, Figure 11). Thus, these tourmaline species cannot be separated by luminescence to UV radiation.

Using the same Raman spectrometer and laser described above, photoluminescence (PL) spectra of both liddicoatites presented a series of bands in the near-infrared region, with the main feature at 870 nm (Figure 13), possibly due to Nd^{3+} (Lenz *et al*. 2015; Milisenda & Müller 2017). It is notable that both samples had equivalent PL spectra, even though one of them showed visible greenish fluorescence and the other was inert. By comparison, the elbaite lacked this series of bands and had only a wide, weak PL peak at 877 nm. It appears that the cause of the greenish luminescence of the 1.14 ct liddicoatite is not linked with Nd^{3+} giving the PL features in the NIR region, and might be due to another rare-earth element (Lenz *et al*. 2015) or even a completely different cause.

Raman and PL spectroscopy appear to be useful for separating liddicoatite and elbaite Paraíba-type tourmaline, even when the analyses are done in random crystallographic orientations. Further research is needed to confirm this and, in parallel, to check whether this can be done with mobile instruments. The presence of luminescence under long- and short-wave UV radiation cannot be used to separate these species of Paraíba-type tourmaline. The cause of the UV luminescence shown by some Paraíba-type liddicoatite needs to be better understood.

Ugo Hennebois, Aurélien Delaunay and
Dr Stefanos Karampelas (s.karampelas@lfg.paris)
LFG, Paris, France

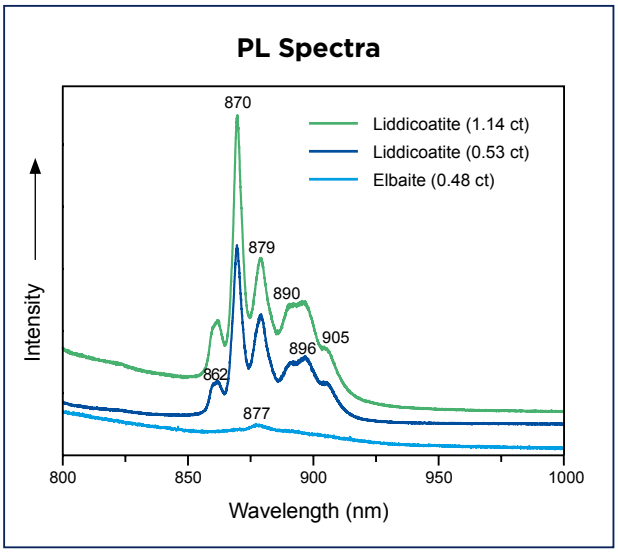

Figure 13: Differences between liddicoatite and elbaite are also seen in the NIR region of PL spectra obtained for the three Paraíba-type tourmalines.

References

Fritsch, E., Shigley, J.E., Rossman, G.R., Mercer, M.E., Muhlmeister, S.M. & Moon, M. 1990. Gem-quality cuprian-elbaite tourmalines from São José da Batalha, Paraíba, Brazil. *Gems & Gemology*, **26**(3), 189–205, https://doi.org/10.5741/gems.26.3.189.

Karampelas, S. & Klemm, L. 2010. Gem News International: "Neon" blue-to-green Cu- and Mn-bearing liddicoatite tourmaline. *Gems & Gemology*, **46**(4), 323–325.

Katsurada, Y. & Sun, Z. 2017. Cuprian liddicoatite tourmaline. *Gems & Gemology*, **53**(1), 34–41, https://doi.org/10.5741/gems.53.1.34.

Katsurada, Y., Sun, Z., Breeding, C.M. & Dutrow, B.L. 2019. Geographic origin determination of Paraíba tourmaline. *Gems & Gemology*, **55**(4), 648–659, https://doi.org/10.5741/gems.55.4.648.

Lenz, C., Nasdala, L., Talla, D., Hauzenberger, C., Seitz, R. & Kolitsch, U. 2015. Laser-induced REE^{3+} photoluminescence of selected accessory minerals – An "advantageous artefact" in Raman spectroscopy. *Chemical Geology*, **415**, 1–16, https://doi.org/10.1016/j.chemgeo.2015.09.001.

Milisenda, C.C. & Müller, S. 2017. REE photoluminescence in Paraìba type tourmaline from Mozambique. *35th International Gemmological Conference*, Windhoek, Namibia, 11–15 October, 71–73.

Okrusch, M., Ertl, A., Schüssler, U., Tillmanns, E., Brätz, H. & Bank, H. 2016. Major- and trace-element composition of Paraíba-type tourmaline from Brazil, Mozambique and Nigeria. *Journal of Gemmology*, **35**(2), 120–139, https://doi.org/10.15506/JoG.2016.35.2.120.

Watenphul, A., Burgdorf, M., Schlüter, J., Horn, I., Malcherek, T. & Mihailova, B. 2016. Exploring the potential of Raman spectroscopy for crystallochemical analyses of complex hydrous silicates: II. Tourmalines. *American Mineralogist*, **101**(4), 970–985, https://doi.org/10.2138/am-2016-5530.

Gem-quality Variscite from Central Iran

Variscite ($AlPO_4 \cdot 2H_2O$) is a phosphate mineral that forms a solid-solution series with strengite ($FePO_4 \cdot 2H_2O$). It is a secondary mineral that occurs as a result of the reaction of phosphate-bearing groundwater with aluminous minerals (such as clays). It fills fractures or cavities to form veinlets or masses, and is found together with other secondary minerals such as apatite and wavellite in various rocks, including schist, quartzite and igneous rocks. Variscite can be light green to deep green or light blue.

Variscite is known to occur in the Koushk Zn-Pb deposit (Sherafat *et al*. 2007), which is located in Yazd Province in the centre of Iran, approximately 50 km north-east of Bafq city, 160 km south-east of Yazd city and on the western margin of the Lut Desert. In terms of its tectono-sedimentary setting, the deposit is located in the Central Iran microcontinent. The host rock of this sedimentary-exhalative deposit, and also of the variscite, is Early Cambrian black shale (Rajabi *et al*. 2020). In the present authors' field observations of the open-pit part of the mine, variscite was found in nodules up to 8 cm in diameter, in formless masses and in veinlets along with quartz and calcite. The Al and P necessary to form the variscite were mobilised by weathering, possibly aided by acidic leaching of the apatite that is associated with the iron ore.

Approximately 10 kg of rough material suitable for cutting was obtained by the authors for examination (e.g. Figure 14). One representative piece was chosen to prepare a thin section and another sample was analysed by Raman spectroscopy. The remaining material was cut and polished into about 20 carats of cabochons

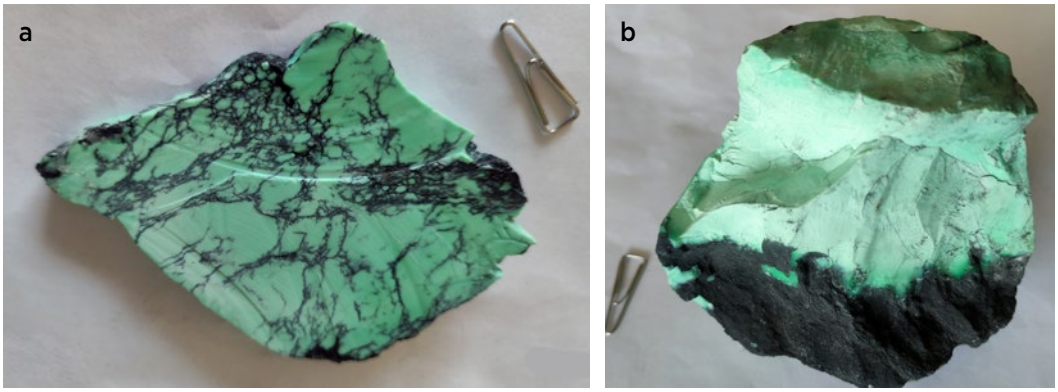

Figure 14: Variscite from the Koushk mine in Iran is represented here by (**a**) a slice with spiderweb patterning and (**b**) a rough sample of light green colour. The paperclip (shown for scale) is 3 cm long. Photos by B. Rahimzadeh.

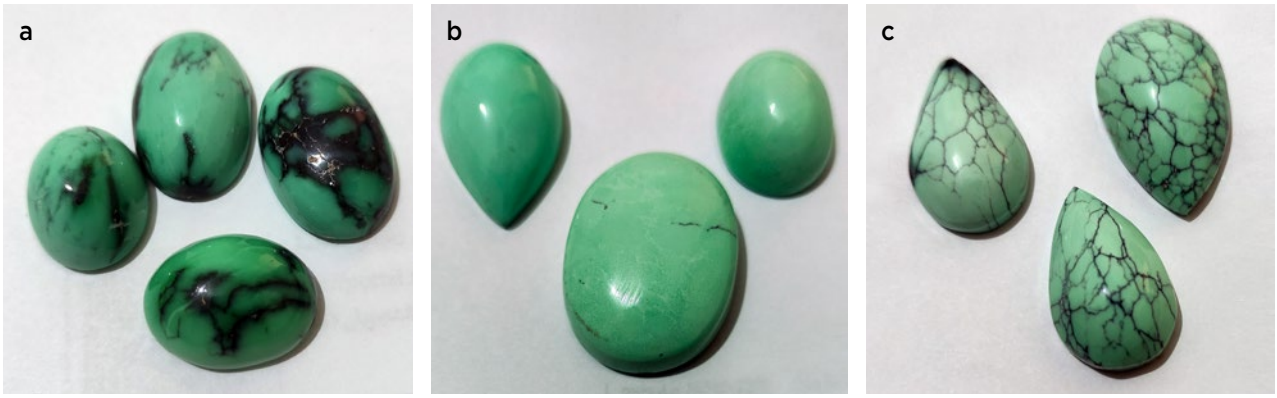

Figure 15: Cabochon-cut samples of variscite from Koushk studied for this report include (**a**) deep green material with dark veins (up to 1.8 cm long), (**b**) light green samples (up to 4.0 cm long) and (**c**) stones with spiderweb patterning (up to 3.1 cm long). Photos by B. Rahimzadeh.

(e.g. Figure 15), which were characterised by standard gemmological methods. All data were collected at the Gemology Center of Shahid Beheshti University.

The variscite ranged from light blue to deep green. The green samples were of gem quality, and commonly had dark veins or spiderweb patterning that were found to consist mostly of clays and a little iron oxide. The properties of our samples are listed in Table I, where they are compared with those of variscite from Western Australia (from Willing *et al.* 2008). Although they were similar in many ways, our Iranian variscite was inert to the Chelsea Colour Filter and had lower hardness than the Australian material. Microscopic examination of our samples showed impurities composed of clay, quartz, iron oxides and shale (Figure 16), whereas Australian samples may have gold inclusions in addition to matrix composed of clay, quartz and iron oxides.

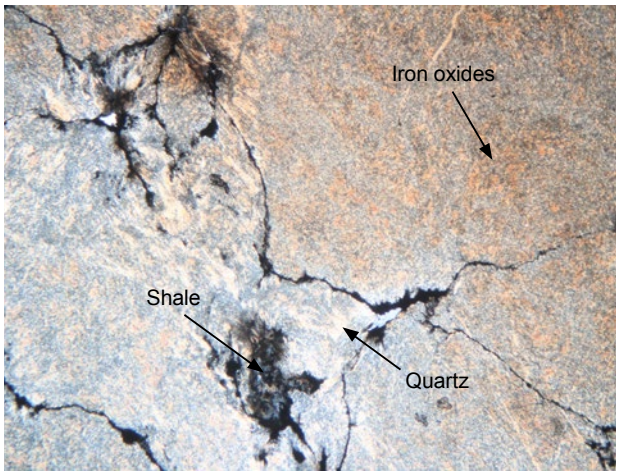

Figure 16: Microscopic examination of a thin section of the Iranian variscite shows the presence of clay, quartz and iron oxides, as well as shale impurities. Photomicrograph by B. Rahimzadeh; magnified 4×.

Table I: Properties of variscite from the Koushk mine, Iran, and from Western Australia.

Property	Koushk mine, Iran (this study)	Western Australia (Willing *et al.* 2008)
Typical colour	Light green	Light bluish green, light to dark green
Mohs hardness	3½–4½	~5
Lustre	Greasy	Waxy (takes a high polish)
Transparency	Opaque	Opaque to translucent
RI	1.58 (spot)	1.570–1.582
SG	2.57	2.49–2.55
Fracture	Splintery	Uneven
UV fluorescence Long-wave Short-wave	 Very weak Inert	 Inert Inert
Chelsea filter	Inert	Grey to pale pink
Impurities	Clay, quartz, iron oxides and shale	Gold inclusions, matrix containing clay, quartz and iron oxides

The Raman spectra of variscite from Iran and from Tajikistan (Litvinenko *et al.* 2016) show considerable overlap, with peaks at approximately 223, 435, 1033 and 1049 cm^{-1} in the Iranian material (Figure 17).

Due to its rather low hardness and the presence of veining, some fragmentation and breakage of the Iranian variscite occurred during cutting, although polishing was easy on account of its relatively low hardness. Also, we found that it is best to keep the material cool and wet during the fashioning process in order to prevent it from heating up, which bleaches its colour. The Koushk deposit hosts large reserves of variscite and could be an important source of gem-quality material in the future.

Dr Bahman Rahimzadeh (b_rahimzadeh@sbu.ac.ir), Sahar Raeiszadeh and Parisa Hadipanah
Shahid Beheshti University, Tehran, Iran

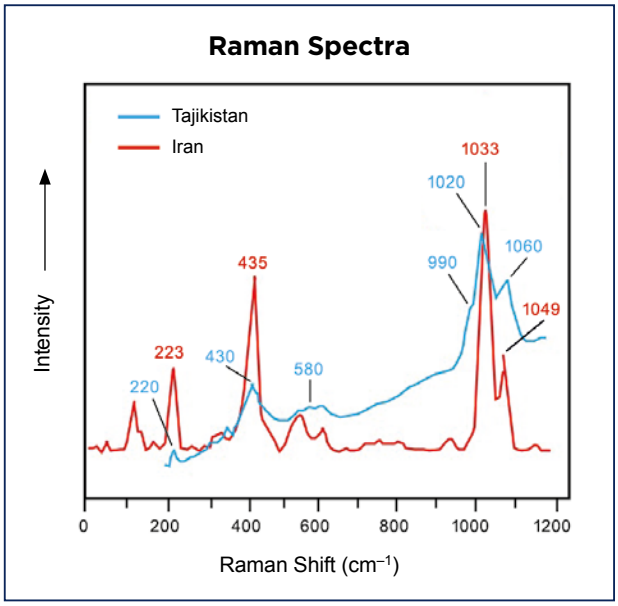

Figure 17: A comparison of the Raman spectra of variscite from the Koushk mine and from Tajikistan (Litvinenko *et al.* 2016) shows considerable overlap of their features.

References

Litvinenko, A.K., Sorokina, E.S., Karampelas, S., Krivoschekov, N.N. & Serov, R. 2016. Variscite from central Tajikistan: Preliminary results. *Gems & Gemology*, **52**(1), 60–65, https://doi.org/10.5741/gems.52.1.60.

Rajabi, A., Alfonso, P., Canet, C., Rastad, E., Niroomand, S., Modabberi, S. & Mahmoodi, P. 2020. The world-class Koushk Zn-Pb deposit, central Iran: A genetic model for vent-proximal shale-hosted massive sulfide (SHMS) deposits – Based on paragenesis and stable isotope geochemistry. *Ore Geology Reviews*, **124**, article 103654, https://doi.org/10.1016/j.oregeorev.2020.103654.

Sherafat, S., Mohammady Nasab, E., Mackizadeh, M.A. & Khodami, M. 2007. Variscite occurrence in Kushk deposit, Bafg (Yazd Province). *Journal of Geotechnical Geology*, **3**(4), 260–265 (in Persian).

Willing, M., Stöcklmayer, S. & Wills, M. 2008. Ornamental variscite: A new gemstone resource from Western Australia. *Journal of Gemmology*, **31**(3–4), 111–124, https://doi.org/10.15506/JoG.2008.31.3.111.

Copper-bearing Silicified Wood from Indonesia

Colourful specimens of opal containing native copper inclusions are known to occur in fossilised (silicified) wood in the Garut Regency of West Java, Indonesia (Laurs 2018). They are hosted by volcaniclastic deposits that covered forests in this region during large eruptions. In addition to opal, Garut Regency is also the source of silicified wood containing dense aggregations of native copper inclusions. According to rough supplier Mahendra Malik and gem collector Mike Bowers, the material is mined from the Lawang Kori area by local people who dig tunnels into the steep hillsides for 20–50 m using simple hand tools (Figure 18). They mostly find

Figure 18: In the Lawang Kori area of West Java, Indonesia, miners dig tunnels in search of silicified wood that sometimes contains abundant inclusions of native copper. Note the 'logs' of petrified wood that are stacked under the feet of the person in the photo. Photo courtesy of Mike Bowers.

Figure 19: This sawn slab of copper-bearing silicified wood measures 17.0 × 9.5 cm, and the cabochons range from 33.92 to 54.33 ct. Courtesy of Mike Bowers; photo by Orasa Weldon.

Figure 20: A closer view of one of the cabochons in Figure 19 shows a dense network of dendritic copper inclusions that are infilled by microcrystalline silica (probably chalcedony). Photo by Orasa Weldon; field of view 15 × 10 cm.

colourful petrified wood and occasionally they produce attractive copper-bearing 'agatised' (silicified) wood such as the material shown in Figure 19.

The copper inclusions are highly reflective when polished and occur in dendritic formations that are infilled by translucent to transparent microcrystalline silica (probably chalcedony; Figure 20). The inclusions are so densely formed that the stones reportedly conduct electricity, so local dealers commonly call it 'high-voltage agate'.

The occurrence of native copper inclusions in microcrystalline silica is quite uncommon. Amygdaloidal agate containing native copper inclusions is known from just a few localities, including Houghton County, Michigan, USA (Rosemeyer 2001), and eastern Kamchatka, Russia (Palyanova *et al.* 2020). However, the specimens documented here from Indonesia contain much denser aggregates and larger dendritic crystals of native copper than reported previously as inclusions in agate or chalcedony.

Brendan M. Laurs FGA

References

Laurs, B.M. 2018. Gem Notes: Copper-bearing opal from West Java, Indonesia. *Journal of Gemmology*, **36**(1), 10–11.

Palyanova, G., Sidorov, E., Borovikov, A. & Seryotkin, Y. 2020. Copper-containing agates of the Avacha Bay (eastern Kamchatka, Russia). *Minerals*, **10**(12), article 1124 (24 pp.), https://doi.org/10.3390/min10121124.

Rosemeyer, T. 2001. A spectacular find of amygdaloidal agates with native copper inclusions from Michigan's copper country. *Rocks & Minerals*, **76**(6), 403, https://doi.org/10.1080/00357520109603247.

SYNTHETICS AND SIMULANTS

Synthetic Moissanite with the Reflectivity of Diamond

Recently, the Swiss Gemmological Institute SSEF received a transparent, colourless, round-brilliant-cut stone (1.81 ct) for diamond grading (Figure 21, inset). Testing with a Presidium Duo Tester yielded a thermal conductivity result in the range of both diamond and synthetic moissanite (Figure 22a). To distinguish the two materials, the DuoTester also allows the measurement of reflectivity. The manufacturer provides a scale that is calibrated so the typical reflectivity value of synthetic moissanite is between 100 and 116, while that of diamond ranges from 87 to 96 (identical ranges are given for the newer model, Presidium Duo Tester II). The sample described here showed a reflectivity of only 86 (Figure 22b), even after thorough cleaning and despite having a good polish. Although this relatively low reflectivity was suggestive of diamond, prior testing of the sample according to our standard procedure proved otherwise.

Unlike diamond, synthetic moissanite is optically anisotropic and strongly doubly refractive, resulting in a doubling of inclusions and of facet edges on the opposite side of the stone when observed with the 10× loupe. This doubling usually cannot be seen when looking directly through the table facet since synthetic moissanite is typically cut with the table perpendicular to the optic axis, but it can be observed easily through the crown main facets, as was the case here (Figure 23a).

Another telltale feature of synthetic moissanite is the presence of sub-parallel whitish channels or 'stringers' that follow the direction of the optic axis, although these were absent from this specimen. Instead, it showed an unusual spindle-shaped, branching inclusion (Figure 23b), as well as a multitude of tiny particles, some of which appeared needle-shaped. In addition, some of the pavilion facets had polishing marks that were parallel on adjacent facets. As a consequence of diamond's extreme hardness, the polishing orientation must be re-adjusted for each individual facet, but this is not the case for other gem materials (including synthetic moissanite). Thus, parallel polishing lines on adjacent facets indicate that a stone cannot be a diamond.

Raman (Figure 21) and IR spectroscopy unequivocally identified the specimen as synthetic moissanite. The relative intensity of the Raman lines of synthetic moissanite depends on the orientation of the sample as well as the SiC polytype present. The specimen described here appears to be of the 4H polytype (cf. Kiefert *et al.* 2001). No Raman peak for diamond at 1332 cm^{-1} was detected. In addition, the sample's hydrostatic SG value of 3.22 is typical for synthetic moissanite, and EDXRF spectroscopy revealed the presence of Si, as expected

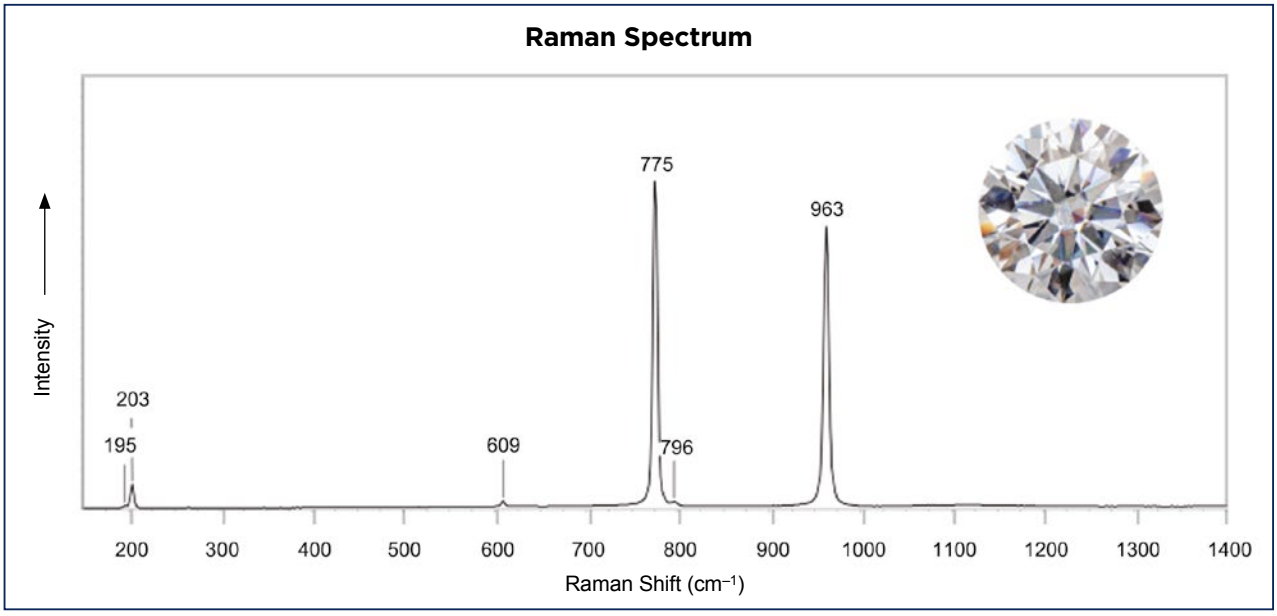

Figure 21: A 1.81 ct round brilliant submitted to SSEF for diamond grading was identified as synthetic moissanite, and its Raman spectrum was indicative of the 4H polytype that is typical of this diamond imitation. Photo by Luc Phan, SSEF.

Figure 22: (**a**) Testing of the 1.81 ct sample with a Presidium Duo Tester shows a thermal conductivity result typical for synthetic moissanite (i.e. in the diamond range). (**b**) The reflectivity value of 86 is exceedingly low for synthetic moissanite, and closer to that expected for diamond. The gem was cleaned thoroughly before testing, and the cylinder cap was removed only for the photo and did not influence the reflectivity reading. Photos by Julien Xaysongkham, SSEF.

for this diamond imitation. (Carbon cannot be detected with this method.)

Another interesting feature of the specimen was an inscription on the polished girdle (characters 'GRA' followed by a nine-digit number) which, at a glance, resembled laser inscriptions commonly found on GIA-graded diamonds. Fraudulent GIA laser inscriptions on synthetic moissanite have been reported recently (Hlatshwayo & Eaton-Magaña 2020).

To summarise, the synthetic moissanite described here has some unusual characteristics that could complicate correct identification, especially if only relying on readily available testing instruments that depend on thermal conductivity and reflectivity. Heat treatment can lower the reflectivity of synthetic moissanite so that it approximates that of diamond (or is even lower), as described more than two decades ago (Chalain 2000). However, synthetic moissanite treated in this way has never been submitted to SSEF for grading or authentication. Visually, there was no difference in the lustre, brilliance or 'fire' (dispersion) of the sample when compared to other synthetic moissanites from SSEF's reference collection. Nevertheless, careful observation with a gemmological loupe revealed strong doubling,

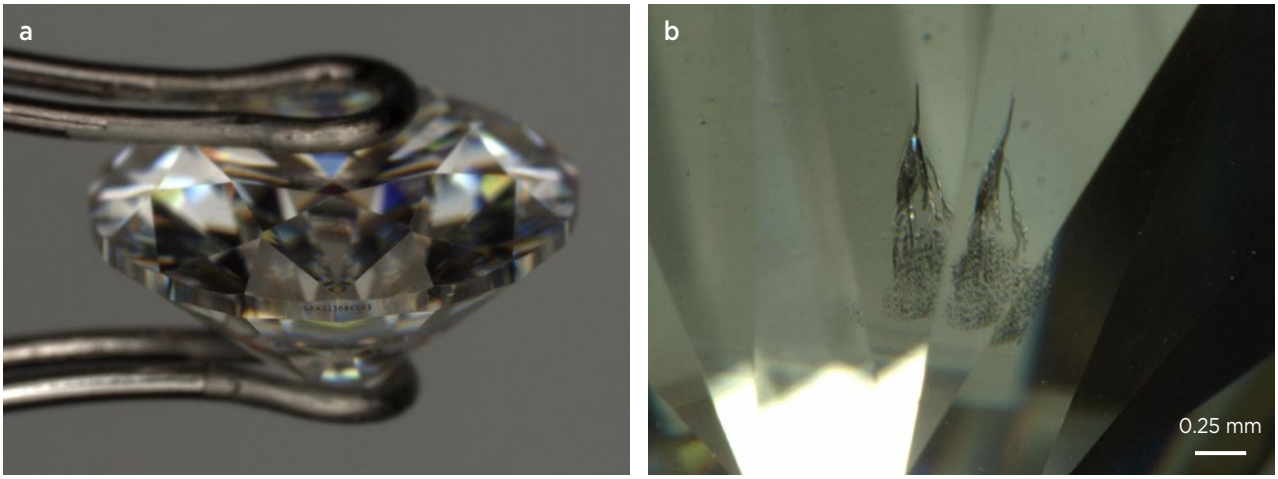

Figure 23: (**a**) Strong doubling of facet edges is visible on the opposite side of the 1.81 ct synthetic moissanite when viewed through the crown main facets. (**b**) This unusual branching inclusion appears twice here because it is seen through two separate pavilion mains. Photos by (a) Julien Xaysongkham and (b) L. Speich (taken using a polarising filter to eliminate doubling).

excluding diamond as a possible identity. This case highlights that the identification of diamond and its simulants should always be based on multiple tests and observations.

Dr Laura Speich FGA (diamonds@ssef.ch),
Jean-Pierre Chalain and
Dr Michael S. Krzemnicki FGA
Swiss Gemmological Institute SSEF
Basel, Switzerland

References

Chalain, J.-P. 2000. Update on moissanite identification. *Journal of the Gemmological Association of Hong Kong*, **21**, 12–15.

Hlatshwayo, S. & Eaton-Magaña, S. 2020. Lab Notes: Synthetic moissanite with fraudulent GIA inscription. *Gems & Gemology*, **56**(3), 424–425.

Kiefert, L., Schmetzer, K. & Hänni, H.A. 2001. Synthetic moissanite from Russia. *Journal of Gemmology*, **27**(8), 471–481, https://doi.org/10.15506/JoG.2001.27.8.471.

Black Sapphire Melee as a Black Diamond Imitation

As black diamond has become increasingly fashionable in recent years, various simulants have appeared. Among them, black synthetic moissanite is commonly used in jewellery (e.g. in cluster settings), as well as cubic zirconia, boron carbide and others (e.g. Kammerling *et al*. 1991; Li *et al*. 2011; Choudhary 2013).

Recently, a pendant set with 22 black stones was submitted to the National Gemstone Testing Center's (NGTC) Beijing laboratory for identification (Figure 24, centre). Due to the opacity of most black diamonds, Fourier-transform infrared (FTIR) spectra usually cannot be collected, but Raman spectroscopy can quickly distinguish diamonds from imitations. Raman spectra of the black stones in the pendant revealed that all of them were diamonds except for one, which lacked the 1332 cm^{-1} feature characteristic of diamond; it was identified as sapphire.

All of the stones in the pendant showed a high lustre, with excellent cut and polish, making it difficult to pick out imitations, even under a microscope. However, with closer examination the black sapphire showed a rougher surface, slightly less sharp facet edges and a slightly weaker lustre (Figure 24, left) as compared to the diamonds' smooth surface, sharp edges and adamantine lustre (Figure 24, right). In addition, when illuminated from the side using a fibre-optic light source, the sapphire appeared almost opaque while the diamonds were semi-transparent.

This is the first time we have encountered black sapphire as a diamond imitation. This serves as a reminder that various melee-sized black materials are being mixed with black diamonds and set into jewellery. In addition to Raman spectroscopy, methods such as DiamondView imaging and thermal conductivity testing are helpful for identifying imitations in black diamond jewellery.

Yang Wang (wangyang@ngtc.com.cn),
Zhonghua Song and Ting Zheng
NGTC, Guangzhou and Beijing, China

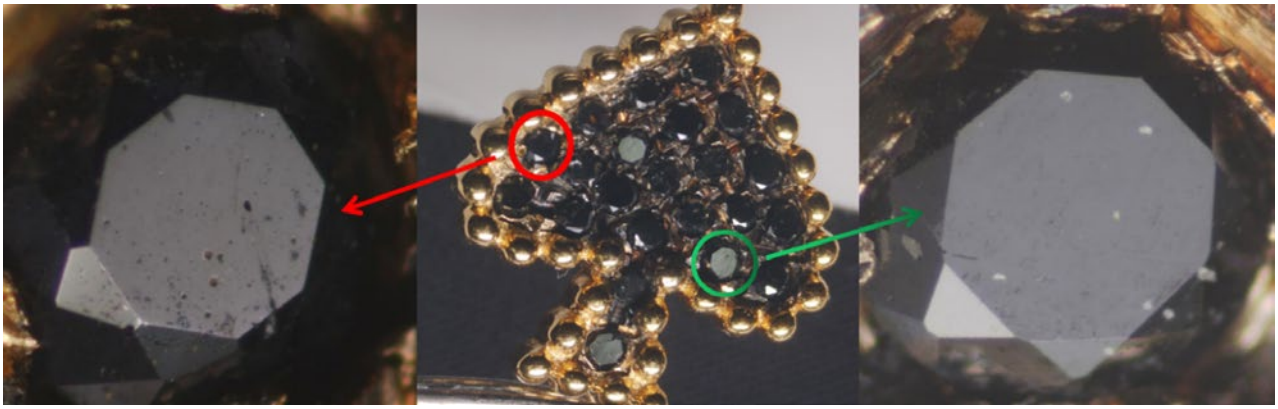

Figure 24. In this pendant (centre, approximately 2 × 2 cm), the stone marked by the red circle is a black sapphire and the others are diamonds. With 50× magnification, the sapphire (left) shows a rougher surface, slightly less sharp facet edges and a slightly weaker lustre than the diamonds (e.g. right). Photos by Z. Song.

References

Choudhary, G. 2013. Gem News International: Boron carbide: A new imitation of black diamond. *Gems & Gemology*, **49**(3), 180–181.

Kammerling, R.C., Koivula, J.I., Kane, R.E., Fritsch, E., Muhlmeister, S. & McClure, S.F. 1991. An examination of nontransparent "CZ" from Russia. *Gems & Gemology*, **27**(4), 240–246, https://doi.org/10.5741/gems.27.4.240.

Li, H., Lu, T., Shen, M., Zhang, J. & Zhou, J. 2011. Identification of black synthetic moissanites in diamond jewelry with cluster setting. *Journal of Gems and Gemology*, **13**(1), 22–24, https://doi.org/10.3969/j.issn.1008-214X.2011.01.005 (in Chinese).

A Convincing Rough Diamond Imitation Manufactured from Topaz

A purported diamond crystal weighing 20.30 ct was recently submitted to the GCS Laboratory in London (Figure 25). It was found to be anisotropic when viewed with a polariscope, and it showed a partial biaxial interference figure with the use of a conoscope. It had a vitreous lustre, and was inert to both long- and short-wave UV radiation. Both thermal and dual handheld diamond testers indicated the specimen was not a diamond. We obtained a spot RI reading of approximately 1.61 and the SG (measured hydrostatically) was 3.56; these values are consistent with those of topaz. Microscopy revealed internal features very unlike those of diamond, consisting of complex fluid inclusions and feathers. In addition, a small area of incipient cleavage extended into the stone from a percussion on the surface. The surface of the apparent octahedral 'faces' was unusual in that it showed a pitted texture much like hammered metal, and lacked any trigons—the triangular etch marks commonly seen on diamonds. UV-Vis-NIR, FTIR, Raman and EDXRF spectroscopic analyses unequivocally confirmed the specimen was topaz.

Figure 25: This 20.30 ct specimen of what appears to be an octahedral diamond crystal was identified as topaz. Photo by Beth West FGA DGA.

The SG of topaz is very similar to that of diamond (3.52 for diamond vs 3.50–3.57 for topaz). Because of the equivalent heft, topaz has historically served as a popular diamond simulant, and various examples have been reported in the literature that resemble waterworn diamond crystals (e.g. Crowningshield & Reinitz 1997; DelRe 1997; Sehgal & Befi 2015). The present stone was unusual because it had been carefully worked to form a rounded octahedron, and it was superficially very convincing, with 'etched' faces and an apparent octahedral form. More like a miniature sculpture than a common simulant, the attention to detail was surprising: a concerted effort by someone with significant knowledge of rough diamonds.

With current concerns about separating laboratory-grown and natural diamonds, traditional diamond simulants and imitations are at risk of being overlooked. Although this specimen would be unlikely to fool a gemmologist performing even standard tests, it was an unexpectedly good fake, and it would be difficult to spot smaller versions mixed into a rough parcel. This serves as a reminder that, as the Roman poet Phaedrus said, 'Things are not always what they seem; the first appearance deceives many; the intelligence of a few perceives what has been carefully hidden'.

Naomi Vane-Wright FGA DGA
(contact@gcslab.co.uk)
GCS Laboratory, London

References

Crowningshield, G.R. & Reinitz, I. 1997. Lab Notes: Topaz fashioned to imitate diamond rough. *Gems & Gemology*, **33**(3), 217–218.

DelRe, N. 1997. Gem Trade Lab Notes: [Diamond] Imitation. *Gems & Gemology*, **33**(1), 57.

Sehgal, A. & Befi, R. 2015. Lab Notes: Polished freeform topaz imitating diamond rough. *Gems & Gemology*, **51**(3), 321–322.

TREATMENTS

Basaltic Sapphire Heated with Pressure

Recently, the authors examined a multi-coloured sapphire (blue, green and yellow) weighing more than 30 ct (Figure 26). Microscopic observation revealed uneven colour distribution with straight green-blue colour zoning in the yellow portion of the stone (Figure 27a). Some of the blue zoning was blurred, as would be expected from high-temperature heat treatment. Also, minute particles were observed near the girdle (Figure 27b). UV-Vis spectroscopy showed a prominent Fe-related band centred at 800 nm, identifying the stone as having a basalt-related geological origin.

Exposure to long-wave UV radiation showed that the blue region of the sapphire was inert, while the green to yellow parts fluoresced patchy orange to red (Figure 28a). This luminescence could be related to traces of Cr, consistent with a Cr-related peak at approximately 693 nm seen in the UV-Vis spectrum. Chemical analysis by EDXRF spectroscopy revealed around 120–190 ppm Cr, as well as an average of more than 6800 ppm Fe, a typical amount for basalt-related sapphire. Exposure to short-wave UV radiation showed zonal patterns of chalky bluish white fluorescence (Figure 28b).

FTIR spectroscopy showed a series of bands around 3300 cm^{-1} in both the blue and yellow parts of the stone, with a prominent band at 3309 cm^{-1} accompanied by smaller bands at 3369, 3233 and 3187 cm^{-1} (Figure 29). A distinct broad band centred at 3030 cm^{-1} was present only in the yellow portion, along with weak bands at 2627, 2461, 2413 and 2245 cm^{-1}. Such a pattern indicates heat treatment under pressure (also known as PHT: see Wathanakul *et al.* 2016; Peretti *et al.* 2018; Sun & Gao 2019).

Figure 26: This 30+ ct basaltic sapphire displaying blue-green-yellow colouration showed evidence of heating with pressure. Photo by Kaiyin Deng.

PHT treatment is typically applied to light blue sapphires of metamorphic origin in order to intensify blue colouration. This is the first time we have encountered a PHT-treated basalt-related sapphire. It is surprising to encounter such a stone, given that its colouration is quite unlike the material typically treated by this technique.

Yujie Gao, Xueying Sun
(shirley.sun@guildgemlab.com)
and Yizhi Zhao
Guild Gem Laboratories
Shenzhen, China

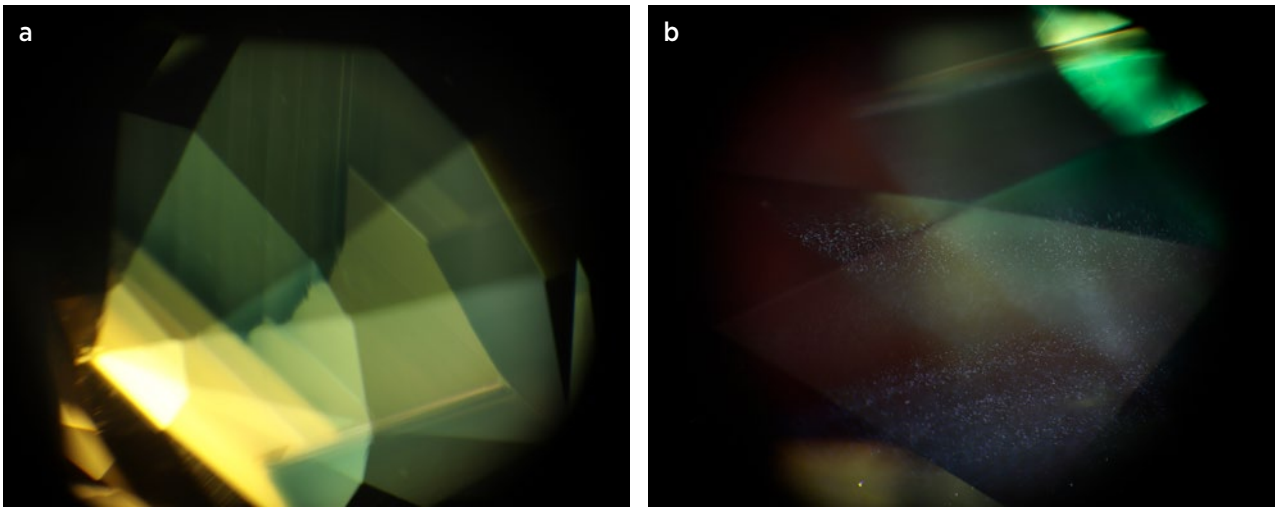

Figure 27: (**a**) Green-blue colour zoning in the yellow portion and (**b**) tiny particles scattered along the girdle are present in the sapphire. Photomicrographs by Y. Zhao; image width (a) 2.8 mm and (b) 3.1 mm.

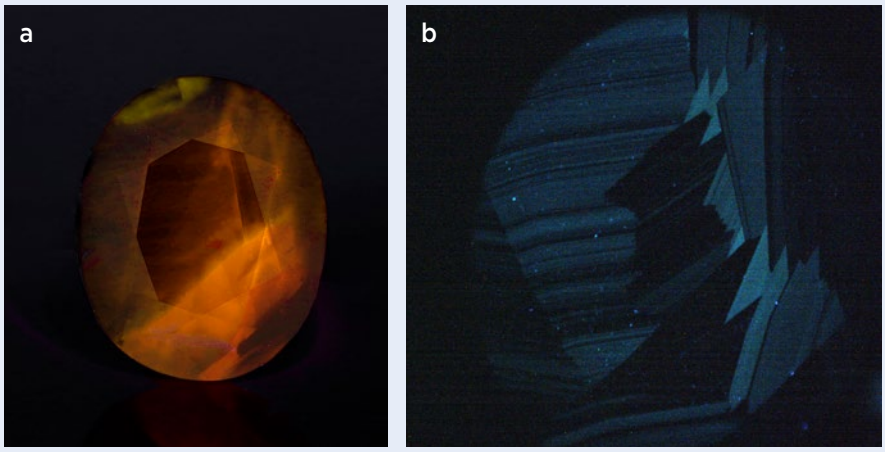

Figure 28: The sapphire fluoresces (**a**) patchy orange to red to long-wave UV and (**b**) chalky bluish white to short-wave UV radiation. Photos by (a) Kaiyin Deng and (b) Y. Zhao.

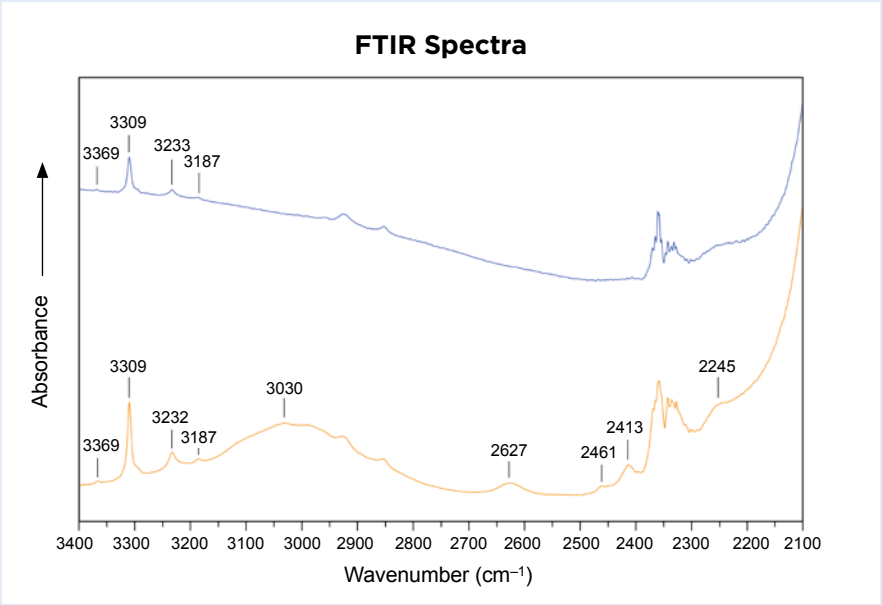

Figure 29: FTIR spectra are shown for the blue and yellow portions of the sapphire. The yellow portion displays a broad band centred at 3030 cm^{-1} and a series of bands at 2627, 2461, 2413 and 2245 cm^{-1} that are indicative of heat treatment under pressure. The spectra are offset vertically for clarity.

References

Peretti, A., Musa, M., Bieri, W., Cleveland, E., Ahamed, I., Alessandri, M. & Hahn, L. 2018. Identification and characteristics of PHT ('HPHT') - treated sapphires - An update of the GRS research progress. GRS GemResearch Swisslab AG, https://www.gemresearch.ch/news/2018/11/03/hpht-update, 14 November, accessed 7 October 2022.

Sun, X. & Gao, Y. 2019. Gem News International: Recrystallization of baddeleyite as an indicator of PHT ("HPHT") treatment in sapphire. *Gems & Gemology*, **55**(3), 448–450.

Wathanakul, P., Leelawatanasuk, T., Atsawatanapirom, N., Ounorn, P. & Lhuaamporn, T. 2016. Gem Notes: HPHT-treated blue sapphire: An update. *Journal of Gemmology*, **35**(3), 208–210.

ERRATUM

On p. 22 of the Gem Note by Dr J. C. (Hanco) Zwaan titled 'Imitations of trapiche ruby and emerald' (Vol. 37, No. 1, 2020, pp. 21–22), Raman spectroscopy of the matrix of the trapiche ruby imitation showed a spectrum that entirely corresponds to polystyrene (cf. Bertoldo Menezes *et al.* 2017). Therefore, only polystyrene was detected in the matrix, and not a mixture of resin and silica. We thank Dr Lutz Nasdala for kindly pointing out this error.

Reference

Bertoldo Menezes, D., Reyer, A., Marletta, A. & Musso, M. 2017. Glass transition of polystyrene (PS) studied by Raman spectroscopic investigation of its phenyl functional groups. *Materials Research Express*, **4**(1), article 015303 (11 pp.), https://doi.org/10.1088/2053-1591/4/1/015303.

Demantoid from Kerman Province, South-east Iran: A Mineralogical and Gemmological Overview

Vahid Ahadnejad, Michael S. Krzemnicki and Ann Marie Hirt

ABSTRACT: Demantoid from Kerman Province in south-east Iran was investigated using microscopy, spectroscopy (optical absorption, FTIR and Raman), chemical analysis (EDXRF and LA-ICP-TOF-MS) and magnetic susceptibility measurements. The samples were transparent to semi-transparent and commonly contained acicular chrysotile inclusions. Their spectroscopic and chemical properties were consistent with demantoid from serpentinite host rock. The samples ranged from yellowish green to deep green, depending on Cr and Fe content. These two elements are also largely responsible for the material's paramagnetic susceptibility. Our samples contained relatively high concentrations of the trace elements Cr, Ge, Ni and Co. Comparison with available chemical data on serpentinite-hosted demantoid from the literature suggests that Iranian demantoid can be separated from stones of other localities.

The Journal of Gemmology, **38**(4), 2022, pp. 329–347, https://doi.org/10.15506/JoG.2022.38.4.329

Andradite, ideally $Ca_3Fe^{3+}_2Si_3O_{12}$, is the Ca-Fe end member of the ugrandite garnet subgroup and occurs in three colour-related varieties: black melanite, yellow to brown topazolite and yellowish green to green demantoid (Figure 1; O'Donoghue 2006). Demantoid usually contains traces of Cr, which is the main cause of the green colour, although stones from some deposits lack this element.

In 1853, Finnish mineralogist Nils Gustaf Nordenskiöld first described demantoid as a new variety of andradite from Nizhniy Tagil in the Central Ural Mountains of Russia (Eichmann 1870). Due to its exceptional brilliance and high dispersion, Nordenskiöld named the material *demantoid* ('diamond-like'). With a dispersion higher than that of diamond and its vivid green colour, it quickly became *au courant* at the Russian royal court as a treasured and expensive gem material.

For decades, demantoid was found almost exclusively in Russia (Phillips & Talantsev 1996). More recently, several other sources of gem-quality demantoid have been reported, such as Canada, Iran, Italy[1], Madagascar, Pakistan and Namibia (Lind *et al.* 1998; Quinn & Laurs

Figure 1: Demantoid from Iran is an attractive gem material. The stone shown here weighs 1.1 ct. Photo courtesy of K. Zebardast.

[1] Although demantoid from Val Malenco, Italy, was first described at the end of the 1800s, it only reached the market in recent decades.

Figure 2: This shaded relief map shows the location of the demantoid mining area near the village of Bagh Borj in Kerman Province (from Google Maps, https://tinyurl.com/2p8eu37y). The inset map indicates the location of this area (red rectangle) and Kerman Province (orange) in Iran.

2005; Du Toit *et al.* 2006; Karampelas *et al.* 2007; Adamo *et al.* 2009; Pezzotta *et al.* 2011). Most reports on demantoid have focused on its occurrence, crystal chemistry and gemmological properties (Gill 1978; Misiorowski & Hays 1993; Krzemnicki 1999; Milisenda *et al.* 2001; Pavese *et al.* 2001; Quinn & Laurs 2005; Adamo *et al.* 2015).

Gem-quality demantoid is commonly found in two very different geological settings (Adamo *et al.* 2011): serpentinite (e.g. Kerman Province, Iran; Val Malenco, Italy; Kaghan Valley, Pakistan; and Ural Mountains, Russia) and skarn (e.g. Antetezambato, Madagascar; and Erongo, Namibia). Most demantoid from serpentinite contains very fine and often curved needles, predominantly consisting of chrysotile, $Mg_3Si_2O_5(OH)_4$, a member of the kaolinite-serpentine group. These inclusions are characteristic of demantoid from Iran, Italy, Pakistan and Russia (Palke & Pardieu 2014). They do not, however, occur in skarn-related demantoid from Madagascar or Namibia. In addition, the chrysotile fibres in demantoid from serpentinites often radiate from a central chromite inclusion ($CrFe_2O_4$), forming what is commonly referred to as a 'horsetail' inclusion.

In this study, we focus on gem-quality demantoid from serpentinite-hosted deposits near the village of Bagh Borj (also called Bagh-e Borj) in the Soghan District of Kerman Province, south-eastern Iran.[2] Based on detailed fieldwork (by author VA) and laboratory analyses, we report on the geology, mineralogy and gemmology of this Iranian demantoid. In addition to collecting standard gemmological properties, we performed optical absorption spectroscopy, Fourier-transform infrared (FTIR) spectroscopy, Raman spectroscopy, chemical analyses and magnetic susceptibility measurements to characterise the samples.

LOCATION AND MINING

Iran's Kerman Province was first mentioned as a new source of gem-quality demantoid at the International Gemmological Conference in Spain in 2001 (Milisenda *et al.* 2001; Liu 2010). However, interviews by the first author (VA) with local villagers from Bagh Borj revealed that some Russian gem dealers were aware of this deposit many years earlier. These dealers occasionally bought demantoid of significant size and quality at rather low prices, so it is possible that some of the material marketed as being of Russian origin might have actually come from Iran.

The demantoid mining area is located between the towns of Jiroft and Baft in Kerman Province, about 960 km south-east of Tehran (Figure 2). High-quality demantoid

[2] Not included in this study is skarn-related demantoid from deposits in western and north-western Iran (Takab, Sarab, Hormozgan and Kurdistan). Although these localities have occasionally produced large crystals, they are usually highly fractured and thus of only limited use as gems.

Figure 3: (**a**, **b**) Demantoid mining near Bagh Borj has been done in tunnels and open cuts excavated by local residents. The underground workings can reach more than 50 m. (**c**) Demantoid is hosted by weathered serpentinite and is easily separated from it. (**d**) These demantoid crystals average 1 g each. Photos by V. Ahadnejad.

was first found near Bagh Borj, which is located in a cold, mountainous region. The roads to the village are very rugged and cannot be passed by car during the winter season. Additional garnet localities have been mined by local inhabitants of other villages in this region, such as Solouiyeh, Rosedar, Madan-e Abdasht, Sargaz, Parantabad, Anbarabad, Fathabad, Dowlatabad and Vakilabad. However, gem-quality demantoid has not yet been found at most of these locations; almost all commercially significant production has been mined in the mountains around Bagh Borj (Figure 3).

Currently, the annual production of demantoid from the Bagh Borj area is estimated at several thousand grams of rough material of various qualities. The weight of a piece of rough seldom exceeds 0.2 g (Figure 4), but occasionally larger crystals are produced (up to 1 g) and, very rarely, even some giant ones weighing up to several dozen grams (Figure 5). However, most of the larger crystals are quite included. The gem-quality material is consumed by the jewellery trade in Iran and also exported to Europe, India and China, both as rough and cut stones.

Figure 4: These small crystals (approximately 0.2 g each) of gem-quality Iranian demantoid show attractive vivid green to yellowish green colour and excellent transparency. Photo courtesy of A. Badamegan.

Figure 5: This giant demantoid crystal from Kerman Province weighs 137 g. Photo by V. Ahadnejad.

GEOLOGICAL SETTING

The demantoid deposits in Kerman Province are located in the south-eastern part of the Sanandaj-Sirjan zone, an elongated geological system (about 1,500 km long and 70 km wide) extending north-west to south-east throughout Iran (Figure 6). It represents the north-eastern suture of the Neo-Tethys that formed by continental collision between the northern margin of Gondwana and the southern part of Eurasia during the late Eocene (Allen & Armstrong 2008) or Oligocene (McQuarrie & van Hinsbergen 2013). The Sanandaj-Sirjan zone contains scattered elements of Pan-African basement rocks, interpreted as the south-western margin of the Cimmerian continental fragment (Celâl Şengör 1984; Ricou 1994; Stampfli & Borel 2002; Fergusson *et al.* 2016). The continental collision was preceded by complex tectonic events that followed Mesozoic convergence along the Tethys Ocean's northern margin and ophiolite obduction on its southern margin.

The Sanandaj-Sirjan zone consists of highly deformed metamorphic rocks, including ophiolitic mélange (ophiolitic blocks mixed with serpentinite and pelagic sediments and flysch) and ultramafic-mafic complexes that indicate an active tectonic regime (Ahmadipour *et al.* 2003; Barrois *et al.* 2012, 2013). Ophiolites represent former oceanic crust and underlying mantle materials that have been tectonically uplifted to the surface, typically during the closing of an ocean basin. They consist of an assemblage of mafic and ultramafic lavas and hypabyssal rocks found in association with sedimentary rocks, such as greywacke and chert. Most of the ultramafic rocks are altered to serpentinite.

Investigations by author VA showed that the green fibrous serpentinite that hosts most of the demantoid occurrences in Kerman Province is very soft (like soapstone) and consists of chrysotile, antigorite, bastite (as a pseudomorph), brucite and talc. Chromite, which is potentially the source of Fe and Cr in the demantoid, is abundant in the serpentinised rocks. Several chromite deposits are exploited in the area, such as the Abdasht mine with an ore concentration of 35–40% Cr_2O_3. There is a close relationship between Cr deposits and demantoid genesis. The study area (Bagh Borj and its surroundings) consists of oceanic lithosphere that is represented by ophiolitic sequences including peridotites. These peridotites were uplifted along detachment faults and underwent hydrothermal alteration. The mineral association—including chromite, magnesiochromite, Cr-spinel, picotite, uvarovite and magnetite—imply

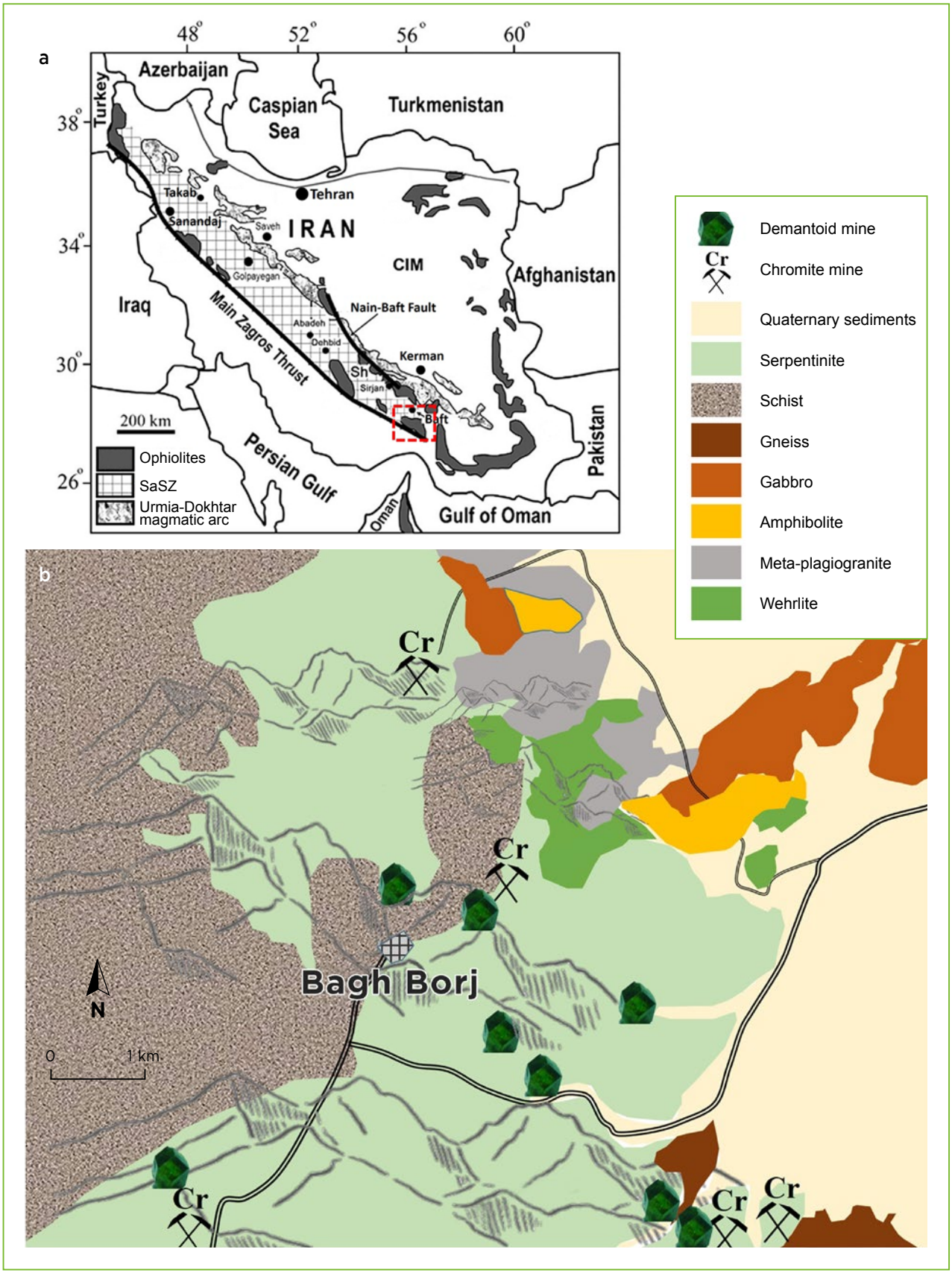

Figure 6: (**a**) Demantoid deposits in Iran's Kerman Province are hosted by ophiolitic rocks at the south-east end of the Sanandaj-Sirjan Zone (SaSZ; see red rectangle; modified after Emami *et al.* 1993 and Ghazi *et al.* 2011). (**b**) The local geological map of Bagh Borj (after Shahraki-Ghadimi *et al.* 2002) shows the distribution of the main rock types, including serpentinite, which hosts the demantoid localities as well as chromite deposits in the area.

a hydrothermal system containing Cr and Fe associated with demantoid genesis in the fissures and veins within metasomatised serpentinite. Finally, the tectonically convergent movements of Iranian-Arabian plates caused uplift of the crust and exposure of demantoid-bearing serpentinite. Demantoid is loosely bound by the serpentinite matrix and therefore crystals may appear in the local rivers after heavy rain.

MATERIALS AND METHODS

From a large parcel of rough demantoid, partly collected by one of the authors (VA) and partly bought from local miners in the Bagh Borj area, we selected 10 representative gem-quality rough samples originating from various localities within the study area (Table I). A window was cut and polished on one side of each specimen to facilitate analyses and observation of internal features. These samples (0.25–1.02 g) ranged from yellowish green to vivid green and were transparent to semi-transparent. In addition, two faceted demantoid gemstones (0.63 and 0.80 ct) from Kerman Province were used for standard gemmological testing and microscopic examination.

All the specimens were analysed at the Swiss Gemmological Institute SSEF in Basel, Switzerland, with standard gemmological tools including a refractometer, a hydrostatic balance, long- and short-wave UV lamps, and a microscope. Optical absorption spectra (375–900 nm) were collected using a Cary 500 spectrophotometer with a scan rate of 70 nm/minute and a data interval of 0.35 nm. FTIR spectra were recorded with a Thermo Nicolet iS50 spectrometer using the condensed beam mode and 4.0 cm^{-1} resolution. Each analysis consisted of 256 scans of the sample and background. Raman spectroscopy of demantoid and the inclusions in selected samples was performed with a Renishaw inVia confocal Raman microscope equipped with an argon-ion laser (514.5 nm), using 20× magnification and a resolution of about 1.5 cm^{-1}.

The chemical composition of each sample was measured at SSEF by energy-dispersive X-ray fluorescence (EDXRF) spectroscopy using a Thermo Scientific ARL Quant'X instrument. All specimens were analysed under vacuum with five different excitation energies (8, 12, 16, 25 and 40 kV) to optimise sensitivity for silicate analysis. In addition, each of the samples was analysed at SSEF with laser ablation inductively coupled plasma time-of-flight mass spectrometry (LA-ICP-TOF-MS, referred to below as GemTOF). The instrument consisted of a high-performance 193 nm laser ablation unit (NWR193UC from ESI, Huntingdon, UK) coupled to an ICP-TOF-MS (icpTOF from Tofwerk AG, Thun, Switzerland). Detailed information about instrumental parameters, analytical conditions and raw data processing can be found in Wang *et al.* (2016), Phyo *et al.* (2020) and Wang & Krzemnicki (2021). The benefit of TOF-MS (compared with more conventional quadrupole MS) is the simultaneous acquisition of the full mass spectrum, which makes it ideal for constantly monitoring elemental

Table I: Demantoid study samples and their localities in Kerman Province, Iran.

Sample no.	Main colour	Weight (g)	Latitude	Longitude	Nearest town (village)	Lithology
1	Green	1.02	28° 44′ 27.7″	57° 28′ 16.0″	Jiroft (Sargaz)	Serpentinised lherzolite
2	Dark green	0.83	28° 33′ 21.4″	57° 09′ 32.5″	Jiroft (Bagh Borj)	Serpentinised lherzolite
3	Light green	0.59	28° 29′ 37.5″	56° 53′ 37.4″	Baft (Parantabad)	Serpentinite schist
4	Yellowish green	0.57	28° 24′ 05.3″	56° 56′ 43.1″	Baft (Anbarabad)	Serpentinite schist
5	Green	0.53	28° 20′ 21.2″	56° 45′ 23.7″	Baft (Madan-e-Abdasht)	Serpentinised lherzolite
6	Dark green	0.37	28° 15′ 43.6″	56° 46′ 35.6″	Baft (Fathabad)	Serpentinised dunite
7	Green	0.32	28° 15′ 05.3″	56° 45′ 01.8″	Baft (Fathabad)	Serpentinite schist
8	Olive green	0.39	28° 12′ 59.9″	56° 25′ 56.4″	Baft (Dowlatabad)	Serpentinite schist
9	Yellowish green	0.36	28° 18′ 59.0″	56° 22′ 51.4″	Orzueeyeh	Serpentinised dunite
10	Dark green	0.25	28° 22′ 36.9″	56° 05′ 09.5″	Orzueeyeh (Vakilabad)	Serpentinised lherzolite

variations (such as those due to growth zoning), and also detecting accidentally ablated (sub-microscopic) inclusions (Wang *et al*. 2016). We analysed three spots with an ablation diameter of 100 µm on visually inclusion-free areas of each sample. NIST SRM 612 glass was used as the external standard and stoichiometric Si (for ideal andradite) as the internal standard.

Some demantoids are attracted by a strong magnet due to their relatively high Fe content. To investigate this, we tested 84 demantoid crystals from the study area with a very strong neodymium magnet that measured 2 × 10 × 20 mm. In addition, we measured the magnetic susceptibility (see Box A) of the 10 demantoid samples characterised for this report in order to collect data that might be useful in the future for separating Iranian demantoid from its counterparts from other localities. Magnetic susceptibility can indicate if ferromagnetic inclusions are present and may also provide information regarding chemical variability. The magnetic susceptibility and its directional dependence—that is, the anisotropy of magnetic susceptibility (AMS)—was analysed at ETH Zurich in Switzerland with an AGICO MFK1-FA Kappabridge instrument, using an applied field of 200 A/m and a frequency of 976 Hz. AMS is mathematically described by a symmetric second-order tensor, and can be geometrically represented with an ellipsoid whose principal axes are the three eigenvalues of the tensor, where $K_1 \geq K_2 \geq K_3$. Mean magnetic susceptibility (K_m) is defined as:

$$K_m = (K_1 + K_2 + K_3)/3$$

Induced magnetisation as a function of high field was used to determine if there were any ferromagnetic inclusions present. Because the bulk susceptibility turned out to be similar for all samples, only one of them was evaluated in this way. Garnet is a paramagnetic mineral and should follow the Curie law, in which $K = C/(T-\theta_p)$, where C is a constant, T is temperature and θ_p is the paramagnetic Curie temperature. The value of θ_p has not been experimentally determined, but is an important and unique magnetic property of a mineral. The induced magnetisation was measured on a Princeton Measurements Corporation vibrating sample magnetometer outfitted with a liquid helium cryostat in fields of ±1 tesla and temperatures between 20 and 270 K.

BOX A: MAGNETIC SUSCEPTIBILITY

The characterisation of the magnetic properties of materials is a rather rarely applied method for gem identification and classification, although it has been used for determining the purity of diamond for a number of decades (Sigamony 1944). In general, materials can be separated into three categories based on their reaction to a magnetic field:

1. *Diamagnetic* materials have no magnetic moment when no magnetic field is applied and a negative susceptibility when a magnetic field is applied (i.e. the induced magnetic moment is in the opposite direction from the applied field).
2. *Paramagnetic* materials also have no magnetic moment when no magnetic field is applied, but have a weak magnetic moment in the direction of the applied magnetising field, and therefore have a positive magnetic susceptibility.
3. *Ferromagnetic* materials retain their magnetisation in the absence of an applied field over time. Their susceptibility is positive and can be significantly stronger than that of paramagnetic materials.

Because magnetic susceptibility is directly dependent on the elemental composition of a mineral (particularly Fe content), it can be useful in the study of gems. Hoover (2011) demonstrated that by combining information on RI and magnetic susceptibility, the chemical composition of garnets can be inferred. In the case of olivine, a quantitative relationship between magnetic susceptibility and Fe content has been used to determine the fayalite mole fraction (cf. Hoye & O'Reilly 1972). Pure forsterite is diamagnetic (due to the absence of Fe) and has a mass susceptibility of about -3.9×10^{-9} m^3/kg. Olivine may become paramagnetic due to the presence of Fe, whereby the mass susceptibility increases with greater Fe content, reaching a value of 1.1×10^{-6} m^3/kg for pure fayalite. Typical peridot gains its green colour from Fe and has a much higher magnetic susceptibility index (~500) than colourless forsterite (~52; Feral 2010).

Furthermore, the maximum susceptibility in peridot is parallel to the *c*-axis (Biedermann *et al*. 2014). The anisotropy of magnetic susceptibility can be used to determine the orientation of the *c*-axis and thus can help the lapidary obtain the best colour of a cut stone.

Figure 7: (**a**) Distinct colour zoning in demantoid sample no. 5 shows a rather transparent green core surrounded by a yellowish green intermediate zone containing a dense micro-crack pattern and followed by a vivid green rim. (**b**) A closer view of the intermediate zone shows the honeycomb-like pattern of the micro-cracks. (**c**) The botryoidal surface of serpentinite-related demantoid is seen on this specimen. Photos by M. S. Krzemnicki; magnified (a) 10×, (b) 50× and (c) 30×.

RESULTS

Standard Gemmological Testing

Testing of our samples by classical gemmological methods gave results consistent with the reported physical properties for demantoid (cf. O'Donoghue 2006). The SG value ranged from 3.82 to 3.87. The RI could not be measured using a standard refractometer (based on total internal reflection) because the value is above that of the contact liquid (i.e. >1.81). Under long-wave UV radiation, our samples were inert or showed very weak yellowish green fluorescence, and they were inert to short-wave UV.

Microscopic Observations

The investigated demantoid samples were quite included. Most exhibited distinct angular growth zones with a saturated green core surrounded by a yellowish green intermediate zone that was overgrown by a vivid green rim (Figure 7a). The intermediate zone locally exhibited a dense pattern of honeycombed micro-cracks, whereas the rim of the crystals was commonly characterised by a botryoidal outline and tiny radial fissures (Figure 7b, c). Similar botryoidal surfaces are well known in serpentinite-related demantoid from other deposits. The faceted stones examined for this study displayed both colour zoning and micro-cracks, which were common in the culet area (Figure 8a–c).

Straight-to-curved fibres were the most prominent inclusion feature. They usually were present mostly in the rim zone as fine bundles or layers of rather parallel fibres (partly chrysotile, partly hollow; Figure 8d–f) or in the core of the crystals as randomly oriented curved fibres (Figure 8d). Raman micro-spectroscopy of several whitish fibrous inclusions in one sample revealed that

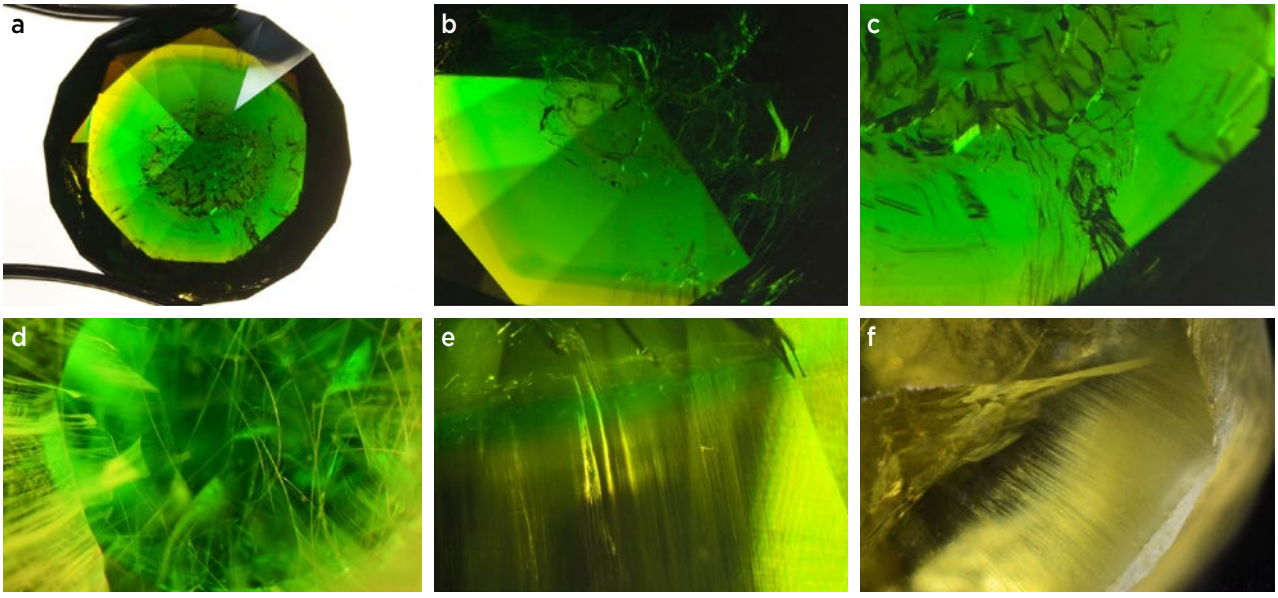

Figure 8: A faceted demantoid from Kerman Province reveals colour zoning (**a**, **b**), micro-cracks in the culet area (**a**–**c**) and fine fibres (**d**–**f**). These fibres occur in bundles or layers in the intermediate and rim zones, but most of the fibres in the core are distinctly curved. Photomicrographs by M. S. Krzemnicki; magnified (a) 10×, (b) 20×, (c) 30×, (d, e) 40× and (f) 50×.

they consisted of chrysotile (see Raman section below). Fibrous calcite, as reported by Karampelas *et al.* (2007), was not found in our samples.

In some cases, the fibres were aggregated into small whitish 'cotton balls'. Although small black chromite inclusions were present, our samples showed no radiating 'horsetails' from these grains, as known in demantoid from serpentinite-related deposits such as in Russia and Val Malenco, Italy (Laurs 2002; Du Toit *et al.* 2006; Karampelas *et al.* 2007; Adamo *et al.* 2009; Liu 2010; Hennebois *et al.* 2021). In addition, most samples contained fine veils of partially healed fissures ('fingerprints').

As reported in the gemmological literature, Iranian demantoid occasionally exhibits a cat's-eye effect when properly cut as a cabochon. This effect is caused by long parallel fibrous inclusions (Laurs 2002; Douman & Dirlam 2004; Kiefert & Koivula 2005; Karampelas *et al.* 2007; Liu 2010). However, we did not see any chatoyancy in our samples.

Optical Absorption Spectroscopy

To better understand the colour variations seen in Iranian demantoid, we analysed five samples: green (no. 1), light green (no. 3), olive green (no. 8), yellowish green (no. 9) and dark green (no. 10), thus covering the full range of colours we observed in demantoid from Kerman Province. The spectra of all samples were dominated by Cr^{3+} absorption bands at 625 and 640 nm (Figure 9), consistent with demantoid from other serpentinite-hosted deposits (e.g. Russia and Val Malenco, Italy). Samples 3 and 8 also showed an Fe^{3+}-related peak at around 440 nm, but this feature could not be observed in the others due to their absorption edges. A more detailed analysis of those spectra revealed that overlapping absorption of Cr^{3+} and Fe^{3+} chromophores leads to the absorption edge at around 390 nm.

The 440 nm Fe^{3+} band was narrow and displayed a sharp edge. A shoulder at about 465 nm, most visible for the green sample (no. 1), is presumably due to a broad chromium band towards the UV. It was not present in the Cr-poor yellowish green sample (no. 9). Samples 3 and 8 also showed a transmission window at about 400 nm.

Thus, common features among our samples include: (a) very strong Fe^{3+} absorption between 430 and 444 nm; (b) a shoulder between approximately 465 and 480 nm; (c) a weak band at around 690 nm that is correlated

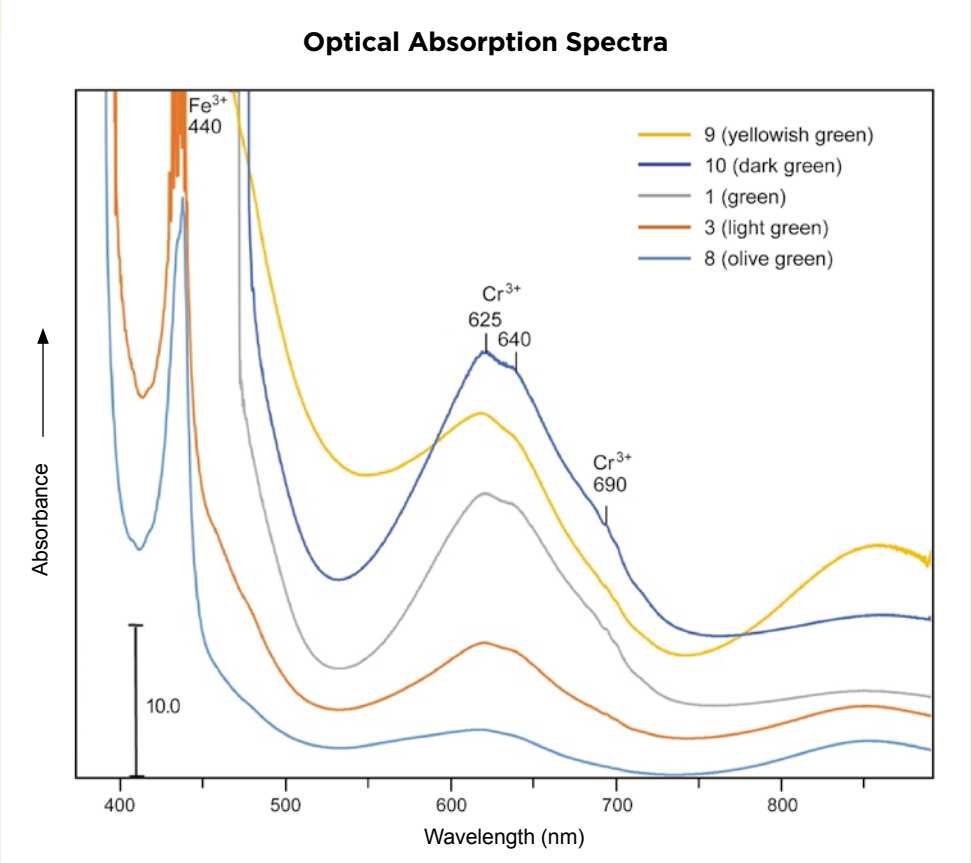

Figure 9: The optical absorption spectra of the demantoid samples are characterised by a broad absorption band caused by peaks at 625 and 640 nm related to Cr^{3+}. Samples 3 and 8 also show a distinct Fe^{3+} peak at about 440 nm. The absorption edge in the blue region of the spectrum is due to overlapping features related to Cr^{3+} and Fe^{3+}. The spectra are offset vertically for clarity. The path lengths of the beam were 3.0 mm (no. 1), 3.8 mm (no. 3), 4.2 mm (no. 8), 5.2 mm (no. 9) and 3.7 mm (no. 10).

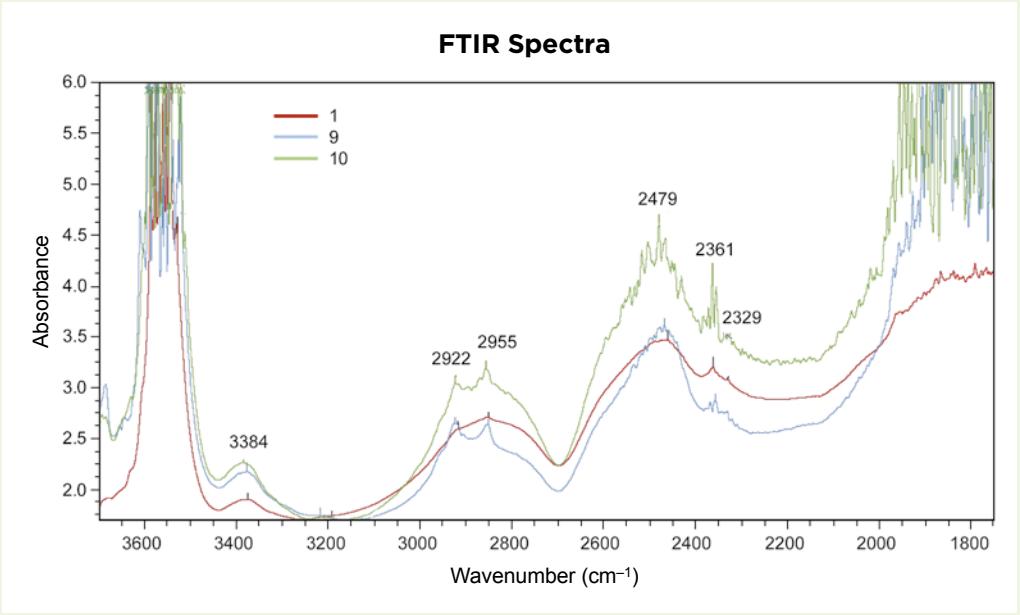

Figure 10: FTIR spectra for selected demantoid samples (nos. 1, 9 and 10) show a large asymmetric band at about 3500 cm^{-1} related to the presence of OH^-.

to Cr^{3+}; (d) strong Cr^{3+} absorption bands at 625 and 640 nm; and (e) a main transmission window between 530 and 535 nm that accounts for the green colour of demantoid. The samples show different absorption levels that correspond to their variations in colour.

FTIR Spectroscopy

The FTIR spectra in the 3700–1800 cm^{-1} region of three demantoid samples (nos. 1, 9 and 10) are shown in Figure 10. The large asymmetric band at about 3500 cm^{-1} is related to the presence of OH^- (Amthauer & Rossman 1998; Adamo *et al.* 2011; Geiger & Rossman 2018).

The FTIR spectra show a good match with those of typical andradite.

Raman Spectroscopy

The Raman spectra of the samples are also characteristic for andradite, with main peaks at 371 and 515 cm^{-1}, and a triplet at 817–875 cm^{-1} (Figure 11). Also present are a H_2O-related peak at 3703 cm^{-1}, and photoluminescence

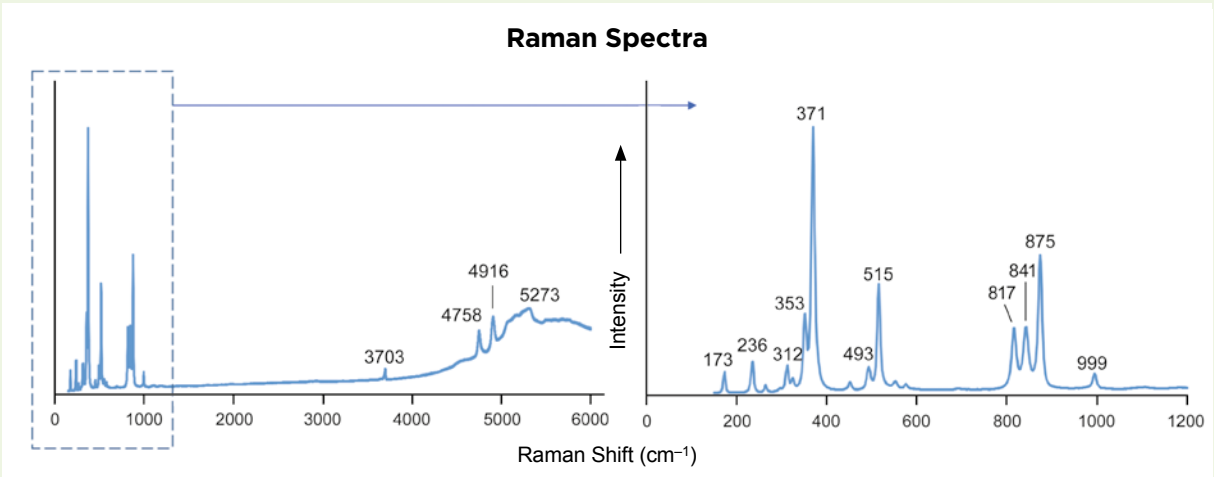

Figure 11: Raman spectra for a representative demantoid sample (no. 7) show main peaks at 371 and 515 cm^{-1}, as well as a triplet at 817–875 cm^{-1}, an H_2O-related peak at 3703 cm^{-1} and photoluminescence peaks at 4750–5300 cm^{-1} that are presumably related to Cr^{3+}.

peaks at 4750–5300 cm^{-1} presumably related to Cr^{3+} (681.3 and 688.7 nm and a multiband series centred at 706.1 nm; Gaft *et al.* 2005; Jasinevicius 2009).

Raman spectroscopy of a whitish fibrous inclusion in sample 2 provided the best fit with that of chrysotile in the RRUFF database (https://rruff.info), showing main Raman bands at 1103, 690, 620, 387 and 233 cm^{-1} (Rinaudo *et al.* 2003; Petriglieri *et al.* 2015).

Chemical Analysis

EDXRF chemical data for the demantoid samples are presented in Table II. Although the ten specimens came from three different locations in the Bagh Borj area (see Table I), their compositions were very similar. As expected for andradite, the samples contained elevated Fe (mean value of 32.21 wt.% Fe_2O_3) and Ca (36.05 wt.% CaO), but also a considerable amount of Cr (2.31 wt.% Cr_2O_3). Also present were minor amounts of Mg (1.20 wt.% MgO) and traces of Mn (0.17 wt.% MnO), K (0.10 wt.% K_2O) and V (0.02 wt.% V_2O_3). Thus, the analysed specimens had only small pyrope and very small spessartine components. Sample 9 (slightly yellowish green) contained distinctly lower Cr than those showing a more vivid green colour.

Chemical data obtained with the GemTOF instrument are presented in Table III. As noted for the EDXRF analyses, Fe was the predominant transition metal in the samples, followed by Cr, Mn, Ti and V (Table III). Additional trace elements included Co, Ni, Ge>Ga, As, Sr, Y, Zr, Nb, Sn, Hf, Ta, REE, W and U>Th.

Magnetic Susceptibility

Testing of 84 Iranian demantoid crystals with a very strong neodymium magnet showed that 72 of them (85%) had weak to strong attraction to the magnet, while only 12 crystals were inert.

The mean mass magnetic susceptibility of the 10 analysed demantoid samples was between 6.00×10^{-7} to 6.54×10^{-7} m^3/kg, with an average value of 6.38×10^{-7} m^3/kg (Table II). The magnetic susceptibility of all samples was isotropic (i.e. it was not dependent on the direction of the applied field).

The specimen that was evaluated as a function of high field at temperatures between 20 and 270 K showed an induced magnetisation that was linearly related to the applied field for all temperatures (Figure 12a), which indicates that the sample is paramagnetic in this temperature range and that no ferromagnetic inclusions are present. The increase in magnetic susceptibility with decreasing temperature follows the Curie Law, as seen from the linear trend of inverse susceptibility as a function of temperature (Figure 12b). Because the projection of the linear trend extends to a temperature of <0 K, the projected value of the paramagnetic Curie temperature

Table II: Chemical composition by EDXRF and magnetic susceptibility of demantoid from Kerman Province, Iran.

Oxide (wt. %)	1	2	3	4	5	6	7	8	9	10
SiO_2	29.22	27.37	29.68	28.26	29.03	26.45	26.78	26.27	25.99	27.28
Al_2O_3	bdl*	bdl	bdl	bdl	bdl	bdl	bdl	bdl	bdl	bdl
Cr_2O_3	1.77	2.73	1.46	2.32	2.04	2.77	2.93	2.70	0.33	4.09
V_2O_3	0.015	0.004	0.011	0.013	0.026	0.032	0.026	0.024	0.021	0.031
Fe_2O_3	33.48	31.05	34.03	33.63	33.42	31.41	30.69	30.88	35.31	28.23
MnO	0.14	0.18	0.11	0.16	0.17	0.17	0.21	0.19	0.10	0.21
MgO	0.88	0.30	0.53	0.66	1.01	0.60	2.47	2.07	0.43	3.06
CaO	34.18	37.99	33.81	34.61	33.95	38.16	36.46	37.43	37.39	36.56
K_2O	0.07	0.08	0.08	0.10	0.10	0.10	0.11	0.11	0.14	0.12
Total	99.76	99.70	99.71	99.75	99.75	99.69	99.68	99.67	99.71	99.58
Magnetic susceptibility (10^{-7} m^3/kg)	6.11	6.00	6.42	6.54	6.46	6.49	6.37	6.48	6.51	6.47

* Al_2O_3 was below the detection limit (bdl) of our EDXRF setup in all analyses. In addition, S, Ga, Ge, As, Rb, Sr, Zr, Sb, Cs, Ba and Pb were not detected.

Table III: Chemical analyses by GemTOF of demantoid from Kerman Province, Iran.*

Element (ppmw)	1	2	3	4	5	6	7	8	9	10
Sc	48.5	62.6	16.6	115.1	2092	137.4	80.8	95.2	36.1	78.7
Ti	126.2	419.0	34.2	202.6	62.0	133.4	237.3	241.5	109.8	238.2
V	136.1	174.3	21.8	77.7	25.2	196.2	102.4	75.0	99.1	61.7
Cr	26830	31720	1117	18390	11060	18590	29080	22170	4032	26720
Mn	235	242	245	267	256	226	255	250	297	260
Al	68.78	38.64	143.2	102.3	123.8	45.86	67.26	79.04	284.7	98.96
Fe	213280	210890	238100	216090	224560	220160	212880	216870	236340	211140
Co	3.05	2.77	3.55	3.46	2.95	2.33	2.86	2.83	2.17	2.72
Ni	na	3.80	6.32	9.22	3.69	4.47	9.81	na	2.82	5.46
Cu	0.401	0.225	0.275	0.174	0.240	0.457	0.222	0.400	0.219	0.256
Ga	0.127	0.156	0.084	0.065	0.097	0.137	0.132	0.102	0.138	0.095
Ge	27.5	32.2	22.5	25.8	22.5	35.5	26.8	27.4	25.2	22.4
As	0.529	0.496	0.520	0.451	0.542	0.410	0.369	0.452	0.410	0.356
Sr	0.377	0.219	0.496	0.235	0.295	0.277	0.190	0.202	0.106	0.293
Y	0.726	0.775	0.058	1.678	0.123	2.50	1.05	1.24	0.284	0.617
Zr	1.38	2.27	0.069	1.18	0.107	2.87	1.71	1.91	0.896	0.799
Nb	0.745	8.70	na	0.430	0.048	0.232	0.323	0.503	0.248	0.541
Sn	2.37	2.47	1.26	1.41	1.73	1.89	1.41	0.97	3.23	1.19
Hf	0.054	0.067	0.007	0.053	0.008	0.093	0.056	0.048	0.022	0.027
Ta	0.011	0.170	0.003	0.007	na	0.003	0.005	0.006	na	0.007
W	1.82	0.049	3.24	3.43	4.37	1.83	1.79	2.82	na	3.71
Th	0.008	0.015	0.010	0.040	0.018	na	0.026	0.065	0.013	0.061
U	0.047	0.056	0.086	0.123	0.125	0.023	0.106	0.160	0.400	0.131
La	0.062	0.052	0.133	0.128	0.140	0.045	0.097	0.162	0.197	0.147
Ce	0.282	0.392	0.288	0.596	0.346	0.190	0.488	0.908	0.548	0.701
Pr	0.049	0.081	0.018	0.072	0.024	0.039	0.072	0.098	0.022	0.081
Nd	0.287	0.307	0.053	0.254	0.054	0.200	0.255	0.336	0.055	0.224
Sm	0.082	0.046	na	0.104	0.048	0.052	0.045	0.051	na	0.104
Eu	0.011	0.017	na	0.021	0.009	0.028	0.015	0.018	0.013	0.016
Gd	0.038	0.045	na	0.111	na	0.096	0.049	0.060	0.030	0.046
Tb	0.008	0.009	0.004	0.021	0.005	0.024	0.013	0.010	0.007	0.010
Dy	0.083	0.068	0.014	0.201	0.017	0.275	0.128	0.094	0.037	0.076
Ho	0.025	0.025	0.003	0.077	0.005	0.092	0.029	0.036	0.009	0.018
Er	0.114	0.111	0.009	0.287	0.020	0.411	0.176	0.194	0.038	0.094
Tm	0.311	0.027	na	0.069	0.004	0.072	0.059	0.045	0.008	0.023
Yb	0.272	0.311	0.022	0.750	0.029	0.649	0.508	0.587	0.067	0.317
Lu	0.067	0.079	0.002	0.175	0.007	0.131	0.131	0.155	0.014	0.083
Σ REE	1.69	1.57	0.55	2.87	0.71	2.30	2.07	2.75	1.05	1.94
Σ LREE	0.77	0.90	0.49	1.18	0.62	0.55	0.97	1.77	0.84	1.27
Σ HREE	0.92	0.68	0.05	1.69	0.09	1.75	1.09	1.18	0.21	0.67
Σ LREE / Σ HREE	0.84	1.33	9.11	0.69	7.14	0.32	0.89	1.33	3.98	1.91

* Mean values of three analyses each. Abbreviation: na = not analysed.

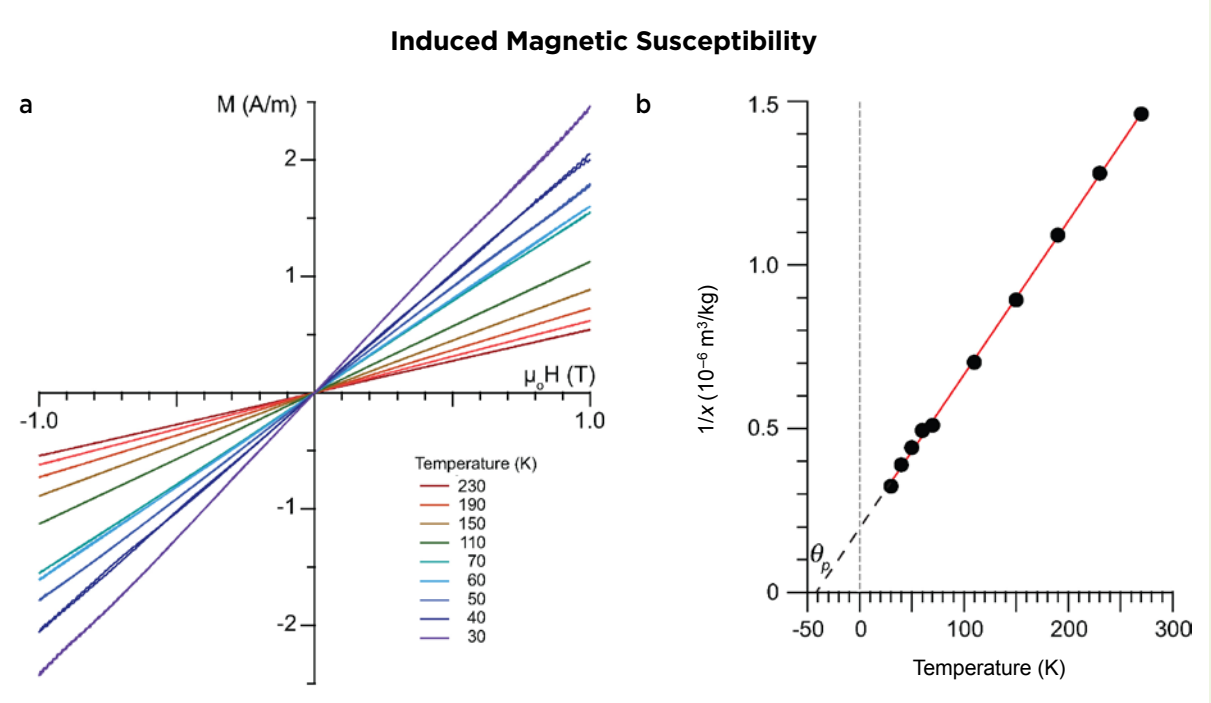

Figure 12: (**a**) For a representative demantoid sample, induced magnetisation as a function of applied field at different temperatures illustrates its paramagnetic behaviour. (**b**) Inverse susceptibility as a function of temperature shows a linear temperature dependency and a projected value of the paramagnetic Curie temperature θ_p = –41.9 K.

is negative with θ_p = –41.9 K. In this case, θ_p is referred to as the asymptotic Néel temperature[3] because the demantoid must undergo antiferromagnetic ordering at a very low temperature (Néel 1948). The asymptotic Néel temperature is indicative of a predominantly antiferromagnetic character of the exchange interactions in the spin system (Néel 1948; Lowrie 1990; Tauxe 2014).

DISCUSSION

Demantoid is found in two types of geological settings: contact metamorphic skarn-type (e.g. Madagascar, Mexico, Namibia and Takab in Iran) and serpentinite-type (e.g. China, Italy, Pakistan, Russia, Slovakia and Kerman in Iran). Demantoid that forms in skarn-type deposits is usually associated with topazolite (±melanite) varieties of andradite, while serpentinite-hosted demantoid does not show this assemblage (Kievlenko 2003). This is also the case for Kerman demantoid, which formed in serpentinite. The distinct Cr^{3+} bands in the optical spectra confirm a serpentinite-related genesis for these samples. In general, the increase in absorption from 500 to 450 nm can be assigned to Fe^{2+}–O–Ti^{4+} charge transfer (e.g. Yu *et al*. 2019). As seen from the compositions listed in Tables II and III, there is no significant concentration of another transition metal that could be responsible for this band, other than traces of Mn (typically 410 nm for Mn^{2+}).

In the FTIR spectra, the OH^- mode energy (i.e. between 3660 and 3550 cm^{-1}) may be a function of the X- and Y-cation masses due to mode coupling and/or mixing. These OH^- modes have been assigned to a hydrogarnet substitution in the andradite end member, which has the same space as katoite (hydrogrossular), and four H^+ cations can substitute for Si without charge imbalance (Geiger & Rossman 2018). This is consistent with the appreciable water content of the serpentinite that hosts Kerman demantoid.

Serpentinite-hosted demantoid displays characteristic fibrous and acicular inclusions that are mostly chrysotile. These inclusions, which are a notable feature for the identification of demantoid, are typical in demantoid from Russia's Ural Mountains. In the literature, horsetails in demantoid from the Ural Mountains have been attributed to: (1) chrysotile asbestos (Alexandrov 1975; Kropantsev 1997); (2) byssolite (actinolite asbestos; Kropantsev 1997); and (3) tubular hollow channels, sometimes containing inclusions of chrysotile

[3] The Néel temperature describes a temperature limit at which an antiferromagnetic substance becomes paramagnetic.

or byssolite, or filled with other minerals such as limonite or serpentine (Kissin & Murzin 1990, 2015; Kissin *et al.* 2021). The presence of chrysotile fibres in demantoid from Kerman Province implies that the ultramafic host rocks (mainly serpentinised lherzolite) underwent hydrothermal alteration at temperatures no higher than about 400°C (Evans 2004), followed by decompression and autometasomatism. Serpentinisation and following autometamorphism made thermodynamically suitable conditions for the simultaneous sectoral growth of demantoid and formation of fibrous chrysotile inclusions (Holm *et al.* 2015).

Using Raman spectroscopy, it is possible to identify—to a certain extent—garnet end members or intermediate compositions. Kolesov and Geiger (1998) indicated that garnets have three main Raman bands that are sensitive to their composition, which can be used as a tool to calculate their approximate chemical composition and to estimate if they are (near) end members or have an intermediate solid-solution composition. These bands are found at about 350, 550 and 900 cm^{-1}, and are related to Si-O stretching, Si-O bending and $R(SiO_4)^{4-}$ rotational vibrations, respectively. The main characteristic Raman peaks for the studied demantoid samples are at about 353, 371, 515, 817, 841 and 875 cm^{-1} (see Figure 11). These are slightly different from the peaks reported for andradite by Kolesov and Geiger (1998), which could imply a solid-solution composition between andradite and uvarovite. These fingerprint characteristics of the Raman spectra obtained for our Kerman samples are identical to those of their Russian counterparts and, therefore, cannot be used for separating demantoid from these two localities. The EDXRF and GemTOF results also show that Kerman demantoid is predominantly of the andradite-uvarovite solid-solution series with 85–98% molar proportion of andradite (Figure 13).

The concentrations of some trace elements (e.g. Cr, Ge, Ni and Co) are significantly high in Kerman demantoid. The relatively high content of Cr in our samples, which is responsible for their typically deep green hue, is consistent with the results of Bocchio *et al.* (2010). There is a strong positive correlation between Ca and Cr (Figure 14a). This is consistent with lherzolitic[4] garnet (coexisting with clinopyroxene), and confirms lherzolite rather than harzburgite as the primary host rock (prior to serpentinisation) for Kerman demantoid. By contrast, a harzburgitic trend of garnet composition features a weaker correlation between Ca and Cr (Hill *et al.* 2015). A strong negative correlation between Fe and Cr is consistent with a major bulk-composition control on Fe content in the original ultramafic host rocks through melt removal in the shallower parts of the lithospheric mantle (Griffin *et al.* 1999).

A plot of Cr_2O_3 vs MnO/TiO_2 appears useful for separating Iranian demantoid from other localities (Figure 14b). Our Iranian samples show a Mn/Ti ratio greater than 1, while the available data for Russian and Pakistani demantoid yields a ratio between 0.1 and 1. In addition, relatively lower Cr concentrations are found in demantoid from Russia (Murzin *et al.* 1995; Bocchio *et al.* 2010; Pei *et al.* 2019) and Pakistan (Bocchio *et al.* 2010; Adamo *et al.* 2015) as compared to Iranian material. In demantoid from Namibia and Madagascar the Cr concentration is very low (Cairncross & Bahmann 2006; Pezzotta *et al.* 2011).

Although the concentrations of Ga and Ge are rather low in silicate-rich parts of the earth (i.e. crust and upper mantle), these elements can substitute for Al and Si in silicates at high pressure. This is because the ratio of the ionic radius of O to Si at high pressure is similar to that of O to Ge at low pressure (White 2013). The presence of Ge in the studied demantoid samples therefore implies that they formed under high-pressure conditions. U and Th have very low concentrations in the mantle where the ultramafic-related host rocks originally formed. The presence of rare-earth elements (REE) in demantoid is

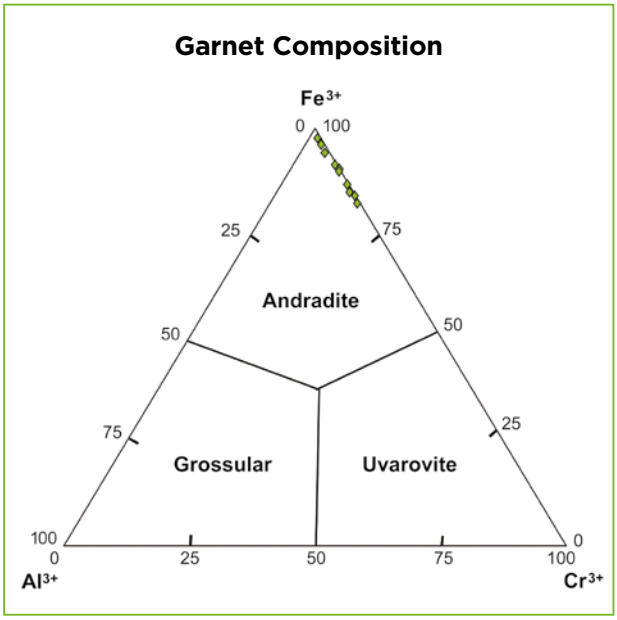

Figure 13: This ternary classification diagram for ugrandite garnets shows that Kerman demantoid compositions plot in the andradite field and contain varying amounts of the uvarovite component (Cr).

[4] Lherzolite is a type of peridotite containing olivine, orthopyroxene and clinopyroxene that formed in the earth's mantle.

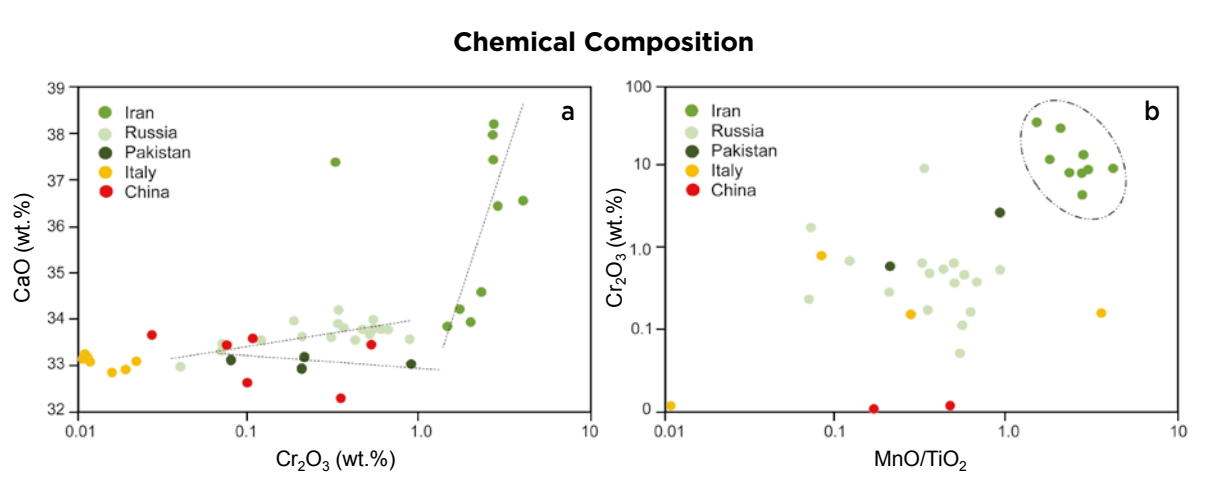

Figure 14: (**a**) This plot of CaO vs Cr_2O_3 (with the latter shown on a logarithmic scale) can help separate demantoid from Iran (this study), Russia (data from Murzin *et al.* 1995; Pei *et al.* 2019), Pakistan (Adamo *et al.* 2015), Italy (Adamo *et al.* 2009) and China (Liu *et al.* 1986), which all come from serpentinite host rocks. Note that the correlation trend of Ca vs Cr in Iranian demantoid is highly positive, while Russian demantoid exhibits a slightly positive correlation trend, and the available data from Pakistani and Chinese demantoids show a slightly negative correlation trend. Data for Italian garnets does not show a meaningful trend. (**b**) A logarithmic plot of Cr_2O_3 vs MnO/TiO_2 also provides a way to separate Iranian demantoid from the other localities. Further, it illustrates how Iranian demantoid typically contains a significantly higher Cr content than in stones from the other localities.

not unusual (e.g. Ayres & Harris 1997; Klimpel *et al.* 2021). Both heavy rare-earth elements (HREE) and light rare-earth elements (LREE) have relatively low concentrations in our samples (see Table III), but HREEs are enriched (relative to chondrite standard) in some samples. The REE concentrations in Kerman demantoid—with an average total of 1.76 ppmw (Table III)—are significantly lower than in stones of Russian origin, which average 4.85 ppmw (Pei *et al.* 2019). The overall abundance of LREE compared to HREE is similar in demantoid from both Iran and Russia.

Magnetic susceptibility was found to be similar for all our Iranian demantoid samples, particularly nos. 3–9 (Figure 15). This could be expected because the total amount of Fe + Cr (the elements with the strongest paramagnetic susceptibility) was similar in our specimens. The susceptibility is isotropic, which would be expected for a mineral of the cubic crystal system in which

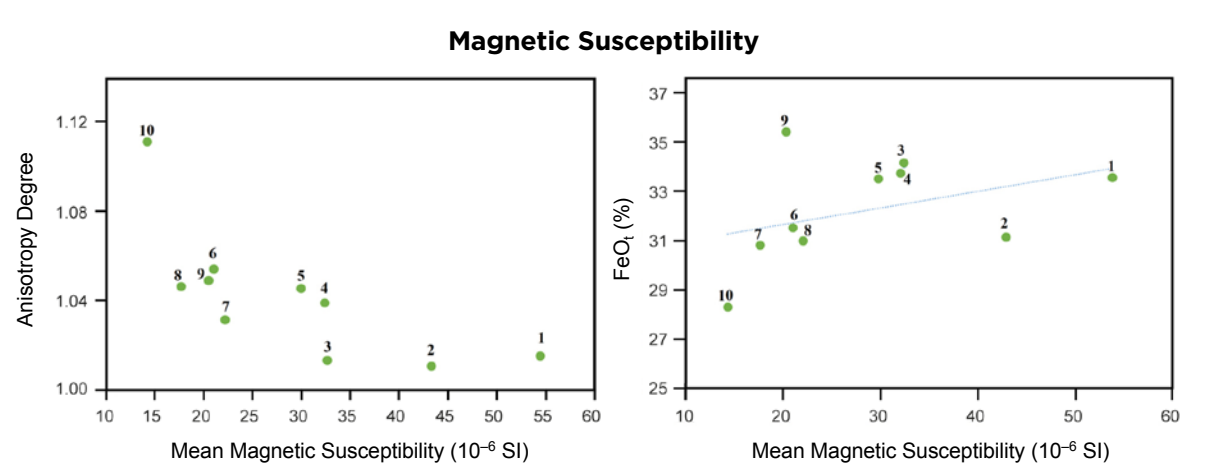

Figure 15: (**a**) The relationship between mean magnetic susceptibility and anisotropy degree for Kerman demantoid is similar for all samples, especially nos. 3–9. (**b**) The mean magnetic susceptibility shows a weak positive correlation with increasing Fe concentration. This suggests that the bulk magnetic susceptibility is mainly related to the Fe content of these garnets.

Figure 16: These crystals of demantoid (and topazolite) from Kerman Province weigh up to about 1 g and show good transparency. Photo by A. Badamegan.

Fe and Cr are distributed homogeneously within the lattice structure. A study by Frost (1960) of the magnetic susceptibility of garnets showing various compositions demonstrated that the susceptibility in the pyrope-almandine solid-solution series is linearly related to Fe content (Bleil & Petersen 1982). The higher the Fe content, the greater the susceptibility. Frost (1960) analysed one andradite sample and found a value of 6.31×10^{-7} m^3/kg, which is in good agreement with the results of our study. We also have shown that Kerman demantoid remains paramagnetic to at least 30 K, and would undergo antiferromagnetic ordering at very low temperature with an asymptotic Néel temperature of approximately –41.9 K.

CONCLUSIONS

Demantoid from Kerman Province in south-eastern Iran forms transparent to semi-transparent crystals with yellowish green to vivid or deep green colour. Crystals are occasionally very large (up to several dozen grams), but most are much smaller (e.g. Figure 16), so faceted stones tend to be small. The optical absorption spectra and chemical data obtained in this study are consistent with demantoid from serpentinite host rocks. Both Cr and Fe contribute significantly to the colour of Kerman demantoid. Raman spectroscopy revealed that the acicular inclusions in our samples consisted of chrysotile or open channels. Relatively high contents of trace elements such as Co, Ni, Ge and Cr are typical of Kerman demantoid, with low REE concentrations. Magnetic susceptibility measurements show that Kerman demantoid is paramagnetic.

Iran is an important source of gem-quality demantoid, while production from deposits in Russia has been decreasing in recent years. Demantoid is mainly found as rough material in the Iranian market, although some fine cut gemstones are also seen there. Jewellery containing demantoid is very rare in Iran, which is probably why this gem variety is not well known domestically. Fortunately, demantoid reserves in the Bagh Borj area of Kerman Province contain sufficient quantities to meet global market demand for decades.

REFERENCES

Adamo, I., Bocchio, R., Diella, V., Pavese, A., Vignola, P., Prosperi, L. & Palanza, V. 2009. Demantoid from Val Malenco, Italy: Review and update. *Gems & Gemology*, **45**(4), 280–287, https://doi.org/10.5741/gems.45.4.280.

Adamo, I., Gatta, G.D., Rotiroti, N., Diella, V. & Pavese, A. 2011. Green andradite stones: Gemmological and mineralogical characterisation. *European Journal of Mineralogy*, **23**(1), 91–100, https://doi.org/10.1127/0935-1221/2011/0023-2079.

Adamo, I., Bocchio, R., Diella, V., Caucia, F. & Schmetzer, K. 2015. Demantoid from Balochistan, Pakistan: Gemmological and mineralogical characterization. *Journal of Gemmology*, **34**(5), 428–433, https://doi.org/10.15506/JoG.2015.34.5.428.

Ahmadipour, H., Sabzehei, M., Whitechurch, H., Rastad, E. & Emami, M.H. 2003. Soghan complex as an evidence for paleospreading center and mantle diapirism in Sanandaj-Sirjan zone (south-east Iran). *Journal of Sciences, Islamic Republic of Iran*, **14**(2),

157–172, https://jsciences.ut.ac.ir/article_31685_02d519463548da0b9dc93843527737aa.pdf.

Alexandrov, A.I. 1975. Demantoid, chrome-containing andradite from Elizavetinskaya Bobrovska (Middle Urals). *Mineralogy and Petrography of the Urals, Sverdlovsk Institute of Mining*, **106**, 140–145.

Allen, M.B. & Armstrong, H.A. 2008. Arabia–Eurasia collision and the forcing of mid-Cenozoic global cooling. *Palaeogeography, Palaeoclimatology, Palaeoecology*, **265**(1–2), 52–58, https://doi.org/10.1016/j.palaeo.2008.04.021.

Amthauer, G. & Rossman, G.R. 1998. The hydrous component in andradite garnet. *American Mineralogist*, **83**(7–8), 835–840, https://doi.org/10.2138/am-1998-7-815.

Ayres, M. & Harris, N. 1997. REE fractionation and Nd-isotope disequilibrium during crustal anatexis: Constraints from Himalayan leucogranites. *Chemical Geology*, **139**(1–4), 249–269, https://doi.org/10.1016/s0009-2541(97)00038-7.

Barrois, O., Giuliani, G., Hafeznia, Y., Zeenabad, H.A., Rakotondrazafy, A.F.M., Ohnenstetter, D., Fallick, A.E., Mathieu, S. *et al*. 2012. Caractéristiques minéralogique et chimique des demantoides de Bagh Borj (Iran) et d'Antetezambato (Madagascar) : Consequences géologiques, 1ère partie, cadre géologique. *Revue de Gemmologie A.F.G.*, No. 182, 15–19.

Barrois, O., Giuliani, G., Hafeznia, Y., Zeenabad, H.A., Rakotondrazafy, A.F.M., Ohnenstetter, D., Fallick, A.E., Mathieu, S. *et al*. 2013. Caractéristiques minéralogique et chimique des demantoides de Bagh Borj (Iran) et d'Antetezambato (Madagascar) : Consequences géologiques, 2ème partie, études minéralogique et chimique. *Revue de Gemmologie A.F.G.*, No. 183, 10–15.

Biedermann, A.R., Pettke, T., Reusser, E. & Hirt, A.M. 2014. Anisotropy of magnetic susceptibility in natural olivine single crystals. *Geochemistry, Geophysics, Geosystems*, **15**(7), 3051–3065, https://doi.org/10.1002/2014GC005386.

Bleil, V. & Petersen, N. 1982. Magnetic properties of natural minerals: Paramagnetism. *In*: Angenheister, G. (ed) *Physical Properties of Rocks (Landolt-Börnstein: Numerical Data and Functional Relationships in Science and Technology–New Series–Group 5, Volume 1b)*. Springer-Verlag, Berlin, Germany, 312–320.

Bocchio, R., Adamo, I. & Diella, V. 2010. The profile of trace elements, including the REE, in gem-quality green andradite from classic localities. *Canadian Mineralogist*, **48**(5), 1205–1216, https://doi.org/10.3749/canmin.48.5.1205.

Cairncross, B. & Bahmann, U. 2006. Minerals from the Goboboseb Mountains: Brandberg region, Namibia. *Rocks & Minerals*, **81**(6), 442–457, https://doi.org/10.3200/rmin.81.6.442-457.

Celâl Şengör, A.M. 1984. *The Cimmeride Orogenic System and the Tectonics of Eurasia*. Geological Society of America Special Paper 195, 74 pp., https://doi.org/10.1130/SPE195-p1.

Douman, M. & Dirlam, D. 2004. Gem News International: Update on demantoid and cat's-eye demantoid from Iran. *Gems & Gemology*, **40**(1), 67–68.

Du Toit, G., Mayerson, W., van der Bogert, C., Douman, M., Befi, R., Koivula, J.I. & Kiefert, L. 2006. Demantoid from Iran. *Gems & Gemology*, **42**(3), 131.

Eichmann, E. 1870. Nils von Nordenskiöld. *Transactions of the St. Petersburg Emperor's Mineralogical Society, Series 2*, **5**, 189–192.

Emami, M.H., Mir Mohammad Sadeghi, M. & Omrani, S.J. 1993. *Magmatic map of Iran, 1:1,000,000*. Geological Survey of Iran, Tehran, Iran.

Evans, B.W. 2004. The serpentinite multisystem revisited: Chrysotile is metastable. *International Geology Review*, **46**(6), 479–506, https://doi.org/10.2747/0020-6814.46.6.479.

Feral, K. 2010. *Magnetic Susceptibility Index for Gemstones*, https://tinyurl.com/2c7wsnyc, accessed 25 October 2022.

Fergusson, C.L., Nutman, A.P., Mohajjel, M. & Bennett, V.C. 2016. The Sanandaj–Sirjan zone in the Neo-Tethyan suture, western Iran: Zircon U–Pb evidence of late Palaeozoic rifting of northern Gondwana and mid-Jurassic orogenesis. *Gondwana Research*, **40**, 43–57, https://doi.org/10.1016/j.gr.2016.08.006.

Frost, M.J. 1960. Magnetic susceptibility of garnet. *Mineralogical Magazine*, **32**(250), 573–576, https://doi.org/10.1180/minmag.1960.032.250.07.

Gaft, M., Reisfeld, R. & Panczer, G. 2005. *Modern Luminescence Spectroscopy of Minerals and Materials*. Springer-Verlag, Berlin, Germany, xvi + 356 pp., https://doi.org/10.1007/b137490.

Geiger, C.A. & Rossman, G.R. 2018. IR spectroscopy and OH^- in silicate garnet: The long quest to document the hydrogarnet substitution. *American Mineralogist*, **103**(3), 384–393, https://doi.org/10.2138/am-2018-6160CCBY.

Ghazi, J.M., Moazzen, M., Rahghoshay, M. & Moghadam, H.S. 2011. The geodynamic setting of the Nain ophiolites, central Iran: Evidence from chromian spinels in the chromitites and associated rocks. *Ofioliti*, **36**(1), 59–76.

Gill, J.O. 1978. Demantoid: The complete story. *Lapidary Journal*, **32**(7), 1542–1545.

Griffin, W.L., Fisher, N.I., Friedman, J., Ryan, C.G. & O'Reilly, S.Y. 1999. Cr-pyrope garnets in the lithospheric mantle. I. Compositional systematics and

relations to tectonic setting. *Journal of Petrology*, **40**(5), 679–704, https://doi.org/10.1093/petroj/40.5.679.

Hennebois, U., Delaunay, A., Karampelas, S. & Fritsch, E. 2021. *G&G* Micro-World: Faceted demantoid garnet with spectacular "horsetail" inclusions. *Gems & Gemology*, **57**(4), 384.

Hill, P.J.A., Kopylova, M., Russell, J.K. & Cookenboo, H. 2015. Mineralogical controls on garnet composition in the cratonic mantle. *Contributions to Mineralogy and Petrology*, **169**(2), article 13 (20 pp.), https://doi.org/10.1007/s00410-014-1102-7.

Holm, N.G., Oze, C., Mousis, O., Waite, J.H. & Guilbert-Lepoutre, A. 2015. Serpentinization and the formation of H_2 and CH_4 on celestial bodies (planets, moons, comets). *Astrobiology*, **15**(7), 587–600, https://doi.org/10.1089/ast.2014.1188.

Hoover, D.B. 2011. Determining garnet composition from magnetic susceptibility and other properties. *Gems & Gemology*, **47**(4), 272–285, https://doi.org/10.5741/gems.47.4.272.

Hoye, G.S. & O'Reilly, W. 1972. A magnetic study of the ferro-magnesian olivines $(Fe_xMg_{1-x})SiO_4$, $0 < x < 1$. *Journal of Physics and Chemistry of Solids*, **33**(7–9), 1827–1834, https://doi.org/10.1016/S0022-3697(72)80476-1.

Jasinevicius, R. 2009. *Characterization of vibrational and electronic features in the Raman spectra of gem minerals*. M.S. thesis, University of Arizona, Tucson, Arizona, USA, 151 pp., https://www.geo.arizona.edu/Antevs/Theses/JasineviciusThesis.pdf.

Karampelas, S., Gaillou, E., Fritsch, E. & Douman, M. 2007. Les grenats andradites-démantoïdes d'Iran : Zonage de couleur et inclusions. *Revue de Gemmologie A.F.G.*, No. 160, 14–20.

Kiefert, L. & Koivula, J.I. 2005. Idol's eyes: Chatoyant demantoid. *AGTA GTC's Laboratory Update*, May.

Kievlenko, E.Y. 2003. *Geology of Gems*. Ocean Pictures Ltd, Littleton, Colorado, USA, 432 pp.

Kissin, A.Y. & Murzin, V.V. 1990. New data on inclusions in the Urals demantoid. *In*: *Urals Summer Mineralogist School-97*, Ural State Academy of Mining and Geology, Ekaterinburg, Russia, 153–155 (in Russian).

Kissin, A.Y. & Murzin, V.V. 2015. Horsetail-like inclusions in Urals demantoid. *All-Russian Conference with International Participation, "Deposits of Stone-Colored and Non-Metallic New Materials of Various Geodynamics Settings"*, Ekaterinburg, Russia, 43–47 (in Russian).

Kissin, A.Y., Murzin, V.V. & Karaseva, E.S. 2021. "Horsetail" inclusions in the Ural demantoids: Growth formations. *Minerals*, **11**(8), article 825 (13 pp.), https://doi.org/10.3390/min11080825.

Klimpel, F., Bau, M. & Graupner, T. 2021. Potential of garnet sand as an unconventional resource of the critical high-technology metals scandium and rare earth elements. *Scientific Reports*, **11**(1), article 5306 (10 pp.), https://doi.org/10.1038/s41598-021-84614-x.

Kolesov, B.A. & Geiger, C.A. 1998. Raman spectra of silicate garnets. *Physics and Chemistry of Minerals*, **25**(2), 142–151, https://doi.org/10.1007/s002690050097.

Kropantsev, S. 1997. Novo-Karkodinsky deposit of demantoid. *In*: *Urals Summer Mineralogist School-97*, Ural State Academy of Mining and Geology, Ekaterinburg, Russia, 132–142 (in Russian).

Krzemnicki, M.S. 1999. Diopside needles as inclusions in demantoid garnet from Russia: A Raman microspectrometric study. *Gems & Gemology*, **35**(4), 192–195, https://doi.org/10.5741/gems.35.4.192.

Laurs, B.M. (ed) 2002. Gem News International: Demantoid garnet from Iran. *Gems & Gemology*, **38**(1), 96.

Lind, T., Henn, U. & Bank, H. 1998. New occurrence of demantoid in Namibia. *Australian Gemmologist*, **20**(2), 75–79.

Liu, S.I 2010. Demantoid garnet cat's eye from Iran and Russia. *Journal of the Gemmological Association of Hong Kong*, **31**, 74–78.

Liu, G., Kang, X. & Zhang, L. 1986. On the genesis of demantoid from Xinjiang, China. *Chinese Journal of Geochemistry*, **5**(4), 381–390, https://doi.org/10.1007/BF02866713.

Lowrie, W. 1990. Identification of ferromagnetic minerals in a rock by coercivity and unblocking temperature properties. *Geophysical Research Letters*, **17**(12), 159–162, https://doi.org/10.1029/GL017i002p00159.

McQuarrie, N. & van Hinsbergen, D.J.J. 2013. Retrodeforming the Arabia-Eurasia collision zone: Age of collision versus magnitude of continental subduction. *Geology*, **41**(3), 315–318, https://doi.org/10.1130/g33591.1.

Milisenda, C., Henn, U. & Henn, J. 2001. Demantoide aus Pakistan. *Gemmologie: Zeitschrift der Deutschen Gemmologischen Gesellschaft*, **50**(1), 51–56.

Misiorowski, E.B. & Hays, N.K. 1993. Jewels of the Edwardians. *Gems & Gemology*, **29**(3), 152–171, https://doi.org/10.5741/gems.29.3.152.

Murzin, V.V., Mamin, N.A., Kissin, A.Y. & Demchuk I.G. 1995. Demantoid garnet mineralization of the Verh-Neivinskii alpinotype ultramafic intrusion (Urals). *3rd Bi-annual Meeting "Intergems"*, 24 June–1 July, Turnov, Czech Republic, 38–41.

Néel, L. 1948. Propriétés magnétiques des ferrites ; Ferrimagnétisme et antiferromagnétisme. *Annales de Physique*, **12**(3), 137–198, https://doi.org/10.1051/anphys/194812030137.

O'Donoghue, M. (ed) 2006. *Gems*, 6th edn. Butterworth-Heinemann, Oxford, xxix + 873 pp.

Palke, A.C. & Pardieu, V. 2014. Gem News International: Demantoid from Baluchistan Province in Pakistan. *Gems & Gemology*, **50**(4), 302–303.

Pavese, A., Diella, V., Pischedda, V., Merli, M., Bocchio, R. & Mezouar, M. 2001. Pressure-volume-temperature equation of state of andradite and grossular, by high-pressure and -temperature powder diffraction. *Physics and Chemistry of Minerals*, **28**(4), 242–248, https://doi.org/10.1007/s002690000144.

Pei, J., Huang, W., Zhang, Q. & Zhai, S. 2019. Chemical constituents and spectra characterization of demantoid from Russia. *Spectroscopy and Spectral Analysis*, **39**(12), 3849–3854 (in Chinese).

Petriglieri, J.R., Salvioli-Mariani, E., Mantovani, L., Tribaudino, M., Lottici, P.P., Laporte-Magoni, C. & Bersani, D. 2015. Micro-Raman mapping of the polymorphs of serpentine. *Journal of Raman Spectroscopy*, **46**(10), 953–958, https://doi.org/10.1002/jrs.4695.

Pezzotta, F., Adamo, I. & Diella, V. 2011. Demantoid and topazolite from Antetezambato, northern Madagascar: Review and new data. *Gems & Gemology*, **47**(1), 2–14, https://doi.org/10.5741/gems.47.1.2.

Phillips, W.R. & Talantsev, A.S. 1996. Russian demantoid, czar of the garnet family. *Gems & Gemology*, **32**(2), 100–111, https://doi.org/10.5741/gems.32.2.100.

Phyo, M.M., Wang, H.A.O., Guillong, M., Berger, A., Franz, L., Balmer, W.A. & Krzemnicki, M.S. 2020. U–Pb dating of zircon and zirconolite inclusions in marble-hosted gem-quality ruby and spinel from Mogok, Myanmar. *Minerals*, **10**(2), article 195 (18 pp.), https://doi.org/10.3390/min10020195.

Quinn, E.P. & Laurs, B.M. 2005. Gem News International: Demantoid from northern Pakistan. *Gems & Gemology*, **41**(2), 176–177.

Ricou, L.-E. 1994. Tethys reconstructed: Plates, continental fragments and their boundaries since 260 Ma from Central America to south-eastern Asia. *Geodinamica Acta*, **7**(4), 169–218, https://doi.org/10.1080/09853111.1994.11105266.

Rinaudo, C., Gastaldi, D. & Belluso, E. 2003. Characterization of chrysotile, antigorite and lizardite by FT-Raman spectroscopy. *Canadian Mineralogist*, **41**(4), 883–890, https://doi.org/10.2113/gscanmin.41.4.883.

Shahraki-Ghadimi, A., Sahandi, M.R., Atapour, H., Poshtkuhi, M. & Zolfaghari, S. 2002. *1:100,000 Geological Map of Esfandaqeh (Geological Maps of Iran, Sheet 7447)*. Geological Survey of Iran, Tehran, Iran.

Sigamony, A. 1944. Magnetic susceptibility of diamond. *Proceedings of the Indian Academy of Sciences - Section A*, **19**(5), article 310 (5 pp,), https://doi.org/10.1007/bf03173459.

Stampfli, G.M. & Borel, G.D. 2002. A plate tectonic model for the Paleozoic and Mesozoic constrained by dynamic plate boundaries and restored synthetic oceanic isochrons. *Earth and Planetary Science Letters*, **196**(1–2), 17–33, https://doi.org/10.1016/s0012-821x(01)00588-x.

Tauxe, L. 2014. *Essentials of Paleomagnetism*. University of California Press, Berkeley, California, USA, 512 pp., https://doi.org/10.1525/9780520946378.

Wang, H.A.O. & Krzemnicki, M.S. 2021. Multi-element analysis of minerals using laser ablation inductively coupled plasma time of flight mass spectrometry and geochemical data visualization using t-distributed stochastic neighbor embedding: Case study on emeralds. *Journal of Analytical Atomic Spectrometry*, **36**(3), 518–527, https://doi.org/10.1039/d0ja00484g.

Wang, H.A.O., Krzemnicki, M.S., Chalain, J.-P., Lefèvre, P., Zhou, W. & Cartier, L. 2016. Simultaneous high sensitivity trace-element and isotopic analysis of gemstones using laser ablation inductively coupled plasma time-of-flight mass spectrometry. *Journal of Gemmology*, **35**(3), 212–223, https://doi.org/10.15506/JoG.2016.35.3.212.

White, W.M. 2013. *Geochemistry*. Wiley-Blackwell, Chichester, viii + 660 pp.

Yu, J., He, X. & Lu, Z. 2019. Cause analysis of chatoyancy of sapphires from Shandong, China. *RSC Advances*, **9**(42), 24420–24427, https://doi.org/10.1039/c9ra03585k.

The Authors

Dr Vahid Ahadnejad
Geology Department, Payame Noor University, 19395-4697 Tehran, Iran
Email: v.ahadnejad@pnu.ac.ir

Dr Michael S. Krzemnicki FGA
Swiss Gemmological Institute SSEF, Aeschengraben 26, CH-4051 Basel, Switzerland

Dr Ann Marie Hirt
Institute of Geophysics, ETH Zurich, Sonneggstrasse 5, CH-8092 Zurich, Switzerland

Acknowledgements

We are grateful to the Swiss Gemmological Institute SSEF and the Institute of Geophysics of ETH Zurich for their cooperation in the analysis of the samples. The assistance of Saeed Jabbari Bookani with the field trip of author VA is greatly appreciated.

Spectroscopic Characteristics and Causes of Colour Modification in Heat-Treated Pink-to-Red Spinel from Luc Yen, Vietnam

Chawalit Chankhantha, Ratthaphon Amphon, Habib Ur Rehman, Pinit Kidkhunthod and Andy H. Shen

ABSTRACT: In this study, 15 pink-to-red spinel samples from Luc Yen, Vietnam, were enhanced by heat treatment (850°C and 1000°C under oxidising conditions) to study the causes of their colour modification. After heating to 850°C, the yellow and blue colour modifiers were reduced slightly, resulting in a more pleasing pink-to-red appearance. Heating to 1000°C decreased the colour modifiers further but also produced a darker and more grey appearance. UV-Vis and FTIR spectral analyses revealed that the heated spinels underwent partial disordering, which could facilitate the reduction of the yellow and blue modifiers. Also, a shift to higher wavelengths of the peak at about 538 nm due to Cr^{3+}±V^{3+} in the UV-Vis spectrum, and the lack of a 575 cm^{-1} band in the FTIR spectrum, appear to be indicative of heat treatment. XANES spectroscopy indicates that some Fe^{2+} changed to Fe^{3+}, which is most likely the main cause of the reduction in blue colouration after heating, whereas there was no change in the valence state of vanadium.

The Journal of Gemmology, **38**(4), 2022, pp. 348–362, https://doi.org/10.15506/JoG.2022.38.4.348

Spinel is an important gem material that is found in metamorphic and magmatic rocks, and red spinel (Figure 1) is in high demand in the global marketplace (after ruby). Gem spinel may have various chemical compositions, and is most commonly the mineral spinel ($MgAl_2O_4$), or occasionally gahnite ($ZnAl_2O_4$). The structure of natural $MgAl_2O_4$ spinel can consist of a disordered cation distribution of approximately 5%. The cation distribution of spinel is expressed as $^{IV}(Mg_{1-x}Al_x)^{VI}(Mg_xAl_{2-x})O_4$, where x represents the degree of inversion, which correlates to the fraction of Al^{3+} cations occupying tetrahedral sites. The value of x can vary from 0 (normal spinel) to 1 (inverse spinel; Lucchesi & Della Giusta 1997; Widmer *et al.* 2015). Cation disordering in spinel may influence colouration. For example, cationic disorder between Mg in tetrahedral sites and Al in octahedral sites has been reported as causing a dark appearance in spinel (Saeseaw *et al.* 2009).

Spinel occurs in many colours, which are generally caused by the substitution of transition metal cations (Schmetzer *et al.* 1989; Taran *et al.* 2005, 2009; Malsy *et al.* 2012; Fregola *et al.* 2014; D'Ippolito *et al.* 2015; Andreozzi *et al.* 2019). Chromium (Cr^{3+}) at octahedral sites can generate pink and red hues, whereas Fe^{2+} at tetrahedral sites produces grey-to-blue or green as Fe^{2+} content increases, and Fe^{2+}–Fe^{3+} intervalence charge transfer (IVCT) can also create blue colouration. In addition, concentration levels of a few parts per million (e.g. >10 ppm) Co^{2+} can give rise to vibrant blue spinel, which is rare and may compare in price to that of fine red spinel. Manganese can cause yellow-to-brown colouration, and orange colour in spinel increases with octahedral V^{3+} content

Figure 1: Pink-to-red spinel commonly displays orangey or purplish tints that can be reduced by heat treatment. These Vietnamese spinels (which are not known to be heated) consist of (from left) a 1.16 ct pear from Luc Yen, a matched pair of round brilliants weighing 0.39 ct each from Lang Chap, a 0.74 ct oval from Bai Son, a 0.99 ct pear from Cong Troi (upper right) and the 0.96 ct pear from Lang Chap (lower right). Specimens courtesy of The Gem Trader (Cave Creek, Arizona, USA); photo by Brad Payne.

(Kleišmantas & Daukšytė 2016). 'Red' spinel is commonly modified by other colours that make the colour appearance less desirable than pure red. Heat treatment can help eliminate these secondary colours.

The mechanisms of colour modification in spinel after heat treatment are not well understood and little information has been published. This study investigates the causes of such colour modifications using X-ray absorption near-edge structure (XANES). This type of X-ray absorption spectroscopy (see Box A) uses a synchrotron radiation source and is a well-established analytical technique to determine the oxidation state of metal cations. XANES spectroscopy has been employed to study spinel from Myanmar (Chankhantha *et al.* 2021), as well as various other gem materials such as amethyst, tourmaline, aquamarine and kunzite (e.g. Di Benedetto *et al.* 2009; Phichaikamjornwut *et al.* 2019; Bunnag *et al.* 2020; Rehman *et al.* 2020). The present study investigates the causes of colour modification in heat-treated red-to-pink spinel from Vietnam using a combination of ultraviolet-visible (UV-Vis), Fourier-transform infrared (FTIR) and XANES spectroscopy.

BACKGROUND ON SPINEL HEAT TREATMENT

Heat treatment of gem-quality spinel from different localities, using various heating conditions, has been reported by several previous researchers. Sriprasert *et al.* (2008) documented a reduction in orange and blue tinges in red spinel from Myanmar after heating at 1000°C in an oxidising atmosphere. In addition, stones from Tanzania have been heat treated from 1100°C to 1700°C in an oxidising atmosphere to enhance their appearance, although their final colours were dull (Saeseaw *et al.* 2009). The yellow component in red spinel from Lang Chap, Vietnam, was partially removed at a lower temperature (850°C) in an oxidising atmosphere (Malsy *et al.* 2012). Orange and brown tints in pink and red spinel from Myanmar have been reduced by heating in air at about 1200°C for 30–40 minutes (Peretti *et al.* 2015). Pink-to-purple spinel samples from Myanmar turned saturated red after being heated at 1600°C for 10 hours (Ren *et al.* 2016). Most of these studies also reported that the spinels became darker in tone after heating at high temperatures, possibly caused by Mg-Al cation disordering.

Evidence of the thermal history of spinel can be detected through advanced gemmological methods. For example, an increase in the width of the 405 cm^{-1} band in Raman spectra, as well as the expansion of the Cr^{3+} zero-phonon line at 685.5 nm in photoluminescence spectra, may be noticeable after heating above 750°C (Widmer *et al.* 2015; Wang *et al.* 2020). The absorption band of Cr^{3+}±V^{3+} is typically present in unheated spinel at approximately 535 nm, but after heating this

BOX A: X-RAY ABSORPTION SPECTROSCOPY

X-ray absorption spectroscopy (XAS) is a non-destructive analytical technique for determining the oxidation states, bond distances and/or symmetrical sites (e.g. tetrahedral or octahedral) of neighbouring atoms with atomic numbers from 7 to 36 (N to Sr), and is not restricted to any particular ions (Waychunas *et al.* 1983). This method is advantageous for materials with low concentrations of the investigated elements or a small total sample size (Koningsberger & Prins 1988; Borda & Sparks 2007). Previously, XAS has been applied in the gemmological and mineralogical sciences mainly to investigate the cause of colour. For example, XANES spectroscopy has been used to determine the oxidation states of Fe and Ti in blue sapphire after heat treatment (Monarumit *et al.* 2016; Wongrawang *et al.* 2016; Phlayrahan *et al.* 2019), the oxidation state of Fe in quartz (Di Benedetto *et al.* 2009; Monarumit *et al.* 2021) and the Fe valence in beryl (Chankhantha *et al.* 2016; Bunnag *et al.* 2020), as well as elucidate the local crystallographic and electronic structure around Cr impurities in emerald (Gaudry *et al.* 2007).

The XAS technique works by absorbing X-ray photons into a core orbital level and then producing photoelectrons at a certain higher energy level. The resulting spectra are divided into two energy regions (Figure A-1): the near-edge absorption (XANES) and the extended absorption fine structure (EXAFS; Bianconi 1980). XANES is the region below about 50 eV of the absorption edge representing a Fermi-level transition, comprising *K*-edge and pre-edge absorption regions, which can give information about the oxidation state of metal cations. EXAFS is the oscillatory region about 50 eV above the absorption edge, and is useful for studying the local environment of atoms (for more information on that technique, see Vlaic & Olivib 2004).

During XAS analysis, the X-ray photon energy is tuned (Popmintchev *et al.* 2018), using a monochromator, to a range where core electrons can be excited (0.1–100 keV). The technique measures the absorption coefficient of an element within a material as a function of incident photon energy. When the incident X-ray energy is equal to the binding energy of a core electron of the absorbing atom, a sharp increase in absorption is observed, giving rise to an absorption edge, resulting in the excitation of a core electron ($1s$) to an unoccupied level (Figure A–2). The letters *K*, *L* and *M* correspond to specific electron shells in atoms, and their subshells are shown in parentheses ($1s$, $2s$, $2p$, etc.; Kelly *et al.* 2008; Evans 2018).

In XANES spectroscopy, the absorption edge is usually defined as energy of the first derivative (E_0), measured halfway up the edge step (Hummer & Rompel 2013). The pre-edge feature is generally a weak band occurring at about 10 eV that can be observed for the first-row transition metals, resulting from forbidden transitions such as $1s \rightarrow 3d$ transitions or due to *p-d* orbital mixing. The energy and intensity of a pre-edge feature are generally used to obtain information on the oxidation state and

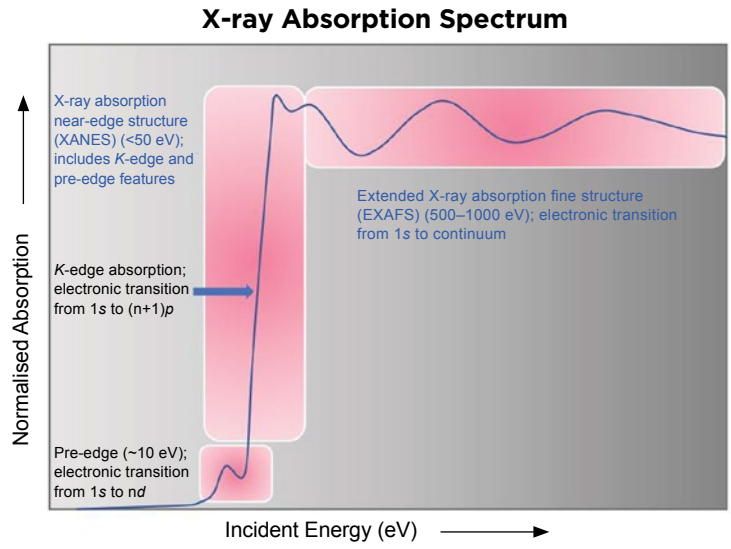

Figure A-1: This diagram illustrates the two regions of XAS data, comprising XANES and EXAFS. For XANES, the spectral data consist of both *K*-edge and pre-edge absorption regions.

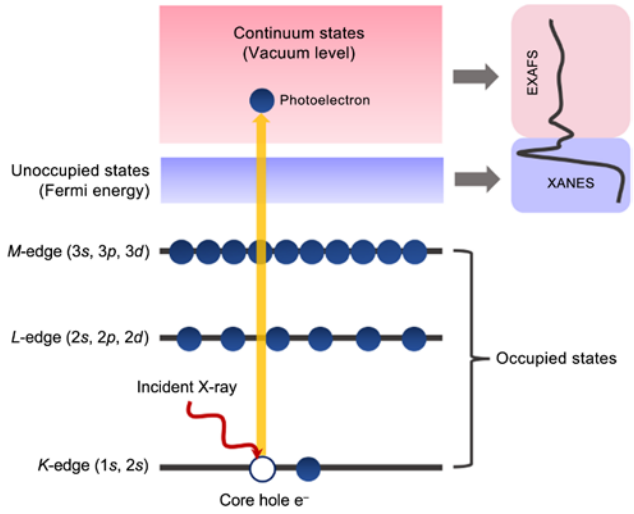

Figure A-2: The excitation process involved in XAS is shown in this diagram. Incident X-rays can promote a core electron either to unoccupied (Fermi energy) or continuum (vacuum level) states, thus leaving a core hole e^-. Transitions to unoccupied states result in spectral features in the XANES region, while transitions to continuum states produce an outgoing photoelectron which is scattered by the nearest-neighbour atom and gives rise to EXAFS oscillations. Modified after Koziej (2016).

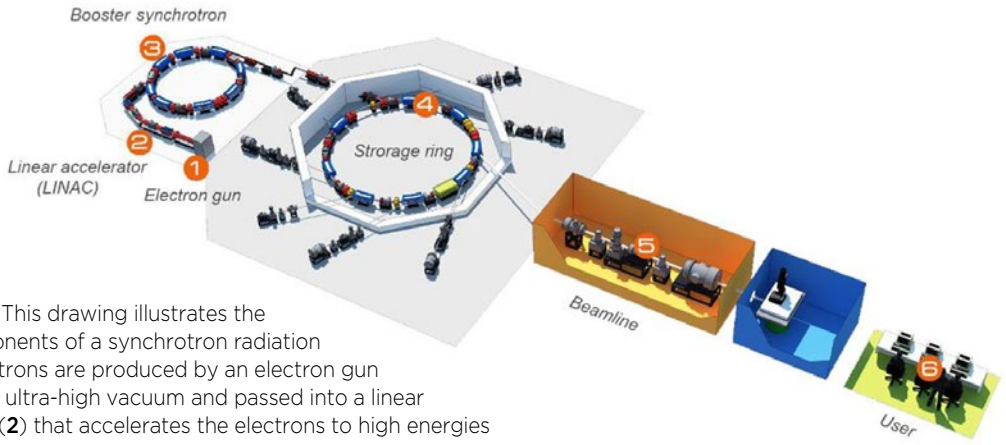

Figure A-3: This drawing illustrates the main components of a synchrotron radiation facility. Electrons are produced by an electron gun (**1**) under an ultra-high vacuum and passed into a linear accelerator (**2**) that accelerates the electrons to high energies (MeV to GeV) before entering a booster synchrotron (**3**), and then a storage ring (**4**) to accelerate the electrons to near light speed. As the electrons travel around the storage ring, synchrotron radiation is emitted at the bends in the ring. The beamline (**5**) is a system of slits, monochromators, focusing mirrors and other optical elements used to select the specific energy of the synchrotron light for the users (**6**).

coordination site of metal ions (Farges *et al.* 2004; Henderson *et al.* 2014). *K*-edge absorption involves both the threshold to ionisation and higher-energy-bound states, including $1s \rightarrow 4p$ transitions, together with ligand-to-metal charge-transfer transitions known as 'shakedowns' (Baker *et al.* 2017), and its position generally shifts towards higher energy with increasing oxidation states.

Linear combination fitting analysis is performed on XANES spectra by comparison to chemical standards of known oxidation state and coordination environment. It provides the weight fraction of each chemical standard and the sample (totally 1 or 100%). If the chemical standard is not a sample constituent, then its weight fraction will be 0 (Mantalidi 2016).

Both XANES and EXAFS spectroscopy are performed using synchrotron radiation. Synchrotron sources are particle accelerators with a circular orbit (Figure A-3) in which charged particles are accelerated to reach ultra-high velocities. Synchrotron radiation covers a continuous range of infrared, visible, ultraviolet and X-ray regions, allowing researchers to select the suitable energy for their research, which can then be applied to a variety of analytical techniques. For example, the beamline at the Synchrotron Light Research Institute of Thailand is used for X-ray absorption spectroscopy, X-ray imaging and X-ray tomographic microscopy, photoelectron emission spectroscopy, infrared spectroscopy and imaging, deep X-ray lithology, macromolecular crystallography, and more.

band broadens and shifts towards a higher wavelength (Saeseaw *et al*. 2009; Malsy *et al*. 2012; Ren *et al*. 2016). In FTIR spectra, a band at 1430 cm^{-1} present in unheated spinel can also broaden with increasing temperature (Munsch 2017).

MATERIALS AND METHODS

For this study, we obtained 15 rough spinel samples from Luc Yen, Vietnam, from a Vietnamese dealer who bought the samples directly from a local miner. The stones were pink to red with yellow and blue modifiers, resulting in an overall orangey red to purplish red colouration. All were of medium quality and contained visible inclusions. Eight of them were found to be suitable for faceting and the resulting cut stones weighed 0.33–1.79 ct. The other seven pieces were polished on opposite sides for spectral analysis (0.1–1.1 g).

The gemmological properties of all samples were recorded at the Gemmological Institute, China University of Geosciences (Wuhan). Refractive index was obtained with a GR-6 refractometer, and SG values were measured hydrostatically using a Sartorius BT 224 S balance. Reaction to long-wave (365 nm) and short-wave (254 nm) UV radiation was observed using a standard handheld gemmological 4 W lamp (mercury bulb) produced by Wuhan Xueyuan Jewelry Technology Co. Ltd.

Chemical analyses of all 15 spinel samples were performed by energy-dispersive X-ray fluorescence (EDXRF) spectroscopy using a Thermo Scientific ARL Quant'X spectrometer (equipped with an Rh tube and Peltier-cooled detector) at the Gemmological Institute, China University of Geosciences (Wuhan). The Co concentration in five spinel samples (SPVN1–SPVN5) was measured by laser ablation inductively coupled plasma mass spectrometry (LA-ICP-MS) at Wuhan Sample Solution Analytical Technology Co. Ltd with an Agilent 7700 Series ICP-MS coupled to a GeoLasPro 193 nm excimer laser. The laser had a 5 Hz pulse rate and a 44 μm diameter spot size. Reference materials included USGS glasses (BCR-2G, BHVO-2G and BIR-1G) and NIST glass (SRM 610). After every two samples, analyses were followed by calibration of the instrument using the SRM610 standard and ICPMSDataCal software (Liu *et al*. 2008).

Heat-treatment experiments were performed on all samples at the Department of Geological Sciences, Chiang Mai University, Thailand. The samples were heated to 850°C and 1000°C in an oxidising atmosphere (O_2 gas) using an electric furnace. The heating and cooling rates were set at 5°C/min, and the total heating duration (including ramp-up time) was 290 minutes for heating at 850°C and 320 minutes for heating at 1000°C. To prevent cracking of the samples due to thermal shock, they were removed from the furnace only after the chamber had returned to room temperature.

UV-Vis and FTIR spectra were obtained for all samples before and after heat treatment at the Department of Geological Sciences, Chiang Mai University. UV-Vis absorption spectra were recorded in the 300–800 nm range using a Hitachi U-4001 spectrophotometer, with a sampling interval of 0.5 nm and scan speed of 300 nm/minute. FTIR spectra were obtained using a Bruker Tensor 27 spectrometer in transmission mode. The spectra were recorded in the 1000–450 cm^{-1} range using an He-Ne laser as the reference source. The resolution was 4 cm^{-1} and 120 scans were measured for each sample.

Two of the spinel samples (orangey red SPVN6 and purplish red SPVN13) were analysed before and after heat treatment with XANES spectroscopy to determine the oxidation states of V and Fe. The analyses were performed after only one of the heating experiments (850°C) due to limited allocation of beamtime. We used the BL5.2 SUT-NANOTEC-SLRI X-ray absorption spectroscopy beamline (see Figure 2) at the Synchrotron Light Research Institute, Nakhon Ratchasima, Thailand. It was operated in fluorescence mode using a four-element Si drift detector, along with chemical standards for V^{3+}, V^{4+}, Fe^{2+} and Fe^{3+}. The ionisation energy (E_0) used for probing V and Fe was 5465 and 7112 eV, respectively, with a scan range from 150 eV below E_0 to 200 eV above E_0. (The energies of edges and emissions of the *K* absorption of all the first-row transition metals can be found in Evans [2018].) The XANES spectra were processed using Athena software (Ravel & Newville 2005). To ensure precision of the data, energy calibration was necessary prior to analysis, by defining the first derivative peak of the chemical foil (Berry *et al*. 2010). Technical information on the beamline used in this study was published by Kidkhunthod (2017).

RESULTS AND DISCUSSION

Gemmological Characteristics

The RI of the spinel samples ranged from 1.714 to 1.720 and their SG varied from 3.59 to 3.61. All samples were isotropic without anomalous birefringence. They exhibited moderate to strong red fluorescence to both long- and short-wave UV radiation. These properties fall within the typical ranges described for gem spinel in the pink-to-red colour range (e.g. Malsy & Klemm 2010; Schwarz *et al*. 2022).

Figure 2: X-ray absorption spectroscopy instrumentation at the BL5.2 SUT-NANOTEC-SLRI XAS beamline at the Synchrotron Light Research Institute in Thailand was used for this study. Photo by C. Chankhantha.

Chemical Composition

Chemical analyses obtained in this study are presented in Table I, along with comparison data reported by Malsy and Klemm (2010), Kleišmantas and Daukšytė (2016) and Giuliani *et al.* (2017). As expected for gem spinel, Mg and Al were the main components of the samples. Various chromophoric trace elements were present (V < Cr < Fe), while Ti, Ga, Zn and Sn were generally low. The purplish red spinels contained more Fe than the orangey red samples.

LA-ICP-MS analysis showed low concentrations of Co (3.4–13 ppmw), which is consistent with a previous report on pink-to-red Vietnamese spinel (Malsy & Klemm 2010). However, pale to vivid pink spinels from Luc Yen in Vietnam reportedly can contain 200–1000 ppmw Co (Kleišmantas & Daukšytė 2016), which is higher than recorded in our samples. The Fe content of our spinels (up to 1.16 wt.% Fe_2O_3) was much greater than the amount of Co, and we believe that Co was insignificant as a blue colour modifier in these samples.

Table I: Chemical data for pink-to-red spinels from Luc Yen, Vietnam, from this study and from the literature for comparison.

Oxide (wt.%)	This study[a]	Malsy & Klemm (2010)[b]	Kleišmantas & Daukšytė (2016)[c]	Giuliani *et al.* (2017)[d]
MgO	29.23–29.66	–	–	27.36–28.54
Al_2O_3	68.42–69.07	–	–	70.25–72.62
TiO_2	0.002–0.02	nd–0.03	–	nd–0.02
V_2O_3	0.05–0.08	0.004–0.3	0.04–0.33	nd–0.52
Cr_2O_3	0.08–0.35	0.05–1.27	0.04–0.20	0.01–1.15
Fe_2O_3	0.46–1.16	0.18–2.23	0.22–2.17	0.41–1.41
ZnO	0.04–0.17	0.01–0.89	–	nd–1.27
Ga_2O_3	0.01–0.02	0.003–0.05	–	–
SnO_2	0.01	nd	–	–
Element (ppmw)				
Co	3.4–13	0.28–15	200–1000	–

[a] All analyses by EDXRF except Co analysed by LA-ICP-MS. Abbreviations: nd = not detected; – = not reported.
[b] Data for Ti and Ga were obtained by LA-ICP-MS and converted to wt.% TiO_2 and Ga_2O_3.
[c] Data were obtained by SEM-EDS; wt.% CoO was converted to ppmw Co.
[d] Data were obtained by electron probe micro-analysis.

Colour Modification Due to Heat Treatment

Before heat treatment, the spinels were pink to red with yellow and blue modifiers. After heating at 850°C for 290 minutes, most samples showed a minor reduction of the yellow and blue tints. Further heating at 1000°C for 320 minutes noticeably reduced the yellow and blue components, but some specimens darkened or developed a greyish tone (Figure 3), and fractures in many samples were more developed.

The effects of heat treatment on the colour modification of our spinel samples were comparable to previous results of heating Vietnamese spinels by Malsy *et al.* (2012), although those authors only included orangey red samples.

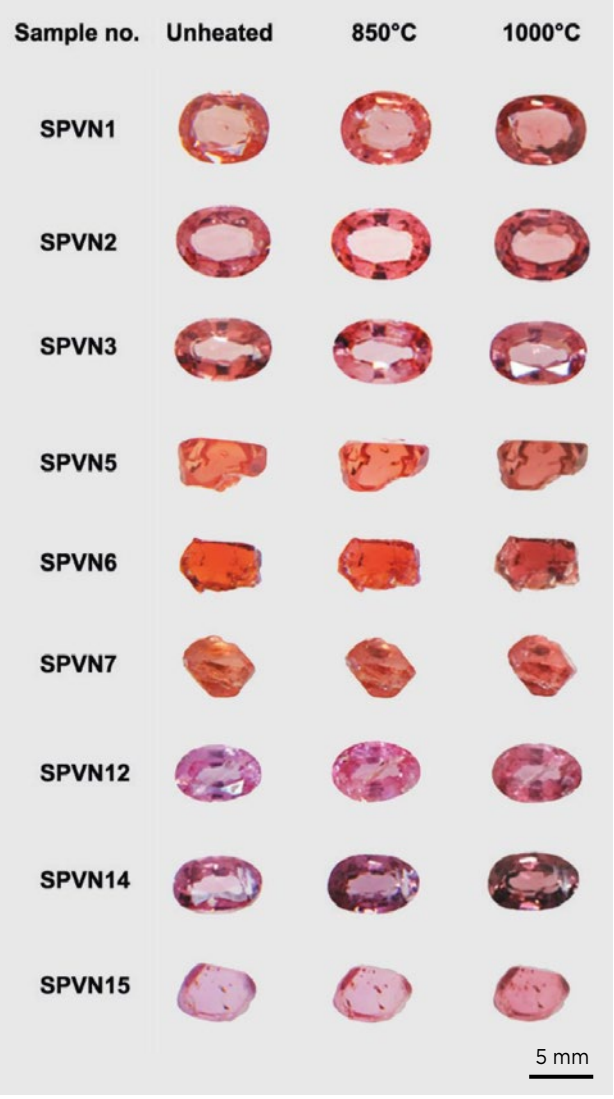

Figure 3: Some of the spinel samples analysed for this report are pictured before and after heating at 850°C and 1000°C. These are representative of the two colour groups of spinel samples in this study: orangey red and purplish red. Photos by C. Chankhantha.

UV-Vis Absorption Spectroscopy

UV-Vis spectra of two representative spinel samples (orangey red and purplish red) are presented in Figure 4 before and after heat treatment. The absorption bands at 392 and 538 nm are related to spin-allowed electronic *d-d* transitions $^4A_{2g} \rightarrow {}^4T_{1g}(F)$ and $^4A_{2g} \rightarrow {}^4T_{2g}(F)$ in Cr^{3+} at the octahedral sites, while the weak band at approximately 415 nm has been assigned to the spin-forbidden transition $^4A_{2g}(^4F) \rightarrow {}^2T_{1g}(^2G)$ in Cr^{3+} at the octahedral sites (Hålenius *et al.* 2010; Andreozzi *et al.* 2019). The orangey tint in spinel may be related to V^{3+} at the octahedral sites (Kleišmantas & Daukšytė 2016), but this could not be confirmed in our spectra due to the overlap of features related to Cr^{3+}±V^{3+}. In addition, a magenta component in spinel can be caused by Fe^{2+}–Fe^{3+} IVCT, seen as a weak band at around 588 nm (Hålenius *et al.* 2002). However, this peak was not observed in the spectra of this study, since it was obscured by a strong Cr^{3+}±V^{3+} absorption band at 538 nm. The spinel samples contained rather small amounts of Fe (i.e. 0.46–1.16 wt.% Fe_2O_3), although this amount is probably sufficient for Fe interactions to cause colour.

Furthermore, the absorption spectra showed a low-energy wing, or absorption edge (<320 nm) in some samples, caused by ligand-to-metal charge transfer (LMCT) of O^{2-}–Fe^{2+} or O^{2-}–Fe^{3+} clusters (Andreozzi *et al.* 2019). This absorption edge has been reported to increase dramatically in red spinel after heat treatment at 1600°C (Ren *et al.* 2016). However, the maximum temperature used in this study was much lower (1000°C), which did not appear to have an effect on this area. Iron-related absorption at 372 nm due to tetrahedral Fe^{2+} was found in some of the samples (i.e. purplish red ones). This peak generally relates to grey-to-blue modifiers in spinel (Fregola *et al.* 2014; D'Ippolito *et al.* 2015). After heating at 850°C and 1000°C, the peak at 372 nm slightly decreased, possibly due to a reduction in the amount of Fe^{2+} (associated with the oxidation of Fe^{2+} to Fe^{3+}).

After heating to 1000°C, the Cr^{3+}±V^{3+} band at 538 nm shifted towards higher wavelengths (545–555 nm; again, see Figure 4). This feature seemed to broaden and its tail extended towards the yellow-orange region of the spectra. Therefore, yellow-orange hues were reduced. However, the general absorption feature in the 350–430 nm range represented by overlapping Fe^{2+}, Cr^{3+} and V^{3+} bands changed insignificantly. It is possible that the heating temperatures used in our experiments might not, or negligibly, affect O^{2-}–Fe^{2+} or O^{2-}–Fe^{3+} LMCT.

The heat-induced broadening of the Cr^{3+}±V^{3+} band mentioned above might be associated with several causes. For example, it could be influenced by the

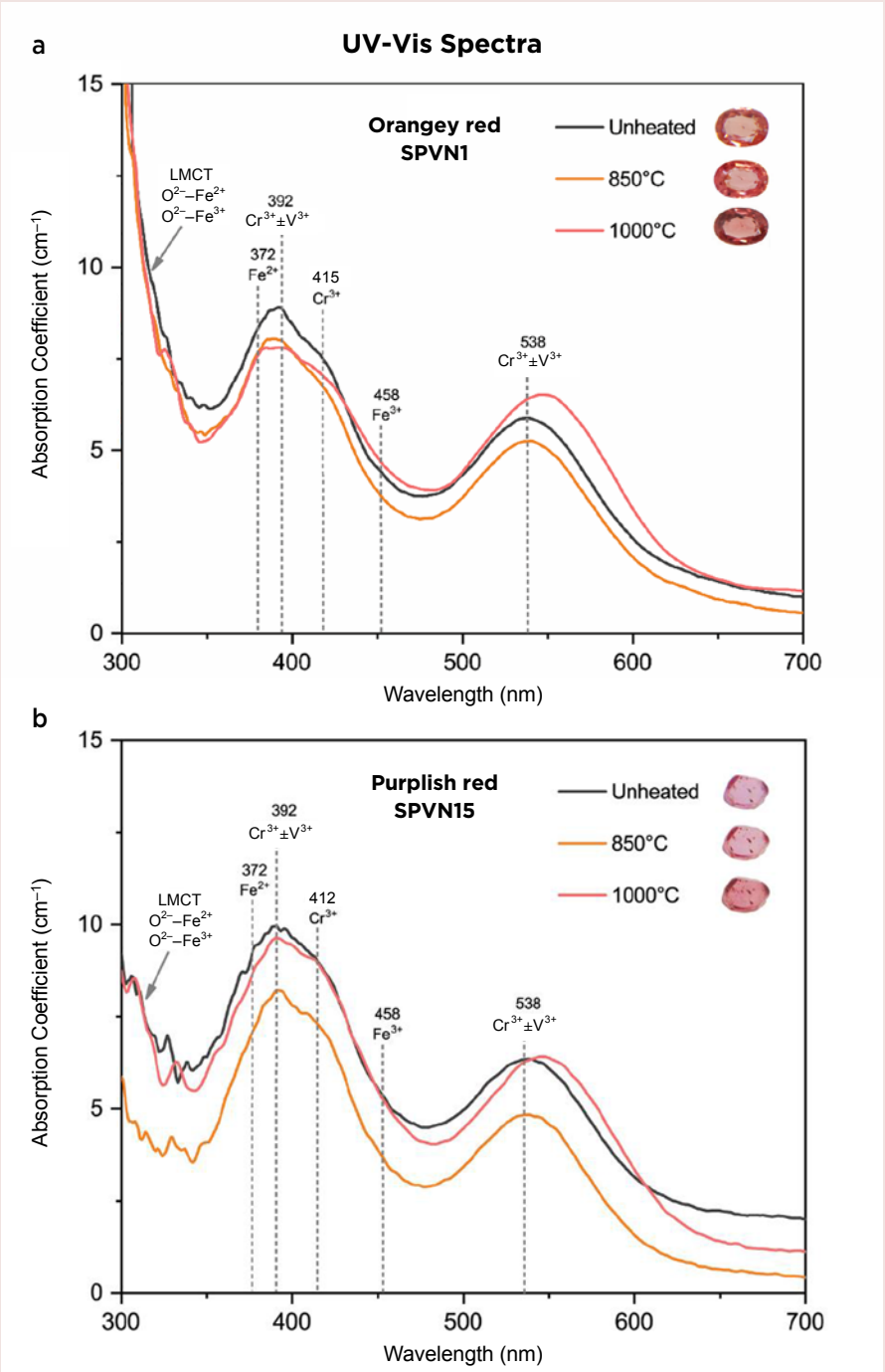

Figure 4: Representative UV-Vis spectra are shown before and after heating at 850°C and 1000°C for (**a**) orangey red spinel SPVN1 and (**b**) purplish red spinel SPVN15. Typical absorption bands for octahedral Cr^{3+} are present at approximately 392, 415 and 538 nm. (Overlapping absorption from V^{3+} can also occur at 392 and 538 nm.) After heating, the Cr^{3+}±V^{3+} band centred between 500 and 600 nm appears broader and has shifted to a higher wavelength.

increase of Mg-Al cation disorder occurring in the structure (i.e. $^{IV}Mg^{2+} + {}^{VI}Al^{3+} \rightarrow {}^{IV}Al^{3+} + {}^{VI}Mg^{2+}$; Lucchesi & Della Giusta 1997). The inter-site exchange of the Mg-Al reaction can induce a significant change in the shape of the electrostatic potential of Cr^{3+} at octahedral sites, causing a decrease in the crystal-field-splitting value 10*Dq* (Hålenius *et al*. 2010). Furthermore, the inter-site exchange of Mg^{2+} and Fe^{3+} can occur with heating over 650°C in spinel containing elevated Fe^{3+}, which could also play an important role in the cation disorder (Martignago 2006). Finally, the spinel specimens used in this study were rather thick (approximately 2.0–4.8 mm), and some contained fractures that could influence the quality of the spectra, especially since there were some artefacts in the 350–500 nm range. Therefore, further research on polished wafers and faceted stones is needed to test whether UV-Vis spectroscopy can be used to reliably distinguish heat treatment in spinel.

FTIR Spectroscopy

Only one report of FTIR spectroscopy of gem spinel before and after heat treatment has been published previously (Munsch 2017). This study found that a band at 1430 cm^{-1} in unheated spinel broadened following heating at 1000°C. In the present study, we narrowed our focus on the 1000–500 cm^{-1} range since it contains several bands attributed to lattice vibrations, and also because this region has been previously investigated for gem spinels, including dark red specimens from Myanmar (Fabian *et al.* 2001), various coloured samples of unspecified origin (He *et al.* 2021) and cobalt-blue spinel from Vietnam (Tao *et al.* 2022). We anticipated that certain bands in the infrared spectra would alter in intensity or that a new band would develop following heat treatment.

The FTIR results from our spinel samples all showed a similar series of FTIR absorption features, consisting of two prominent bands at about 815 and 624 cm^{-1} (Figure 5), which are reportedly related to Al-O stretching vibrations in AlO_6 octahedra (Preudhomme & Tarte 1971). Subsequent research has demonstrated that these bands are mainly assigned to vibrations involving the metal cations in either tetrahedral or octahedral sites (Fabian *et al.* 2001; He *et al.* 2021; Tao *et al.* 2022). Also present was a sideband at 575 cm^{-1} attributed to a more complex origin (Preudhomme & Tarte 1971). After heating at 850°C, the 575 cm^{-1} band disappeared from the spectra of all our samples (e.g. Figure 5). Several studies have demonstrated that a reduction of this band may be due to a phase transition in the spinel structure from an ordered to a more disordered state, which has also been observed in synthetic spinel (e.g. Fabian *et al.* 2001). Furthermore, this disordered cation distribution indicates that some Mg^{2+} and Al^{3+} switched their initial coordination sites (Peretti *et al.* 2015; Widmer *et al.* 2015; Wang *et al.* 2020). Thus, the lack of a band at 575 cm^{-1} in FTIR spectra could be diagnostic for both synthetic and heated spinels.

Oxidation States of Vanadium and Iron

Vanadium can occur in various oxidation states, from +2 to +5 (Righter *et al.* 2006), which generate different colourations in minerals. For example, V^{3+} produces green colour in beryl (Hu & Lu 2020) and tsavorite (Mazurak & Czaja 1996), as well as a colour-change effect in corundum and garnet (Schmetzer 1980). In addition, V^{4+} may be responsible for the blue-violet colour of tanzanite (Pluthametwisute *et al.* 2020).

Before heating, XANES spectroscopy of our spinel samples showed an edge energy (E_0) at approximately 5477 eV, which somewhat fits the chemical standard for

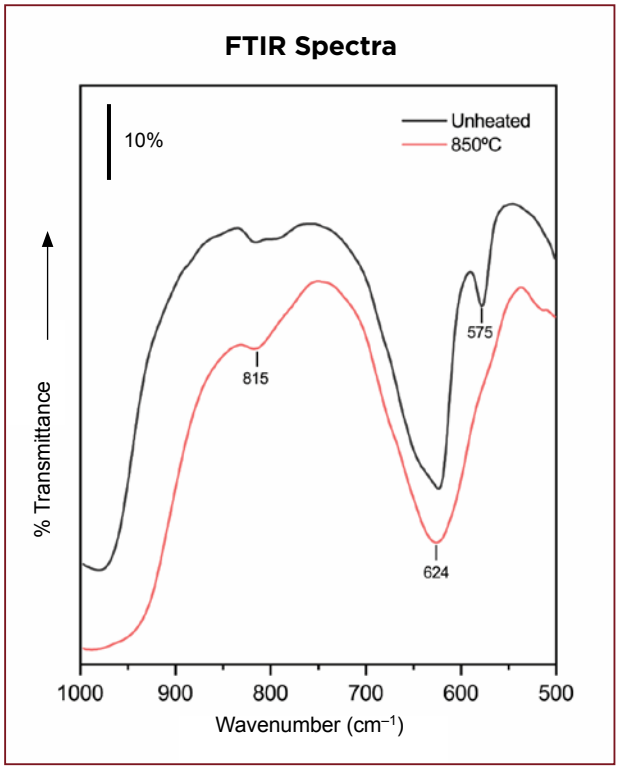

Figure 5: Representative FTIR spectra are shown for an unheated and heated (850°C) spinel sample (SPVN3). The feature at 575 cm^{-1} for the unheated spinel is not seen after heating. The spectra are offset vertically for clarity.

V^{3+} (5476.17 eV) rather than V^{4+} (5478.78 eV), as shown in Figure 6a. It could therefore be concluded that only V^{3+} is present in our specimens. We also calculated the fractional weight (%) of V^{3+} and V^{4+} using the linear combination fitting (LCF) algorithm from their spectra. This further demonstrated that the spinel samples contained only V^{3+}. The ionic radius of V^{3+} is 0.64 Å, so it can relatively easily replace Al^{3+} (ionic radius = 0.535 Å) to maintain electroneutrality (Shannon 1976). Furthermore, the pre-edge feature from the vanadium *K*-edge in the XANES spectra revealed two components at about 5468.19 and 5470.55 eV, which indicate that V^{3+} resides in the distorted octahedral site (Burger *et al.* 2015).

After heating, we found that both pre-edge features and E_0 showed insignificant changes (again, see Figure 6a). Although vanadium could be responsible for yellow-to-orange components in our spinel samples, we believe that the reduction of this colour modifier after heating was mainly influenced by structural disordering, as mentioned in the UV-Vis spectroscopy section.

Iron can be present in three valence states (+2, +3 and +4). The unheated spinel samples showed E_0 at approximately 7119 eV, which is closer to the Fe^{2+} chemical standard than to Fe^{3+} (Figure 6b), indicating the samples had $Fe^{2+} > Fe^{3+}$. In terms of ionic incorporation, Fe^{2+} has

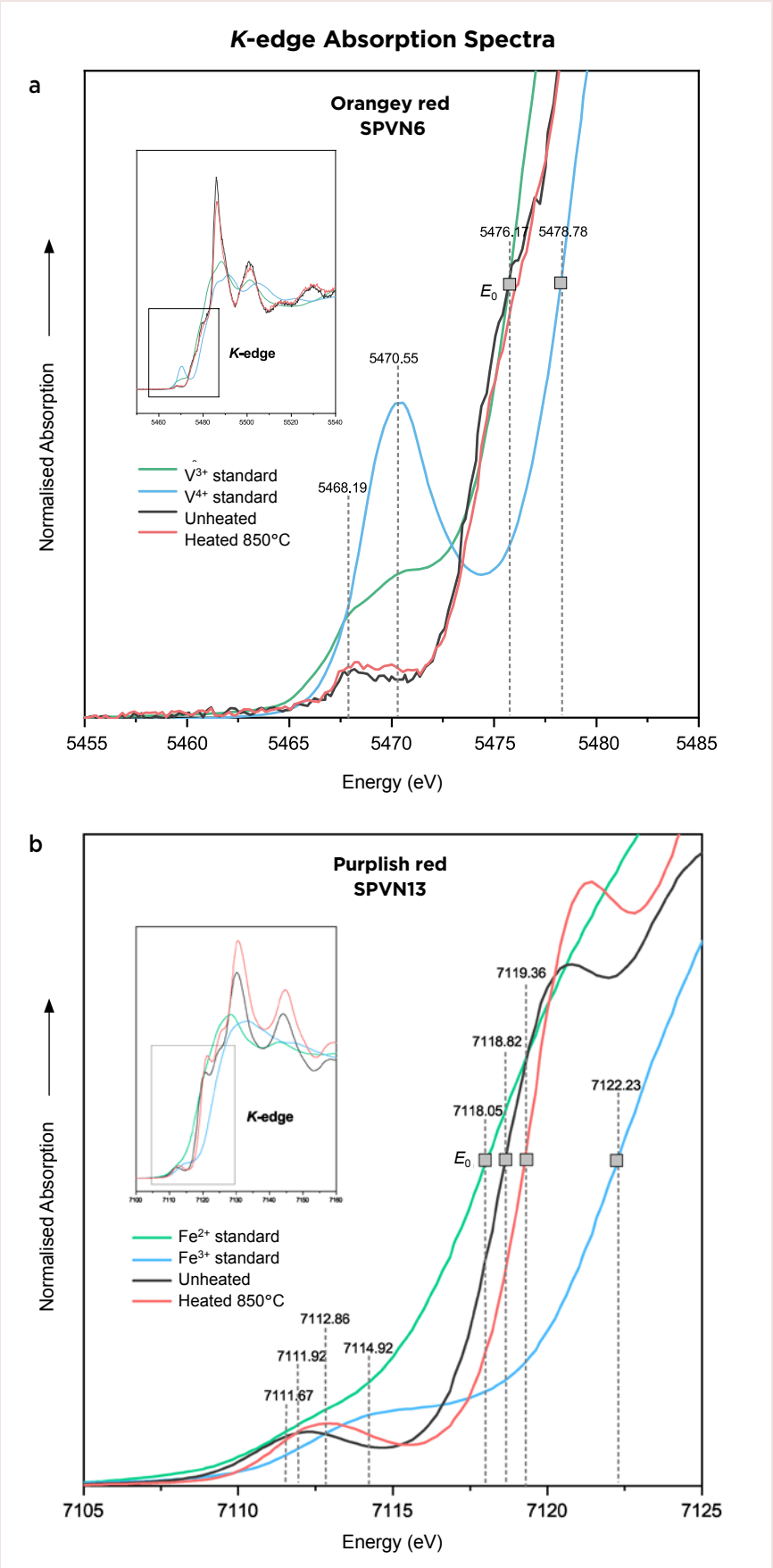

Figure 6: Normalised *K*-edge absorption spectra for vanadium and iron are shown for representative spinel samples SPVN6 and SPVN13 before and after heating at 850°C and compared with V^{3+}, V^{4+}, Fe^{2+} and Fe^{3+} standards. (**a**) For vanadium, the edge energy (E_0) around 5477.04 eV (unheated) and 5477.39 eV (after heating) is closer in both cases to the chemical standard for V^{3+} (5476.17 eV) than V^{4+} (5478.78 eV). The E_0 and pre-edge features show insignificant changes after heating. (**b**) For iron, the E_0 value before heat treatment at approximately 7118.82 eV is closer to the Fe^{2+} standard than the Fe^{3+} standard, indicating $Fe^{2+} > Fe^{3+}$. After heating at 850°C, the E_0 and pre-edge values marginally migrated towards higher energies, closer to the Fe^{3+} standard.

an ionic radius of 0.63 Å, which readily replaces Mg^{2+} (0.57 Å), whereas Fe^{3+} (0.55 Å) has a smaller radius than Fe^{2+}, preferentially replacing Al^{3+} (0.535 Å; Shannon 1976). The pre-edge feature of iron was present as a weak peak at 7111.92 eV. Considering the position and intensity of the pre-edge peaks of iron observed in many Fe-bearing minerals reported by Wilke *et al.* (2001), the iron in our studied spinel samples is preferentially located in tetrahedral sites.

After heating at 850°C, the pre-edge and *K*-edge energies migrated marginally towards higher energies, closer to the Fe^{3+} standard (again, see Figure 6b). This is in good accordance with previous investigations of the oxidation states of colouring elements in red spinel from Myanmar (Chankhantha *et al.* 2021; Pluthametwisute *et al.* 2022). LCF analysis of the heated samples revealed a partial conversion of oxidation states from Fe^{2+} to Fe^{3+} (from 15.9 to 38.3%), as shown in the linear plot in Figure 7. This suggests that during heating some Fe^{3+} cations migrated to the octahedral sites, thus reducing the blue tint in the red spinel as follows:

$$4Fe^{2+} + O_2 \rightarrow 4Fe^{3+} + 2O^{2-}$$

or, as the oxide:

$$4FeO + O_2 \rightarrow 2Fe_2O_3$$

or in the spinel lattice:

$$Mg_{1-x}2Al_{2-2x}Fe_{2x}O_{3-x} + xO_2 \rightarrow Mg_{1-x}2Al_{2-2x}Fe_{2x}O_3$$

CONCLUSIONS

Pink-to-red spinel (Figure 8) can be heat-treated to marginally improve its colour appearance, and such material may currently be encountered in the global gem market. However, the mechanism of the colour modification has not been well understood. In this study, the colouration of orangey red and purplish red spinel from Luc Yen, Vietnam, was enhanced by heating under oxidising conditions to decrease the yellow and blue secondary hues. Chemical analyses showed the samples contained relatively high Cr and low Fe contents. We found that heating at 850°C could slightly remove the yellow and blue tints, whereas further heating at 1000°C removed these subtle colour components more significantly, but the samples also became darker and more greyish. An expansion of the Cr^{3+}±V^{3+} absorption band to 545–555 nm in UV-Vis spectra and the lack of a 575 cm^{-1} band in FTIR spectra indicate that partial Mg-Al cation disordering occurred during heat treatment, which caused a reduction in the yellow colour modifier. In addition, XANES results showed the partial conversion of iron from Fe^{2+} to Fe^{3+}, thus reducing the blue modifier.

Although detection of heat-treated spinel can be accomplished using PL and/or Raman spectroscopy, this study shows that additional evidence for identifying this treatment can be provided by FTIR and also probably UV-Vis spectroscopy.

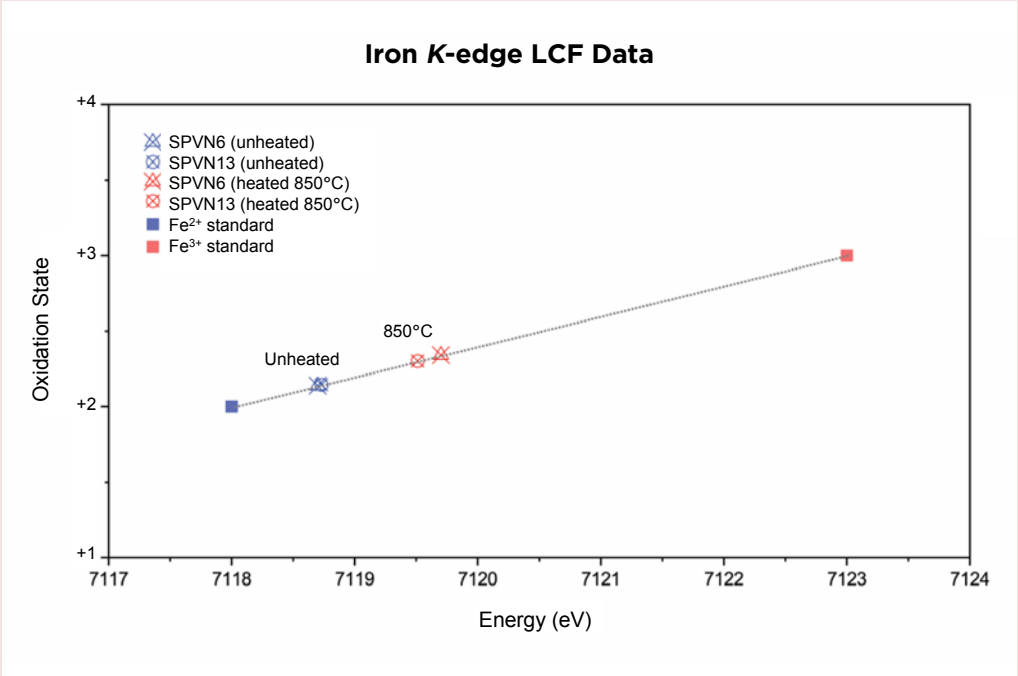

Figure 7: LCF data of iron *K*-edge energy of spinel samples SPVN6 and SPVN13 are plotted before and after heating at 850°C, with a calibration line fitted between the Fe^{2+} and Fe^{3+} standards. The oxidation state of iron in both samples appears to increase after heating.

Figure 8: Pink-to-red spinel is an attractive gem material that is gaining popularity in the global marketplace. These unheated stones weigh 1.28 ct (left), 4.37 ct (centre) and 2.11 ct (right). Courtesy of RareSource, Chattanooga, Tennessee, USA; photo by Orasa Weldon.

REFERENCES

Andreozzi, G.B., D'Ippolito, V., Skogby, H., Hålenius, U. & Bosi, F. 2019. Color mechanisms in spinel: A multi-analytical investigation of natural crystals with a wide range of coloration. *Physics and Chemistry of Minerals*, **46**(4), 343–360, https://doi.org/10.1007/s00269-018-1007-5.

Baker, M.L., Mara, M.W., Yan, J.J., Hodgson, K.O., Hedman, B. & Solomon, E.I. 2017. K- and L-edge X-ray absorption spectroscopy (XAS) and resonant inelastic X-ray scattering (RIXS) determination of differential orbital covalency (DOC) of transition metal sites. *Coordination Chemistry Reviews*, **345**, 182–208, https://doi.org/10.1016/j.ccr.2017.02.004.

Berry, A.J., Yaxley, G.M., Woodland, A.B. & Foran, G.J. 2010. A XANES calibration for determining the oxidation state of iron in mantle garnet. *Chemical Geology*, **278**(1–2), 31–37, https://doi.org/10.1016/j.chemgeo.2010.08.019.

Bianconi, A. 1980. Surface X-ray absorption spectroscopy: Surface EXAFS and surface XANES. *Applications of Surface Science*, **6**(3–4), 392–418, https://doi.org/10.1016/0378-5963(80)90024-0.

Borda, M.J. & Sparks, D.L. 2007. Kinetics and mechanisms of sorption-desorption in soils: A multiscale assessment. *In*: Violante, A., Huang, P.M. & Gadd, G.M. (eds) *Biophysico-Chemical Processes of Heavy Metals and Metalloids in Soil Environments*. John Wiley & Sons Inc., Hoboken, New Jersey, USA, 97–124, https://doi.org/10.1002/9780470175484.ch3.

Bunnag, N., Kasri, B., Setwong, W., Sirisurawong, E., Chotsawat, M., Chirawatkul, P. & Saiyasombat, C. 2020. Study of Fe ions in aquamarine and the effect of dichroism as seen using UV–Vis, NIR and X-ray. *Radiation Physics and Chemistry*, **177**, article 109107 (7 pp.), https://doi.org/10.1016/j.radphyschem.2020.109107.

Burger, P.V., Papike, J.J., Bell, A.S. & Shearer, C.K. 2015. Vanadium valence in spinel from a Y98 composition melt as determined by X-ray absorption near edge structure (XANES). *Proceedings of the 46th Lunar and Planetary Science Conference*, The Woodlands, Texas, USA, 16–20 March, abstract 2743 (2 pp.).

Chankhantha, C., Thanasuthipitak, P. & Kidkhunthod, P. 2016. Iron *K*-edge XANES study of heated green beryl from Madagascar. *Walailak Journal of Science & Technology*, **13**(12), 977–983, https://wjst.wu.ac.th/index.php/wjst/article/view/2380/641.

Chankhantha, C., Shen, A.H. & Amphon, R. 2021. Preliminary study on color modification of heat-treated spinel using X-ray absorption near-edge structure (XANES). *7th International Gem & Jewelry Conference (GIT2021)*, Chanthaburi, Thailand, 228–232, https://www.git.or.th/eng/conference_en/2021/e_proceeding_2021.pdf.

D'Ippolito, V., Andreozzi, G.B., Hålenius, U., Skogby, H., Hametner, K. & Günther, D. 2015. Color mechanisms in spinel: Cobalt and iron interplay for the blue color. *Physics and Chemistry of Minerals*, **42**(6), 431–439, https://doi.org/10.1007/s00269-015-0734-0.

Di Benedetto, F., D'Acapito, F., Fornaciai, G., Innocenti, M., Montegrossi, G., Pardi, L.A., Tesi, S. & Romanelli, M. 2009. A Fe *K*-edge XAS study of amethyst. *Physics and Chemistry of Minerals*, **37**(5), 283–289, https://doi.org/10.1007/s00269-009-0332-0.

Evans, J. 2018. *X-ray Absorption Spectroscopy for the Chemical and Materials Sciences*. John Wiley & Sons Inc., Hoboken, New Jersey, USA, 224 pp.

Fabian, D., Posch, T., Mutschke, H., Kerschbaum, F. & Dorschner, J. 2001. Infrared optical properties of spinels. *Astronomy & Astrophysics*, **373**(3), 1125–1138, https://doi.org/10.1051/0004-6361:20010657.

Farges, F., Lefrère, Y., Rossano, S., Berthereau, A., Calas, G. & Brown, G.E. 2004. The effect of redox state on the local structural environment of iron in silicate glasses: A combined XAFS spectroscopy, molecular dynamics, and bond valence study. *Journal of Non-Crystalline Solids*, **344**(3), 176–188, https://doi.org/10.1016/j.jnoncrysol.2004.07.050.

Fregola, R.A., Skogby, H., Bosi, F., D'Ippolito, V., Andreozzi, G.B. & Hålenius, U. 2014. Optical absorption spectroscopy study of the causes for color variations in natural Fe-bearing gahnite: Insights from iron valency and site distribution data. *American Mineralogist*, **99**(11–12), 2187–2195, https://doi.org/10.2138/am-2014-4962.

Gaudry, E., Cabaret, D., Brouder, C., Letard, I., Rogalev, A., Wilhlem, F., Jaouen, N. & Sainctavit, P. 2007. Relaxations around the substitutional chromium site in emerald: X-ray absorption experiments and density functional calculations. *Physical Review B*, **76**(9), article 091140 (10 pp.), https://doi.org/10.1103/PhysRevB.76.094110.

Giuliani, G., Fallick, A.E., Boyce, A.J., Pardieu, V. & Pham, V.L. 2017. Pink and red spinels in marble: Trace elements, oxygen isotopes, and sources. *Canadian Mineralogist*, **55**(4), 743–761, https://doi.org/10.3749/canmin.1700009.

Hålenius, U., Skogby, H. & Andreozzi, G.B. 2002. Influence of cation distribution on the optical absorption spectra of Fe^{3+}-bearing spinel *s.s.*–hercynite crystals: Evidence for electron transitions in $^{VI}Fe^{2+}$–$^{VI}Fe^{3+}$ clusters. *Physics and Chemistry of Minerals*, **29**(5), 319–330, https://doi.org/10.1007/s00269-002-0240-z.

Hålenius, U., Andreozzi, G.B. & Skogby, H. 2010. Structural relaxation around Cr^{3+} and the red-green color change in the spinel (sensu stricto)-magnesiochromite ($MgAl_2O_4$-$MgCr_2O_4$) and gahnite-zincochromite ($ZnAl_2O_4$-$ZnCr_2O_4$) solid-solution series. *American Mineralogist*, **95**(4), 456–462, https://doi.org/10.2138/am.2010.3388.

He, S., Cao, P., Tan, H. & Zu, E. 2021. Comparative study on spectral characteristics of natural and flame-melting synthetic spinels. *Laser & Optoelectronics Progress*, **58**(5), article 0530001 (8 pp.), https://doi.org/10.3788/LOP202158.0530001 (in Chinese).

Henderson, G.S., de Groot, F.M.F. & Moulton, B.J.A. 2014. X-ray absorption near-edge structure (XANES) spectroscopy. *In*: Henderson, G.S, Neuville, D.R. and Downs, R.T. (eds) *Spectroscopic Methods in Mineralogy and Materials Sciences*. Reviews in Mineralogy and Geochemistry, **78**, 75–138, https://doi.org/10.2138/rmg.2014.78.3.

Hu, Y. & Lu, R. 2020. Color characteristics of blue to yellow beryl from multiple origins. *Gems & Gemology*, **56**(1), 54–65, https://doi.org/10.5741/gems.56.1.54.

Hummer, A.A. & Rompel, A. 2013. X-ray absorption spectroscopy: A tool to investigate the local structure of metal-based anticancer compounds *in vivo*. *In*: Christov, C.Z. (ed) *Biomolecular Spectroscopy: Advances from Integrating Experiments and Theory*. Academic Press, Elsevier, Kidlington, Oxford, **93**, 257–305, https://doi.org/10.1016/b978-0-12-416596-0.00008-7.

Kelly, S.D., Hesterberg, D. & Ravel, B. 2008. Analysis of soils and minerals using X-ray absorption spectroscopy. *In*: Ulery, A.L. & Drees, L.R. (eds) *Methods of Soil Analysis Part 5—Mineralogical Methods*. Soil Science Society of America Inc., Madison, Wisconsin, USA, 387–463, https://doi.org/10.2136/sssabookser5.5.c14.

Kidkhunthod, P. 2017. Structural studies of advanced functional materials by synchrotron-based X-ray absorption spectroscopy: BL5.2 at SLRI, Thailand. *Advances in Natural Sciences: Nanoscience and Nanotechnology*, **8**(3), article 035007 (6 pp.), https://doi.org/10.1088/2043-6254/aa7240.

Kleišmantas, A. & Daukšytė, A. 2016. The influence of Vietnam and Sri Lanka spinel mineral chemical elements on colour. *Chemija*, **27**(1), 45–51, http://mokslozurnalai.lmaleidykla.lt/publ/0235-7216/2016/1/45%E2%80%9351.pdf.

Koningsberger, D.C. & Prins, R. (eds) 1988. *X-ray Absorption: Principles, Applications, Techniques of EXAFS, SEXAFS and XANES*. John Wiley & Sons Inc., Hoboken, New Jersey, USA, 688 pp.

Koziej, D. 2016. Revealing complexity of nanoparticle synthesis in solution by in situ hard X-ray spectroscopy—Today and beyond. *Chemistry of Materials*, **28**(8), 2478–2490, https://doi.org/10.1021/acs.chemmater.6b00486.

Liu, Y., Hu, Z., Gao, S., Günther, D., Xu, J., Gao, C. & Chen, H. 2008. In situ analysis of major and trace elements of anhydrous minerals by LA-ICP-MS without applying an internal standard. *Chemical Geology*, **257**(1–2), 34–43, https://doi.org/10.1016/j.chemgeo.2008.08.004.

Lucchesi, S. & Della Giusta, A. 1997. Crystal chemistry of a highly disordered Mg-Al natural spinel. *Mineralogy and Petrology*, **59**(1–2), 91–99, https://doi.org/10.1007/bf01163063.

Malsy, A. & Klemm, L. 2010. Distinction of gem spinels from the Himalayan mountain belt. *Chimia*, **64**(10), article 741 (6 pp.), https://doi.org/10.2533/chimia.2010.741.

Malsy, A.K., Karampelas, S., Schwarz, D., Klemm, L., Armbruster, T. & Tuan, D.A. 2012. Orangey-red to orangey-pink gem spinels from a new deposit at Lang Chap (Tan Huong-Truc Lau), Vietnam. *Journal of Gemmology*, **33**(1–4), 19–27, https://doi.org/10.15506/JoG.2012.33.1.19.

Mantalidi, A. 2016. *Understanding the formation of gold and iron based nanomaterials using X-ray absorption spectroscopy*. PhD thesis, University College London, 268 pp., https://discovery.ucl.ac.uk/id/eprint/1530968/1/PhD%20Thesis%20Anastasia%20Mantalidi.pdf.

Martignago, F. 2006. Thermodynamics and kinetics of cation ordering in natural and synthetic $Mg(Al,Fe^{3+})_2O_4$ spinels from in situ high-temperature X-ray diffraction. *American Mineralogist*, **91**(2–3), 306–312, https://doi.org/10.2138/am.2006.1880.

Mazurak, Z. & Czaja, M. 1996. Optical properties of tsavorite $Ca_3Al_2(SiO_4)_3$:Cr^{3+},V^{3+} from Kenya. *Journal of Luminescence*, **65(**6), 335–340, https://doi.org/10.1016/0022-2313(95)00086-0.

Monarumit, N., Wongkokua, W. & Satitkune, S. 2016. Fe^{2+} and Fe^{3+} oxidation states on natural sapphires probed by X-ray absorption spectroscopy. *Procedia Computer Science*, **86**, 180–183, https://doi.org/10.1016/j.procs.2016.05.053.

Monarumit, N., Sakkaravej, S., Wanthanachaisaeng, B., Saiyasombat, C. & Wongkokua, W. 2021. Causes of color in purple- and yellow- quartz. *Journal of Physics: Conference Series*, **1719**(1), article 012001 (5 pp.), https://doi.org/10.1088/1742-6596/1719/1/012001.

Munsch, B. 2017. *Spinelles naturels traités thermiquement*. Diplôme d'Université de Gemmologie thesis, University of Nantes, France, 102 pp., https://gemmologie-francophonie.com/wp-content/uploads/2021/10/Munsch_2017_DUG-Spinelles-naturels-traite%CC%81s-thermiquement.pdf.

Peretti, A., Tun, N.L. & Armbruster, T. 2015. Heat-treatment of spinel. *Contributions to Gemology*, No. 11, 269–278, https://www.gemresearch.ch/assets/documents/publication-articles/2015-05-spinel-heat-treatment-1.pdf.

Phichaikamjornwut, B., Pongkrapan, S., Intarasiri, S. & Bootkul, D. 2019. Conclusive comparison of gamma irradiation and heat treatment for color enhancement of rubellite from Mozambique. *Vibrational Spectroscopy*, **103**, article 102926 (9 pp.), https://doi.org/10.1016/j.vibspec.2019.102926.

Phlayrahan, A., Monarumit, N., Lhuaamporn, T., Satitkune, S. & Wathanakul, P. 2019. Spectroscopic investigation of properties of blue sapphire samples depending on heating conditions. *Journal of Applied Spectroscopy*, **86**(5), 810–816, https://doi.org/10.1007/s10812-019-00898-y.

Pluthametwisute, T., Wanthanachaisaeng, B., Saiyasombat, C. & Sutthirat, C. 2020. Cause of color modification in tanzanite after heat treatment. *Molecules*, **25**(16), article 3743 (15 pp.), https://doi.org/10.3390/molecules25163743.

Pluthametwisute, T., Wanthanachaisaeng, B., Saiyasombat, C. & Sutthirat, C. 2022. Minor elements and color causing role in spinel: Multi-analytical approaches. *Minerals*, **12**(8), article 928 (19 pp.), https://doi.org/10.3390/min12080928.

Popmintchev, D., Galloway, B.R., Chen, M.-C., Dollar, F., Mancuso, C.A., Hankla, A., Miaja-Avila, L., O'Neil, G. *et al*. 2018. Near- and extended-edge X-ray-absorption fine-structure spectroscopy using ultrafast coherent high-order harmonic supercontinua. *Physical Review Letters*, **120**(9), article 093002 (6 pp.), https://doi.org/10.1103/PhysRevLett.120.093002.

Preudhomme, J. & Tarte, P. 1971. Infrared studies of spinels—III: The normal II–III spinels. *Spectrochimica Acta Part A: Molecular Spectroscopy*, **27**(9), 1817–1835, https://doi.org/10.1016/0584-8539(71)80235-0.

Ravel, B. & Newville, M. 2005. *ATHENA, ARTEMIS, HEPHAESTUS*: Data analysis for X-ray absorption spectroscopy using *IFEFFIT*. *Journal of Synchrotron Radiation*, **12**(4), 537–541, https://doi.org/10.1107/s0909049505012719.

Rehman, H.U., Martens, G., Tsai, Y.L., Chankhantha, C., Kidkhunthod, P. & Shen, A.H. 2020. An X-ray absorption near-edge structure (XANES) study on the oxidation state of chromophores in natural kunzite samples from Nuristan, Afghanistan. *Minerals*, **10**(5), article 463 (11 pp.), https://doi.org/10.3390/min10050463.

Ren, Q., Chen, M., Wang, C. & Wu, G. 2016. Analysis of UV-Vis spectrum on pink-purple spinel from Burma before and after heat treatment. *Journal of Gems & Gemmology*, **18**(3), 24–30, https://doi.org/10.15964/j.cnki.027jgg.2016.03.004 (in Chinese).

Righter, K., Sutton, S.R., Newville, M., Le, L., Schwandt, C.S., Uchida, H., Lavina, B. & Downs, R.T. 2006. An experimental study of the oxidation state of vanadium in spinel and basaltic melt with implications for the origin of planetary basalt. *American Mineralogist*, **91**(10), 1643–1656, https://doi.org/10.2138/am.2006.2111.

Saeseaw, S., Wang, W., Scarratt, K., Emmett, J.L. & Douthit, T.R. 2009. Distinguishing heated spinels from unheated natural spinels and from synthetic spinels: A short

review of on-going research. Gemological Institute of America, 2 April, 13 pp., https://www.gia.edu/gia-news-research-NR32209A.

Schmetzer, K. 1980. The alexandrite effect in minerals: Chrysoberyl, garnet, corundum, fluorite. *Neues Jahrbuch für Mineralogie, Abhandlungen*, No. 138, 147–164.

Schmetzer, K., Haxel, C. & Amthauer, G. 1989. Colour of natural spinels, gahnospinels and gahnites. *Neues Jahrbuch für Mineralogie, Abhandlungen*, **160**(2), 159–180.

Schwarz, D., Liu, Y., Zhou, Z., Lomthong, P. & Rozet, T. 2022. Spinel from the Pamir Mountains in Tajikistan. *Journal of Gemmology*, **38**(2), 138–154, https://doi.org/10.15506/JoG.2022.38.2.138.

Shannon, R.D. 1976. Revised effective ionic radii and systematic studies of interatomic distances in halides and chalcogenides. *Acta Crystallographica Section A*, **32**(5), 751–767, https://doi.org/10.1107/s0567739476001551.

Sriprasert, B., Atichat, W., Wathanakul, P., Pisutha-Arnond, V., Sutthirat, C., Leelawattanasuk, T., Saejoo, S., Jakkawanvibul, J. *et al*. 2008. The heat-treatment experiments of red spinel from Myanmar. *Proceedings of the 2nd International Gem & Jewelry Conference – GIT 2008*, Bangkok, Thailand, 9–12 March, 278–282.

Tao, L., Shi, M., Xu, L., Han, X. & Liu, Z. 2022. Research on spectral characteristics and coloration of natural cobalt spinel. *Spectroscopy and Spectral Analysis*, **42**(7), 2130–2134 (in Chinese).

Taran, M.N., Koch-Müller, M. & Langer, K. 2005. Electronic absorption spectroscopy of natural (Fe^{2+}, Fe^{3+})-bearing spinels of spinel s.s.-hercynite and gahnite-hercynite solid solutions at different temperatures and high-pressures. *Physics and Chemistry of Minerals*, **32**(3), 175–188, https://doi.org/10.1007/s00269-005-0461-z.

Taran, M.N., Koch-Muller, M. & Feenstra, A. 2009. Optical spectroscopic study of tetrahedrally coordinated Co^{2+} in natural spinel and staurolite at different temperatures and pressures. *American Mineralogist*, **94**(11–12), 1647–1652, https://doi.org/10.2138/am.2009.3247.

Vlaic, G. & Olivib, L. 2004. EXAFS spectroscopy: A brief introduction. *Croatica Chemica Acta*, **77**(3), 427–433, https://hrcak.srce.hr/file/151254.

Wang, C., Shen, A.H. & Liu, Y. 2020. Characterization of order-disorder transition in $MgAl_2O_4$:Cr^{3+} spinel using photoluminescence. *Journal of Luminescence*, **227**, article 117552 (8 pp.), https://doi.org/10.1016/j.jlumin.2020.117552.

Waychunas, G.A., Apted, M.J. & Brown, G.E. 1983. X-ray *K*-edge absorption spectra of Fe minerals and model compounds: Near-edge structure. *Physics and Chemistry of Minerals*, **10**(1), 1–9, https://doi.org/10.1007/bf01204319.

Widmer, R., Malsy, A.-K. & Armbruster, T. 2015. Effects of heat treatment on red gemstone spinel: single-crystal X-ray, Raman, and photoluminescence study. *Physics and Chemistry of Minerals*, **42**(4), 251–260, https://doi.org/10.1007/s00269-014-0716-7.

Wilke, M., Farges, F., Petit, P.-E., Brown, G.E. & Martin, F. 2001. Oxidation state and coordination of Fe in minerals: An Fe *K*-XANES spectroscopic study. *American Mineralogist*, **86**(5–6), 714–730, https://doi.org/10.2138/am-2001-5-612.

Wongrawang, P., Monarumit, N., Thammajak, N., Wathanakul, P. & Wongkokua, W. 2016. Oxidation states of Fe and Ti in blue sapphire. *Materials Research Express*, **3**(2), article 026201 (7 pp.), https://doi.org/10.1088/2053-1591/3/2/026201.

The Authors

Chawalit Chankhantha[1,2], Pinit Kitkhunthod[3], Ratthaphon Amphon[1,4], Habib Ur Rehman[5] and Prof. Andy H. Shen[1],*

[1] Gemmological Institute, China University of Geosciences (Wuhan), No. 388 Lumo Rd., 430071 Wuhan, China

[2] Division of Creative Industry Development, Department of Industrial Promotion, Ministry of Industry, Rama 4 Rd., Phra Khanong, Klong Toei, 10110 Bangkok, Thailand

[3] Synchrotron Light Research Institute (Public Organization), 111 University Avenue, Muang District, 30000 Nakhon Ratchasima, Thailand

[4] Gemology Program, Department of Geological Sciences, Faculty of Science, Chiang Mai University, 239 Huay Kaew Rd., Muang District, 50200 Chiang Mai, Thailand

[5] Gems & Jewellery Centre of Excellence, University of Engineering & Technology, Peshawar, Pakistan

* Email: shenxt@cug.edu.cn

Acknowledgements

The authors are grateful to the Synchrotron Light Research Institute (Nakhon Ratchasima, Thailand) for allocating XAS beamtime at BL5.2. Thanks to Siwakon Chimnakphant for his assistance with heat treatment experiments, and with UV-Vis and FTIR spectroscopy, at Chiang Mai University, Thailand. Three anonymous reviewers are thanked for their valuable suggestions and comments.

catawiki

Bid on exceptional gemstones, selected by Catawiki experts

Every day, our in-house Experts carefully select a wide range of gemstones from around the world for every collector.

Naomi Howard, FGA, GIA DG, AJP
Expert Gemstones

Buy and sell on catawiki.com

Download on the App Store

GET IT ON Google Play

The 'Star of David' Pattern and Presence of Macrosteps on Ruby and Sapphire Crystals from Aappaluttoq, Greenland

Isabella Pignatelli, Gaston Giuliani, Christophe Morlot and Vincent Pardieu

ABSTRACT: A 'Star of David' appearance is rarely exhibited on gem corundum crystals due to triangular step patterns in opposing orientations on each pinacoidal face. Such samples were recently found at the Aappaluttoq mine in Greenland, and are characterised by eye-visible triangular macrosteps with micrometre- to millimetre-size edges, an uncommon feature on natural corundum crystals. The edge height, as well as the presence of wide terraces and trench-like defects on the crystals, suggest that the macrosteps result from step bunching and faceting[1] processes. The macrosteps likely formed under high-temperature conditions and intense fluid-rock interactions, in a growth medium where impurities and direction of fluid flow played an important role in the step formation. Large macrosteps are also found on corundum crystals from other deposits of both magmatic and metamorphic origin.

The Journal of Gemmology, **38**(4), 2022, pp. 364–375, https://doi.org/10.15506/JoG.2022.38.4.364

Unusual gem crystals displaying shapes resembling a 'Star of David' pattern (i.e. formed by two opposing triangles)—such as those exhibited by diamond, spinel and ruby—have been reported in the literature, although this term may actually refer to different types of growth features.

Williams (1932) described a diamond specimen resembling a 'Star of David' and suggested that it consisted of two rotated twins, joined on a common (111) plane. Decades later, Yacoot *et al.* (1998) confirmed the coexistence of two twins in a diamond sample, each with a flat triangular habit typical of the spinel-twin law[2]. However, the two twins grew independently and came into contact with a misorientation of approximately 178° during the latter stages of their growth. Thus, Yacoot *et al.* (1998, p. 774) suggested that 'the Star of David appearance in [this] diamond is merely fortuitous and it was not the result of further twinning'.

Since early 2000, the Mogok area of Myanmar has yielded some flat spinel crystals with a surface pattern resembling a Star of David (e.g. Figure 1a; see also Daneu *et al.* 2007; Pardieu *et al.* 2016). Spinel, like diamond, can be twinned on {111}. It is commonly a single contact twin, resulting in a flat, triangular habit, but when two consecutive 180° rotations about the [111] axis occur, the sample shows a Star of David pattern (Daneu *et al.* 2007).

[1] In crystal growth terminology, the word *facet* refers to a surface that slightly deviates from the orientation of low-index faces of the crystal habit.
[2] The spinel-twin law is the symmetry operation relating two individuals either rotated 180° about a [111] twin axis or reflected across a {111} twin plane.

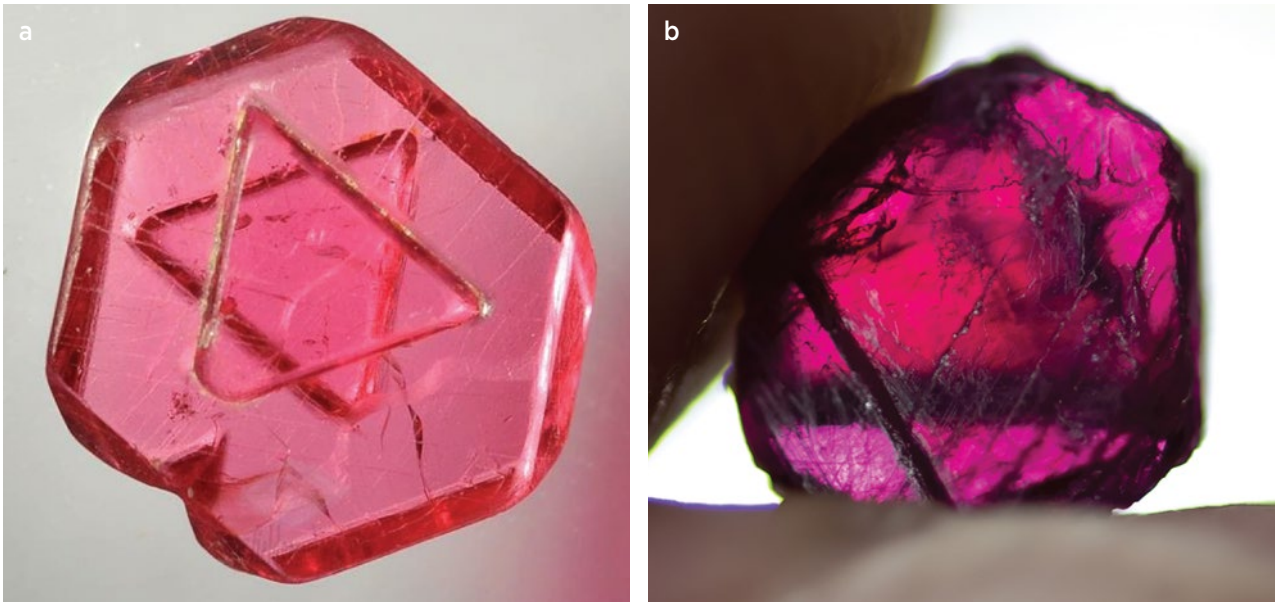

Figure 1: Examples of the Star of David pattern in gem minerals include (**a**) a spinel from Mogok, Myanmar (approximately 10 mm across), and (**b**) a ruby from Aappaluttoq, Greenland (approximately 6 mm across). Both crystals have raised triangular growth patterns pointing in opposing directions on opposite sides of the crystals. Photos by V. Pardieu.

A 2.5 ct ruby from Yogo Gulch (Montana, USA) with the Star of David appearance was reported in Hughes (1997). The specimen displayed triangular protrusions in opposing positions on each pinacoidal face.

Such corundum samples with surface patterns resembling the Star of David are incredibly rare, and in May 2018, after 18 years in the field, author VP encountered such a ruby while checking the production from Gemfields' operation near Montepuez, Mozambique (Figure 2). Unfortunately, he was unable to acquire the sample, which was reportedly cut. Later, in 2019 and then 2020, he encountered two such specimens from the production of the Aappaluttoq mine in Greenland (e.g. Figure 1b). The acquisition of one of these specimens for his reference collection motivated the authors to understand more about the similarity of rubies and spinels displaying the Star of David pattern. Although these minerals have different symmetry (trigonal and cubic, respectively), both can occur as attractive hexagonal-shaped specimens with enough transparency that the two triangles in opposing directions can be seen (again, see Figure 1). Unlike for diamond and spinel, in which the Star of David pattern is due to twinning, the formation of this appearance in corundum had not been explained in the literature. From the authors' initial observations, it became clear that the Star of David appearance in gem corundum from Greenland is related to triangular step patterns that are pointed in opposing directions on pinacoidal {0001} faces (Figure 3). Triangular step patterns on corundum have been known for a long time; Goldschmidt (1913)

Figure 2: Rubies from the May 2018 Gemfields production from Montepuez, Mozambique, show triangular step patterns on their pinacoidal faces. The hexagonal specimen at the lower left (approximately 12 mm across) showed the Star of David pattern when viewed with transmitted light. Photo by V. Pardieu.

Figure 3: These two Aappaluttoq ruby crystals (**a** and **b**) show triangular step patterns on both pinacoidal faces. With greater transparency, they might show a Star of David pattern. Photos by I. Pignatelli.

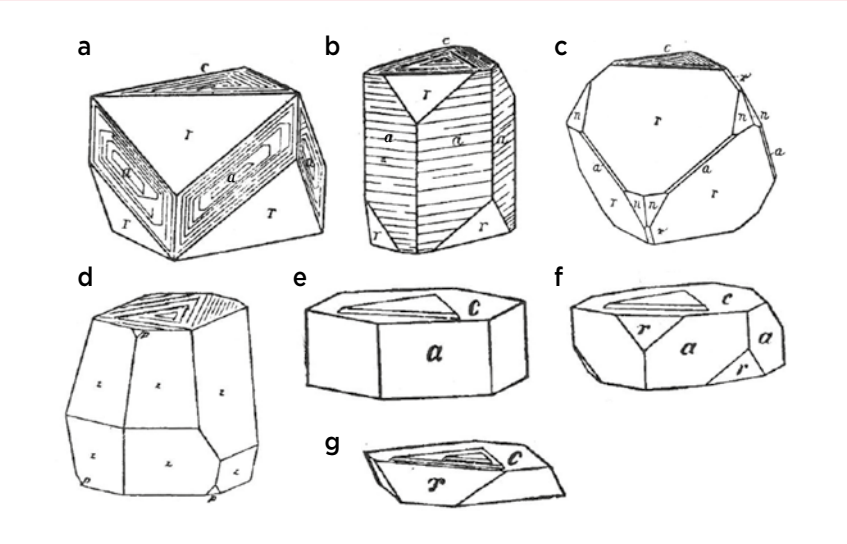

Figure 4: Some corundum crystals illustrated in Goldschmidt's 1913 *Atlas der Kristallformen* (*Atlas of Crystal Forms*) display triangular surface microtopographic features. Faces are designated as follows: *c* {0001}, *r* {10$\bar{1}$1}, *n* {22$\bar{4}$3}, *a* {11$\bar{2}$0} and *z* {22$\bar{4}$1}. The samples came from present-day Myanmar (**a**, **b**, **c**); Haute-Loire, France (**d**); North Carolina, USA (**e**, **g**); and Montana, USA (**f**).

illustrated several specimens (Figure 4). However, the Star of David pattern is quite rare for corundum, since the triangular step pattern is usually observed only on one of the two pinacoidal faces. In addition, the specimen must be transparent enough for the triangular step patterns on both pinacoidal faces to be seen at the same time.

What makes Greenland rubies particularly interesting from a crystal-growth standpoint is that their triangular step patterns are made of relatively large macrosteps with eye-visible edge heights. By contrast, macrosteps on inorganic crystals generally have edges with nanometre- or micrometre-scale heights. Previous studies of macrosteps on corundum have been carried out on synthetic material, which has numerous technological applications in the fields of electronics, optics and chemical catalysis (Stará *et al.* 1995; Dyer *et al.* 1996; Minvielle *et al.* 1996). However, the formation of macrosteps on natural corundum has not been previously documented. The present study reports our investigation of the relationships between the growth and geological conditions of Greenland rubies showing triangular step patterns, as well as other macrostep-bearing corundum crystals from different geological environments (i.e. from Madagascar, India and France).

GEOLOGICAL SETTING OF GREENLAND GEM CORUNDUM

The Aappaluttoq ruby and pink sapphire deposit is located in the Archean Fiskenæsset anorthosite complex of south-west Greenland. According to the classification of corundum deposits proposed by Giuliani *et al.* (2014, 2020), Aappaluttoq belongs to metamorphic primary deposits (type II) and is categorised as sub-type IIB_1, which comprises metamorphic-metasomatic deposits characterised by high fluid-rock interactions and metasomatism of mafic-ultramafic rocks. Gem corundum occurs in a metasomatic reaction zone formed by pegmatite intrusions at the contact between an anorthite-rich rock (leucogabbro) and a metamorphosed ultramafic rock (peridotite). The metasomatic zones resulting from fluid percolation are typically 0.5–5 m wide and contain corundum, phlogopite, cordierite, spinel, sapphirine, calcic amphibole, sillimanite and kornerupine. The reaction zones consist of three main groups: (1) phlogopitite with 80% mica and up to 20% corundum, (2) sapphirine-gedrite rocks, and (3) anthophyllite-cummingtonite(-pargasite) assemblages. The gem corundum is inferred to have formed at upper amphibolite facies conditions (approximately 640°C and 7 kbar) when pegmatites intruded into the anorthite-rich rock and the adjacent ultramafic unit 2.71 billion years ago (Fagan 2018; Keulen *et al.* 2014, 2020).

MATERIALS AND METHODS

Three ruby and sapphire crystals from the Aappaluttoq mine in Greenland (Figure 5) were analysed by X-ray computed tomography (CT), a non-destructive technique that can reveal high-resolution three-dimensional details of solid objects such as crystals. The specimens were mined in 2020 and obtained by author VP while sorting production from Aappaluttoq.

CT imaging has been used previously for rubies by Bouts (2014) to reveal their existence within marble host

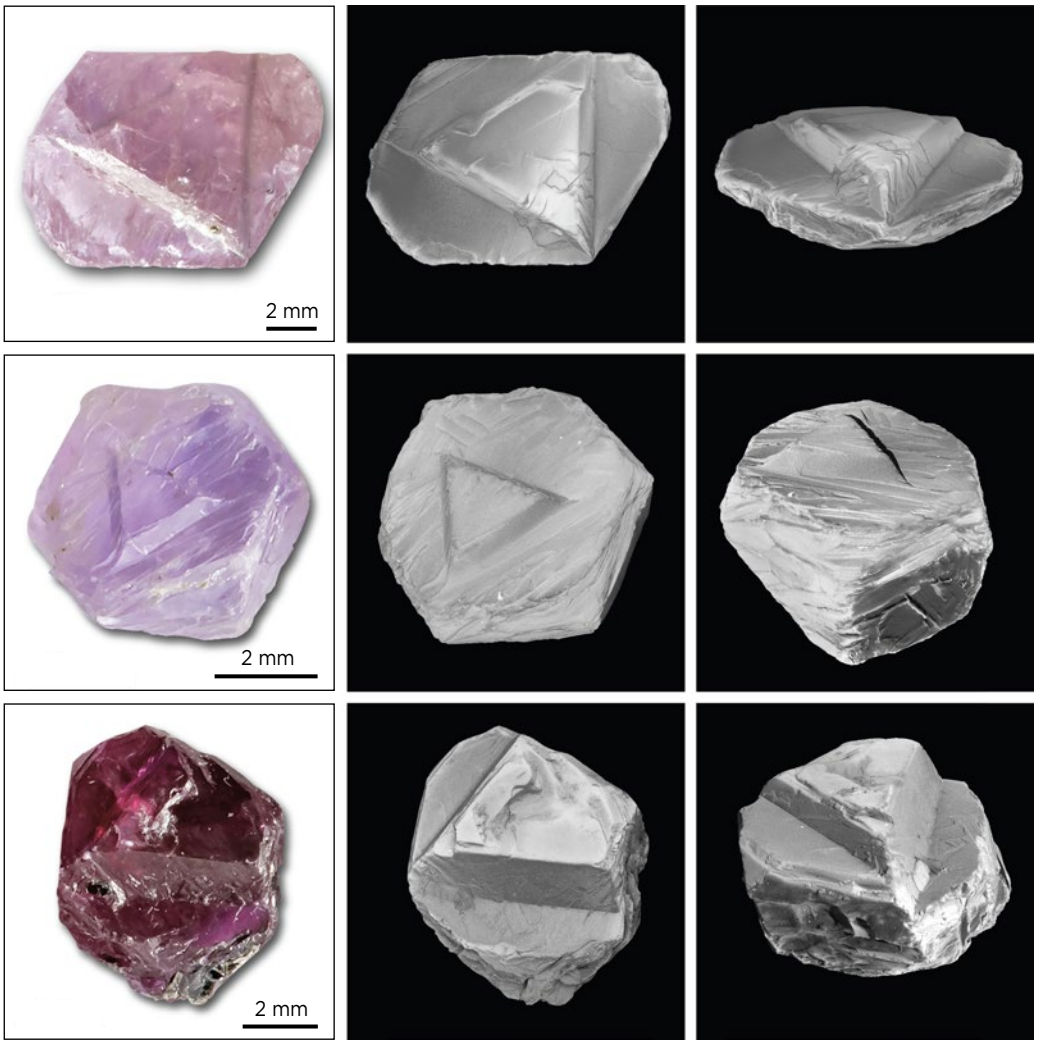

Figure 5: Three Aappaluttoq ruby and sapphire samples are depicted in these photos (left side) and CT images (centre and right side, showing two views of each specimen). The sample at the bottom is the same as that shown in Figure 1b. Photos by V. Pardieu and CT images by C. Morlot.

rock, and by Pignatelli *et al.* (2019, 2020) to describe the trapiche texture of rubies from Myanmar and Vietnam. For the present study, CT images were collected with a Phoenix Nanotom S scanner, using resolutions between 3.0 and 6.75 µm/voxel, and an X-ray tube tension of 75 kV. The tomography files had voxel (3D pixel) resolutions between 30 and 0.6 µm/voxel as a function of sample size. Virtual cross-sections were extracted and analysed with VGStudio 3.5 and Avizo 2021.1 software in order to determine the heights of the macrosteps, the widths of terraces and the orientations of facets.

Vertical scanning interferometry (VSI) was also used to analyse the surface topography of the macrosteps. This technique allows for rapid digitising and processing of the interference pattern to obtain two-dimensional (2D) and three-dimensional (3D) topographical maps of a surface with nanometre resolution (up to 0.1 nm in the z-direction; Kumar *et al.* 2013). A Zygo ZeGage Pro HR interferometer fitted with a 5.5× Michelson objective (numerical aperture = 0.15) was used to collect images with a scan length of 100 µm and an acquisition time of 8 s. This setup permitted visualisation of a scanning area measuring 1.56 mm × 1.56 mm per image field.

Also briefly examined for comparison were corundum crystals from Madagascar (three samples), India (one sample) and France (one sample).

RESULTS AND DISCUSSION

The Aappaluttoq corundum crystals analysed in this study are not twinned, but rather are characterised by spiral step patterns that have a triangular shape (Figure 5) due to the three-fold axis perpendicular to the pinacoidal faces. Such patterns have been observed on low-index faces of several crystals, including natural and synthetic corundum (e.g. Pham Van *et al.* 1998; Kurnosikov *et al.* 2000; Sunagawa 2005). Although triangular features may be present on diamond crystals, they are distinct from the step patterns described here on corundum (see Box A).

The triangular patterns on the {0001} faces of the Aappaluttoq corundum samples we examined had step heights varying from several tens of micrometres to a few millimetres (e.g. Figure 6). Due to these large dimensions, they cannot be elementary steps of a screw dislocation whose height is determined by the Burgers vector[3] (i.e. measuring a few angstroms). Instead, they are macrosteps with thick edges and are separated by wide terraces, resulting in a terrace-step morphology already described in the literature for {0001*f* faces of synthetic corundum (Heffelfinger & Carter 1997;

Box A: Triangular Step Patterns vs Trigons

Polygonal step patterns (such as those shown in Figure 4) follow the symmetry element perpendicular to the crystal face on which they occur. Therefore, a triangular form is observed on the {0001} faces of corundum (e.g. Figure 3), which belongs to the trigonal crystal system.

Triangular step patterns are commonly called *trigons* by gemmologists, and when applied to corundum this term can refer to both raised step patterns and etch pits. This ambiguity arises from the 'trigons' observed on {111} faces of natural diamonds (e.g. Figure A-1), whose origin due to growth or dissolution has been debated for many years. Although it was subsequently established that trigons are etch pits due to dislocations or point defects (Sunagawa 2005), this terminology is still misused in gemmology. The term *trigon* should be used only for triangular surface microtopographic features (i.e. those on faces perpendicular to a crystallographic three-fold axis)—which is not the case for all gems nor for all faces of the same crystal. For example, unlike the microtopographic features on pinacoidal faces of corundum, those on *a* {11$\bar{2}$0} faces are not triangular (see Figure 4a). Therefore, we propose applying the term *trigons* only to diamond, and we do not use it further in this article.

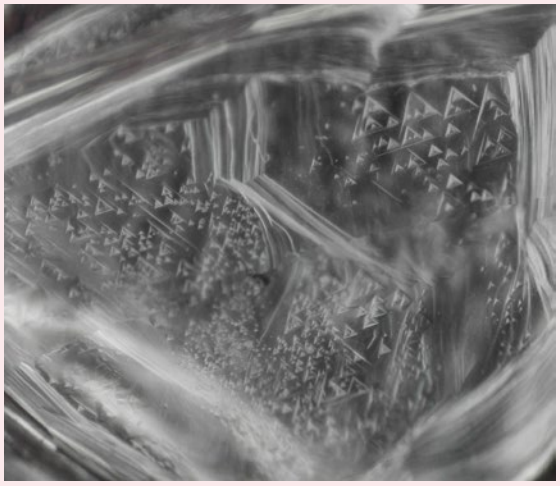

Figure A-1: Trigons decorate the surface of this diamond macle. Photomicrograph by Henry Mesa, Gem-A; magnified 45×.

[3] The vector characterising a dislocation is called Burgers vector. It represents the magnitude and direction of lattice distortion due to the dislocation.

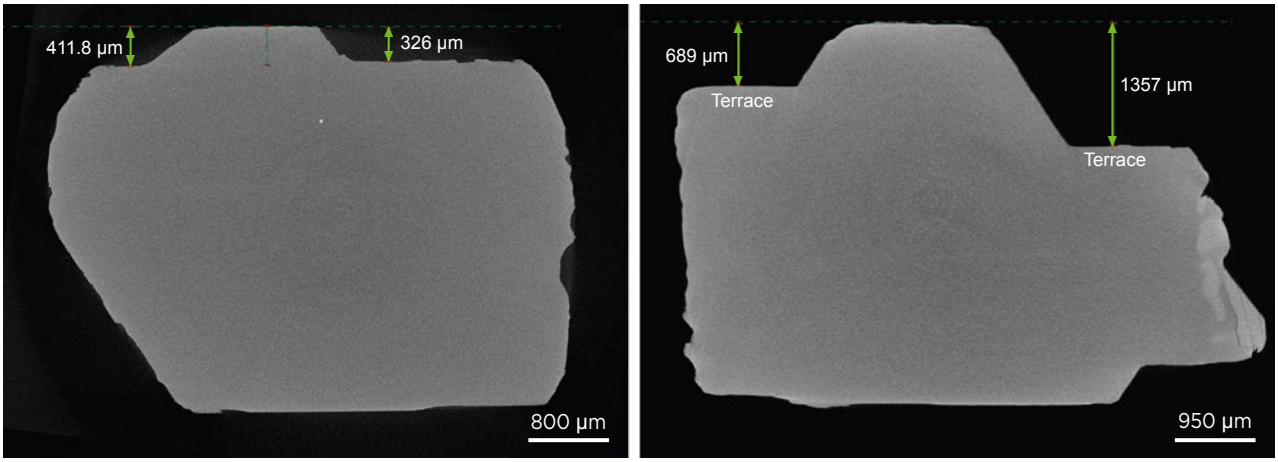

Figure 6: CT images of two of the analysed Aappaluttoq corundum crystals show examples of measured step heights, which here range from 0.33 to 1.36 mm. Images by C. Morlot.

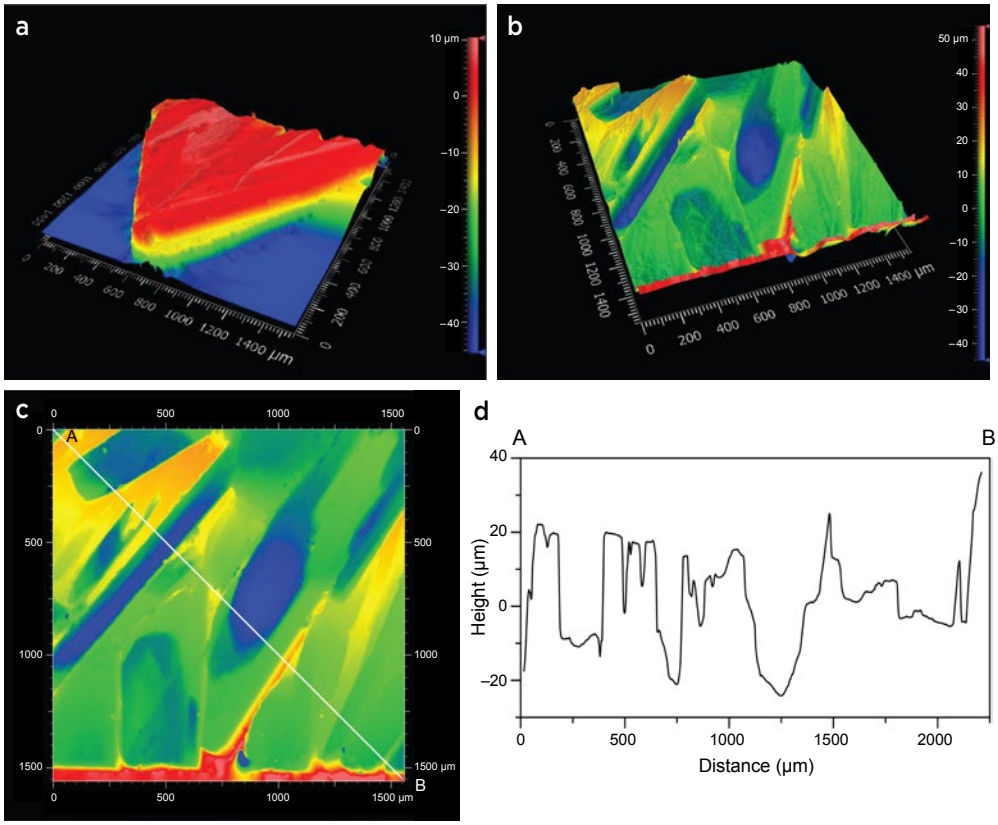

Figure 7: (**a**, **b**) 3D topographic images obtained using VSI show the surface roughness of two terraced areas on a pinacoidal face of one of the studied Aappaluttoq corundum crystals (see Figure 5, centre). (**c**) A 2D image of the same area shown in (**b**) is marked with the line A–B, corresponding to the cross-section profile in (**d**). The terrace is corrugated by the presence of small steps across its surface. Images by I. Pignatelli.

Cuccureddu *et al*. 2010). The terraces on the Aappaluttoq specimens we analysed ranged from 70 to 415 µm wide on one sample, and from 332 µm to 3.2 mm wide on another one. The terrace surfaces appear to be flat macroscopically, but they are actually corrugated by the presence of smaller steps (Figure 7). Such surface roughening has been considered a consequence of severe step bunching[4] during the growth of inorganic crystals (Mitani *et al*. 2015).

VSI images confirmed this step bunching by showing the 'zipper-like' coalescence of steps with smaller heights joining to form a higher step (Pham Van *et al*. 1998; Figure 8a, b). As these junctions progress, the steps 'zip' together and provide a mechanism for step faceting (i.e. a process by which a step edge decomposes into two or more vicinal surfaces whose orientation slightly deviates

[4] Bunching consists of the gathering of smaller steps, allowing the formation of multiple steps with considerable height.

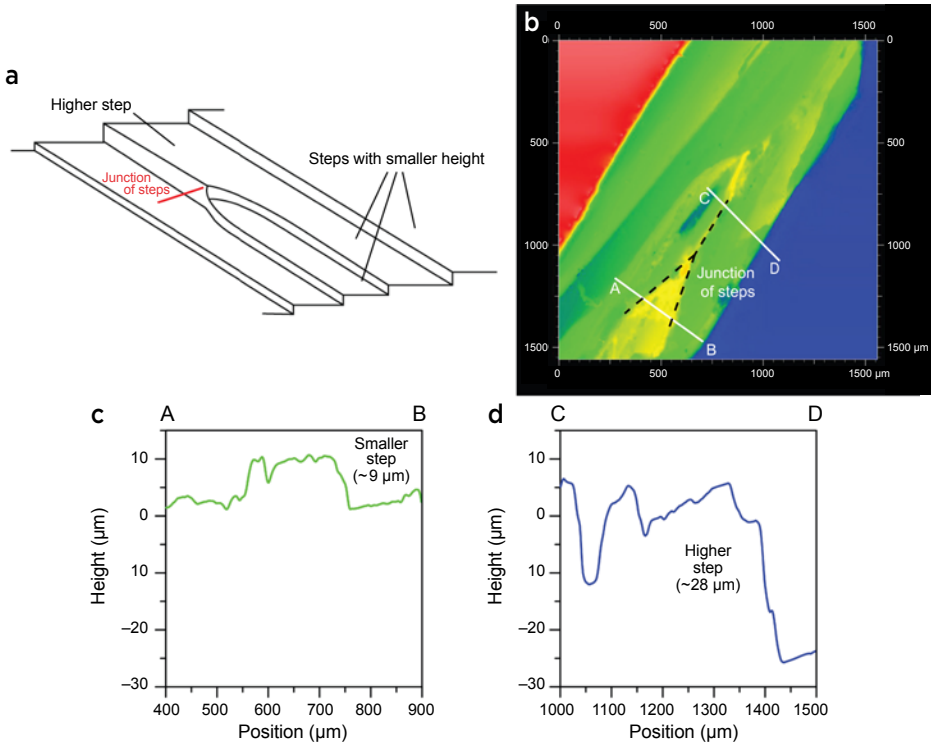

Figure 8: (**a**) This diagram shows how steps with smaller heights join together to form a higher step via a 'zipper-like' coalescence (modified from Pham Van *et al.* 1998). (**b**) A 2D VSI topographical image of a ruby from Aappaluttoq shows such a junction of steps. The cross-section profiles along the lines A–B and C–D show, respectively: (**c**) separate smaller steps with heights of approximately 9 Þm and (**d**) a higher step (approximately 28 Þm) where smaller steps have joined. Image by I. Pignatelli.

from the orientation of low-index faces of the crystal habit). This provides a mechanism whereby smaller steps bunch together to form a higher step (i.e. macrostep). The step profiles along the marked lines A–B and C–D in Figure 8b and shown in Figures 8c and 8d, respectively, indicate how the height of larger steps (~28 µm) can be measured as an approximate multiple of smaller steps (~9 µm), in agreement with previous experimental observations (Pham Van *et al.* 1998; Cuccureddu *et al.* 2010).

Our data also highlighted trench-like defects developed on those macrosteps with wider terraces (Figure 9). These trenches form in the following way: a 2D nucleation island formed on the terrace, and then it expanded to the advancing macrostep. Where they meet, a trench is formed in front of the macrostep (Zhu *et al.* 2013).

In order to determine the orientation of facets, we considered only macrosteps with heights greater than 100 µm to facilitate measurement. CT images were used to measure the angle between the facets and {0001} faces (e.g. Figure 10). From 18 measurements on the three samples, we obtained mean angles of 124.5° and 132.4°. This suggests that they are oriented along the traces of first-order rhombohedral $\{h0\bar{h}l\}$ faces with l = 2 or 3 (theoretical angles are 122.4° and 133.6°, respectively). For $l > 4$, the difference between the measured and theoretical angles is too high (e.g. for $\{10\bar{1}4\}$ it

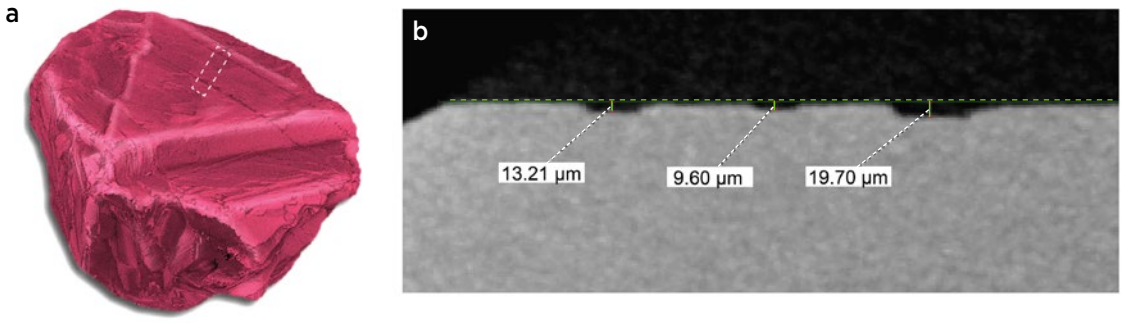

Figure 9: (**a**) This false-colour CT image of the ruby in the lower part of Figure 5 shows (**b**) an area with trench-like defects. Images by C. Morlot.

is almost 10°). Considering that the space group of corundum is $R\bar{3}c$ (i.e. its point group symmetry is $\bar{3}\,2/m$), the multiplicity of first-order rhombohedral $\{h0\bar{h}l\}$ faces is six, consisting of three faces on the positive side of the *c*-axis—$(h0\bar{h}l)$, $(\bar{h}h0l)$ and $(0\bar{h}hl)$—and three on the negative side—$(0h\bar{h}\bar{l})$, $(h\bar{h}0\bar{l})$ and$(\bar{h}0h\bar{l})$. Each set of three rhombohedral faces results in a triangle, so when both sets are visible simultaneously through a transparent crystal, they give rise to a Star of David pattern.

In previous studies of synthetic corundum, the facets were described to be (1) not aligned along any low-index crystallographic direction (Pham Van *et al.* 1998), or (2) oriented along traces of $\{11\bar{2}0\}$ and $\{10\bar{1}0\}$ planes (Heffelfinger & Carter 1997; Kurnosikov *et al.* 2000). However, we found different orientations from the aforementioned ones (i.e. $\{10\bar{1}2\}$ and $\{10\bar{1}3\}$), and our results are supported by theoretical data (Bakholdin & Maslov 2015). Mathematical simulations that take into account only internal, structural factors (i.e. periodic bond chains) which affect the morphology, and neglect all external factors, predicted that the rhombohedral faces $\{10\bar{1}2\}$ could be present in the crystal habit of corundum (Bakholdin & Maslov 2015), even if they are not the most common faces. This means that it is possible to develop facets oriented along the traces of these planes.

Role of Chemical Impurities in the Formation of Macrosteps

The formation of macrosteps on Aappaluttoq rubies and sapphires is related to step-bunching and step-faceting processes, as suggested by the following features:

- large step heights that can be millimetre-size
- terrace-step morphology
- zipper-like step junctions
- wide, rough terraces with trench-like defects

Several possible causes have been reported in the literature to explain macrostep formation by step bunching and step faceting: (1) fluctuations of supersaturation on the surface (Sunagawa 2005); (2) asymmetry in the surface diffusion between the upper and lower terraces of the step, which results in fluctuations of its rate of advance (i.e. Schowoebel effect; Schowoebel & Shipsey 1966); and (3) impurity adsorption described as the 'pinning effect' (Cabrera & Vermileya 1958).

Although it is not possible to determine which one of the cited causes is predominant in a natural environment to explain the step bunching and faceting on corundum, the role of impurities in the parental growth medium should not be neglected in the formation of macrosteps

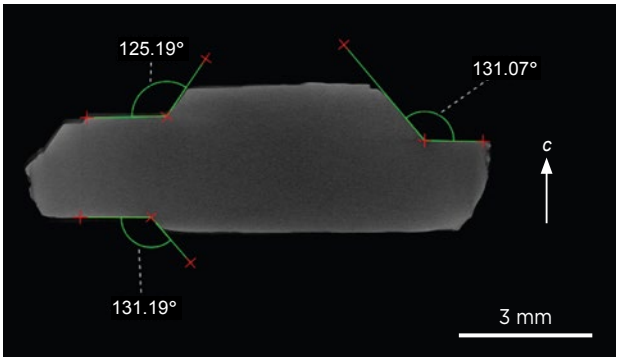

Figure 10: A CT image of an Aappaluttoq ruby crystal shows the angles between the facets and the {0001} faces. Image by C. Morlot.

on Aappaluttoq corundum. In the geological context of the deposit, it is important to take into account not only the role of chromophores (e.g. 269–1816 ppm Cr and 655–2516 ppm Fe; Giuliani *et al.* 2020), but also that of elements needed for the crystallisation of host-rock-forming minerals, such as feldspars and micas. Indeed, the atomic nature and the quantity of elements can strongly affect the {0001} surface evolution of corundum (Cuccureddu *et al.* 2010). Cations with ionic radii greater than Al^{3+} can produce more perturbed step patterns with a larger number of spiral growth steps on {0001} and will modify the final crystal habit, also affecting the growth rates of other faces (Watanabe & Sunagawa 1983). The combination of high Ca and low K adsorptions stabilises the elementary steps, preventing the formation of macrosteps, whereas a high amount of K or the presence of Ba and Si in the parental growth medium accelerates step bunching and faceting, generating macrosteps (Heffelfinger & Carter 1997; Curiotto & Chatain 2009; Ravishankar & Barry Carter 2011).

Role of Driving Force in the Parental Growth Medium

Both step bunching and step faceting are favoured by high driving-force conditions on both organic and inorganic crystals (Sangwal *et al.* 1997). Although unlikely for natural corundum, for synthetic corundum it has been proven that these processes are favoured by annealing (Heffelfinger & Carter 1997; Kurnosikov *et al.* 2000). Why do macrosteps form at high temperature (i.e. at low driving-force conditions) in corundum?

Macrosteps can be considered as evidence for growth resurrection after entering the 'dead zone'—that is, a regime of low supersaturation (σ_d) where growth ceases (Land *et al.* 1999). This allows crystallisation under low driving force and low purity of solute conditions that do not favour crystal growth in models of the Cabrera-

Vermileya type (Cabrera & Vermilyea 1958). These models predict no growth taking place above a sufficiently high supersaturation (σ^*), in contrast to what was observed experimentally by Land *et al.* (1999). The latter authors showed the presence of two dead zones: one for elementary steps—whose height is determined by the Burgers vector of the screw dislocation—and the other for macrosteps. When supersaturation (σ) is lower than σ^*, the impurities block the motion of elementary steps and growth is stopped, whereas when $\sigma_d < \sigma < \sigma^*$, macrosteps are still mobile and move at a rate relative to their height (Land *et al.* 1999; Lutsko *et al.* 2016; Sleutel *et al.* 2017). Thus, macrosteps interact differently with impurities, bypassing their impeding effect.

Atomistic simulations[5] have shown that when elementary steps are stopped by a grid of impurities: (1) macrosteps are unstable where no impurities are present on the surface, (2) macrostep advancement through a field of impurities depends on their height and (3) macrosteps facilitate the transition from a 2D to 3D nucleation mechanism, breaching the impurity fence (i.e. a barrier for the crystal growth; Lutsko *et al.* 2016).

High temperature has the same effect as low supersaturation on decreasing driving-force conditions. Various authors have demonstrated that for the {0001} faces of corundum, step bunching is a thermally activated process with a rate that depends exponentially on temperature, helping the step heights to increase (Pham Van *et al.* 1998; Kurnosikov *et al.* 2000; Cuccureddu *et al.* 2010).

These studies suggest that rubies with macrosteps from the Aappaluttoq deposit likely formed under low driving-force conditions, due to their high temperatures of formation. As this deposit is characterised by intense fluid-rock interactions, it is likely that not only the temperature and supersaturation played a role in the formation of corundum macrosteps, but also the fluid flow. This is corroborated by the presence of both wide terraces and trenches on the macrosteps (Figure 9), and confirms previous studies of inorganic crystal growth (Zhu *et al.* 2013; Mitani *et al.* 2015). If the fluid flow is parallel to the step flow, the solute concentration gradient near the edge of the macroterraces is larger than in front of the macrosteps. Thus, the elementary steps on the macroterraces accelerate near their edges and run into the next macrosteps, where they accumulate (Zhu *et al.* 2013). This also favours the formation of a micrometre-size terrace between macrosteps, which facilitates the formation of 2D nucleation islands. When the 2D island expands and meets the macrostep, a trench is generated nearby, and the surface roughness increases (Zhu *et al.* 2013; Mitani *et al.* 2015).

On the contrary, when the fluid flow is opposite to the step flow, the concentration gradient is higher in front of the macrosteps. The elementary steps bunched in the macrosteps are, thus, accelerated and run out of the macrosteps. In this way, as the growth proceeds, the height of macrosteps decreases gradually and then disappears (Zhu *et al.* 2013). The fluid flow effect may explain why some crystals of corundum—formed in the same deposit, under the same temperature and pressure conditions—show macrosteps on their {0001} surfaces and others do not.

Comparison with Corundum Crystals from Other Localities

We looked for the presence of macrosteps on other corundum crystals (Figures 11 and 12) and discovered that they are not rare. For example, we found macrosteps on sapphires from Sahambano, Madagascar (Figures 11a, 11b and 12), which come from a deposit of sub-type IIB_2 (i.e. a shear-zone-related or fold-controlled metamorphic-metasomatic deposit in different substrata, such as Mg-Cr-bearing biotite schist, gneiss or marble; Giuliani *et al.* 2020). Although no Star of David pattern was visible, one of these samples showed a composite step pattern consisting of spiral steps originating from several coexisting screw dislocations (see Figure 12c).

We also observed macrosteps on corundum crystals from metamorphic *sensu stricto* deposits in metamorphosed mafic and ultramafic rocks (sub-type IIA_1 of Giuliani *et al.* 2020) such as Ejeda in Madagascar, Mysore in India (Figure 11c) and Montepuez in Mozambique (Figure 2).

Interestingly, eye-visible macrosteps can also be present on the pinacoidal faces of magmatic-type corundum. Blue sapphire xenocrysts from alkali basalt found in alluvial deposits of the Sioulot stream in the French Massif Central (Puy-de-Dôme) show beautiful triangular step patterns giving rise to a Star of David pattern (Figure 11d).

Our visual observations indicate that the occurrence of macrosteps is not related to the overall crystal habit of corundum. We observed them on platy crystals from Aappaluttoq as well as on both small and centimetre-sized prismatic ones, such as from Zazafotsy, Madagascar, and from Mysore, India (Figure 11c).

Thus, these observations underscore that the presence of macrosteps on rubies and sapphires is not related to a specific geological context, such as metasomatic-metamorphic deposits (e.g. Aappaluttoq and Sahambano).

[5] Atomistic simulations are numerical methods for the investigation of crystal structure on an atomic scale.

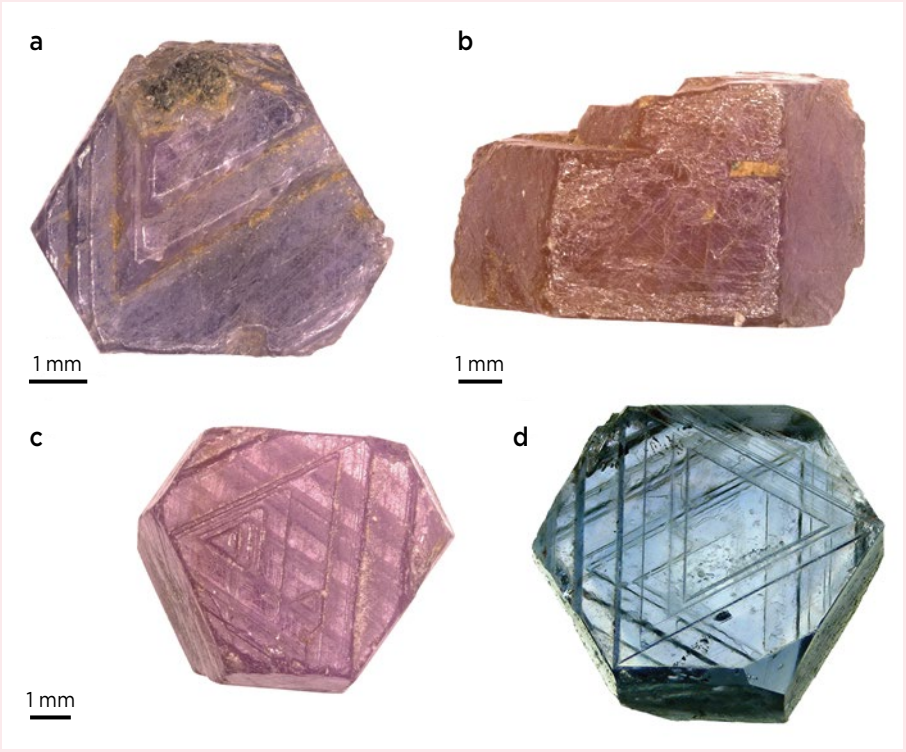

Figure 11: These corundum samples from various geological and geographical origins show macrosteps. The samples include (**a**, **b**) metamorphic-metasomatic purple and orange sapphires from Sahambano, Madagascar; (**c**) a metamorphic ruby from Mysore, India; and (**d**) a blue sapphire of magmatic origin from Sioulot, Puy-de-Dôme, French Massif Central. The blue sapphire is 1.4 mm across; photo and collection of F. Périnet. The other photos are by I. Pignatelli.

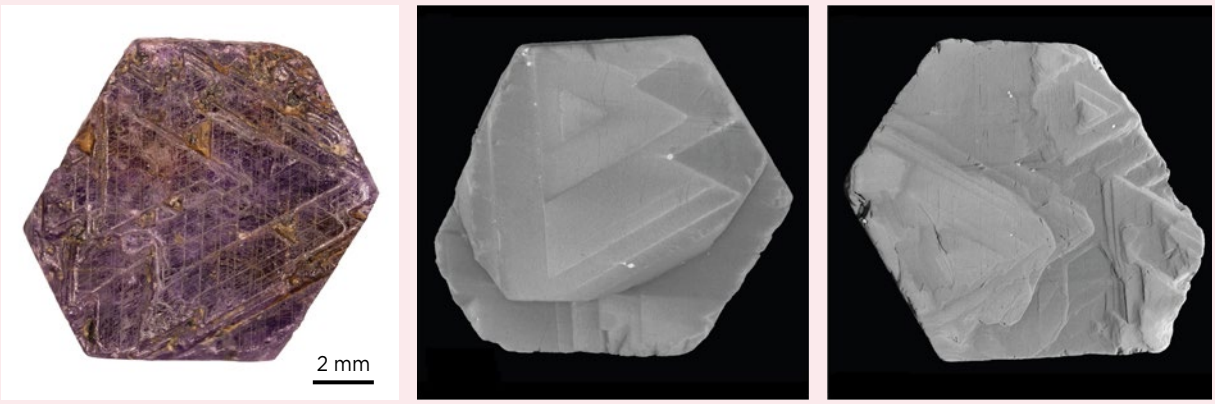

Figure 12: A sapphire from Sahambano (Madagascar) is depicted in this photo (left) and CT images (centre and right, showing each pinacoidal face). The image on the right displays a composite step pattern made of triangular spiral steps originating from three coexisting screw dislocations on a pinacoidal face. Photo by I. Pignatelli (a) and CT images by C. Morlot (b, c).

CONCLUSION

Macrosteps with micrometre- to millimetre-sized edges on the pinacoidal faces of gem corundum from the Aappaluttoq deposit can give rise to a rare Star of David pattern in transparent specimens. The following conditions were likely involved in macrostep development:

1. Low driving-force conditions due to high temperatures of their formation, which facilitates the step bunching and step faceting processes.
2. An impurity-rich growth medium characterised by the presence of other elements in addition to Al and O, which seem to play a role in stabilising the macrosteps. These elements could be the chromophores, but they might also be atoms that cannot be incorporated into the corundum structure, such as alkalis or Si. They are present in the growth medium, as shown by the formation of coexisting minerals in the host rock (e.g. phlogopite associated with gem corundum at Aappaluttoq).

3. A geological context marked by intense fluid-rock interactions (i.e. metamorphic-metasomatic type). When the direction of fluid flow is parallel to the step flow direction, macrosteps form; otherwise, the development of macrosteps is hampered. This explains the inconsistent presence of macrosteps on Aappaluttoq gem corundum.

This study also highlights that macrosteps can occur on both rubies and sapphires, independent of their crystal habit (e.g. platy crystals from Aappaluttoq and prismatic crystals from Mysore). Macrosteps are found in both magmatic and metamorphic deposits, so their occurrence is not due to a specific geological environment or geographical origin.

REFERENCES

Bakholdin, S.I. & Maslov, V.N. 2015. Modeling habit forms of sapphire crystals using the principles of periodic-bond-chain method. *Crystallography Reports*, **60**(2), 306–311, https://doi.org/10.1134/s1063774515020029.

Bouts, A. 2014. Detection of ruby crystals in marble host rock by X-ray computed tomography. *Journal of Gemmology*, **34**(1), 50–54, https://doi.org/10.15506/JoG.2014.34.1.50.

Cabrera, N. & Vermilyea, D.A. 1958. The growth of crystals from solution. *In*: Doremus, R.H., Roberts, B.W. & Turnbull, D. (eds) *Growth and Perfection of Crystals: Proceedings of an International Conference on Crystal Growth*, Cooperstown, New York, USA, 27–29 August 1958, Chapman and Hall, London, and John Wiley & Sons Ltd, New York, New York, USA, 609 pp. (see p. 393).

Cuccureddu, F., Murphy, S., Shvets, I.V., Porcu, M., Zandbergen, H.W., Sidorov, N.S. & Bozhko, S.I. 2010. Surface morphology of *c*-plane sapphire (α-alumina) produced by high temperature anneal. *Surface Science*, **604**(15–16), 1294–1299, https://doi.org/10.1016/j.susc.2010.04.017.

Curiotto, S. & Chatain, D. 2009. Surface morphology and composition of *c*-, *a*- and *m*-sapphire surfaces in O_2 and H_2 environments. *Surface Science*, **603**(17), 2688–2697, https://doi.org/10.1016/j.susc.2009.07.004.

Daneu, N., Rečnik, A., Yamazaki, T. & Dolenec, T. 2007. Structure and chemistry of (111) twin boundaries in $MgAl_2O_4$ spinel crystals from Mogok. *Physics and Chemistry of Minerals*, **34**(4), 233–247, https://doi.org/10.1007/s00269-007-0142-1.

Dyer, P.E., Jackson, S.R., Key, P.H., Metheringham, W.J. & Schmidt, M.J.J. 1996. Excimer laser ablation and film deposition of Ti:sapphire. *Applied Surface Science*, **96–98**, 849–854, https://doi.org/10.1016/0169-4332(95)00565-x.

Fagan, A.J. 2018. *The ruby and pink sapphire deposits of SW Greenland: Geological setting, genesis, and exploration techniques*. PhD thesis, University of British Columbia, Vancouver, Canada, 747 pp., https://doi.org/10.14288/1.0372956.

Giuliani, G., Ohnenstetter, D., Fallick, A.E., Groat, L.A. & Fagan, A. 2014. The geology and genesis of gem corundum deposits. *In*: Groat, L.A. (ed) *Geology of Gem Deposits*. Mineralogical Association of Canada Short Course Series Vol. 44, Québec City, Québec, Canada, 29–112.

Giuliani, G., Groat, L.A., Fallick, A.E., Pignatelli, I. & Pardieu, V. 2020. Ruby deposits: A review and geological classification. *Minerals*, **10**(7), article 597 (83 pp.), https://doi.org/10.3390/min10070597.

Goldschmidt, V. 1913. *Atlas der Kristallformen, Band I. Adamin–Buntkupfererz*. Carl Winters Universitätsbuchhandlung, Heidelberg, Germany, vi + 248 pp.

Heffelfinger, J.R. & Carter, C.B. 1997. Mechanisms of surface faceting and coarsening. *Surface Science*, **389**(1–3), 188–200, https://doi.org/10.1016/s0039-6028(97)00411-1.

Hughes, R.W. 1997. *Ruby & Sapphire*. RWH Publishing, Bangkok, Thailand, 511 pp.

Keulen, N., Schumacher, J.C., Næraa, T., Kokfelt, T.F., Scherstén, A., Szilas, K., van Hinsberg, V.J., Schlatter, D.M. *et al*. 2014. Meso- and Neoarchaean geological history of the Bjørnesund and Ravns Storø supracrustal belts, southern West Greenland: Settings for gold enrichment and corundum formation. *Precambrian Research*, **254**, 36–58, https://doi.org/10.1016/j.precamres.2014.07.023.

Keulen, N., Thomsen, T.B., Schumacher, J.C., Poulsen, M.D., Kalvig, P., Vennemann, T. & Salimi, R. 2020. Formation, origin and geographic typing of corundum (ruby and pink sapphire) from the Fiskenæsset complex, Greenland. *Lithos*, **366–367**, article 105536 (26 pp.), https://doi.org/10.1016/j.lithos.2020.105536.

Kumar, A., Reed, J., Sant, G. & Biernacki, J. 2013. Vertical scanning interferometry: A new method to measure the dissolution dynamics of cementitious minerals. *Journal of the American Ceramic Society*, **96**(9), 2766–2778, https://doi.org/10.1111/jace.12482.

Kurnosikov, O., Pham Van, L. & Cousty, J. 2000. High-temperature transformation of vicinal (0001) Al_2O_3-α

surfaces: An AFM study. *Surface and Interface Analysis*, **29**(9), 608–613, https://doi.org/10.1002/1096-9918(200009)29:9%3C608::AID-SIA906%3E3.0.CO;2-B.

Land, T.A., Martin, T.L., Potapenko, S., Palmore, G.T. & De Yoreo, J.J. 1999. Recovery of surfaces from impurity poisoning during crystal growth. *Nature*, **399**(6735), 442–445, https://doi.org/10.1038/20886.

Lutsko, J.F., Van Driessche, A.E.S., Durán-Olivencia, M.A., Maes, D. & Sleutel, M. 2016. Step crowding effects dampen the stochasticity of crystal growth kinetics. *Physical Review Letters*, **116**(1), article 015501 (5 pp.), https://doi.org/10.1103/PhysRevLett.116.015501.

Minvielle, T.J., White, R.L., Hildner, M.L. & Wilson, R.J. 1996. Temperature dependence of the epitaxial growth of Pt on basal-plane sapphire. *Surface Science*, **366**(3), L755–L759, https://doi.org/10.1016/0039-6028(96)00941-7.

Mitani, T., Komatsu, N., Takahashi, T., Kato, T., Harada, S., Ujihara, T., Matsumoto, Y., Kurashige, K. *et al.* 2015. Effect of aluminum addition on the surface step morphology of 4H–SiC grown from Si–Cr–C solution. *Journal of Crystal Growth*, **423**, 45–49, https://doi.org/10.1016/j.jcrysgro.2015.04.032.

Pardieu, V., Sangsawong, S., Vertriest, W. and Raynaud, V. 2016. Gem News International: "Star of David" spinel twin crystal with multiphase inclusions from Mogok. *Gems & Gemology*, **52**(1), 100–101.

Pham Van, L., Kurnosikov, O. & Cousty, J. 1998. Evolution of steps on vicinal (0001) surfaces of α-alumina. *Surface Science*, **411**(3), 263–271, https://doi.org/10.1016/s0039-6028(98)00329-x.

Pignatelli, I., Giuliani, G., Morlot, C. & Van Long, P. 2019. The texture and chemical composition of trapiche ruby from Khoan Thong, Luc Yen mining district, northern Vietnam. *Journal of Gemmology*, **36**(8), 726–746, https://doi.org/10.15506/JoG.2019.36.8.726.

Pignatelli, I., Giuliani G., Morlot C., Cathelineau M. & Liu, S.I 2020. Flower-shaped trapiche ruby from Mong Hsu, Myanmar: A revised growth mechanism. *Journal of Gemmology*, **37**(4), 404–415, https://doi.org/10.15506/JoG.2020.37.4.404.

Ravishankar, N. & Barry Carter, C. 2011. Bunching of surface steps and facet formation on an alumina surface. *Journal of Materials Research*, **17**(1), 98–106, https://doi.org/10.1557/jmr.2002.0016.

Sangwal, K., Torrent-Burgues, J., Sanz, F. & Gorostiza, P. 1997. Atomic force microscopic study of step bunching and macrostep formation during the growth of L-arginine phosphate monohydrate single crystals. *Journal of Crystal Growth*, **172**(1–2), 209–218, https://doi.org/10.1016/s0022-0248(96)00764-6.

Schwoebel, R.L. & Shipsey, E.J. 1966. Step motion on crystal surfaces. *Journal of Applied Physics*, **37**(10), 3682–3686, https://doi.org/10.1063/1.1707904.

Sleutel, M., Lutsko, J. & Van Driessche, A.E.S. 2017. Mineral growth beyond the limits of impurity poisoning. *Crystal Growth & Design*, **18**(1), 171–178, https://doi.org/10.1021/acs.cgd.7b01057.

Stará, I., Nehasil, V. & Matolín, V. 1995. The influence of particle size on CO oxidation on Pd/alumina model catalyst. *Surface Science*, **331–333**, 173–177, https://doi.org/10.1016/0039-6028(95)00183-2.

Sunagawa, I. 2005. *Crystals: Growth, Morphology & Perfection*. Cambridge University Press, Cambridge, xii + 295 pp., https://doi.org/10.1017/cbo9780511610349.

Watanabe, K. & Sunagawa, I. 1983. Effects of trivalent rare-earth ions upon the morphology of corundum crystals. *Journal of Crystal Growth*, **65**(1–3), 568–575, https://doi.org/10.1016/0022-0248(83)90104-5.

Williams, A.F. 1932. *The Genesis of the Diamond*, Vols. 1 and 2. E. Benn Ltd, London, 636 pp. + indexes.

Yacoot, A., Moore, M. & Machado, W.G. 1998. Twinning in natural diamond. I. Contact twins. *Journal of Applied Crystallography*, **31**(5), 767–776, https://doi.org/10.1107/s0021889898005317.

Zhu, C., Harada, S., Seki, K., Zhang, H., Niinomi, H., Tagawa, M. & Ujihara, T. 2013. Influence of solution flow on step bunching in solution growth of SiC crystals. *Crystal Growth & Design*, **13**(8), 3691–3696, https://doi.org/10.1021/cg400706u.

The Authors

Dr Isabella Pignatelli and Christophe Morlot
Université de Lorraine, GeoResources UMR 7359 CNRS-UL, BP 70239, 54506 Vandœuvre-lès-Nancy cedex, France
Email: isabella.pignatelli@univ-lorraine.fr

Dr Gaston Giuliani
Université Paul Sabatier, GET/IRD, UMR CNRS-IRD-CNES 5563, 14 avenue Edouard Belin, 31400 Toulouse, France
and
Université de Lorraine, CRPG UMR 7358 CNRS-UL, 15 rue Notre-Dame-des-Pauvres, BP 20, 54501 Vandœuvre-lès-Nancy cedex, France

Vincent Pardieu
VP Consulting, Manama, Bahrain

Acknowledgements

The authors thank François Périnet for the photo of the basaltic blue sapphire from the French Massif Central. The anonymous reviewers are thanked for their corrections and suggestions, helping us to improve the final version of the manuscript.

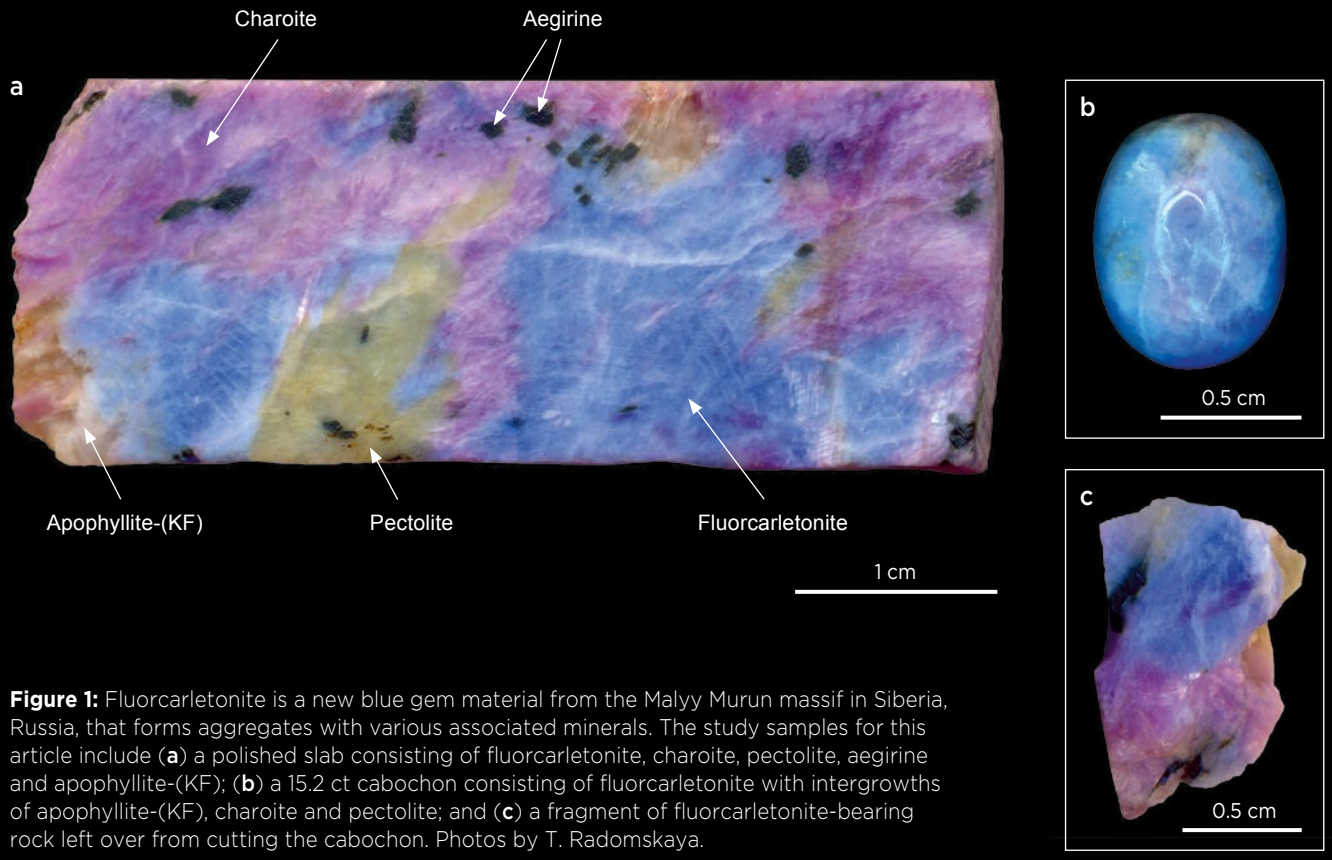

Figure 1: Fluorcarletonite is a new blue gem material from the Malyy Murun massif in Siberia, Russia, that forms aggregates with various associated minerals. The study samples for this article include (**a**) a polished slab consisting of fluorcarletonite, charoite, pectolite, aegirine and apophyllite-(KF); (**b**) a 15.2 ct cabochon consisting of fluorcarletonite with intergrowths of apophyllite-(KF), charoite and pectolite; and (**c**) a fragment of fluorcarletonite-bearing rock left over from cutting the cabochon. Photos by T. Radomskaya.

Fluorcarletonite—A New Blue Gem Material

Ekaterina Kaneva, Tatiana Radomskaya and Roman Shendrik

ABSTRACT: Fluorcarletonite is a very rare, recently described blue phyllosilicate mineral that occurs together with charoite in the Malyy Murun massif in Siberia, Russia. It forms compact aggregates suitable for jewellery use and has a Mohs hardness of 4–4½. Its RI values are n_o = 1.520 and n_e = 1.515, and its SG is 2.49, although actual measurements of these values may vary due to the presence of different associated minerals. These mainly include charoite, apophyllite-(KF), aegirine and pectolite, with minor apatite, calcite, wollastonite, quartz, microcline, native copper, and copper and lead sulphides. The blue colouration of fluorcarletonite is attributed to the presence of carbonate anion radicals ($CO_3^{\bullet-}$). The presence of the various associated minerals creates a multicoloured appearance that can be creatively incorporated into jewellery and ornamental items.

The Journal of Gemmology, **38**(4), 2022, pp. 376–385, https://doi.org/10.15506/JoG.2022.38.4.376

Fluorcarletonite—$KNa_4Ca_4Si_8O_{18}(CO_3)_4F \bullet H_2O$—is a very rare and relatively new blue mineral (Figure 1), first described by Kaneva *et al.* (2020). It occurs together with charoite in the Severny District, which is hosted by the Malyy Murun massif, forming part of the Murun volcano-plutonic complex. The Murun complex is located in the north-western part of the Aldan Shield in Siberia, Russia, and covers an area of about 150 km^2. It consists of a large body of alkaline rocks showing potassium enrichment. The Malyy Murun massif has an extremely complex multiphase internal structure, and today there is no single generally recognised scheme for its formation (see, e.g., Rogova *et al.* 1978; Vladykin *et al.* 1983; Vorob'ev 2008). Similarly, the origin of charoitites (dominantly charoite-bearing rocks; Figure 2) within the massif has not been well established. The occurrence of charoite is associated with the widespread development of several unusual minerals, demonstrating the complex paragenesis and unique character of the mineralisation in the Malyy Murun massif.

Fluorcarletonite is the F-analogue of carletonite—$KNa_4Ca_4Si_8O_{18}(CO_3)_4(OH) \bullet H_2O$—a rare mineral that was first described by Chao (1971) and named after Carleton University in Ottawa, Canada. Fluorcarletonite and carletonite provide an example of anion exchange, where F is replaced by an OH group and vice versa depending on the conditions of formation.[1]

So far, the only known occurrence of carletonite is the Poudrette quarry, Mont Saint-Hilaire, Canada. It occurs as pale pink to bright blue prismatic crystals up to 6 cm long or as massive aggregates. Until the early 1990s, collectors' specimens of carletonite were available, but currently it is almost impossible to find an attractive sample for sale. Since the most productive area of the Poudrette quarry has been flooded (Pohwat & Cook 2015), it seems unlikely that additional new carletonite specimens will enter the market in the future. Carletonite has also been found in the peripheral parts of zoned grains of fluorcarletonite from the Malyy Murun massif (Kaneva *et al.* 2018, 2020), but single crystals of carletonite have not yet been found there.

According to Kaneva *et al.* (2020), fluorcarletonite is tetragonal (space group *P*4/*mbm*) with a uniaxial negative

[1] As noted by Kaneva *et al.* (2020), the International Mineralogical Association's formula for carletonite shown above is inconsistent with that given in the first description of the mineral. According to chemical data given by Chao (1971), the content of the anionic position is $F_{0.41}(OH)_{0.59}$. Thus, Chao (1972) gave the ideal formula for carletonite as $KNa_4Ca_4Si_8O_{18}(CO_3)_4(OH,F) \bullet H_2O$ (i.e. containing both OH and F in the anionic position).

Figure 2: An outcrop of charoite-bearing rock is seen here in the Malyy Murun massif. Fluorcarletonite locally occurs in association with charoite. Photo courtesy of V. Sychev (pictured).

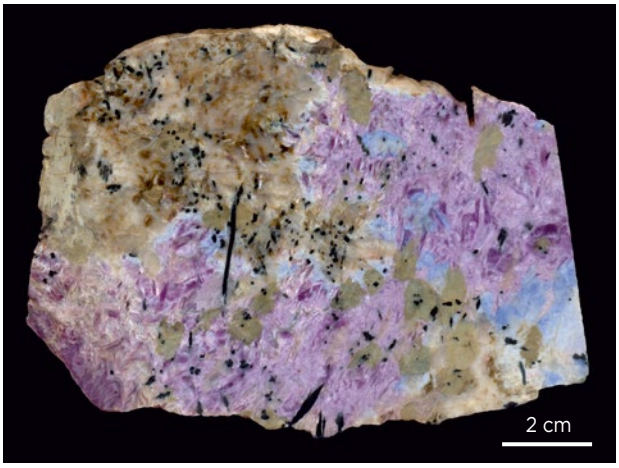

Figure 3: This polished slab of fluorcarletonite-bearing rock (12 × 9 cm) from the Malyy Murun massif shows a variety of associated minerals: aegirine (black), apophyllite-(KF) (brownish pink), charoite (purple), fluorcarletonite (blue) and pectolite (brownish green). Specimen from the collection of the Fersman Mineralogical Museum of the Russian Academy of Sciences, Moscow, Russia; photo by T. Radomskaya.

optic character. It is pale to bright saturated blue (Figure 3) and has a Mohs hardness of 4–4½. Commercial mining of this rare and attractive stone has just begun, and the material is expected to enter the jewellery market soon. Large, collector-quality transparent crystals of fluorcarletonite have not yet been found, but the massive material recovered to date has ornamental and decorative value. This article characterises the mineral assemblage in fluorcarletonite-bearing aggregates, and also provides chemical data, Raman spectra, visible-range transmittance spectra and colourimetric representations for fluorcarletonite.

MATERIALS AND METHODS

Among the samples examined for this study were four fluorcarletonite aggregates (mixed with varying amounts of associated minerals): a polished slab measuring 48.3 × 19.2 × 7.3 mm (Figure 1a), a polished thin section (approximately 40 µm thick), an oval cabochon that weighed 15.2 ct and measured 9.2 × 6.8 mm (Figure 1b), and a rock fragment left over from cutting the cabochon (Figure 1c). The textures and associated minerals in all four of these samples were examined using an Olympus BX-51 polarising microscope; both transmitted and reflected light were used to examine the thin section. The various minerals were identified according to their optical properties. In addition, several small grains of fluorcarletonite were used for different types of analyses, as described below.

Refractive indices were measured by the spot method on flat areas of the small fluorcarletonite grains, and the SG of these same samples was determined hydrostatically.

Chemical analyses of a single small grain of fluorcarletonite (mounted in epoxy) were performed using a JEOL JXA-8230 electron probe microanalyser (EPMA). The analyses were done in wavelength-dispersive mode under the following operating conditions: accelerating voltage = 20 kV, beam current = 15 nA, beam diameter = 10 µm, and count time = 10 s on peaks and 5 s on background. Standards used were albite (Na, Al), diopside (Ca, Si), ilmenite (Ti), pyrope (Fe), orthoclase (K) and fluorapatite (F).

Raman spectra of five small randomly oriented grains of fluorcarletonite—as well as a small grain of blue Canadian carletonite for comparison—were obtained using a WITec alpha300R confocal Raman spectroscopic system coupled with a frequency-doubled 532 nm Nd:YAG laser at room temperature. The spectra were recorded with a diffraction grating (1,800 grooves/mm) and a resolution of 2 cm^{-1}. The output power of the laser was 10 mW and the diameter of the focal spot on the sample was 5–10 µm. The backscattered Raman signal was collected with a Zeiss 50×/0.55 objective and a UHTS 300 spectrometer equipped with a Peltier-cooled, front-illuminated CCD camera. Signal acquisition time was 1 s for a scan of the entire spectral range (140–3700 cm^{-1}), and the signal was averaged over 100 scans. Crystalline silicon was used as a standard (Shendrik *et al*. 2021).

Transmittance spectra in the visible range (390–730 nm) were obtained from the same small grains of fluorcarletonite that were analysed by Raman spectroscopy. They were placed in a quartz tube and the spectra were recorded with a PerkinElmer Lambda 950 spectrophotometer equipped with an integrating sphere. The grains were then annealed at 100°C, 200°C, 300°C and 400°C to investigate the stability of the blue colour, and transmittance spectra were collected after each step. Heating took place in a muffle furnace in air for 20 minutes, and the temperature was controlled using a K-type thermocouple. To restore the colouration, irradiation was performed using an X-ray tube with a Pd anode operated at 40 kV and 20 mA for 30 minutes (dose rate of 104 grays) at room temperature. Colour fading to light was tested on some additional small grains of fluorcarletonite using a 150 W high-pressure Xe lamp with the samples positioned 20 cm away to avoid significant heating. The total time for fade testing was 12 hours, and transmittance spectra were collected during this process at four-hour intervals.

For both unheated and annealed fluorcarletonite, colourimetric representations were calculated from the transmittance spectra for daylight illuminant D with

4500 K colour temperature. The red, green and blue visual signals can be represented by the tristimulus values X, Y and Z according to spectral transmittance $S(\lambda)$, and are given in terms of the relative spectral intensity distribution of the 4500 K light source (expressed as $I(\lambda)$) for the standard observer:

$$X = A\int_{\lambda} S(\lambda)I(\lambda)\bar{x}(\lambda)d\lambda$$

$$Y = A\int_{\lambda} S(\lambda)I(\lambda)\bar{y}(\lambda)d\lambda$$

$$Z = A\int_{\lambda} S(\lambda)I(\lambda)\bar{z}(\lambda)d\lambda$$

where $\bar{x}(\lambda)$, $\bar{y}(\lambda)$ and $\bar{z}(\lambda)$ are the numerical description of the chromatic response of the observer according to the CIE 1931 model (Smith & Guild 1931). A is a constant value and d is the differential of the variable λ (wavelength). The chromaticity coordinates x and y were then calculated using the following formulae:

$$x = \frac{X}{X + Y + Z}$$

$$y = \frac{Y}{X + Y + Z}$$

RESULTS AND DISCUSSION

Mineral Assemblage and Paragenesis

Fluorcarletonite-bearing rock typically has a coarse-grained structure and a spotted appearance. In the examined samples, fluorcarletonite mainly occurred in association with purple fibrous charoite aggregates, brownish pink apophyllite-(KF), acicular prismatic black aegirine crystals and brownish green pectolite (Figures 1 and 3). Minor amounts of apatite, calcite, wollastonite, quartz, microcline, native copper, and copper and lead sulphides were also identified. Morphogenetic features and relationships between the various minerals allowed us to establish their paragenetic sequence of crystallisation, and each rock-forming mineral in the assemblage is described below in the approximate order of formation, followed by the accompanying sulphides and native copper.

Aegirine was one of the earliest minerals to form, occurring as uneven disseminations of euhedral and subhedral acicular black grains up to 3 cm long with a rhombic or rectangular cross-section (Figure 4a, b). In the thin section, the aegirine appeared brownish green in plane-polarised light. The aegirine contained small areas of apatite (Figure 4c), and sometimes grains of chalcocite were present (Figure 4d).

Pectolite was less euhedral and occurred as individual subhedral brownish to greenish grains (colourless in thin section) that were unevenly distributed (Figure 4e, f). Inclusions in the pectolite consisted of euhedral elongated aegirine and prismatic apatite.

Fluorcarletonite (Figure 4a, b) was anhedral with respect to aegirine and pectolite, and was present mainly in the form of unevenly distributed blue prismatic grains (colourless in thin section) up to 0.3 × 0.5 cm that formed clusters up to 0.7 × 1.5 cm. The intergrowth of fluorcarletonite and apophyllite-(KF) (Figure 4g) can locally produce pale blue to dark blue moiré patterns that are seen when the rock is viewed at a certain angle of incident light. The more fluorcarletonite is contained in such intergrowths, the more saturated the blue colour appears (e.g. Figures 1a, 1b and 3). The texture of the fluorcarletonite and apophyllite-(KF) intergrowths suggests their simultaneous crystallisation. In the fluorcarletonite, we occasionally found euhedral aegirine crystals, as well as numerous inclusions of small prismatic subhedral apatite grains (Figure 4g).

We found two generations of apophyllite-(KF). The first was represented by individual pale pink (colourless in thin section) anhedral segregations closely intergrown with fluorcarletonite, as described above. The second had an exogenous origin, in which the apophyllite-(KF) occurred as a secondary mineral after fluorcarletonite. This latter generation formed colourless, small, leafy grains located along cleavage cracks and grain boundaries of fluorcarletonite (Figure 4g).

Charoite formed purple aggregates (colourless in thin section) that occurred in two different textures: 'block' and 'fissile-crenulated'. Block charoite was represented by densely intergrown and parallel-columnar thin fibres elongated in one direction (Figure 4h, i, l). Each individual fibre was 0.5–1 cm long and 1–2 μm wide. Small aggregates of fissile-crenulated charoite were characterised by an acicular-fibrous texture, occasionally with a pinnate structure (Figure 4j, k). Small aggregates of block charoite of dark purple colour, up to 0.5–0.7 cm long and up to 0.3 mm wide, were surrounded by fissile-crenulated segregations of light lilac charoite with a silky lustre. The charoite aggregates occurred between those minerals that had formed earlier: pectolite, fluorcarletonite and apophyllite-(KF). Sometimes an ingrowth of fibres from a charoite aggregate penetrated into fluorcarletonite at the boundary of these two minerals (Figure 4j, k). Charoite was replaced in some places by brown wollastonite (Figure 4a, b, c and l).

Quartz was present in two forms. The first consisted of euhedral elongated crystals with a hexagonal cross-section, which formed vein-like clusters. The second was

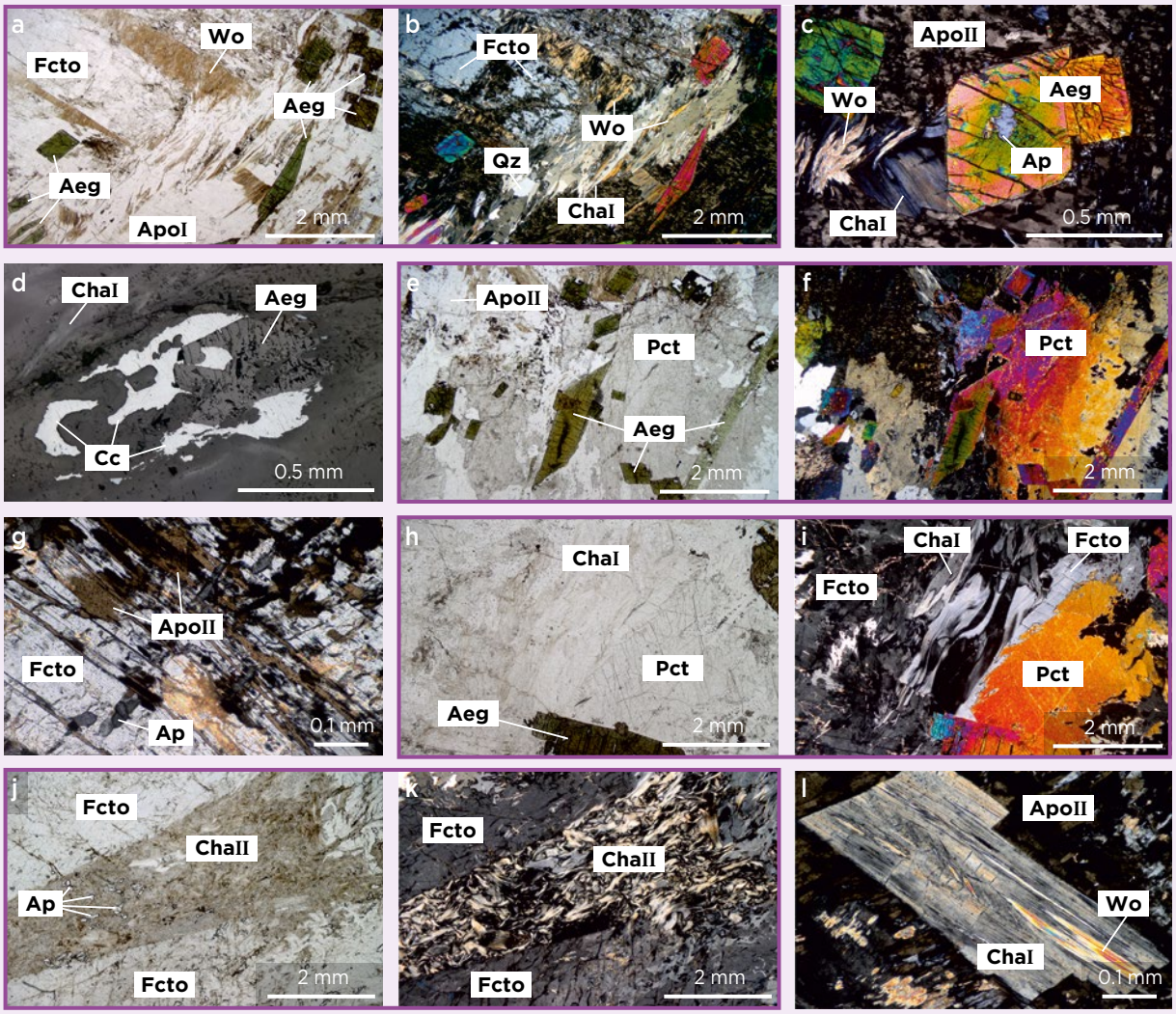

Figure 4: Thin-section photomicrographs illustrate the mineral associations in fluorcarletonite-bearing rock and their textural properties. Images **a–c** and **e–l** were taken in transmitted light using parallel polarisers (a, e, h and j) and crossed polarisers (b, c, f, g, i, k and l); purple outlines designate image pairs showing the same area in plane-polarised and cross-polarised light. Image **d** was taken with reflected light. Mineral abbreviations after Warr (2021): Aeg = aegirine, Ap = apatite, Apo = apophyllite (ApoI = primary apophyllite and ApoII = apophyllite after fluorcarletonite), Cc = chalcocite, Cha = charoite (ChaI and ChaII = 'block' and 'fissile-crenulated' charoite, respectively), Fcto = fluorcarletonite, Pct = pectolite, Qz = quartz and Wo = wollastonite. Photomicrographs by T. Radomskaya.

represented by micro-veinlets up to 10 mm long and 1.5 mm wide, filling cracks in fluorcarletonite and pectolite. The quartz veinlets contained numerous subhedral apatite grains, which often formed clusters that were elongated and curved along the quartz veinlet.

Apatite, as noted above, was found as inclusions in several of the minerals—pyroxene, pectolite, fluorcarletonite and charoite—and in the form of clusters in a quartz veinlet. Microcline was present in minor amounts as anhedral granular aggregates associated with quartz.

Sulphides (chalcocite, galena, digenite, idaite and covellite) and native copper typically occurred as rare isolated anhedral inclusions or intergrowths in the rock-forming minerals, including aegirine, pectolite, fluorcarletonite, apophyllite-(KF) and charoite. Chalcocite was most common (Figure 4d), and was often present together with galena, native copper, idaite, digenite and covellite. Galena sometimes formed intergrowths with chalcocite, but more often occurred as individual grains. Digenite was present as individual grains, always near chalcocite aggregates, and sometimes in intergrowths with chalcocite and idaite. Idaite formed scaly and rounded grains within digenite and chalcocite. Covellite was present as individual small grains, as well as in intergrowths with digenite. Native copper occurred as small segregations along the edges of grains of copper

sulphides and galena. The presence of native copper indicates reducing conditions during mineral formation.

In summary, the mineral paragenesis of fluorcarletonite-bearing aggregates is characterised by: (1) crystallisation of alkali silicates, quartz, apatite and microcline; (2) formation of copper and lead sulphides and native copper; and (3) the transformation of primary rock-forming minerals under supergene conditions that resulted in the growth of secondary apophyllite-(KF) and wollastonite.

Chemical Composition

Chemical data for a single grain of fluorcarletonite are presented in Table I. For comparison, the table also lists previously published analyses of fluorcarletonite from the Malyy Murun massif, as well as carletonite from Canada. The EPMA analyses obtained for this study revealed the presence of some chemical zoning in the fluorcarletonite grain, with areas containing lower contents of F corresponding to a carletonite composition (e.g. spot 5 in this study and spot 1 of Kaneva *et al.* 2018; see Table I). The average formula calculated from the analysed fluorcarletonite grain is $K_{1.05}Na_{3.94}Ca_{3.95}Ti_{0.02}Si_{7.99}Al_{0.01}O_{18}(CO_3)_{3.98}(F_{0.67}OH_{0.33}) \cdot 1.1H_2O$.

Raman Spectroscopy

The Raman spectra of fluorcarletonite and carletonite in the 140–3700 cm^{-1} spectral range are shown in Figure 5, and raw x,y data for fluorcarletonite are available in the online data depository on *The Journal*'s website. All five of the fluorcarletonite grains analysed showed the same Raman bands, with some variations in intensity (but not in peak position) according to the samples' orientation relative to the beam. The positions and relative intensities of most bands of fluorcarletonite are similar to those of carletonite. However, differences were found in the O–H stretching vibration region (1500–3700 cm^{-1}), in the

Table I: EPMA analyses of a fluorcarletonite grain from this study compared to published data (Kaneva *et al.* 2018, 2020) as well as to carletonite from Canada (Chao 1971).[a]

Oxides (wt. %)	Fluorcarletonite (this study)				Fluorcarletonite (Kaneva *et al.* 2018)				Fluorcarletonite (Kaneva *et al.* 2020; average values for each area)				Carletonite[b] (Chao 1971)	
	Spot 2	Spot 4	Spot 5	Spot 7	Spot 1	Spot 2	Spot 3	Spot 4	Area 1	Area 2	Area 4	Area 5	Pink	Blue
SiO_2	43.82	44.37	43.31	43.04	44.2	44.0	43.9	43.6	44.5	44.1	43.65	44.0	44.9	44.7
Al_2O_3	0.03	bdl	bdl	0.06	0.02	0.05	0.05	0.04	0.03	0.03	0.02	0.02	0.5	0.6
K_2O	4.38	4.63	4.40	4.41	4.4	4.4	4.5	4.45	4.5	4.4	4.6	4.54	3.28	3.31
Na_2O	10.96	10.78	10.84	10.88	11.1	10.7	10.6	11.0	11.1	11.1	11.1	10.9	10.23	10.64
CaO	19.53	20.15	20.22	20.20	20.0	19.9	19.7	20.1	20.1	19.6	19.8	20.2	19.92	19.97
MgO	bdl	bdl	bdl	bdl	0.01	bdl	0.04	0.02	0.01	bdl	0.04	0.02	0.09	0.13
FeO[c]	0.08	0.03	0.03	bdl	bdl	0.01	0.06	0.03	0.01	0.01	0.02	0.03	nd	nd
TiO_2	0.32	0.13	bdl	0.26	0.1	0.06	0.1	0.1	0.05	0.04	0.08	0.12	bdl	bdl
F	1.12	1.37	0.65	1.00	0.8	1.3	0.9	0.9	1.4	1.4	1.1	1.1	0.70	0.73
CO_2[d]	15.62	15.77	15.68	15.59	nc	nc	nc	nc	15.66	15.31	15.69	15.75	nc	15.2
H_2O[e]	2.5	2.2	2.8	2.5	nd	nd	nd	nd	2.19	2.13	2.41	2.39	0.70	4.14
–O=F	–0.64	–0.79	–0.37	–0.57	–0.34	–0.54	–0.38	–0.38	–0.57	–0.59	–0.44	–0.46	–0.29	–0.30
Total	97.72	98.64	97.56	97.63	80.29	79.88	79.47	79.86	98.92	97.53	98.07	98.61	80.03	99.12

[a] Abbreviations: bdl = below detection limit; nd = not determined; nc = not calculated.
[b] Data obtained by wet-chemical analysis.
[c] Total iron calculated as FeO.
[d] Calculated according to the principle of electroneutrality of the chemical formula.
[e] Determined by single-crystal X-ray diffraction data refinement in Kaneva *et al.* (2020).

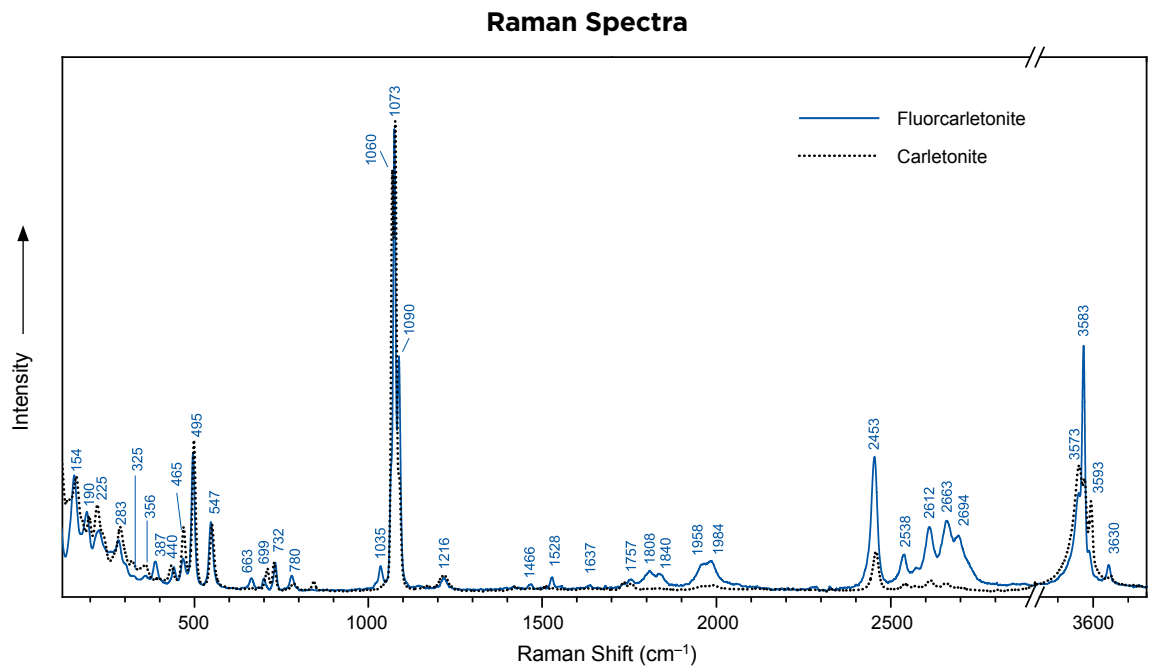

Figure 5: Most bands in the Raman spectra of fluorcarletonite display positions and relative intensities similar to those of carletonite, but with some significant differences.

650–800 cm^{-1} range and in the lattice vibration region (140–400 cm^{-1}), so the two minerals can be differentiated by Raman spectroscopy. The 3593 cm^{-1} band is less intense in fluorcarletonite than in carletonite due to the lower concentration of OH anions in fluorcarletonite. Other differences in the 1500–3700 cm^{-1} region are also evident, but their origins have not yet been studied.

The bands at 1035, 1073 and 1090 cm^{-1} are located in the region of ν_1 symmetric stretching modes of two non-equivalent CO_3 groups (Mysen & Frantz 1992). In addition, the band at 1035 cm^{-1} could be assigned to SiO_4 tetrahedra vibration according to our *ab initio* calculations. In carletonite, this band is shifted to the higher wavenumber region and overlaps with the intense 1073 cm^{-1} band. Therefore, the observed Raman bands could be a combination of Si–O and CO_3 stretching modes. The orientation of the CO_3 complex could be slightly different in fluorcarletonite and carletonite, thus accounting for differences in the 650–800 cm^{-1} region. The bands at 663, 699, 732 and 780 cm^{-1} are attributed to doubly degenerated in-plane bending modes of CO_3 (Koura *et al.* 1996). The *T*–O–*T* (where *T* = Si or Al tetrahedron) symmetric stretching modes are related to the bands at 440, 465, 495 and 547 cm^{-1} (Sykes & Kubicki 1996). The bands below 400 cm^{-1} could be assigned to the lattice modes.

Visible-Range Spectroscopy and Colour Stability

Figure 6 shows the transmittance spectra of the unheated and annealed fluorcarletonite samples, and raw x,y data for unheated fluorcarletonite are available in *The Journal*'s online data depository. In general, the broad absorption in the green-to-red spectral region is responsible for the blue colour of fluorcarletonite. It consists of a band at 690 nm with vibrational structures at 650, 620, 605 and 585 nm. According to Nassau *et al.* (1976) and Kaneva & Shendrik (2022), this broad absorption is attributed to carbonate anion radicals ($CO_3^{\bullet-}$; the dot means an unpaired electron). This anion has also been documented in deep blue Maxixe beryl and irradiated blue cancrinite. The absorption band in Maxixe beryl is located at 687–690 nm with vibrational structures at 645, 625 and 605 nm (Nassau *et al.* 1976; Adamo *et al.* 2008). In irradiated cancrinite, the $CO_3^{\bullet-}$ radical absorption is located at 675 nm with a vibrational side band at 645 nm (Shendrik *et al.* 2021; Kaneva & Shendrik 2022).

Our annealing experiments caused gradual bleaching of the blue colouration of fluorcarletonite, corresponding to a decrease in the broad absorption mentioned above (again, see Figure 6). Nearly all of the colour was bleached at 350–400°C. The blue colour could then be restored by irradiation.

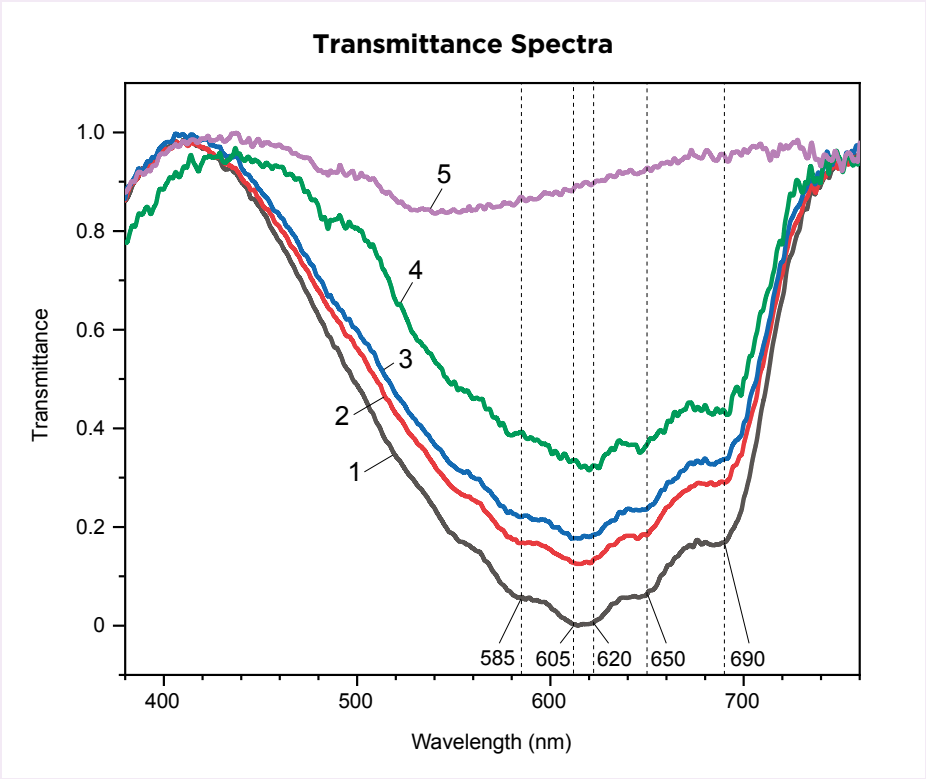

Figure 6: Transmittance spectra of fluorcarletonite were taken before and after annealing: 1 = unheated; 2 = annealed at 100°C; 3 = annealed at 200°C; 4 = annealed at 300°C; 5 = annealed at 400°C. The changes in spectral features are consistent with the loss of blue colour with progressive heating.

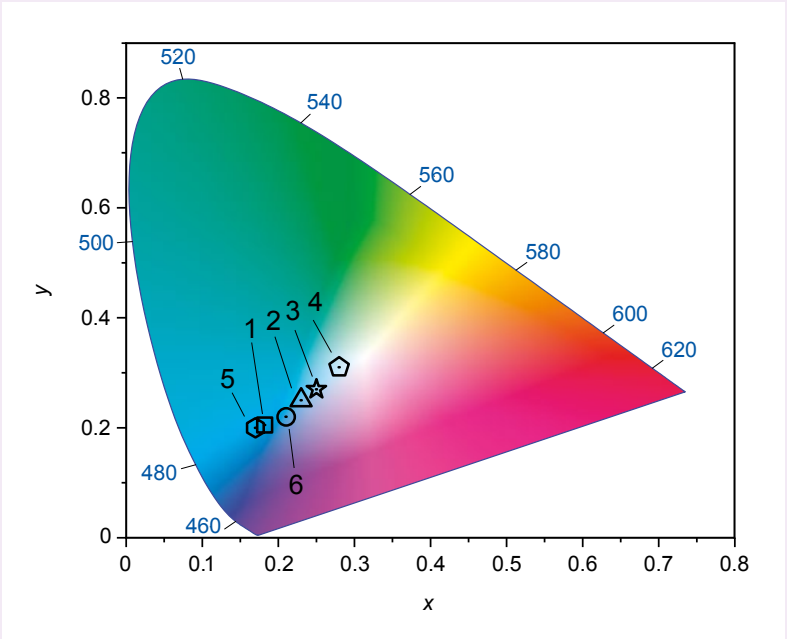

Figure 7: A CIE 1931 chromaticity diagram illustrates colourimetric representations of fluorcarletonite: 1 = unheated, 2 = annealed at 100°C, 3 = annealed at 200°C and 4 = annealed at 300°C. Shown for comparison are colourimetric representations for irradiated cancrinite (5; Kaneva & Shendrik 2022) and Maxixe beryl (6; Adamo *et al.* 2008), which also owe their colouration to carbonate anion radicals ($CO_3^{\bullet-}$).

Fade testing with the Xe lamp did not cause any significant change in colouration after 12 hours of exposure. Therefore, the blue colour of fluorcarletonite is more stable than that typically exhibited by Maxixe beryl (Adamo *et al.* 2008; Cooper *et al.* 2020).

Colourimetric Representations

Figure 7 depicts a CIE 1931 colour-space chromaticity diagram with colourimetric representations plotted for fluorcarletonite, irradiated cancrinite and Maxixe beryl, all of which contain $CO_3^{\bullet-}$ radicals. The most saturated

colour belongs to irradiated cancrinite (Kaneva & Shendrik 2022), but fluorcarletonite plots very close to it. Maxixe beryl has a less intense blue colour, which typically fades on exposure to light (Adamo *et al.* 2008). The diagram also shows the bleaching of fluorcarletonite caused by heating.

CONCLUSION

Fluorcarletonite is currently known only from the Malyy Murun massif in Siberia, Russia, where it is mined together with charoite. Therefore, its production will likely depend on that of charoite. The popularity of charoite as an ornamental and jewellery material is increasing, although presently the government of the Sakha Republic imposes a limit on its extraction (100 tonnes per year). It is difficult to predict the future production of fluorcarletonite due to the discontinuous nature of the mineralised veins and the labour-intensive methods of exploration and production.

Fluorcarletonite-bearing rock is easily polished. However, when processing and manufacturing decorative items, the discolouration of fluorcarletonite at temperatures above 300°C, as described in this article, should be taken into account. One possible limitation to the use of fluorcarletonite as a jewellery material is its softness (Mohs 4–4½). However, this may be partially offset by the presence of harder impurity minerals such as charoite (Mohs 5–6).

REFERENCES

Adamo, I., Pavese, A., Prosperi, L., Diella, V., Ajò, D. & Smith, C.P. 2008. Aquamarine, Maxixe-type beryl, and hydrothermal synthetic blue beryl: Analysis and identification. *Gems & Gemology*, **44**(3), 214–226, https://doi.org/10.5741/gems.44.3.214.

Chao, G.Y. 1971. Carletonite, $KNa_4Ca_4Si_8O_{18}(CO_3)_4(F, OH) \cdot H_2O$, a new mineral from Mount St. Hilaire, Quebec. *American Mineralogist*, **56**(11–12), 1855–1866, http://www.minsocam.org/ammin/AM56/AM56_1855.pdf.

Chao, G.Y. 1972. The crystal structure of carletonite, $KNa_4Ca_4Si_8O_{18}(CO_3)_4(F, OH) \cdot H_2O$, a double-sheet silicate. *American Mineralogist*, **57**(5–6), 765–778, http://www.minsocam.org/ammin/AM57/AM57_765.pdf.

Cooper, A., Sun, Z., Hand, D. & Renfro, N. 2020. Gem News International: Unusual violet Maxixe beryl. *Gems & Gemology*, **56**(3), 439–440.

Kaneva, E. & Shendrik, R. 2022. Radiation defects and intrinsic luminescence of cancrinite. *Journal of Luminescence*, **243**, article 118628 (5 pp.), https://doi.org/10.1016/j.jlumin.2021.118628.

Kaneva, E., Radomskaya, T.A., Suvorova, L., Sterkhova, I.V., Kozlov, A. & Mitichkin, M. 2018. Second occurrence of carletonite, Murun massif (Russia): SCXRD, powder XRD, EPMA, FTIR and TG-DSC study. *Scientific Research Abstracts: 3rd International Conference on Applied Mineralogy and Advanced Materials*, **9**, 40.

Kaneva, E., Radomskaya, T., Suvorova, L., Sterkhova, I. & Mitichkin, M. 2020. Crystal chemistry of fluorcarletonite, a new mineral from the Murun alkaline complex (Russia). *European Journal of Mineralogy*, **32**(1), 137–146, https://doi.org/10.5194/ejm-32-137-2020.

Koura, N., Kohara, S., Takeuchi, K., Takahasi, S., Curtiss, L.A., Grimsditch, M. & Saboungi, M.L. 1996. Alkali carbonates: Raman spectroscopy, ab initio calculations, and structure. *Journal of Molecular Structure*, **382**(3), 163–169, https://doi.org/10.1016/0022-2860(96)09314-3.

Mysen, B.O. & Frantz, J.D. 1992. Raman spectroscopy of silicate melts at magmatic temperatures: Na_2O-SiO_2, K_2O-SiO_2 and Li_2O-SiO_2 binary compositions in the temperature range 25–1475°C. *Chemical Geology*, **96**(3–4), 321–332, https://doi.org/10.1016/0009-2541(92)90062-a.

Nassau, K., Prescott, B.E. & Wood, D.L. 1976. The deep blue Maxixe-type color center in beryl. *American Mineralogist*, **61**(1–2), 100–107, http://www.minsocam.org/ammin/AM61/AM61_100.pdf.

Pohwat, P.W. & Cook, R.B. 2015. Connoisseur's Choice: Carletonite, Mont Saint-Hilaire, La Vallée-du-Richelieu RCM, Montérégie, Québec, Canada. *Rocks & Minerals*, **91**(1), 48–53, https://doi.org/10.1080/00357529.2016.1099133.

Rogova, V.P., Rogov, Yu.G., Drits, V.A. & Kuznetsova, N.N. 1978. Charoite – A new mineral and a new jewellery stone. *Zapiski Vsesojuznogo Mineralogicheskogo Obshchestva*, **107**, 94–100 (in Russian).

Shendrik, R., Kaneva, E., Radomskaya, T., Sharygin, I. & Marfin, A. 2021. Relationships between the structural, vibrational, and optical properties of microporous cancrinite. *Crystals*, **11**(3), article 280 (19 pp.), https://doi.org/10.3390/cryst11030280.

Smith, T. & Guild, J. 1931. The C.I.E. colorimetric standards and their use. *Transactions of the Optical Society*, **33**(3), 73–134, https://doi.org/10.1088/1475-4878/33/3/301.

Sykes, D. & Kubicki, J.D. 1996. Four-membered rings in silica and aluminosilicate glasses. *American Mineralogist*, **81**(3–4), 265–272, https://doi.org/10.2138/am-1996-3-401.

Vladykin, N.V., Matveeva, L.N., Bogacheva, N.G. & Alekseev, Yu.A. 1983. New data on charoite and charoitic rocks. *In*: Glazunov, O.M. (ed) *Mineralogy and Genesis of Gemstones of East Siberia*, Nauka Publishing, Novosibirsk, Russia, 41–56 (in Russian).

Vorob'ev, E.I. 2008. *Charoite*. Academic Publishing House 'Geo', Novosibirsk, Russia, 140 pp. (in Russian).

Warr, L.N. 2021. IMA–CNMNC approved mineral symbols. *Mineralogical Magazine*, **85**, 291–320, https://doi.org/10.1180/mgm.2021.43.

The Authors

Dr Ekaterina Kaneva*, Dr Tatiana Radomskaya and Dr Roman Shendrik
Vinogradov Institute of Geochemistry SB RAS, 1a Favorsky Str., Irkutsk 664033, Russia
and
Sidorov Mineralogical Museum, Irkutsk National Research Technical University, 83 Lermontov Str., Irkutsk 664074, Russia
*Email: kev604@mail.ru

Acknowledgements

The authors are grateful to Sergey Slepnyev and Andrey Romanchenko of Charoite Ltd (Neryungri, Sakha Republic, Russia) for the samples provided for the study. We thank assistant professor Dr Tatiana Anisimova and her students in the Department of Jewellery Design and Technology at the Irkutsk National Research Technical University, who fashioned the cabochon during their classes. We also thank Mikhail Mitichkin and Ludmila Suvorova for their assistance with sample preparation and EPMA analyses. This study was carried out using the facilities of the Centers for Collective Use (Center for Isotopic-Geochemical Investigations) at the Vinogradov Institute of Geochemistry SB RAS.

Editor's Note

The lead author is the discoverer of fluorcarletonite (Kaneva *et al.* 2020), and she has declared the following about the present article: 'Payment for the study was made from the personal own funds of the authors. The research work presented in the manuscript was carried out outside the framework of any state or foundation funding, but only out of my personal interest in telling the public, interested in gemmology, about this new gemstone.' To be clear, the aim of this article is to bring forth new gemmological discoveries, and not to promote the trading or production of a Russian gem material.

Conferences

6TH MEDITERRANEAN GEMMOLOGICAL AND JEWELLERY CONFERENCE

The 6th Mediterranean Gemmological and Jewellery Conference (MGJC) took place 12–14 August 2022 in Thessaloniki, Greece. The 45 participants came from 13 countries spanning four continents. The conference was organised by **Branko Deljanin** (CGL Canadian Gemlab, Vancouver, Canada), **George Spyromilios** (Independent Gemological Laboratory, Athens, Greece) and **David Lazić** (GemHunters, Belgrade, Serbia).

On day one, **Travis Lejman** (Gemological Appraisal Laboratory of America, New York, New York, USA) led a workshop titled 'Opal Testing and Value' that focused on opal types, formation, localities, treatments, properties, grading and valuation, with a vast array of examples and time for hands-on inspection. The quality factors of different types of opal and their pricing were covered, while reviewing items discussed in Paul Downing's 2002 *Opal Identification & Value* book.

Branko Deljanin led a workshop titled 'Identification of Coloured Diamonds', with assistance from **George Spyromilios**. It covered methods to separate natural from synthetic coloured diamonds, treatments of HPHT- and CVD-grown diamonds, and a practical hands-on workshop using visual characteristics, fluorescence, birefringence and spectroscopy (Figure 1). Grading of coloured diamonds using the *Munsell Book of Color* and a master set were reviewed, and included pink diamond masters.

On day two, **Dr Lore Kiefert** (Gemological Consulting, Heidelberg, Germany) offered a 'Gem Country of Origin' workshop for the first time at the MGJC. Part 1 covered emeralds from Colombia, Zambia, Zimbabwe, Pakistan, Russia and Ethiopia, providing a comparison of their inclusions (including the overlapping presence of three-phase inclusions in emeralds from some localities). Part 2 covered rubies from Myanmar (Mogok and Mong Hsu) compared to stones from Mozambique, Thailand, Tajikistan and Vietnam. Part 2 also included a comparison of sapphires from Kashmir to those of Myanmar, Sri Lanka, Madagascar and stones of magmatic origin.

Dr Kiefert opened the gem-session lectures with the same topic, pointing out how similar properties can lead to confusion and that, to date, it is not always possible to distinguish the geographical origin of all sapphires. Also, some relatively new magmatic sapphire sources have been found in Madagascar and Ethiopia. Overlaps in gem characteristics provide a continuous challenge for gemmological laboratories, and it has been necessary to upgrade instrumentation to more high-cost equipment such as LA-ICP-MS. **Dr Stefanos Karampelas** (Laboratoire Français de Gemmologie, Paris, France) discussed the science behind the origin determination of coloured stones and natural pearls. He pointed out that even while using sophisticated instruments there are limitations because geological, biological and political borders are rarely the same. Gems of high quality that lack characteristic inclusions can be especially challenging.

Jeffery Bergman (Eighth Dimension Gems, Bangkok, Thailand) covered the history, origin, treatments, marketing and pricing of spinel. In addition to Mogok and Namya (or Nanyaseik) in Myanmar, spinel is mined in

Figure 1: During the MGJC's coloured diamond workshop, the author observes a treated pink diamond with an OPL spectroscope. Other participants shown are Mike Burnette (USA), Karolina Sobolewska (Poland) and David Weinstein (Israel). Photo by Branko Deljanin.

Figure 2: MGJC round-table participants include (from left to right) Branko Deljanin, Ioannis Alexandris, Jeffery Bergman, Travis Lejman and Dr Lore Kiefert, with moderator Yianni Melas standing. Photo by David Lazić.

Afghanistan, Madagascar, Sri Lanka, Tanzania, Tajikistan, Thailand and Vietnam. In Myanmar, where some of the most beautiful colours are found, spinel was recognised as a separate gem type as early as 1587. Heating experiments on spinels show no or only limited improvement to clarity and colour, and the treatment can easily be detected by microscopy and Raman/PL spectroscopy. **Dr Matthias Krismer** and **Dr Michael Schlamadinger** (Swarovski, Wattens, Austria) spoke on responsible sourcing and marketing of coloured stones. They explained that in the past decade, companies in mineral supply chains have been put under increasing pressure due to public interest in responsible business behaviour. Companies are being asked to provide traceability, prove and disclose the origin of raw materials, and account for their social and environmental footprint.

Day three included a workshop led by **Branko Deljanin** and **George Spyromilios** on the identification of colourless diamonds. Participants examined type Ia, Ib, IIa and IIb diamonds (natural, treated and synthetic) with various tools, including microscopes, mini-UV lamps, portable polariscopes and the EXA Natural Diamond Detector. New CVD-grown diamond samples were tested that do not show any diagnostic features under long- and short-wave UV radiation, requiring the use of cross-polarised filters and advanced instrumentation.

Then the lectures resumed, with **Elena Deljanin** (Gemmological Research Industries, Vancouver, Canada) describing how the study of the morphological features and surface characteristics of rough diamonds are influenced by their geological conditions of formation and deposition, and thus can give indications about their geographical origin. **Branko Deljanin** then provided a comparison of portable instruments used for screening and identifying laboratory-grown diamonds. After evaluating 11 such devices priced at less than USD10,000, he recommended that diamond-trade professionals not rely on just a single instrument. Instead, two or (preferably) three of them from different device groups should be used. In rare cases, advanced desk-model instrumentation may be necessary for robust identification. **John Chapman** (Gemetrix, Perth, Australia) delivered an online lecture on diamond testing. While long- and short-wave UV fluorescence are useful for determining if a diamond is natural or synthetic, in some instances this is insufficient due to low luminescence intensity or overlap in interpretations. Additional methods are then desirable, such as observing birefringence patterns of loose diamonds through crossed polarisers using the StrainView device. However, even these observations can be inconclusive, making photoluminescence and absorption spectroscopy necessary to confirm a diamond's identity.

Ioannis Alexandris (Gemolithos, Munich, Germany) spoke on the importance of antique jewellery in today's marketplace. Greater numbers of people are collecting antique jewellery, and it is critical that they have the knowledge needed to confidently invest in this important sector of the market. Such expertise includes understanding the styles, designs, terminology, available materials, gem materials, cutting techniques and manufacturing methods, along with some awareness of world politics, events and other influences during the era of the jewellery in question.

The day ended with a round-table discussion titled 'Origin of Gems and Grading Opinions on Diamonds when Gem Labs Agree to Disagree', moderated by **Yianni Melas** (Gemexplorer, Limassol, Cyprus) with panellists **Ioannis Alexandris**, **Jeffrey Bergman**, **Dr Lore Kiefert**, **Branko Deljanin** and **Travis Lejman** (Figure 2). Despite tremendous technological advancements, there remains

a small percentage of gems, predominantly sapphires, for which major gem labs disagree on origin determination. For example, in 2015 Christie's Hong Kong sold a sapphire with three lab reports containing three different opinions of origin (Madagascar, Sri Lanka and Myanmar). There are also differences in the quality grading of diamonds between major labs. When it comes to coloured diamonds, variations in hue (brown vs pink vs red) or intensity (Fancy vs Intense vs Vivid) can mean huge differences in value.

Four posters were also presented at the conference: (1) 'Gem minerals of Serbia for collectors' by David Lazić and Branko Deljanin; (2) 'Rubies from the Prilep dolomitic marble in northern Macedonia' by Dr Miha Jeršek, Branko Deljanin and David Lazić; (3) 'Spectroscopic study of Egyptian emeralds' (awarded first place by votes of participants) by Maria Nikopoulou, Dr Stefanos Karampelas, Dr Eloïse Gaillou, Ugo Hennebois, Farida Maouche, Annabelle Herreweghe, Prof. Lambrini Papadopoulou, Prof. Vasilios Melfos, Prof. Nikolaos Kantiranis, Dr Didier Nectoux and Aurélien Delaunay; and (4) 'Serbian gemstone deposits' by Dr Zoran Miladinović.

A post-conference tour took participants to the municipality of Prilep, North Macedonia, where they visited a marble mine which is also a source of ruby. The following day they toured a lapidary and metalsmith workshop that focuses on the cutting of Macedonian ruby. They also visited the home of a local mineral collector to view his world-class collection of rare minerals from North Macedonia. A private tour was also given at the natural history museum in Skopje, with an emphasis on their mineral collection. The group then went to the Rudnik Pb-Zn-Ag mine in Serbia and toured the processing plant. David Lazić then guided a gem hunt for quartz, followed by a visit to the home of a local gem collector to see his impressive collection of Serbian minerals. The tour ended in Belgrade, the capital of Serbia, where participants visited the museum of the Faculty of Mining and Geology at the University of Belgrade.

Branko Deljanin will host a BrankoGems Conference in July 2023 in Brisbane, Australia, and the next MGJC will take place in May 2024 in Italy/Slovenia.

Paula A. Fox (paulafox@paulafoxappraisers.com)
Paula Fox & Co. LLC
Phoenixville, Pennsylvania, USA

23RD FEEG SYMPOSIUM

The 23rd symposium of the Federation for European Education in Gemmology (FEEG) was organised by the Institut National de Gemmologie (ING) in Paris, France, and celebrated the 25th anniversary of the Federation. The event took place on 3 September 2022 at the Institut du Monde Arabe (Arab World Institute) and was attended by 217 people.

Charlotte Carrard (ING, Paris) kicked off the symposium, introducing ING and its role within the Federation as a founding member. Their gemmology courses are attended by 500 students each year, and most of the gemmological professionals in France have received their training at ING. **Dr Alessandra Di Mariano Simoncini** (Escola de Gemmologia, Universitat de Barcelona, Spain) spoke on behalf of **Dr Joaquim M. Nogués Carulla**, former president of FEEG. The main goal of FEEG is to promote excellence in gemmological training. The idea came from the Erasmus Programme, which was launched in European universities in 1987 as a fundamental basis to improve university goals. The harmonisation of basic training is essential, promoting FEEG and gemmological knowledge in the European community, especially in those countries with no FEEG members.

As the current president of FEEG, **this author** welcomed the delegates and special guests, and expressed gratitude to ING for hosting the conference in line with the highest standards of international events. There are many challenges in gemmological education, as today's world is vastly different from that of 25 years ago when FEEG started. The pace of change is accelerating, with increasing globalisation. We are confronted with an explosion of information, and there is a growing need to serve an increasing network of gem enthusiasts and jewellery professionals throughout the European continent. FEEG will have to adapt its teaching to a greater diversity of students, expand its number of teaching centres and continue to be innovative.

Noora Jamsheer (Bahrain Institute for Pearls and Gemstones, Manama, Bahrain) explained that at the end of the 1800s, the Gulf region produced 80% of the world's pearls, which were used in jewellery made by Cartier, Tiffany and others. She pointed out that, for such activity to survive and grow from 1800 BCE to 1910 CE, the industry structure had to be well developed and mature. The Great Depression, World War I and the entrance of cultured pearls into the market all impacted pearl

demand. Currently, markets are starting to emerge from the pandemic, but recession fears and the Russian invasion of Ukraine are hindering consumer confidence. Conferences such as FEEG are valuable for exchanging knowledge and exploring best practices that aim to protect consumer confidence in our industry, which is essential to sustain its growth.

Rui Galopim de Carvalho (CIBJO and Portugal Gemas Academy, Lisbon, Portugal) presented a gemmological study of the Portuguese crown jewels at the Ajuda National Palace, Lisbon. The palace started as a natural history museum, and much of the gold, diamonds and gemstones originated from Brazil, a former Portuguese colony. The gold was mined from alluvial deposits in Minas Gerais State, and diamonds were found in the same sediments. One of the stones on display is the famous Braganza 'diamond', reported as weighing 1,680 old carats (actually 342 g), which subsequently was proven to be beryl (aquamarine). The collection has the largest historical Brazilian diamond crystal (35.8 ct) on public display in Europe, as well as more than 22,000 gems, of which diamond is the most numerous (86%). Others include emerald, ruby, sapphire, spinel, chrysoberyl, quartz and biogenic gem materials.

Dr J. C. (Hanco) Zwaan (Netherlands Gemmological Laboratory, Naturalis Biodiversity Center, Leiden) elaborated on the need for honest disclosure and proper terminology, as his laboratory has been confronted with various examples of fake news and odd certificates. He mentioned serpentine and marble being misrepresented as jade, dyed soapstone sold as pink opal, 'heated' emerald and a sapphire clarity graded VVS_1. He reminded the new graduates that gemmological knowledge is crucial and must be used in an honest way.

Dr Reem Al-Mealla (Bahrain Institute for Pearls and Gemstones) explained that ecological changes have been felt on a global scale as a consequence of climate change. Shifting environmental conditions coupled with human activities strongly influence the growth performance of pearl oysters and impact pearl formation. Bahrain's northern offshore pearl oyster beds (locally called *hayrat*) are known for their uniqueness and pearl production, which earned them a UNESCO World Heritage Site title. In 2012, a scientific study was conducted to determine the status of these pearl oyster beds by investigating the abundance and size of the molluscs in addition to pearl yield. Nearly ten years later (2021), a second study was conducted to detect temporal changes. The preliminary results indicate the number of oysters increased in 2021 vs 2012 with no significant change in the incidence of pearls, and the population shifted from older to younger molluscs based on shell length.

Dr Olivier Segura (Figure 3; School of Jewelry Arts, Paris) described a 910 ct diamond, known as the Lesotho Legend, and how it was cut. Lesotho is situated on the Archean-age Kaapvaal craton of southern Africa, and the diamonds found there range from 1 billion to 3.3 billion years old. The Letšeng mine in Lesotho covers two kimberlite pipes and numerous kimberlite dykes, and its diamonds are unusual for their dodecahedral form and high percentage of type IIa specimens. The mine has produced some of the world's largest diamonds in the past decade. The Lesotho Legend was mined there in January 2018 and is the fifth-largest rough diamond ever found. It was acquired by Van Cleef & Arpels and cut by Diamcad in Antwerp into 67 stones totalling 441.75 carats (nearly half the weight of the rough). The largest one weighs 79.35 ct.

Dr Ewa Wagner-Wysiecka (Gdańsk University of Technology, Gdańsk, Poland) gave an overview of the identification of natural, modified and pressed amber (succinite). The talk started with a description of Baltic amber, its varieties, and the terminology and definitions used by the International Amber Association. She then focused on the most effective gemmological tests to classify succinite. Methods used must be non-invasive, non-destructive, fast, easily available and inexpensive. Microscopy and mid-infrared spectroscopy are the most useful. The relationship between the position and the relative intensities of diagnostic bands in mid-infrared spectra allow the identification of amber that has been subjected to modification.

Dr Emmanuel Fritsch (Institut des Matériaux Jean Rouxel and University of Nantes, France) discussed

Figure 3: At the FEEG symposium, Dr Olivier Segura describes the Lesotho Legend while holding a model of this 910 ct diamond. Photo © Jallal Seddiki.

Figure 4: New FEEG diploma holders gather with CIBJO president Dr Gaetano Cavalieri (centre, blue suit), Dr Ilaria Adamo (president of the FEEG Examination Committee) and Guy Lalous. Photo © Jallal Seddiki.

two types of empty inclusions in gem materials: dissolved dislocations and rose channels. He explained that a dislocation is a crystallography-controlled discontinuity of the crystal lattice, specifically a zone of low electron density with defective bonding. As such, dissolution is made easier. Dissolution starts as etch pits, and the process occurs very quickly along dislocations. Dissolved dislocations have been documented in about 20 gem species. In addition, hollow features called rose channels may appear where two twin lamellae meet. Rose channels can form by deformation twinning, mostly at the intersection of twin lamellae, which creates vacancies. The vacancies often migrate to form a hollow channel. Rose channels have so far been found only in diamond, corundum and calcite.

Dr Tom Stephan (German Gemmological Association, Idar-Oberstein, Germany) gave a gemmological overview of the beryl group, covering crystal structure, colour causes, treatments and varieties. In addition to emerald, aquamarine is one of the most important varieties of the beryl group. Aquamarine is named after the colour of seawater and is strongly desired for its light pastel greenish blue to blue colour. 'Santa Maria' aquamarine is considered the best quality, and is named after a locality in Brazil where specimens were discovered in 1924 (Santa Maria de Itabira in Minas Gerais State). The presentation also included colour mechanisms and heat treatment of Fe-bearing beryl, and the irradiation of Maxixe-type beryl.

The evening of 3 September marked the FEEG diploma ceremony (Figure 4), which celebrated 144 new graduates. The ceremony was opened by **Dr Ilaria Adamo** (Italian Gemmological Institute, Milan, Italy). The graduation address was given by **Dr Gaetano Cavalieri** (CIBJO, the World Jewellery Confederation, Milan, Italy), who spoke about education being vital for the industry in a business that is driven by passion. The new graduates, through their diplomas, represent the very essence of the industry as they show by example their passion for gems and jewellery.

The next FEEG symposium will be held in Barcelona, Spain, on 2 September 2023.

Guy Lalous (guy.lalous@outlook.com)
Leuven, Belgium

2ND DANISH GEMMOLOGICAL SOCIETY SYMPOSIUM

The Danish Gemmological Society held its second symposium in Copenhagen on 1–2 October 2022 at the beautiful Odd Fellow Palæet, one of Copenhagen's historic buildings in the centre of the city. The Rococo-style mansion was built in 1755 as a private home that now belongs to the local branch of the Independent Order of Odd Fellows. The symposium featured five main speakers (Figure 5), and over two days the delegates were treated to a wide variety of subjects of interest to gemmologists and jewellers.

The society's president, **Niels Ruddy Hansen**, opened the symposium with a speech of welcome, and then introduced **Dr J. C. (Hanco) Zwaan** (Netherlands Gemmological Laboratory, Naturalis Biodiversity Center, Leiden), who spoke about demantoid from Madagascar, including differences from those of other sources (e.g. Russia) and how they can usually be distinguished by their inclusions.

It is customary at the Danish symposia for the speakers to give more than one talk. Some go into more detail about their subject, while others speak on totally different topics. Because one of the speakers had to cancel at the last minute, Dr Zwaan generously gave three talks over the two days. His second one was a fascinating lecture on the factors that shape 'System Earth', and what it takes to form minerals and gems. For his third presentation, he described issues being faced in the laboratory today. Among these are the many fakes that are sold online with bogus certifications, such as dyed quartz masquerading as emerald. He also spoke about a rare dark-coloured pearl examined recently in his laboratory and the challenges with identifying its origin.

Sean Gilbertson (Gemfields Group Ltd, London) gave an update on the extensive artisanal ruby and emerald mining activities in Mozambique and Zambia respectively, and explained how the Gemfields umbrella benefits local communities. In his second talk, on 'gemethics', he enlarged on the subject and spoke about the practices that can impede the development of mines and detract from their value, thus negatively impacting local communities and damaging the ecosystem (i.e. by destroying the land and producing greenhouse gases). He explained how, when mines are organised and legal, resources are optimised and squandering of those assets is minimised. The miners and their communities benefit from improved health care and education, and the environment is protected. This in turn benefits the host country, not least by the payment of taxes.

Dr Jack Ogden (London) also gave two talks, both with a historical theme: gem setting in antiquity and the early use of diamonds in jewellery. Early gems were often not cut to any specific shape or size, but were polished while maximising weight. Settings, therefore, had to be made to fit around them. Diamonds were no exception, except that they could not even be polished until medieval times. As a result, they lacked brilliance but were nonetheless highly prized, and were imitated using rock crystal as far back as Roman times. However, diamond 'chips' were employed for cutting and drilling other gem materials, and their use in this way can be traced back at least as far as about 600 BCE.

'Greasy Business' was the title of the first talk by **Richard Hughes** (Lotus Gemology, Bangkok, Thailand). This referred to the increasingly frequent occurrence of gemstones that have been oiled to enhance their appearance. Emerald is no longer the only gem treated in this way, but also ruby, sapphire, spinel, tourmaline and more. Perhaps the biggest problem is with Burmese rubies, which today all seem to be oiled. Methods of testing were explained, although some laboratories are not following such procedures, so it is probable that there are many stones on the market that are not quite what they seem. Hughes has been studying Chinese jade for about four decades, and his second talk was about the 8,000-year history of jade in that country, including the reasons why it has been so highly esteemed and had such symbolism there. In addition, he covered the historical sources of jade

Figure 5: Danish Gemmological Society Symposium speakers and conference committee members gather for a photo. Back row (left to right): Francoise Delvaux (committee member), Vincent Pardieu, Else-Marie Scherning (committee member), Lone Bøgh Nielsen (committee member), Richard Hughes, Dr Jack Ogden, Maggie Campbell Pedersen and Eva Dybkjær (committee member). Front row (left to right): Sean Gilbertson, Dr J. C. (Hanco) Zwaan and Niels Ruddy Hansen. Photo courtesy of Niels Ruddy Hansen.

and the renewed interest in jade carving that started at the end of the last century. He also stepped in to give a third talk, on inclusions and how vital they are to gem identification.

Vincent Pardieu (VP Consulting, Manama, Bahrain) covered the social and environmental aspects of small-scale mining, where criminality is rife. Anyone who is seen to be successful can quickly become a target of crime. Small-scale independent miners are very much at risk of theft and harm, but even those in organised groups can be vulnerable, so many miners find it wise to remain anonymous and low key. Pardieu also described so-called gem paintings. This art form started in Jaipur, India, a long time ago, and is now being done by small-scale miners to make use of low-value gem material for their economic benefit. Run as a community enterprise, gem painting employs many people, including those who sort and grind the stones, the designers, the 'painters' (who can produce any picture, from attractive patterns to copies of the Mona Lisa) and the sellers.

Before closing the Symposium, **Niels Ruddy Hansen** said a few words together with **this author** on 'how to become a gemmologist', a subject which had been discussed over the weekend and was of great interest to delegates who were considering getting qualifications to help with the next step in their careers.

Maggie Campbell Pedersen FGA
(info@maggiecp.com)
London

CANADIAN GEMMOLOGICAL ASSOCIATION CONFERENCE

The 2022 Canadian Gemmological Association (CGA) Gem Conference took place on 21–23 October in Vancouver, British Columbia, Canada. Sixty-six people attended, representing six countries (Canada, Iran, Monaco, South Africa, UK and USA), although many participants cancelled due to COVID-19.

CGA president **Donna Hawrelko** opened the conference, and she then asked various CGA staff and students to take turns introducing the speakers. **Duncan Parker** (Dupuis Fine Jewellery Auctioneers, Toronto, Ontario, Canada) described ancient literature on natural vs artificial gems, including early crystal growth experiments that took place nearly 200 years ago. He mentioned that the first synthetic rubies were sold in 1889 at the Exposition Universelle in Paris, France. Then he recounted the history of efforts to synthesise diamond, culminating with the first gem-quality production by General Electric in 1970.

Mark Cullinan (Cullinan Diamonds, Monaco) surveyed the history, marketing and pricing of diamond, and also reviewed the exceptional properties that make it incredibly useful for a wide variety of industrial and technological applications (Figure 6). He also recounted the history of the 3,106 ct Cullinan diamond, the largest-known gem-quality rough stone that was found by his great-grandfather Sir Thomas Cullinan at the Premier (now Cullinan) mine in South Africa in 1905. In addition, he described more recent diamond prospecting in southern Africa by geologists such as Baxter Brown.

Shane McClure (Gemological Institute of America, Carlsbad, California, USA) reminded the audience that clarity enhancements can be done on *any* stone containing surface-reaching feathers (such as alexandrite, tsavorite and Cu-bearing tourmaline), and that detecting and determining the amount of filler in a stone

Figure 6: Mark Cullinan delivers his presentation on diamonds at the CGA Gem Conference. Photo by B. M. Laurs.

takes practise. Another common enhancement is low-temperature heat treatment, which is done to modify a stone's colour and is commonly not detectable; it may be performed on sapphire, ruby, tanzanite, pink topaz and aquamarine. Recent experiments to test the colour stability of sapphires showed that orangey pink (padparadscha) stones from Ambatondrazaka, Madagascar, are not the only ones exhibiting photochromism from exposure to short-wave UV radiation, but that this behaviour is also shown by some pink sapphires from Vietnam and Myanmar (Mogok) that turn more orange, as well as colourless to pale yellow sapphires from Sri Lanka that become more yellow with UV exposure.

Kelly Ross (security advisor from Edmonton, Alberta, Canada) reviewed current criminal activity in the jewellery industry. He noted some disturbing trends for jewellery store robberies, with increasing violence (including the use of guns) and higher losses. In addition, 'grab-and-run' thefts are becoming quite common. Criminals then sell the stolen goods back into the industry or trade them for drugs, often within hours of stealing them. Anti-money-laundering procedures are more important than ever, and those involved in trading and appraising jewellery should watch for red flags to avoid inadvertently handling stolen goods.

Dr Rhiana Henry (recently graduated from the University of British Columbia, Vancouver, Canada) reviewed gem materials from Canada and their localities, including new fieldwork initiatives at gem-bearing pegmatites in British Columbia (Revelstoke area) and the Northwest Territories (Stargazer claim in the O'Grady Batholith). She then described her recent research on beryl, and explained how red beryl from Utah, USA, is chemically distinct, geologically unique and structurally different than other beryl varieties.

Ray Hill (Opalus, Abbotsford, British Columbia, Canada) profiled rare and exotic gem varieties. He explained how gem rarity can be related to several different factors, such as the naturally low abundance of the mineral, paucity of clean transparent pieces, difficulty in cutting (due to softness, cleavage, etc.), death of the person who is important for supplying the material, source areas that are mined out and/or inaccessible (due to natural disasters, political situations, etc.), and exceedingly high cost of rough. He then showed examples of various rare and exotic stones from his extensive collection.

Jean-Pierre ('JP') Jutras (Jade Leader, Calgary, Alberta, Canada) examined the jade market and the carving of jadeite and nephrite in China. He determined that there are currently up to 500,000 people involved with jade carving there, and in Henan Province's Zhenping County there is a state-built 'jade city' (since 2016) where 300,000 people are involved in the jade trade. He also reviewed the evolution of carving techniques, jade value factors and important localities for jadeite and nephrite, as well as recent exploration work in Wyoming and Washington states, USA, by his company.

Figure 7: This 5 ct tourmaline (12.62 × 9.40 × 6.89 mm) faceted by Lisa Elser is an example of a precision-cut gemstone. Photo by Karlyn Bennet.

Lisa Elser (Lisa Elser Custom Cut Gems, Port Moody, British Columbia) examined the influence of cut on coloured stone pricing. She differentiated three main faceting types: *traditional* (typical cuts found on the market and in gem-producing areas worldwide), *fantasy* (typically employing curved lines) and *precision* (designed to move light and enhance colour, generally using 'meet point' designs and possessing excellent polish and finish). She indicated that precision cuts (e.g. Figure 7) are becoming more common, and that pricing should depend on the overall attractiveness of a stone and not simply its cut type or execution.

Gary Roskin (Roskin Gem News Report, Exton, Pennsylvania, USA) reviewed global gem trade shows, and predicted that in the future the exhibitions in Denver (Colorado, USA) will 'take over' the JCK show in Las Vegas (Nevada, USA). While trade shows provide excellent opportunities to buy and sell stones and also keep track of pricing, various e-commerce platforms (GemBridge, The Jewelers Circle, eBay, etc.), as well as auctions, offer alternatives to the high expenses associated with attending trade shows.

Julia Griffith (The Gem Academy, online education, UK) looked at recent developments in the growth and production of gem-quality synthetic diamonds, including the large (20–30 ct) CVD-grown gems that recently entered the market. She then reviewed historical

developments for growing synthetic diamonds by HPHT and CVD techniques. Next she examined the prevalence of laboratory-grown diamond being sold online, using the Virtual Diamond Boutique trading platform as an example. She also warned against relying solely on handheld testers for separating diamonds and their simulants, since some HPHT-grown samples may test as synthetic moissanite and some newer synthetic moissanites may test as diamond. Finally, she chronicled the price decline for laboratory-grown diamonds since 2016; some of them are currently trading at more than 97% below Rapaport's pricing of equivalent natural stones.

Charles Carmona (Guild Laboratories Inc., Los Angeles, California) examined the past and present of precious metals. He compiled a variety of statistics from online sources, including the total production of various metals as represented by the size of a cube they would occupy: 21 m for gold, 52 m for silver and 7.2 m for platinum. He also reviewed the environmental and health hazards associated with the mining of gold (i.e. mercury contamination) and silver (lead pollution). Some companies are currently evaluating sea-floor mining as a way to obtain precious and critical metals, and in the distant future asteroids may also provide a source of these materials.

Jon Phillips (Corona Jewellery Co., Toronto, Ontario, Canada) reviewed current activities and future prospects for mining diamonds in Canada. Most of Canada's diamond production (>90%) is faceted in India, as well as in Belgium and Botswana; there are only two cutting facilities in Canada. Although there are more than 40 brands of Canadian diamonds, only ≤5% by value are laser inscribed so that they can be accompanied by information such as the mine of origin, original weight of the rough stone and the factory where it was cut.

Emily Waterfall (Bonhams, Los Angeles, California, USA) took conference participants inside the global auction market. The consignment chronology involves several steps: reviewing property, providing auction estimates, negotiating a contract, shipping property to the salesroom, researching and photographing the pieces for the catalogue, marketing the upcoming auction, holding preview exhibitions, selling the item at auction and finally paying the settlement to the consignor. She indicated that nowadays 87% of Bonhams' bidders have registered online and more than half of the buyers purchase sight-unseen. Jewellery sales include pieces ranging from USD500 to the millions, and those from popular designers do especially well.

Stuart Robertson (Gemworld International Inc., Glenview, Illinois, USA) provided a coloured stone market update. Overall the gem industry is seeing a slowdown after two strong years, due to global uncertainties and recession concerns. However, he was cautiously optimistic that there is an appropriate mix of supply and demand to support current price levels. Designers are particularly important drivers of coloured stone trends, and many of them are continuing to focus on ethically sourced gems according to client demand.

The next CGA Gem Conference is scheduled to take place during the weekend of 21 October 2023 (subject to COVID-19 developments) and will celebrate the 65th anniversary of the Association.

Brendan M. Laurs FGA

GEM-A CONFERENCE

On 6 November 2022, 220 attendees gathered for the annual Gem-A Conference at etc.venues County Hall in London. Gem-A CEO **Alan Hart** opened the conference and introduced the speakers during the two-day event.

Richard Hughes (Lotus Gemology, Bangkok, Thailand) covered the history, types and carving of Chinese jade. He indicated that the natural staining of jade can make it more valuable, particularly when the various colours are cleverly incorporated into carvings. Starting in the 1960s, there was a revival in jade carving in art schools in China, in which traditional carving styles transitioned into the more creative and contemporary designs seen today.

Joanna Hardy (independent fine jewellery consultant, London) reviewed the historical use of peridot, which in Roman times was employed in jewellery to create blocks of green colour—symbolising themes such as fertility, nature, rebirth, hope and paradise—and also carved into amulets and talismans. She also showed a video that highlighted activities by Fuli Gemstones in the mining, cutting and marketing of high-quality Chinese peridot.

Dr Federico Pezzotta (Natural History Museum of Milan, Italy) provided an update on gem tourmaline (especially Paraíba-type) from Maraca and Mavuco, Mozambique. The two localities comprise an area measuring 15 km long and up to 1 km wide. The Maraca deposit has been mined out, while Mavuco continues to produce an average of 200–300 g of tourmaline daily

from secondary (residual) deposits. The recent discovery of traces of Cu in tourmaline from an *in situ* pegmatite adjacent to the mining area provides evidence that the residual deposits formed locally from deep weathering, rather than coming from a distal alluvial source.

Prof. Dr H. Albert Gilg (Technical University of Munich, Germany) examined the probable origin of gem materials in late medieval crowns in Europe. They include diamonds from India, sapphires from Sri Lanka, emeralds from Pakistan's Swat Valley and spinels from Kuh-i-Lal in present-day Tajikistan. In addition to the gem materials used and their potential origins, the study of these crowns yields important information on cutting and polishing techniques, enhancements, imitations, later replacements and past terminologies that were used in inventories of the time.

Robert Weldon (Gemological Institute of America, Carlsbad) described some of his travels to exotic destinations as a gemmological photojournalist, and also the travails of gem photography. Based on his widely varied experience, he ascertained that gemmology does not just deal with gems, but is also about the people and places that are so intimately involved with the stones.

David Fisher (De Beers Ignite, Maidenhead, Berkshire) described current and future challenges in identifying treated and laboratory-grown diamonds. He warned against complacency, including the need to be conscious of what you don't know. For example, the colours of fluorescence from as-grown and treated CVD-grown diamonds have become more variable over time (Figure 8), so it is no longer accurate to assume that they exhibit orange luminescence. It is also possible that in the future the properties of treated and synthetic diamonds will be deliberately manipulated to make them more difficult to identify.

Lisa Levinson (Natural Diamond Council, London) examined consumer attitudes towards natural diamonds. Marketing efforts by the Natural Diamond Council are focusing on women in the age range of 18–39, with the goal of eliciting an emotional response to natural diamonds while emphasising the integrity and social benefits of the diamond industry. The Natural Diamond Council also promotes correct terminology and manages the Assure Program to provide third-party testing of commercially available diamond verification instruments for the screening or detection of synthetic diamonds and simulants.

Richard Drucker (Gemworld International Inc., Glenview, Illinois, USA) provided a market update on diamonds, coloured stones and pearls. He estimated that 10% by value of the polished diamonds imported into the USA from India are laboratory grown, and these are generally priced at 85% below natural diamonds. Regarding coloured stones, in the USA the top-selling gem continues to be sapphire (including fancy colours), and there is strong demand for zircon, garnet, spinel, tourmaline and aquamarine. However, demand for Russian demantoid has fallen since the start of Russia's war with Ukraine.

At the close of the conference, **Alan Hart** thanked **Maggie Campbell Pederson** for her six years of service as Gem-A president, and announced **Richard Drucker** as the new Gem-A president. Drucker then summarised the conference presentations.

On 7 November, three workshops were held at Gem-A's headquarters: investigating jade and its imitations with **Pat Daly** (Gem-A, London), coloured stone grading and pricing with **Richard Drucker**, and identifying ivory and its simulants with **Aurore Mathys** (Gem-A, London). In addition, field trips took attendees to a private viewing of the British Crown Jewels at the Tower of London, a behind-the-scenes tour of the gem and mineral collection at the Natural History Museum, and a special tour of the jewellery gallery at the Victoria and Albert Museum. That evening marked Gem-A's graduation ceremony and presentation of awards at the Royal Institution of Great Britain in London.

Next year's Gem-A Conference will take place on the first weekend of November 2023.

Brendan M. Laurs FGA

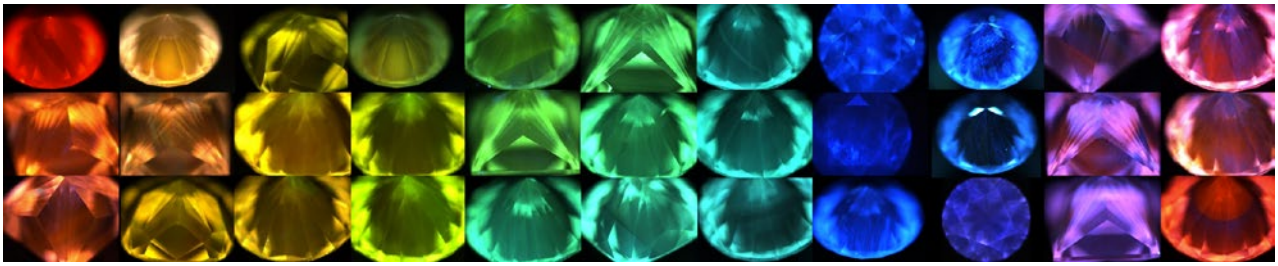

Figure 8: David Fisher's Gem-A Conference presentation on treated and synthetic diamonds included this photomontage titled 'Dale's Rainbow', which shows the variety of fluorescence colours emitted by as-grown and treated CVD synthetic diamonds, as seen with ultra-short-wave UV radiation in the DiamondView instrument. Photo © Matthew Dale, De Beers Group Ignite.

Gem-A Notices

MESSAGE FROM GEM-A CEO ALAN HART

It has been a busy quarter here at Gem-A, with both our conference and our graduation ceremony taking place in early November 2022. For those of you who attended this first in-person conference since the pandemic began, we would like to extend our sincerest thanks for joining the various sessions we ran throughout the day, and what a fantastic day it was. I am sure everyone who attended will agree that our knowledgeable speakers succeeded in delivering an insightful, educational and well-rounded series of talks. For those of you who attended the gala dinner, I am still trying to understand how the clever magician knew the numbers?!

Similarly, our graduation ceremony—which this year took place at the Royal Institution in Green Park—was a resounding success. Meeting and awarding our enthusiastic graduates is always one of the genuine highlights of my year. I would also like to take this opportunity to thank Gem-A chairperson and alumnus Justine Carmody for delivering such an inspirational graduation speech, which illuminated many possibilities that are open to our talented graduates. Congratulations once again to all involved. Due to ongoing difficulties with travel, many of our graduates were not able to join us, but we thought about you, and the celebration was indeed for all our global graduates. Well done!

As 2022 draws to a close, at Gem-A we have been busy planning the year ahead, starting with the gem and mineral shows in Tucson, Arizona, USA. Please save the date for the Gem-A Bash on 2 February 2023 (details to come later). I look forward to catching up with many of you then.

We are also working on delivering our Gemmology and Diamond examinations in February, and looking forward to welcoming our on-site and our online distance-learning students for the February and March terms, respectively.

In addition, we have now opened the window on membership renewals for 2023. You should have already received an email inviting you to renew. What's more, if you renew before 31 December, you can also take advantage of our early-bird discounted fee. We look forward to your continued support, and we hope you enjoy the many benefits of being a Gem-A Member.

From all of us at Gem-A, we wish you a very happy holiday season—whatever this festive time of year holds in store for you—and we look forward to seeing you in 2023.

GEM-A CONFERENCE, GRADUATION AND PRESENTATION OF AWARDS

The Gem-A Conference 2022 took place on Sunday 6 November at etc.venues County Hall overlooking the River Thames in central London. It included a diverse line-up of eight speakers covering a wide range of topics: jade, peridot, Paraíba-type tourmaline from Mozambique, gemstones in late medieval European crowns, gemmological photojournalism, identification challenges of laboratory-grown and treated diamonds, consumer attitudes about natural diamonds and an update on the current gem market. For more details, see the Conferences section of this issue of *The Journal*.

More than 250 people registered to attend, and engagement was high across the talks. This one-day event was followed by a gala dinner, where attendees were entertained by a talented magician, and we managed to raise about GBP1,170 from the raffle. Thank you to all who participated for your generous donations. All proceeds will be sent to Gem Legacy, whose mission is to help support vocational training, entrepreneurship and community development in East African artisanal gem mining communities.

On the morning of Monday 7 November we delivered three private tours and three workshops, all of which received fantastic feedback from all attendees. The Gem-A Graduation Ceremony and Presentation of Awards was held on the evening of 7 November at The Royal Institution in London. It was accompanied by a drinks reception for Graduates and guests in the historic libraries of the Royal Institution.

Participants at Gem-A's 2022 graduation ceremony. Photo by Tempest Photography.

GEMMOLOGY DIPLOMA PASSES

Hisham Alsheari, *Bahrain*

Najmeh Anjomani, *United States of America*

May Thinzar Aung, *Myanmar*

Adeline Auvinet, *France*

Claire Bartlett, *United Kingdom*

Sarah Beckett, *Australia*

Ritsuko Birch, *United Kingdom*

Juliette Bogaers, *Switzerland*

Wang Boran, *P.R. China*

Guillaume Boulfroy, *France*

Elena Bravo, *France*

Gauthier Bührer, *France*

Samuel Burrell, *United States of America*

Xufeng Cao, *P.R. China*

Yanbo Cao, *P.R. China*

Sandy Caramiaux, *France*

Ip Kai Chan, *Macau*

Suet Ting Chan, *Hong Kong (S.A.R.)*

Chia Wei Chang, *Taiwan (R.O.C)*

Caiyunfei Chen, *P.R. China*

Chia Yi Chen, *Hong Kong (S.A.R.)*

Huang-Ju Chen, *Taiwan (R.O.C)*

Huixia Chen, *P.R. China*

Jia-I Chen, *Taiwan (R.O.C)*

Chieh Cheng, *Taiwan (R.O.C)*

Ka Yan Cheng, *Hong Kong (S.A.R.)*

Ka Ming Cheung, *P.R. China*

Wai Man Cheung, *Hong Kong (S.A.R.)*

Yim Ting Chik, *Hong Kong (S.A.R.)*

Kai Ying Chin, *Hong Kong (S.A.R.)*

Tsz Yin Chong, *P.R. China*

Hei Yuen Destin Chow, *Hong Kong (S.A.R.)*

Fan Chuangrong, *P.R. China*

Sze Man Chui, *Hong Kong (S.A.R.)*

Mei Chin Wai Chung, *P.R. China*

Tak Yin Maria Chung, *Hong Kong (S.A.R.)*

Lauréline Colliard, *France*

Lee Cox, *United Kingdom*

Sandrine Croville, *France*

Victoria de La Soujeole, *Switzerland*

Françoise De Rocquigny, *France*

Reshmi Dharmadasa, *United Kingdom*

Mahingoda Jithmini Mathishani Dharmasekara, *Sri Lanka*

Tiffany Didham, *United Kingdom*

Junqing Dong, *P.R. China*

Carolyn Drewery-Harris, *United Kingdom*

Jessie Edmonds, *United Kingdom*

Li-Fei Fang, *Taiwan (R.O.C.)*

Reuben Fernandes, *India*

Oliveira Machado Filipa, *Switzerland*

Tsz Ying Fong, *P.R. China*

Ornella Fontana, *France*

Maria Estela Forjaz de Paiva Pereira de Almeida, *Portugal*

Lai Wa Fung, *Hong Kong (S.A.R.)*

Frédéric Gallet, *France*

Richard Gordon, *United Kingdom*

Georgina Grainger, *United Kingdom*

Elisabeth Griffin, *United Kingdom*

Louisa Guinness, *United Kingdom*

Maxwell Hain, *United States of America*

Melinda Handgen, *United States of America*

Penelope Harris, *United Kingdom*

Katsumasa Hatori, *Japan*

Claire Haywood-Dunn, *United Kingdom*

Yohann Herpin, *France*

Janina Hitchens, *United Kingdom*

Chun Yao Ho, *Taiwan (R.O.C)*

ITing Hsieh, *Taiwan (R.O.C)*

Chu Chun Hsueh, *United States of America*

Bowen Huang, *P.R. China*

Weiyi Huang, *P.R. China*

Ian Ierston, *Wales, UK*

Yuka Ishikawa, *Japan*

Vidhi Jain, *India*

Pan Junfeng, *P.R. China*

Shoko Kawahara, *Japan*

Miki Kawai, *Japan*

Zhang Kexuan, *P.R. China*

Bianca-Larisa Klein, *United Kingdom*

Eru Kotajima, *Japan*

Goto Kunihiro, *Japan*

Pak Sing Jacky Kwok, *Hong Kong (S.A.R.)*

Nge Lay Kyaw, *Myanmar*

Edouard Laborde, *France*

Chun Hin Lai, *P.R. China*

Chun Hwa Lai, *Taiwan (R.O.C)*

Wei Jung Lai, *Taiwan (R.O.C.)*

Po Ha Lam, *Hong Kong (S.A.R.)*

Wei Lanyu, *P.R. China*

King Yu Lau, *Hong Kong (S.A.R.)*

ShiQi Le, *P.R. China*

Britni Le Croy, *United States of America*

Quentin Lecommandeur, *France*

Li-Min Lee, *Taiwan (R.O.C.)*

Po Yan Lee, *Hong Kong (S.A.R.)*

Gaëlle Nelly Michele Lemaître, *France*

Anne-Charlotte Leroux, *France*

Mun Kay Livy Leung, *Hong Kong (S.A.R.)*

Yim Ping Leung, *P.R. China*

Yuet Hang Leung, *Hong Kong (S.A.R.)*

Jun Yi Li, *Taiwan (R.O.C)*

Mengxiao Li, *P.R. China*

Peishan Li, *Hong Kong (S.A.R.)*

Xinlu Li, *P.R. China*

Wentao Liao, *P.R. China*

Yi-Han Liao, *Taiwan (R.O.C)*

Bai Lin, *P.R. China*

Chia-Yen Lin, *Taiwan (R.O.C)*

En-Fan Lin, *Taiwan (R.O.C)*

Floriane Lissart, *France*

Caitlin Little, *Scotland, UK*

Chloé Liu, *France*

Hanba Liu, *P.R. China*

Junfeng Liu, *P.R. China*

Mian Liu, *P.R. China*

Hsuehpin Lu, *Taiwan (R.O.C)*

Ka Man Luk, *Hong Kong (S.A.R.)*

Diyuan Ma, *P.R. China*

Siu Ling Sally Ma, *Hong Kong (S.A.R.)*

Siyu Ma, *P.R. China*

Han Tzu Mai, *Taiwan (R.O.C)*

Elsa Marlin, *France*

Tze Hang Mau, *P.R. China*

Amélie Mazurkiewicz, *Canada*

Yang Meng, *P.R. China*

Sharon Merritt, *United States of America*

Paulina Michel, *Austria*

Daria Mironova, *France*

Bruno Mojonnier, *Switzerland*

Adèle Noel, *France*

Dr Taku Okada, *Japan*

Ying Pan, *United Kingdom*

Meiqi Pang, *P.R. China*

Sanmesh Parab, *India*

Chiara Parenzan, *Switzerland*

Arianna Pedrazzoli, *Scotland, UK*

Rebecca Pelmus, *United Kingdom*

Lirui Peng, *Belgium*

Frédéric Pereira, *France*

Chen PingPing, *P.R. China*

Isabel Pratt, *United Kingdom*

Charlotte Richman, *United Kingdom*

Benoît Ries, *France*

Charlotte Romer, *France*

Marie Roque, *France*

Yang Rui, *P.R. China*

Li Sabina, *Hong Kong (S.A.R.)*

Zahra Saiyed, *Zambia*

Akitsugu Sato, *Switzerland*

Brigitte Scattarreggia-Kellenberger, *Switzerland*

Yu Ann Siah, *Malaysia*

Nicole Singer, *Canada*

Zongjie Song, *P.R. China*

Marie-Pierre Spanagel, *France*

Li Su, *France*

Haiqi Sun, *P.R. China*

Yizhe Sun, *P.R. China*

Lydia Long Yan Sung, *Hong Kong (S.A.R.)*

Ruweesha Suriyaarachchillage, *United Kingdom*

Carla Sylvestre, *France*

Cheung Sze, *Hong Kong (S.A.R.)*

Jen Ping Tai, *Taiwan (R.O.C.)*

Alexia Taylor, *United Kingdom*

Yi Teng, *P.R. China*

Yu Yan Anne Teng, *P.R. China*

Alice Thomson, *United Kingdom*

Lei Ting, *P.R. China*

Amelia Tomkinson, *United Kingdom*

Arthur Touret, *France*

I-Lin Tsai, *Taiwan (R.O.C.)*

Chia Hao Tsao, *Taiwan (R.O.C.)*

Chan Chun Tung, *Taiwan (R.O.C)*

Leungkan Tung, *P.R. China*

Dimitrios Tzortzis, *Greece*

Ilona van Houwelingen-Weijerman, *The Netherlands*

Leslie Vanneste-Damas, *France*

Jinali Vikamsey, *India*

Joshua Walker, *United Kingdom*

Connie Chiayueh Wang, *Taiwan (R.O.C)*

Jiaqi Wang, *P.R. China*

Yueshan Wang, *P.R. China*

Yuzhuo Wang, *P.R. China*

Charlotte Webster, *United Kingdom*

Zheng Wei, *P.R. China*

Huizhen Wen, *P.R. China*

Amber Rose Whittingham, *United Kingdom*

Kwok Ching Wong, *Hong Kong (S.A.R.)*

Wang Ching Wong, *Hong Kong (S.A.R.)*

Aimee Yu-Hsuan Wu, *Taiwan (R.O.C)*

Mengting Wu, *Taiwan (R.O.C)*

Shuai Wu, *Hong Kong (S.A.R.)*

Sitong Wu, *P.R. China*

Wanling Wu, *P.R. China*

Yelei Wu, *P.R. China*

Yi-Chang Wu, *Taiwan (R.O.C.)*

Wu Xiancheng, *P.R. China*

Miao Xie, *P.R. China*

Shoumei Xie, *Taiwan (R.O.C)*

Zhilong Xie, *P.R. China*

Xiao Xue Hui, *Thailand*

On Ting Alice Yang, *Hong Kong (S.A.R.)*

Yingxin Ye, *P.R. China*

Wing Ling Yeung, *Hong Kong (S.A.R.)*

Zhang Yi, *P.R. China*

Dai Yibin, *P.R. China*

Xiao Yikai, *P.R. China*

Kang Yu Yin, *Taiwan (R.O.C.)*

Xintian Yu, *P.R. China*

Ying Yu, *P.R. China*

Shogo Yugami, *Japan*

Gao Yuhang, *P.R. China*

Ma Yun, *P.R. China*

Chen Zean, *P.R. China*

Enjie Zhang, *P.R. China*

Jiamin Zhang, *P.R. China*

Shuwei Zhang, *P.R. China*

Sihui Zhao, *P.R. China*

Guillaume Zuber, *France*

GEMMOLOGY DIPLOMA PASSES WITH MERIT

Annabel Abraham, *United Kingdom*

Hiu Yan Chan, *Hong Kong (S.A.R.)*

Florence Cook, *United Kingdom*

Samantha Durrant, *United Kingdom*

Natasha Fiske De Gouveia, *United Kingdom*

Mizuki Imura, *Japan*

Junqi Li, *P.R. China*

Masakatsu Nozawa, *Japan*

Veronica Olszowska, *United Kingdom*

Maureen Pratt, *United States of America*

Yuming Quan, *P.R. China*

Rachel Smith, *United Kingdom*

Ka Wing Tam, *P.R. China*

Naoya Watanabe, *Japan*

Ting Wei, *Taiwan (R.O.C.)*

Yanhan Wu, *P.R. China*

Zhiyi Zhang, *P.R. China*

Xue Zhiyu, *P.R. China*

GEMMOLOGY DIPLOMA PASSES WITH DISTINCTION

Wen Gao, *P.R. China*

Gabriel Kleinberg, *United Kingdom*

Constance Maure, *France*

Philipp Rank, *Austria*

Mengjie Shan, *P.R. China*

Dr Laura Speich, *Switzerland*

Ravindi Walisinghe Ansar, *United States of America*

Pei-Yun Wang, *Taiwan (R.O.C)*

Mai Yokota, *Japan*

DIAMOND DIPLOMA PASSES

Kok Ling Tina Au, *Hong Kong (S.A.R.)*

Karin Bartha, *The Netherlands*

Cho Ki Chan, *Hong Kong (S.A.R.)*

Wing Tung Chan, *Hong Kong (S.A.R.)*

Georgios Charanas, *Greece*

Ke-Ning Chen, *Taiwan (R.O.C)*

I-Chun Chien, *Taiwan (R.O.C)*

On Ting Choi, *Hong Kong (S.A.R.)*

Oursoula Dipapidou Kingston, *United Kingdom*

Maria Estela Forjaz de Paiva Pereira de Almeida, *Portugal*

Lai Fan Fung, *Hong Kong (S.A.R.)*

Elizabeth Grunfeld, *United Kingdom*

Eleanor Harrison, *United Kingdom*

Chun Kuen Ho, *Hong Kong (S.A.R.)*

Sam Hoare, *United Kingdom*

Melissa Holt, *United Kingdom*

Hsiang-Yun Hu, *Taiwan (R.O.C)*

Lok Ting Ko, *Hong Kong (S.A.R.)*

Man Yi Lai, *Hong Kong (S.A.R.)*

Hoi Ying Lau Yu, *Hong Kong (S.A.R.)*

Melissa Lee-Patrick, *United Kingdom*

Ching Chee Alda Leung, *Hong Kong (S.A.R.)*

Chong Yu Leung, *Hong Kong (S.A.R.)*

Shuk Yi Li, *Hong Kong (S.A.R.)*

Yi-Han Liao, *Taiwan (R.O.C)*

Lydia Micallef, *United Kingdom*

Edith Sophia Monnas, *Greece*

Wing Fai Ng, *Hong Kong (S.A.R.)*

Sandrina Chan Ramanantsoa, *Madagascar*

Harry Richmond, *United Kingdom*

Kwok Yan Victoria So, *Hong Kong (S.A.R.)*

Pui Fung Yeung, *Hong Kong (S.A.R.)*

Wing Sum Yeung, *Hong Kong (S.A.R.)*

DIAMOND DIPLOMA PASSES WITH MERIT

Anne-Christine Brousse De Gersigny, *United Kingdom*

Annabelle Corton, *United Arab Emirates*

Elizabeth Dawson, *United Kingdom*

Anita (Min-Hsin) Eaton, *United Kingdom*

Sammantha Maclachlan, *Scotland, UK*

Sophie Padfield, *United Kingdom*

DIAMOND DIPLOMA PASSES WITH DISTINCTION

Cheng Chen, *Hong Kong (S.A.R.)*

Catherine B. Eisele, *Germany*

Jessica Fall, *United Kingdom*

Yin Yee Fung, *Hong Kong (S.A.R.)*

Elisabeth Griffin, *United Kingdom*

Carina Hanser, *Germany*

Yu Ann Siah, *Malaysia*

PRIZE AND MEDAL WINNERS

Awards and prizes are presented to the best candidates of the year, selected from among our students worldwide.

GEMMOLOGY FOUNDATION CERTIFICATE

Anderson Medal

Awarded to the candidate submitting best papers of the year in the Gemmology Foundation examination.

This medal was established in 1981 in honour of Basil W. Anderson FGA, former director of the Gem Testing Laboratory, London.

2022 Winner: Constance Maure, a student from L'Ecole des Gemmes, Bourg-la-Reine, France

GEMMOLOGY DIPLOMA

Anderson Bank Prize

Awarded to the candidate submitting the best theory papers of the year for the Gemmology Diploma examination.

Established in 1981 and named after Basil W. Anderson FGA and Prof. Dr Hermann Bank FGA, former director of the German Gemmological Association in Idar-Oberstein, Germany.

2022 Winner: Wen Gao, a student from Shanghai Junhao Jewelry Education and Training Center, P.R. China

Christie's Prize for Gemmology

Awarded to the candidate submitting the best papers of the year for the Gemmology Diploma examination.

This prize was established in 1954 as the Rayner Prize, renamed the Diploma Trade Prize in 1991, and replaced and sponsored since 2001 by Christie's London.

2022 Winner: Dr Laura Speich, an online distance learning student from Basel, Switzerland

Read Practical Prize

Awarded to the candidate submitting the best practical papers of the year for the Gemmology Diploma examination.

First awarded in 2009 and named in memory of Peter Read FGA, author and former tutor for Gem-A. In 2022, the prize was sponsored by Richard Drucker FGA (Hons) of Gemworld International Ltd, USA.

2022 Winner: Samuel Burrell, an online distance learning student from New York, USA

DIAMOND DIPLOMA

Bruton Medal

Awarded to the overall best candidate of the year in the Diamond Diploma examination.

This silver medal was established in 1996 in honour of Eric Bruton FGA to recognise his work in the field of diamonds.

2022 Winner: Jessica Fall, an online distance learning student from Leyburn, North Yorkshire, UK

The Deeks Diamond Prize

Awarded to the candidate submitting the best theory papers of the year in the Diamond Diploma examination.

First awarded in 2001, the prize is sponsored by the late Noel W. Deeks FGA DGA, a former vice president of the Association who taught the diamond course for many years. Sadly, Noel passed away in December 2021.

2022 Winner: Jessica Fall, an online distance learning student from Leyburn, North Yorkshire, UK

The Mok Diamond Practical Prize

Awarded to the candidate submitting the best practical papers of the year for the Diamond Diploma examination.

First awarded in 2009, this prize is sponsored by Dr Dominic Mok FGA DGA of the Asian Gemmological Institute and Laboratory Ltd, Hong Kong.

2022 Winner: Lydia Micallef, an online distance learning student from Ipswich, Suffolk, UK

Gem-A would like to congratulate all of our students who achieved such fantastic results!

2022 ANNUAL GENERAL MEETING

This year, Gem-A's Annual General Meeting (AGM) was held on 26 October at Gem-A's headquarters on Ely Place. Louise Goldring stepped down as a trustee of the Gem-A Council. Christopher Smith and Nevin Bayoumi Stefanovic were retired by rotation and were re-appointed to the Gem-A Council by the Members. Maggie Campbell Pedersen retired as Gem-A president after six years of outstanding service to the Association. Richard Drucker was appointed by the Members as the new president of the Association. Members voted on ordinary resolutions via Civica Election Services, and the results were announced at the AGM by board chair Justine Carmody. We thank all Members who participated and voted at the AGM this year.

MEMBERSHIP RENEWAL NOTICE

The renewal window for 2023 is now open to Members. Renew your membership by 31 December 2022 and take advantage of our early-bird discount! Pay now and for just GBP120* get your post-nominals, access to eight publication issues a year—including the prestigious *Journal of Gemmology* and insightful *Gems&Jewellery*—and a discount on all Gemmological Instruments (GI) equipment and books. Check your email for your invitation to renew. If you haven't received an email from us or require assistance with your renewals, please email membership@gem-a.com.

*Membership fee increases to GBP145 after 31 December 2022.

SPECIAL ANNOUNCEMENTS

Prof. Dr Henry A. Hänni has been made a Life Member of the Association for his outstanding service to the gem and jewellery trade, and for his long-time contributions to *The Journal* as an Associate Editor.

Nigel Israel has been awarded the title of Vice President of the Association for his outstanding service as treasurer and trustee over many decades.

Learning Opportunities

CONFERENCES AND SEMINARS

NAJA 59th Winter Education Conference
29–30 January 2023
Tucson, Arizona, USA
https://najaappraisers.com/event/59th-winter-education-conference

AGTA GemFair Tucson
31 January–5 February 2023
Tucson, Arizona, USA
https://agta.org/agta-gem-fair-tucson/seminars
Note: Includes a seminar programme

Accredited Gemologists Association (AGA) Tucson Conference
1 February 2023
Tucson, Arizona, USA (and online)
https://accreditedgemologists.org/currevent.php

Tucson Gem and Mineral Show
9–12 February 2023
Tucson, Arizona, USA
www.tgms.org/show
Note: Includes a seminar programme

International Colored Gemstone Association (ICA) Congress
14–17 February 2023
Dubai, United Arab Emirates
https://icacongress.com

Inhorgenta Munich
24–27 February 2023
Munich, Germany
https://www.inhorgenta.com/en
Note: Includes a seminar programme

MJSA Expo
5–7 March 2023
New York, New York, USA
https://mjsa.org/eventsprograms/mjsa_expo

Hasselt Diamond Workshop 2023 (SBDD XXVII)
15–17 March 2023
Hasselt, Belgium
https://www.uhasselt.be/SBDD#anch-bce-sbdd-xxvii

2023 Rochester Mineralogical Symposium
20–23 April 2023
Rochester, New York, USA
www.rasny.org/mineral-section

Scottish Gemmological Association Conference
28 April–1 May 2023
Location TBA
https://www.scottishgemmology.org

American Gem Society Conclave
1–3 May 2023
Louisville, Kentucky, USA
https://www.americangemsociety.org/conclave-2023

TECHNART 2023: International Conference on Analytical Techniques in Art and Cultural Heritage
7–12 May 2023
Lisbon, Portugal
https://technart2023.com

GemGenève
11–14 May 2023
Geneva, Switzerland
https://gemgeneve.com
Note: Includes a seminar programme

GAC-MAC Sudbury 2023
24–27 May 2023
Sudbury, Ontario, Canada
https://event.fourwaves.com/Sudbury2023/pages
Sessions of interest: Cratons, Kimberlites, and Diamonds; Lithium in Pegmatites: Mineralogy, Petrogenesis and Classic to Innovative Exploration Techniques; On the Beam: Advances and Applications in In-Situ Microanalysis and Geochronology; Spectroscopic Mineral Analysis

JCK Las Vegas
2–5 June 2023
Las Vegas, Nevada, USA
https://lasvegas.jckonline.com/en-us.html
Note: Includes a seminar programme

Sainte-Marie-aux-Mines Mineral & Gem Show
21–25 June 2023
Sainte-Marie-aux-Mines, France
www.sainte-marie-mineral.com
Note: Includes a seminar programme

Jewellery & Gem Asia Hong Kong
22–25 June 2023
Hong Kong
https://jga.exhibitions.jewellerynet.com/why-visit
Note: Includes a seminar programme

V National Diamond and Color Gems Conference
26–27 June 2023
Rome, Italy
Email: michele.macri@uniroma1.it

24th FEEG Symposium
2 September 2023
Barcelona, Spain
http://www.feeg-education.com/symposium

International Conference on the Application of Raman Spectroscopy in Art and Archaeology (RAA2023)
6–9 September 2023
Athens, Greece
https://www.raa2023.ugent.be
Note: A pre-conference Raman Spectroscopy Training School will take place on 4–5 September.

Bangkok Gems & Jewelry Fair
6–10 September 2023
Bangkok, Thailand
https://www.bkkgems.com
Note: Includes a seminar programme

Maine Pegmatite Workshop
6–10 September 2023
Bethel, Maine, USA
http://www.maine-pegmatite-workshop.com

Denver Mineral, Fossil, Gem & Jewelry Show
8–17 September 2023
Denver, Colorado, USA
http://denver.show
Note: Includes a seminar programme

32nd International Conference on Diamond and Carbon Materials
10–14 September 2023
Palma, Mallorca, Spain
https://tinyurl.com/yrzupmwb

HardRock Summit 2023
15–18 September 2023
Denver, Colorado, USA
https://hardrocksummit.com
Note: Includes a seminar programme

Jewellery & Gem World Hong Kong
18–24 September 2023
Hong Kong
https://jgw.exhibitions.jewellerynet.com
Note: Includes a seminar programme

13th Annual Portland Jewelry Symposium
24–26 September 2023
Portland, Oregon, USA
https://portlandjewelrysymposium.com

86th Annual American Society of Appraisers (ASA) International Conference
1–3 October 2023
New Orleans, Louisiana, USA, and online
https://www.appraisers.org/education/conferences-events

International Conference on Applied Mineralogy and Minerals (ICAMM 2023)
7–8 October 2023
New York, New York, USA
https://waset.org/applied-mineralogy-and-minerals-conference-in-october-2023-in-new-york
Theme of interest: Industrial Minerals, Gems, Ores, and Mineral Exploration

37th International Gemmological Conference
23–27 October 2023
Tokyo, Japan
https://www.igc-gemmology.org/igc-2023

OTHER EDUCATIONAL OPPORTUNITIES

Gem-A Workshops and Courses
Gem-A, London
https://gem-a.com/education

***GemIntro* Course**
Gem-A, online
https://gemintro.gem-a.com

Gemstone Safari to Tanzania
11–28 January 2023
5–22 July 2023
https://www.free-form.ch/tanzania/gemstonesafari.html

Lectures with The Society of Jewellery Historians
Society of Antiquaries of London, Burlington House
www.societyofjewelleryhistorians.ac.uk/current_lectures

- Natasha Awais-Dean—Jewels Captured in Perpetuity: The Jewellery Book of Anne of Bavaria
  24 January 2023
- Richard Edgcumbe—'My Beautiful Sapphires': Queen Victoria's Sapphire Coronet Commissioned from Kitching and Abud, 1840-42
  28 February 2023
- Vivian Watson—History of Hatton Garden
  28 March 2023
- Estelle Ottenwelter—Insight Into Early Medieval Elite Jewellery From Bohemia
  23 May 2023
- Patrick Davison—Contemporary Maker Talking About His Own Work
  27 June 2023
- Sébastien Aubry—Greek and Latin Inscriptions on Antique Engraved Gems and Rings (Greek, Etruscan, Roman)
  26 September 2023
- John Benjamin—Jewellery From Anglesey Abbey
  28 November 2023

New Media

Jade: A Gemologist's Guide

Ed. by Richard W. Hughes, 2022. Lotus Publishing, Bangkok, Thailand, and RWH Publishing, Boulder, Colorado, USA, https://tinyurl.com/2vu8n3sr, 534 pages, illus., ISBN 978-0964509757. USD200.00 hardcover.

When it comes to jade, this book has it all, from geology to mineralogy, history to biography, archaeology to anthropology, art to science, stories to facts and macro to micro. It is similar in format to Richard W. Hughes' *Ruby & Sapphire: A Gemologist's Guide*, yet it is also much different. There is a lot of up-to-date information, plus beautiful images and excerpts from antique jade books. It is structured into five parts, labelled A to E. Part A is an introduction to jade, Part B covers jade deposits worldwide, Part C deals with gemmological and appraisal issues, Part D addresses carvings and Part E includes miscellaneous material.

The book starts with an introduction of the many authors, who are all experts in their field and well known in the jade world. This is followed by acknowledgements from the authors and a note from the sponsor, Joel A. Bartsch of the Houston Museum of Natural Science (Texas, USA).

Chapter 1, 'The Jade Conundrum' by R. W. Hughes and Roland Schlüssel, gives a good overview of the thousands-of-years-old history of jade, the different meanings, the various and partly conflicting names, as well as the hard facts, such as chemical, gemmological and mineralogical data.

Chapter 2 is a personal synopsis of R. W. Hughes' extensive experience with jade, including trips to jade mines and visits with carving artists, all written in his distinctive, pleasant, easy-to-read style.

Chapter 3, by Chenglong 'Chris' Jiang, is dedicated to the long history of jade in China, starting in Neolithic time and ending at the beginning of the modern era in the late 1940s. It shows the meaning of jade in the various periods and dynasties, and the extent to which it was used at various times. A useful table of the dynasties is provided as a timeline.

Part B starts with Chapter 4, 'Rock 'n' Roll: The Geology of Jade', written by one of the world's foremost experts in jadeite, Dr George E. Harlow. It gives a very good overview of factors leading to jadeite and nephrite formation, followed by a brief description of currently known deposits worldwide, with maps of the locations, geological maps and tables describing colour causes in jade. The chapter contains a description by Jason K. Chao, in an insert, of the nephrite deposit in Taiwan. He mentions archaeological finds of Taiwanese nephrite in the Philippines and, looking further into this, I came across a mention of a Maritime Jade Road that dates back to 3000 BCE. I would have liked to learn more about this ancient jade trading route, but it was not covered further in the following chapters.

Next is an extensive description of Hetian jade (Chapter 5, by Dr Zhengyu 'Adam' Zhou, R. W. Hughes & Yicen Liu), wonderfully illustrated and completed with stories and history. This is followed by sections covering jade from various origins: Myanmar (Chapter 6, by R. W. Hughes); Mesoamerica (Chapter 7, by Mary Lou Ridinger); New Zealand (Chapter 8, by Donn Salt and R. W. Hughes); Mughal jade (Chapter 9, by Susan Stronge); Canada (Chapter 10, by Kirk Makepeace); USA (Chapter 11, by Dale Blankenship); Russia (Chapter 12, by R. W. Hughes, K. Makepeace and Nikolai B. Kouznetsov); and Japan (Chapter 13, by Dr Ahmadjan Abduriyim). The chapters are beautifully illustrated with images of the mines and carved objects, interspersed with history, stories, adventure and art. Chapter 9 is different in that it focuses on jade objects of Mughal origin. Most of the pieces described are displayed in London's Victoria and Albert Museum, but the geographic origin of these jades is not given.

The six chapters in Part C contain all you need to know about jade identification and give valuable hints for appraisals. The first chapter (Chapter 14, by Prof. Lijian Qi and Dr Z. Zhou) deals with the identification of archaic jade and its imitations, giving many examples of what to look for and how to identify samples with various analytical methods. The table of the dynasties included again here is very helpful, so one does not

have to go back to Chapter 3. However, the chapter does not always state what type of archaic jade is illustrated, probably because many of them are museum items and could not be tested. Also, I was puzzled by the description of Figure 14.17 in the text, where infrared bands between 762 and 1155 cm^{-1} are explained, but the illustrated spectrum ranges from 2000 to 4000 cm^{-1}, thus missing the described region.

Chapter 15, written by Eric J. Hoffman and Dr Z. Zhou, deals with all aspects of identifying nephrite, from basic gemmological methods such as scratch tests and hydrostatic weighing to FTIR spectroscopic analysis. The chapter includes a helpful table of jade materials and imitations and their gemmological properties, explanations about certain types of nephrite, two pages of images showing all types of jades and their imitations, and a list of accessory minerals identified by Raman spectroscopy.

In Chapter 16 (by Dr Dominic W. K. Mok and R. W. Hughes), the same scrutiny is applied to jadeite, describing the types, various treatments, and imitations and synthetics in detail. The table shown in Chapter 15 is repeated for ease of use, and photomicrographs illustrate some of the treatments and imitations. Two pages cover different jadeite types and their simulants. This is followed by Chapter 17, by John I. Koivula, which is exclusively dedicated to photomicrographs of various types of inclusions in jadeite and nephrite.

Chapter 18 (by R. Schlüssel and Jeff Mason) goes into various aspects of how to grade jadeite, explaining the criteria used and giving lots of examples. The Chinese meanings are translated into Western equivalents, such as the expression *ying*, meaning inner glow. The chapter contains a sample appraisal form, what to watch for in cabochons and bangles, care instructions, and many images of high-quality jadeite of all colours.

In Chapter 19, the authors (Stewart Young and E. Billie Hughes) give an insight into the auction world. Included are descriptions of what an auctioneer looks for, stories of outstanding pieces, explanations of the auction business and all its involved costs, a table of the most expensive jade pieces sold at auction, and extra stories about the Hutton necklace, designer Edmond Chin, the jade auction at the Myanma Gems Emporium and jade pieces in Taiwan's National Palace Museum.

Part D consists of two chapters dedicated to carving technologies and artists. Chapter 20 (by Drs Mingying Wang and Guanghai Shi) discusses the evolution of jade carving tools and craftsmanship, starting around 3500 BCE and going all the way to present times. Chapter 21 (by Andrew Shaw) concentrates on contemporary jade carvings in China. Many beautiful carvings are illustrated in both chapters, and profiles of artists Xi Yang and Lei Cui are also provided.

Part E covers miscellaneous aspects of jade and provides book recommendations, an extensive glossary and a bibliography of more than 1,500 references. Chapter 22 (by R. Schlüssel and J. Mason) concentrates on the symbolism of forms and colour in Chinese culture, describing the various shapes and colours and their meanings, again with many images and some small stories in between. Chapter 23 (by R. W. Hughes and E. J. Hoffman) gives insight into the rarest books written about jadeite, many of which are available only in museums or special libraries, but it also covers 'must-have' books for all jade enthusiasts. Chapter 24 (by R. Schlüssel) provides an extensive glossary of jade and its simulants, special terminology for jade in different languages and cultures, and various trade names. Chapter 25 (by R. W. Hughes) is a valuable bibliography subdivided by the author into 'Bibliographic references', 'Magazines', 'Fiction' and—the longest list—'General references'. The book is completed by an autobiographical story from Madame Wellington Koo, a well-known jade lover, followed by an extensive index.

Upon finishing this impressive book, I felt that the title 'A Gemologist's Guide' was a bit misleading because only a few chapters were directly related to gemmology. Another slight criticism is associated with the variety of authors, whose contributions appear not to have been edited in a way to provide a consistency of style, making the reading a bit of a 'bumpy ride'. The same variety also resulted in a fair amount of repetition of information. In addition, some chapters cite the accompanying illustrations in the text, while others do not. And in my opinion, the font size of the text is too small. Finally, I noticed a few typographical and other errors throughout, but considering the sheer volume of the book, these really are negligible.

Quibbles aside, this is probably the most complete book on jade available, covering its myriad aspects, and not just gemmological ones. It is mostly a pleasure to read, and well balanced between beauty and science, including maps, tables, charts and many beautiful images. This book is a must for every gemmological library, and it is also an excellent source of knowledge for all those interested in gems and art.

Dr Lore Kiefert FGA
Gemmology Consulting
Heidelberg, Germany

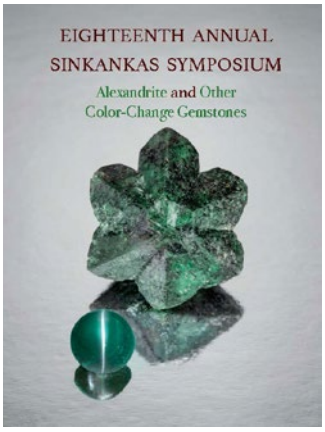

Eighteenth Annual Sinkankas Symposium—Alexandrite and Other Color-Change Gemstones

Ed. by Stuart Overlin, 2022. Pala International Inc., Fallbrook, California, USA, https://sinkankas.dpidirect.com, 106 pages, illus., ISBN 978-0991532063. USD35.00 softcover (no longer available) or free PDF.

The Eighteenth Annual Sinkankas Symposium, focusing on alexandrite and other colour-change gemstones, was co-sponsored by the Gemological Institute of America, the Geo-Literary Society and the Gemological Society of San Diego. It was held online as pre-recorded sessions from 11 speakers that were available on-demand from 25 April to 13 June 2022. The accompanying proceedings volume (reviewed here) contains contributions from all of the speakers, as well as some additional content. It is printed on heavy paper stock and contains numerous photos by accomplished photographers Mia Dixon, Orasa Weldon and Robert Weldon.

The book opens with a dedication, acknowledgements and contents listing, which are followed by speaker and author biographies. The main portion of this volume consists of informative contributions by various experts on several subjects: alexandrite quality factors, commercial sources and notable stones (by Evan Caplan); collecting colour-change minerals and gemstones (by William Larson); diaspore from Turkey (by Dr Çiğdem Lüle); colour-change phenomena in diamond (by Dr Sally Eaton-Magaña); designing with colour-change gemstones (by Niveet Nagpal); causes of their colour-change behaviour (by Drs Aaron Palke and George R. Rossman); the micro-world of alexandrite and other colour-change gems (by Nathan Renfro); pricing trends for alexandrite and other colour-change gemstones (by Stuart Robertson); an overview of the geology and mining of alexandrite (by Wim Vertriest); the challenges of photographing colour-change gemstones (by Robert Weldon); and two articles reprinted from *Gems & Gemology*, titled 'Geographic origin determination of alexandrite' (from the Winter 2019 issue, by Ziyin Sun, Dr Aaron C. Palke, Jonathan Muyal, Dino DeGhionno and Shane F. McClure) and 'Pleochroism and colour change in faceted alexandrite: Influence of cut and sample orientation' (from the Spring 2019 issue, by Dr Karl Schmetzer). The volume closes with a bibliography assembled by Dr James E. Shigley and Sheryl Elen.

The book is both attractive and informative to look at—with abundant images that accurately render the various colour-change appearances—and also very educational to read. This reviewer appreciates the availability of the free PDF file that can be downloaded online, although unfortunately the digital version suffers from poor resolution of many of the figures, some of which are unreadable even when enlarged on the screen. The wide range of topics covered in one volume make this a valuable addition to the literature on alexandrite and other colour-change gem materials. Gemmologists, researchers, enthusiasts, collectors and anyone interested in these fascinating gems should add this beautiful book to their reference library.

Brendan M. Laurs FGA

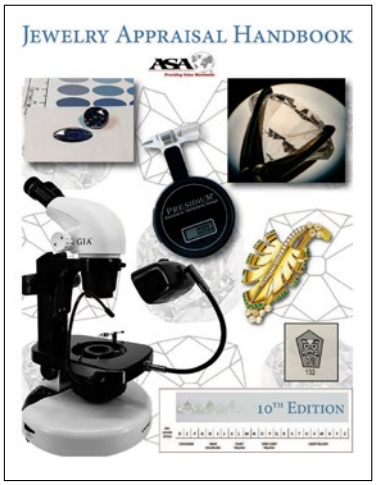

Jewelry Appraisal Handbook, 10th edn.

By American Society of Appraisers, 2021. ASA, Herndon, Virginia, USA, https://www.appraisers.org/shop/publications-and-subscriptions/books/jewelry-appraisal-handbook, 182 pages, illus., no ISBN. USD199.00/USD249.00 (member/non-member) binder + PDF, USD125.00/USD175.00 binder only or USD95.00/USD145.00 PDF only.

Since the review of the 8th edition of the *Jewelry Appraisal Handbook* (2015) in *The Journal*, two more editions have been published. The 9th edition was published in 2016 and expanded from 50 to 60 pages to include chain styles, updated URLs in the Web Links Project, new retail markups data and a basic guide to advanced instrumentation used in the major gemmological laboratories around the world. Published five years later, the 10th edition includes 182 pages—triple the content of its predecessor—both in added material and new formats.

The 'Diamonds' section retains the previous editions' weight-estimation and conversion charts that are so useful to valuers on a daily basis. Added to this is a 'Gallery of Laser Inscriptions' to help users identify sources of the many different grading reports that accompany so many of the diamonds sold over the last decade or so.

The 'Colored Gemstones' section includes the same charts and tables as in previous editions, but the standard hue, tone and saturation notations are accompanied by more easily understood colour graphics. The page on GIA coloured-stone clarity grades is unchanged, as is the section on value factors of pearls.

The section on advanced instrumentation has been moved to a new chapter titled simply 'Gemology'. It includes easy-to-understand information about the most common gem treatments and ends with a Gemstone Durability Chart that differentiates between hardness and toughness.

Following the section on chain styles (which illustrates more than 100 different examples) is a section titled 'Understanding Jewelry Manufacturing Techniques', with more than 50 images and a key to recognising elements of the various manufacturing processes.

A condensed page on common gold coins from the USA and elsewhere is followed by a section on 'Descriptive Elements', which includes full lists of characteristic attributes of mountings, diamonds, coloured stones, carvings, beads, phenomenal stones, opal, jade, pearls and watches.

The main points of the Uniform Standards of Professional Appraisal Practice are discussed in the next section, followed by charts of 'Retail Markups' and 'Definitions Used in Valuation Work'.

The 'Weights and Measures' section includes international unit conversion charts, ring sizes, and weight charts for pearls and watch movements (for both wristwatches and pocket watches).

The final section, Appendices, comprises over one-third of the *Handbook's* contents and includes an updated 'Online Resources Web Links Project'; laboratory-grown diamond history, production, detection and instrumentation; value factors of opal; major jewellery periods; detection of counterfeit watches; and a final discussion of the key elements of an appraisal report.

Overall, this monumental collection of useful information, curated over 25 years by dedicated teams of independent ASA-accredited professional valuers, is an invaluable addition to every practitioner's library.

Charles I. Carmona GG, ASA
Guild Laboratories Inc.
Los Angeles, California, USA

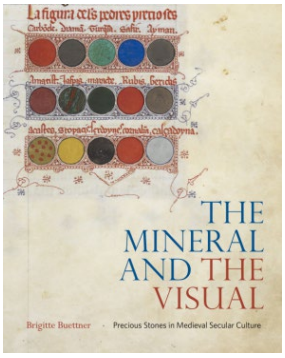

The Mineral and the Visual: Precious Stones in Medieval Secular Culture

By Brigitte Buettner, 2022. Penn State University Press, University Park, Pennsylvania, USA, https://www.psupress.org/books/titles/978-0-271-09250-8.html, 272 pages, illus., ISBN 978-0271092508. USD99.95 hardcover.

The Mineral and the Visual is a good-looking hardcover book that presents us with some less-familiar material relating to gems during a formative period in history. It is a book this reviewer was looking forward to reading. Indeed, the book's title and the chapter names prepare the reader for an intriguing voyage, but if that reader is a gemmologist or jewellery historian, it may be a frustrating one.

Following an introduction, the book is divided into three parts, each with three chapters. Part I deals with gems and royalty, with chapters on 'The Politics of Precious Stones', 'Inventing Mineral Sovereignty' and 'Gothic Regal Materiality'. Then comes Part II with aspects of medieval gems in written and pictorial sources—'A Royal Pursuit', 'Optical Mineralogy and Lithic Magic' and 'Of Stones, Sigils and Stars'. Part III covers geographical and economic aspects, with the chapters 'Edenic Geology

and Surplus', 'Mineral Realism in the Global Thirteenth Century' and 'Networks of Gem Trade'. The book closes with an epilogue, notes, bibliography and index.

In her Acknowledgements, the author thanks the editorial team for 'polishing the prose'. It is unclear what this involved, but the net result is a book written in an over-flowery style. This reviewer has always been puzzled by the need that some art historians have to become living embodiments of their field, writing more as poets than objective researchers. One must read some sentences several times before wondering why they were written in the first place. This reviewer could mention examples of overly florid writing or points to query from almost every page, but there is space here for just a few. On its first page, the introduction asks, 'Were crowns, reliquaries, jewelry and liturgical vessels not crafted from auratic materials, mined in the depths of the earth, and yet imbued with a starlike radiance?' I doubt we are being told that the medieval observer considered that the raw materials of such treasures had auras (the meaning of 'auratic') even if some believed they emitted light (had radiance), so is this just an excuse for modern metaphor?

The section on the fourteenth-century Crown of Bohemia describes the settings as 'cast into funnel shapes'. Casting is a specific manufacturing process, which was not used for these settings, and it is certainly not a synonym for 'formed'. The same description continues: 'Nearly invisible prongs reach out from low collets, as if to prevent the crystalline bubbles from floating away'. 'Crystalline bubble' is a picturesque (if self-contradictory) way to describe a gemstone, but it seems wildly out of place in what one would hope was intended as an academic reference book. The book is on more objective ground when mentioning that one of the red gems in the crown was tested in 1998 and found to be red tourmaline—a rare gem in medieval jewellery (Hyršl *et al*. 2000). Nevertheless, this underlines the author's apparent unfamiliarity with gemmology, as tourmaline is not listed in the index, but 'rubellite' is listed as a sub-entry under 'Rubies'.

This apparent lack of conversance with gemmology might explain why the likely identities of gems named in the myriad early texts are seldom explained. There is a grouping of early gem terms with colours, but little to indicate possible identifications in modern terms or, equally important, to distinguish between the tangible gems we find listed in inventories and those names that appear only in lapidaries with various perceived properties and powers, some of which may have been entirely mythical in medieval times. Distinguishing between old and modern gem terminology should be essential in a book of this nature, but, for example, a fourteenth-century inventory of the gem-encrusted chapel of St Wenceslas is noted as including a topaz. This gem name should surely have been rendered in quotation marks—'topaz'—because while those familiar with medieval gem descriptions will know that peridot was often meant, other readers might take it literally. According to the index, peridot is mentioned twice in the book and topaz 15 times, but there seems to be no suggestion that the latter often referred to the former in medieval texts. The reader is also told, somewhat irresponsibly, that '…topazes collected in Sri Lanka…reached European buyers'. And that '…milky topaz [no quotation marks]… sealed off the windows, letting natural light gradually dissolve into the mellow lambency….' Is 'milky topaz' a literal translation of the old text, in which case it would be very intriguing, or is it just another of the author's lapses into poetic description? In any case it is puzzling to the pedant who assumes that if a window were sealed off, no light would pass through it whatsoever. Equally pretentious is the description of inlays 'cut from violaceous sheets of amethyst'.

Near the start of the chapter titled 'Optical Mineralogy and Lithic Magic', where the author talks about the early classification of gems by colour being superseded by scientific investigation, she states 'Only in the seventeenth century would colors' diagnostic ability become suspect, as chemical probes and crystallographic analyses started to rummage through hidden faces of matter'. Should the author be excused for ignoring the in-depth work by Arabic investigators centuries earlier on distinguishing among gems, even listing their specific gravities? This highlights another deficiency in this book. Islamic texts provide great insights into the medieval understanding of gemstones, and their market and trade, but these are barely touched on here, even though most are available in English or other European-language translations. Even the most familiar of all these sources—Al Biruni—does not appear in the index. One excuse might be that the book is Eurocentric, so Arab sources are considered irrelevant, but this would be to deny their significant impact on medieval European thought and science.

On the rare occasions where the author has turned to modern gemmological literature, it is an eclectic and often outdated selection. We are told that 'fiery red garnets of the pyrope type', as used in Migration Period jewellery, 'were mined in Eastern Europe'. This statement, true to an extent, is referenced to Birgit Arrhenius's groundbreaking work, but that was 40 years ago.

A huge amount of research on the provenance of garnets in medieval and other jewellery has been published since then, including some in *The Journal*. It would now seem that, from the fifth through seventh centuries, garnets in Western European jewellery were typically almandine and probably from India or Sri Lanka, while only after the seventh century was Eastern European pyrope used.

The author apparently believes that the twenty-first century reader would be baffled by the medieval belief that some gem mines kept regenerating gems. True, perhaps, but there is no real attempt to unpack this, or to explain why such a belief might have arisen in the first place. Alluvial gem deposits can seem to regenerate because, in simplistic terms, additional gems get washed down the streams. So rather than seeing this as 'Mineral childbearing traced back to the very ancient postulate of Mother Earth's womb…', why not start from basic geology with an aside that, according to Roman Law, the gold from alluvial deposits was considered 'fruits' of the mine because it was deemed a non-diminishing resource.

Contemporary relative values should be a vital subject to consider in a book on gems in secular culture—after all, gems were seen as riches and treasure, making their worth a primary concern for the merchant, owner and jealous onlooker. Medieval inventories provide copious lists of gems with values, weights and sometimes even shapes and qualities. There is ample information in these early sources to collate and start to sketch out relative values and perhaps some idea of how quality and source impacted these, but the author has not taken advantage of them. Today we know that the most impactful stage in a gem's journey from mine to owner is when it is cut. The huge change in gem-cutting technology in the later medieval period in Europe must surely have been reflected in some way in how gems were viewed and valued. But we search in vain in this book for any meaningful discussion about cutting. And what about imitations? We find various spurious stones, including doublets, listed in inventories and in surviving jewellery, but the book gives little insight as to how these were perceived.

So, one is left wondering who the book is aimed at. The closing words of this volume are 'This book has advocated a cultural approach to the art of precious stones, lapidary knowledge and the workings of the mineral'. It does show gems from the perspective of medieval thought, but it fails to knit this together with research conducted through the lens of the modern gem historian. There seems to be little interest in the gems themselves. One way in which this is manifested is in the remarkable scarcity of the book's illustrations that actually show surviving medieval gems. One might not expect in-depth gemmology or Raman spectra of medieval spinels, but some research or anecdotes would be as fascinating to the lay reader as to the specialist. Lapis lazuli, for example, had an important use as a blue pigment in medieval times. This was hugely impactful on lapis' trade and commerce, but it is not mentioned despite the author's obvious great love for, and knowledge of, medieval manuscript illumination. More than four years ago, and thus surely within the gestation period of this book, the teeth of a woman who lived a millennium ago in a convent in northern Germany were found to have minute traces of lapis lazuli on them, indicating almost certainly that she was working on an important manuscript and quite likely that she licked her paintbrush to form a point—a practice actually recommended in medieval treatises on painting. It seems strange to ignore this, a fascinating discovery almost tailor-made for a book titled *The Mineral and the Visual*.

The author and publisher have done an excellent job in making a visually attractive book, although if they number references by chapter and then list them all at the back of the book, then they should take pity on the inquisitive reader by adding the chapter number to the chapter names in the page footers. But the big question, of course, is: Why did the author (or publisher) not see the need for this book about gems to be written in close collaboration with, or strong editorial influence from, someone with gemmological knowledge? Ignoring the style of the prose, which other readers may find less irritating than this reviewer did, and ignoring the lack of gemmological familiarity, it is a good survey of precious stones as depicted in medieval secular art and literature—and that would have made a more accurate subtitle for the volume. This book will no doubt find a place on the shelves of many readers of *The Journal*, but it is difficult to recommend it to a gem historian or gemmologist as an accurate and incisive study of the topic.

Dr Jack M. Ogden FGA
London

Reference

Hyršl, J., Neumanová, P., Kouřimský, J. & Burdová, P. 2000. Rubelit ve svatováclavské koruně, *Vesmír*, **79**(1), 18–23, https://vesmir.cz/cz/casopis/archiv-casopisu/2000/cislo-1/rubelit-ve-svatovaclavske-korune.html.

Other Book Titles

COLOURED STONES

Celestial Beings and Bird-Men: Human Flight in Chinese Jade
By Angus Forsyth, 2020. Philip Wilson Publishers, London, 336 pages, ISBN 978-1781300718. GBP40.00 hardcover.

Purely Paraiba
Doris Hangartner, 2021. Self-published by Doris Hangartner AG, Zurich, Switzerland, 149 pages, ISBN 978-3952538708. CHF150.00 hardcover.

DIAMOND

Diamonds, 3rd rev. edn.
By Marijan Dundek, 2022. Noble Gems Publications, London, 96 pages, ISBN 978-0953788439. GBP24.95 softcover.

GEM LOCALITIES

Nephrite Jade of Washington and Associated Gem Rocks
By Lanny R. Ream, 2022. LR Ream Publishing, Coeur d'Alene, Idaho, USA, 128 pages, ISBN 978-1387791279. USD19.95 softcover.

JEWELLERY HISTORY

Navajo and Pueblo Jewelry Design: 1870–1945
By Paula A. Baxter, Barry Katzen and Robert Bauver, 2022. Schiffer Publishing, Atglen, Pennsylvania, USA, 320 pages, ISBN 978-0764364082. USD60.00 hardcover.

The Tudors: Art and Majesty in Renaissance England
By Elizabeth Cleland, Adam Eaker, Marjorie E. Wieseman and Sarah Bochicchio, 2022. Yale University Press, New Haven, Connecticut, USA, 352 pages, ISBN 978-1588396921. USD65.00 hardcover.

JEWELLERY AND *OBJETS D'ART*

Bulgari Eden: The Garden of Wonders
By Simone Marchetti and Lucia Silvestri, 2022. Rizzoli, New York, New York, USA, 200 pages, ISBN 978-8891835871. USD100.00 hardcover.

Cartier: The Story Behind the Style
By Rachael Taylor, 2022. Self-published via Studio Press, 160 pages, ISBN 978-1800783409. GBP12.99 hardcover.

The Crown in Vogue
By Robin Muir and Josephine Ross, 2022. Octopus Publishing Group, London, 304 pages, ISBN 978-1840918205 or e-ISBN 978-1840918304. GBP30.00 hardcover or eBook.

Diamonds: The Queen's Collection
By Caroline de Guitaut, 2022. Royal Collection Trust, London, 120 pages, ISBN 978-1909741843. GBP14.95 hardcover.

Eveli: A Jeweler's Memoir
By Eveli Sabatie, 2022. ACC Art Books, Woodbridge, Suffolk, 336 pages, ISBN 978-1788841924. GBP55.00 hardcover.

Ice Cold. A Hip-Hop Jewelry History
By Vikki Tobak, 2022. Taschen, Cologne, Germany, 388 pages, ISBN 978-3836584975. EUR80.00 hardcover.

Inspired by India: How India Transformed Global Design
By Phyllida Jay, 2022. Roli Books, New Delhi, India, 256 pages, ISBN 978-9392130564. INR4495.00 hardcover.

Tiffany & Co.: The Story Behind the Style
By Rachael Taylor, 2022. Self-published via Studio Press, 160 pages, ISBN 978-1800783416. GBP12.99 hardcover.

MISCELLANEOUS

Homo Lapidibus: La Passion des Pierres (Man and Stones: The Passion of Stones)
By Anne de Jouvenel-Tugny, 2022. Editions EdiSens, Paris, France, 240 pages, ISBN 978-2351133866 (in French). EUR19.00 softcover.

Naissance d'un Tresor: L'Oeuvre de Toute une Vie (Birth of a Treasure: The Work of a Lifetime)
By Henri-Jean Schubnel, 2022. Editions Jets d'Encre, Paris, France, 268 pages, ISBN 978-2355236785 (in French). EUR21.90 softcover.

Pegmatites and Their Gem Minerals
By Michael Menzies and Jeff Scovil, 2022. The Canadian Mineralogist Special Publication 15, Mineralogical Association of Canada, Québec City, Québec, Canada, 602 pages, ISBN 978-0921294665. CAN125.00 hardcover.

Pegmatology: Pegmatite Mineralogy, Petrology and Petrogenesis, 2nd edn.
By William 'Skip' Simmons, Karen L. Webber, Alexander L. Falster, Encar Roda-Robles and Donald A. Dallaire, 2022. Rubellite Press, Cana, Virginia, USA, 287 pages, ISBN 978-0974061351. USD80.00 hardcover.

Silhouette
By Stuart Wilensky, Troy Wilensky and Evan D'Arpino, 2022. Wilensky Exquisite Minerals, New York, New York, USA, 65 pages, no ISBN. USD25.00 softcover.

SSEF 1972–2022
By Michael Krzemnicki and Laurent Cartier, 2022. Swiss Gemmological Institute SSEF, Basel, Switzerland, 208 pages, ISBN 978-3033093300. CHF50.00 hardcover.

ORGANIC/BIOGENIC GEMS

Amber: From Antiquity to Eternity
By Rachel King, 2022. Reaktion Books, London, 272 pages, ISBN 978-1789145915 or e-ISBN 978-1789145922 (ePub). GBP30.00 hardcover, ePub or PDF.

PEARLS

Pearl: Nature's Perfect Gem
By Fiona Lindsay Shen, 2022. Reaktion Books, London, 288 pages, ISBN 978-1789146219 or e-ISBN 978-1789146226. GBP25.00 hardcover or eBook.

SOCIAL STUDIES

A Brilliant Commodity: Diamonds and Jews in a Modern Setting
By Saskia Coenen Snyder, 2022. Oxford University Press, Oxford, 320 pages, ISBN 978-0197610473. GBP26.99 hardcover.

Thank You, Guest Reviewers

The following individuals served as guest reviewers during the past publication year. A special thanks is extended to each one of them for lending their expertise to reviewing manuscripts submitted to *The Journal*. Together with the Associate Editors, these individuals have enhanced the quality of *The Journal* through their knowledge and professionalism.

Dr Ilaria Adamo
Italian Gemological Institute, Milan, Italy

Dr Giovanni B. Andreozzi
Sapienza University of Rome, Italy

Prof. Dr Leander Franz
University of Basel, Switzerland

Richard W. Hughes
Lotus Gemology Co. Ltd, Bangkok, Thailand

Prof. John A. Jaszczak
Michigan Technological University, Houghton, Michigan, USA

Dr Anna-Kathrin Malsy
Switzerland

Prof. Gérard Panczer
Claude Bernard University Lyon 1, France

Sarah Steele
Ebor Jetworks Ltd, Whitby, United Kingdom

Literature of Interest

COLOURED STONES

Beryllium incorporation in corundum. M.C. Jollands and E. Balan, *Mineralogical Magazine*, 2022, **86**(5), 758–766, https://doi.org/10.1180/mgm.2022.63.

Causes of color in purple- and yellow- quartz. N. Monarumit, S. Sakkaravej, B. Wanthanachaisaeng, C. Saiyasombat and W. Wongkokua, *Journal of Physics: Conference Series*, **1719**(1), 2021, article 012001 (5 pp.), https://doi.org/10.1088/1742-6596/1719/1/012001.*

Characterization of structural orientation and optical properties of Al and Cr in rubies. A. Bootchanont, C. Wattanawikkam, P. Porjai, W. Sailuam, W. Busayaporn, C. Saiyasombat, P. Kidkhunthod, J. Borsup *et al.*, *Radiation Physics and Chemistry*, **199**, 2022, article 110315 (6 pp.), https://doi.org/10.1016/j.radphyschem.2022.110315.

Characterization of yellow-green Hetian jade in Qiemo–Ruoqiang, Xinjiang. X. Zhang, Y. Feng, Y. Zhang and A. Matiuohuti, *Rock and Mineral Analysis*, **41**(4), 2022, 586–597, https://tinyurl.com/bdfr62m3 (in Chinese with English abstract).

Colour origin of brown opal in Ethiopia. J. Moon, *Journal of the Gemmological Association of Hong Kong*, **43**, 2022, 58–63, http://www.gahk.org/journal/2022/a13.pdf.*

The composition & lithological characteristics of Tianhuang stone from Shoushan, China. T. Chen, C. Yao and Y. Liu, *Journal of the Gemmological Association of Hong Kong*, **43**, 2022, 18–21, http://www.gahk.org/journal/2022/a8.pdf (in Chinese with English abstract).*

Crystal-chemical observations and the relation between sodium and H_2O in different beryl varieties. R.E. Henry, L.A. Groat, R.J. Evans, J. Cempírek and R. Škoda, *Canadian Mineralogist*, **60**(4), 2022, 625–675, https://doi.org/10.3749/canmin.2100050.

The inner architecture of tourmaline crystals, as inferred from the morphology of color zones in thin slices. P. Rustemeyer, *Journal of Geosciences*, **67**(2), 2022, 103–128, https://doi.org/10.3190/jgeosci.348.*

Mineralogy and mineral chemistry of quartz: A review. J. Götze, Y. Pan and A. Müller, *Mineralogical Magazine*, **85**(5), 2021, 639–664, https://doi.org/10.1180/mgm.2021.72.*

Play-of-colour from Down Under: Looking at the Australian opal industry. *Gems&Jewellery*, **31**(3), 2022, 10–14.

Relationship between moganite and origin of blue chalcedony color in Turkey. K. Zhang, H. Yu, B. Li and Y. Lan, *Superhard Material Engineering*, **34**(3), 2022, 61–66, https://tinyurl.com/2p8n9a89 (in Chinese with English abstract).

Spectroscopic characteristics and color origin of red tourmaline from Brazil. M. Li and D. Sajan, *Journal of Spectroscopy*, 2022, article 1769710 (6 pp.), https://doi.org/10.1155/2022/1769710.*

CULTURAL HERITAGE

Análisis arqueométrico, contextual e iconográfico de piezas de ámbar romano localizadas en Augusta Emerita (Mérida, Badajoz) [Archaeometric, contextual and iconographic analysis of pieces of Roman amber located in Augusta Emerita (Mérida, Badajoz)]. M. Bustamante, M. Murillo-Barroso and R. Sabio Gutiérrez, *Conimbriga*, **60**, 2021, 107–142, https://doi.org/10.14195/1647-8657_60_3 (in Portuguese with English abstract).*

Garnet trade in early medieval Europe: The Italian network. C. Boschetti, B. Gratuze and N. Schibille, *European Journal of Archaeology*, 2022, 1–19, https://doi.org/10.1017/eaa.2022.25.*

Gems on canvas: Pigments historically sourced from gem materials. B. LeCroy, *Gems & Gemology*, **58**(3), 2022, 318–337, https://doi.org/10.5741/gems.58.3.318.*

DIAMONDS

Approaches to the diamond potential of the Siberian craton: A new paradigm. V.P. Afanasiev and N.P. Pokhilenko, *Ore Geology Reviews*, **147**, 2022, article 104980 (12 pp.), https://doi.org/10.1016/j.oregeorev.2022.104980.*

Diamond Reflections: The liquids lurking inside your diamonds. E.M. Smith, *Gems & Gemology*, **58**(3), 2022, 370–374, https://tinyurl.com/5537s6y4.*

Electron probe microanalysis and microscopy of polishing-exposed solid-phase mineral inclusions in Fuxian kimberlite diamonds. D. Zhao, *Minerals*, **12**(7), 2022, article 844 (36 pp.), https://doi.org/10.3390/min12070844.*

An insight into the Indian diamond exploration and mining: Past and present. S.V. Satyanarayana, *Journal of the Geological Society of India*, **98**(8), 2022, 1110–1113, https://doi.org/10.1007/s12594-022-2130-y.

Laser ablation of 'diamonds-in-water' for trace element and isotopic composition analysis. Y. Weiss, S. Jockusch, J.M. Koornneef, O. Elazar and G.R. Davies, *Journal of Analytical Atomic Spectrometry*, **37**(7), 2022, 1431–1441, https://doi.org/10.1039/d2ja00088a.

Methods and challenges of establishing the geographic origin of diamonds. E.M. Smith, K.V. Smit and S.B. Shirey, *Gems & Gemology*, **58**(3), 2022, 270–288, https://doi.org/10.5741/gems.58.3.270.*

GEM LOCALITIES

Meta-bauxite deposit in the Tavşanlı zone, NW Turkey: A new locality for gem-quality diaspore formation. İ. Gündoğan, *Journal of Asian Earth Sciences: X*, **8**, 2022, article 100114 (20 pp.), https://doi.org/10.1016/j.jaesx.2022.100114.*

Sapphire beneath the rich black soil of Muling, northeastern China. Y. Liu and R. Lu, *Gems & Gemology*, **58**(3), 2022, 290–317, https://doi.org/10.5741/gems.58.3.290.*

World's largest gem-quality ruby unearthed in Mozambique. R.G. Sikri, *Gems&Jewellery*, **31**(3), 2022, 16–17.

INSTRUMENTATION AND TECHNOLOGY

Discrimination of precious and semi-precious gemstones using laser-induced breakdown spectroscopy and machine learning approaches. A. Zamira, S.Z.H. Rizvi, M.S. Roslan, N.N. Adnan, S.N.A. Razak and M.A. Jalil, in A.B. Mustapha, S. Shamsuddin, S.Z.H. Rizvi, S.B. Asman & S.S. Jamaian, Eds., *Proceedings of the 7th International Conference on the Applications of Science and Mathematics 2021*. Springer Nature, Singapore, 2022, 165–174, https://doi.org/10.1007/978-981-16-8903-1_17.

DNA fingerprinting as a tool in modern gemmology. L.E. Cartier, M.S. Krzemnicki and B. Lendvay, *Journal of the Gemmological Association of Hong Kong*, **43**, 2022, 13–16, http://www.gahk.org/journal/2022/a7.pdf.*

Element identification of different gemstones by using LIBS-PCA method. N.M. Saufi, N.N. Adnan, S.Z.H. Rizvi, M.S. Roslan, S.N. Razak, N. Hasim and N.I. Mansor, in A.B. Mustapha, S. Shamsuddin, S.Z.H. Rizvi, S.B. Asman & S.S. Jamaian, Eds., *Proceedings of the 7th International Conference on the Applications of Science and Mathematics 2021*. Springer Nature, Singapore, 2022, 155–163, https://doi.org/10.1007/978-981-16-8903-1_16.

JEWELLERY HISTORY

Platinum Jubilee: The Queen's accession. R. Church, *Gems&Jewellery*, **31**(3), 2022, 41–45.

The tradition of mourning jewellery among the royal family. *Gems&Jewellery*, **31**(3), 2022, 38–40.

Ulrike Sophie Von Levetzow's jewels collection: Identification and restoration. R. Hanus, P. Hladký and G. Vyskočilová, *International Journal of Conservation Science*, **13**(2), 2022, 367–380, https://ijcs.ro/public/IJCS-22-27_Hanus.pdf.*

MISCELLANEOUS

Beauty frozen in a crystalline world. S.L.F. To, *Journal of the Gemmological Association of Hong Kong*, **43**, 2022, 78–84, http://www.gahk.org/journal/2022/a16.pdf.*

Damage caused to gemstones by lasers during jewellery repair. M.S. Krzemnicki, L. Kiefert and K. Schollenbruch, *Journal of the Gemmological Association of Hong Kong*, **43**, 2022, 23–27, http://www.gahk.org/journal/2022/a9.pdf.*

The impact of durability & technology on gemstone fashioning. D. Wallace, *Gems&Jewellery*, **31**(3), 2022, 34–37.

Microscopic exploration of gem and mineral surfaces. N. Renfro, *Gems&Jewellery*, **31**(3), 2022, 22–25.

The new Allison and Roberto Mignone Halls of Gems and Minerals at the American Museum of Natural History, New York City. P.K.M. Megaw, *Rocks & Minerals*, **97**(2), 2022, 114–129, https://doi.org/10.1080/00357529.2022.2004510.

NEWS PRESS

After Queen Elizabeth II's death, many Indians are demanding the return of the Kohinoor diamond. C. De Guzman, *Time*, 9 September 2022, https://time.com/6212113/queen-elizabeth-india-kohinoor-diamond.*

How India is building a pearl farming industry. P. Gupta, BBC, 6 September 2022, https://www.bbc.com/news/business-62204515.*

ORGANIC/BIOGENIC GEMS

Analysis of amber components by matrix-assisted laser desorption/ionisation time-of-flight mass spectrometry. Z. Zhang and A.H. Shen, *Journal of Gems & Gemmology*, **24**(4), 2022, 1–9, https://tinyurl.com/2p8yb7xj (in Chinese with English abstract).*

Research progress on identification characteristics of ambers from different product areas. J. Liu and L. Xinyi, *Superhard Material Engineering*, **34**(2), 2022, 63–66, https://tinyurl.com/59m5jfmc (in Chinese with English abstract).

Spectroscopic characteristics of amber in Kaliningrad, Russia. S. Lu and X. He, *Journal of the Gemmological Association of Hong Kong*, **43**, 2022, 45–55, http://www.gahk.org/journal/2022/a12.pdf (in Chinese with English abstract).*

PEARLS

Alchemy and the production of artificial pearls. M. Klčo, *Gemologický spravodajca (Gemmological Newsletter)*, **12**(1), 2022, 18–24, https://www.gu.fpv.ukf.sk/images/GS/2022_1_klco.pdf (in Slovak with English abstract).*

Impact of culture period on quality of image pearls produced by the freshwater mussel, *Lamellidens marginalis*, in Bangladesh. M.B. Tanu, A.C. Barman, M.F. Siddque, S. Sku, M.N. Hossen, P.C. Southgate and Y. Mahmud, *Journal of Shellfish Research*, **41**(1), 2022, 75–83, https://doi.org/10.2983/035.041.0104.*

Progress towards reestablishing Latin America as a major pearl producing region: A review. P.E. Saucedo, D. McLaurin, C. Lodeiros, L. Freites, L. León, J.I. Cáceres-Puig, M.C.P. Albuquerque, P.C. Southgate *et al.*, *Reviews in Aquaculture*, **15**(1), 2022, 242–260, https://doi.org/10.1111/raq.12714.

A study on improving the surface appearance of low-quality *Pinctada maxima* bead cultured pearls. N. Nilpetploy and K. Lawanwong, *Journal of the Gemmological Association of Hong Kong*, **43**, 2022, 65–73, http://www.gahk.org/journal/2022/a14.pdf.*

SIMULANTS

Copper-doped artificial blue glass containing synthetic wollastonite inclusions. J. Štubňa, *Gemologický spravodajca (Gemmological Newsletter)*, **12**(1), 2022, 5–11, https://www.gu.fpv.ukf.sk/images/GS/2022_1_stubna_a.pdf (in Slovak with English abstract).*

Gemmological characteristic of colour coated cubic zirconia. S. He, M. Chen and K. Luo, *Journal of Gems & Gemmology*, **24**(4), 2022, 26–32, https://tinyurl.com/3yytyatz (in Chinese with English abstract).*

Glass production from rice husk ash as an imitation gemstone products. S. Ravangvong, S. Khunnarong, S. Temmawat, S. Chaichalerm, W. Nissapa, K. Pinnak, B. Sriumnuay, K. Sriwongsa *et al.*, *Materials Today: Proceedings*, **65**(4), 2022, 2376–2379, https://doi.org/10.1016/j.matpr.2022.05.359.

Identification of "green phantom crystal" imitation. Y. Bao, *Journal of Gems & Gemmology*, **24**(4), 2022, 33–36, https://tinyurl.com/5n86fsta (in Chinese with English abstract).*

SOCIAL STUDIES

The benefits of gemstone mining. The Gemstones and Jewellery Community Platform, *Gemmology Today*, September 2022, 18–21, https://tinyurl.com/5ferwrnj.*

Mine games: Big fish, small fry [formal gem mines vs artisanal operations]. G. Dominy, *Gemmology Today*, September 2022, 64–75, https://tinyurl.com/y8rn7mnu.*

SYNTHETICS

Application of ultraviolet-visible optical fiber spectrometer in the identification of synthetic emerald. H. Zhou, C. Fang, P. Wu and B. Wang, *Superhard Material Engineering*, **34**(2), 2022, 53–57, https://tinyurl.com/28tkttbv (in Chinese with English abstract).

Effect of viscous metals on the synthesis of high grade diamond. S. Xue, *Superhard Material Engineering*, **34**(3), 2022, 31–34, https://tinyurl.com/2p8t2nm6 (in Chinese with English abstract).

Gemological characteristic difference between colorless CVD synthetic diamonds and natural diamonds. Q. Lu, H. Gong, Q. Guo, X. Huang and J. Cai, *Materials*, **14**(20), 2021, article 6225 (11 pp.), https://doi.org/10.3390/ma14206225.

Synthesis of transparent polycrystalline jadeite under high pressure and temperature. K. Mitsu, T. Irifune, H. Ohfuji and A. Yamada, *Journal of Mineralogical and Petrological Sciences*, **116**(4), 2021, 203–210, https://doi.org/10.2465/jmps.210319.*

TREATMENTS

Baking color experiment of Burmese amber at different temperatures and its different identification characteristics with natural blood amber. R. Xiao, F. Gong and H. Zhang, *Superhard Material Engineering*, **34**(2), 2022, 47–52, https://tinyurl.com/44newc3r (in Chinese with English abstract).

Color mechanism and spectroscopic thermal variation of pink spinel reportedly from Kuh-i-Lal, Tajikistan. Y. Liu, L. Qi, D. Schwarz and Z. Zhou, *Gems & Gemology*, **58**(3), 2022, 338–353, https://doi.org/10.5741/gems.58.3.338.*

Identification of blue, red and green [treated] beads from India. J. Štubňa, *Gemologický spravodajca (Gemmological Newsletter)*, **12**(1), 2022, 12–17, https://www.gu.fpv.ukf.sk/images/GS/2022_1_stubna_b.pdf (in Slovak with English abstract).*

Identification characteristics of Burmese root amber with filling treatment. T. Wu and Y. Bai, *Superhard Material Engineering*, **34**(3), 2022, 51–56, https://tinyurl.com/sf8zer9n (in Chinese with English abstract).

COMPILATIONS

***G&G* Micro-World.** Breyite in diamond • Diopside in elbaite • Purple fluid in quartz • Rutile in chameleon diamond • 'Smoke rings' in heated sapphire • Stellate zircon in Paraíba tourmaline • Fluorapatite in quartz from Panasqueira, Portugal. *Gems & Gemology*, **58**(3), 2022, 364–369, https://tinyurl.com/yk89v24e.*

Gem News International. Saltwater cultured pearls with rectangular beads • Colour-zoned quartz with oriented inclusions from Brazil • Mozambique ruby mining update • Pressed amber imitation of 'root amber' • Synthetic sapphire with rose channels • 'Gel-filled' turquoise • Report on Turquoise United conference • Dr Ahmadjan Abduriyim receives JAMS Award for applied mineralogy • Hidden Gems at the San Diego Natural History Museum • The Year of Mineralogy at the Perot Museum • In Memoriam: Andrew Cody. *Gems & Gemology*, **58**(3), 2022, 370–374, https://tinyurl.com/3ak636xn.*

Lab Notes. 1.21 ct fancy red diamond • Treated Ni-bearing green diamond • Brazilian emerald with *gota de aceite* effect • Treated orange and pink CVD synthetic diamonds • Non-nacreous pearl reportedly from *Telescopium telescopium* • Kashmir star sapphire • Fraudulently inscribed synthetic moissanite • Synthetic moissanite imitating a diamond crystal • Cat's-eye Paraíba tourmaline with copper inclusions. *Gems & Gemology*, **58**(3), 2022, 354–363, https://tinyurl.com/5n6ryd8y.*

CONFERENCE PROCEEDINGS

6th Mediterranean Gemmological and Jewellery Conference. Thessaloniki, Greece, 12–14 August 2022, 40 pp., https://www.brankogems.com/shop/proceedings/proceedings-2022-mediterranean-gem-and-jewellery-conference-thessaloniki.

**Article freely available for download, as of press time*

REGISTER NOW!

GemINTRO

GemIntro is a Level 2, online, entry-level course which will introduce you to the fascinating world of gemmology and the enormous variety of beautiful gems available. You can discover the basics of gemmology at your own pace - perfect for anyone looking to start or grow their career in the gems and jewellery trade, or for those completely new to gemmology and with an interest in gems.

Register now at **gem-a.com/gemintro**

Gem-A
THE GEMMOLOGICAL ASSOCIATION OF GREAT BRITAIN

Gem-A, 21 Ely Place, London, EC1N 6TD, UK. T: +44 (0)20 7404 3334, W: www.gem-a.com. Registered charity no. 1109555.